



The
University
Of
Sheffield.

Nanotribological properties, nanopatterning and biological interactions of poly(cysteine methacrylate) brushes

By

Omed Qadir Al-jaf

A thesis submitted in partial fulfillment of the requirements for the degree of Doctor of
Philosophy

The University of Sheffield

Faculty of Science

Department of Chemistry

Submission Date: September 2016

Declaration

This work described in this thesis was undertaken at the University of Sheffield between October 2012 and October 2016 under the supervision of Professor Graham J. Leggett. Unless otherwise stated, it is the work of the author and has not been submitted in whole or in part for any other degree at this or any other institute.

September 2016

Signed

Omed Qadir Al-jaf

Department of Chemistry

Dainton Building

University of Sheffield

Brook Hill

Sheffield, UK

S3 7HF

Acknowledgment

First of all, I would like to thank my supervisor Professor Graham J. Leggett for giving me the opportunity to join his group. Thanks for his patient, kind support and advice during my research. Without him, this thesis would not have been possible. Secondly, I would like to thank all of the members of Graham's group. A special mention has to go to Alexander Johnson, Paul Chapman, Robert Ducker, Oscar Siles Brugge, Abdullah Souwaileh, Nan Cheng, Anna Tsargorodska, Osma El. Zubair, Mar Cardellah, Charlie Smith, Sijin Xia, Jeppe A Pedersen, Brice Darroch, Hang Xu, Max W. Chamber, Deborah B Hammond and Martin Munz.

I would like to thank Fawcett Sandra, Curran Jude and Hunt John for collaboration, work, help and constructive discussion about cell adhesion work. My special thanks also go to Peng Bao and Stephen Evans for collaboration, help and work about the Cell membrane project.

I would like to thank all of the friends and relatives for their support and advice over the last few years, with much respect going to my brother Ahmed, my cousin Salih Kakabra, Mr Akram Ali, Mr Usman Amin, Mr Nariman Ahmed, Mr Dler Kadir, Dr Hiwa Karim, Dr Masud Hassan, Dr Jamal Hussein, Mr Esmail Qadir and Mr Aidn Ahmed.

I gratefully acknowledge the funding received towards my PhD from the Kurdistan Regional Government (KRG)-Human Capacity Development program Scholarship.

I would like to thank my parents Qadir and Auzar, my wife Kwestan and my children. I would not have been able to do this without their support.

Acronyms

SAMs = self-assembled Monolayers

OTS = octadecyltrichlorosilane

XPS = X-ray photoelectron spectroscopy

AFM = atomic force microscopy

APTES = 3-aminopropyltriethoxysilane

NPPOC = 2-nitrophenylpropyloxycarbonyl

NVOC = o-nitroveratryloxycarbonyl

TFAA = trifluoroacetic anhydride

ATRP = atom transfer radical polymerization

SI-ATRP = surface-initiated atom

transfer radical polymerization

PCysMA = poly(cysteine methacrylate)

NMP = nitroxide mediated polymerization

ROMP = ring opening metathesis

polymerization

SET-LRP = single electron transfer living
radical polymerization

CRP = controlled radical polymerization

P2VP = poly(2-vinylpyridine)

CMPE = 1-trichlorosilyl-2-(m-
pchloromethylphenyl)ethane

PAAm = polyacrylamide

PAA = poly(acrylic acid)

PGMA = poly(glycidyl methacrylate)

PMMA = poly(methyl methacrylate)

PGMA = poly glycidyl methacrylate

UV = ultra-violet

μ CP = microcontact printing

DPN = dip-pen lithography

TBAF = tetrabutylammonium fluoride

SIPP = surface initiated photopolymerization

PDMS = polydimethylsiloxane

PEI = polyethyleneimine

PINPAAM = poly(N-isopropylacrylamide)

EBL = electron beam lithography

PHEMA = poly(2-hydrxyethyl methacrylate)

PTFEMA = poly(2,2,2-trifluoroethyl
methacrylate)

PIBMA = poly(isobutyl methacrylate)

PNMPA = poly(neopentyl methacrylate)

IL = interference lithography

POEGMA = poly(oligo ethylene glycol)
methacrylate)

BIBB-APTES = bromoisobutyryl
amidotriethoxysilane

Bipy = 2,2'-bipyridyl

NPPOC-APTES = 2-
nitrophenylpropyloxycarbonyl-3-
aminotriethoxysilane

RAFT = reversible addition fragmentation
chain transfer

SLBs = supported lipid bilayers

FCS = fluorescence correlation spectroscopy

TIRF = total internal reflection fluorescence

FRAP = fluorescence recovery after
photobleaching

PDMA = poly(2-
dimethylamino)ethylmethacrylate)

PEG = poly(ethylene glycol)

PLLA = poly(L-lactic acid)

MEM = microelectromechanical

NEM = nanoelectromechanical

CFM = chemical force microscopy

JKR = Johnson, Kendall and Roberts

DMT = Derjaguin, Muller and Toporov

COS = Carpick, Oligotree, and Salmeron

TCCM = thin-coated contact mechanics

InvOSL = inverse optical lever sensitivity

PDOPBr = polydopamine

PBL = particle beam lithography

FIBL = focused ion beam lithography

FDTES = perfluorodecyltriethoxysilane

SNOM = scanning near-field optical
microscopy

IBL = ion beam lithography

DMPP = dimethylphenyl phosphine

DCM = dichloromethane

MUA = 11-mercaptoundecanoic acid

CysMA = cysteine methacrylate

POPC = 1-palmitoyl-2-oleoyl-sn-glycero-3-
phosphocholine

DOTAP = 1,2-dioleoyl-3-
trimethylammonium-propane

RCA = radio corporation of america solution

FWHM = full width at half maximum

MSCs = mesenchymal stem cells

cps = counts per second

CTCS = 2-(4-cholorosulfonylphenyl)-
ethyltrichlorosilane

PMMA = poly(methyl methacrylate)

hMSC = human Mesenchymal stem cell

PPEGMA = poly[poly(ethylene glycol)
methacrylate]

PCL = poly(ϵ -caprolactone)

CMPTS = 4-(chloromethyl)phenyl
trichlorosilane

Contents

Chapter 1: Introduction	3
1.1 General Introduction.....	3
1.2 Self-assembled Monolayers (SAMs).....	3
1.2.1 Kinetics of Monolayer formation	5
1.2.2 Alkylsilane Films	7
1.3 Polymer Brushes	11
1.3.1 Structural definition of polymer brushes.....	14
1.3.2 Patterned Polymer brushes.....	19
1.4 Biological Membrane	22
1.5 Supported-Lipid Bilayers (SLBs).....	23
1.6 Cells patterning	28
1.7 Nanotribology	32
1.7.1 Chemical force Microscopy (CFM)	34
1.7.2 Contact Mechanics in AFM	36
1.7.3 Thin-film contact mechanics	42
1.7.4 Quantification of friction in FFM.....	44
1.7.5 Calibration of Normal force in AFM	47
1.7.6 Calibration of Lateral forces and Tip radius of the cantilever	50
1.8 Lithographic techniques for surface patterning.....	53
1.8.1 Soft lithography.....	53
1.8.2 Microcontact printing (μC_p)	53
1.8.3 Particle beam lithography (PBL).....	55
1.8.4 Photolithography	56
1.8.5 Interference Lithography (IL).....	57
Chapter2: Aims	61
Chapter 3: Experimental	62
3.1 Materials	62
3.2 Cleaning Glassware and silicon wafers.....	63
3.3 Surface self-assembled layer formation and subsequent surface initiation.....	63
3.4 Formation of MUA and ODT self-assembled monolayers on a gold	63
3.5 Synthesis	64

3.5.1 Synthesis of Cysteine Methacrylate monomer (CysMA).....	64
3.5.2 Synthesis of 2-nitrophenylpropyloxycarbonyl-3-aminopropyltriethoxysilane (NPPOC-APTES).....	64
3.6 Formation of NPPOC-APTES film.....	66
3.7 Photolithography.....	67
3.7.1 Nanometre and micrometre scale patterns of APTES-BIBB film.....	67
3.7.2 Gradient PCysMA brushes.....	68
3.7.3 photodegradation of 2-nitrophenylpropyloxycarbonyl-3-aminotriethoxysilane NPPOC-APTES.....	68
3.7.4 Preparation of nanodot and micrometer structures of gold films by photolithography.....	68
3.8 polymerization reaction.....	69
3.9 SLB formation.....	69
3.10 Cell fabrications.....	70
3.11 Surface characterization techniques.....	71
3.11.1 Contact Angle Measurements.....	71
3.11.2 Ellipsometry.....	72
3.11.3 X-ray Photoelectron Spectroscopy (XPS).....	73
3.11.4 Atomic Force Microscopy (AFM).....	75
3.11.5 Friction Force Microscopy (FFM).....	77
3.11.5.1 Modification of AFM probes.....	77
3.11.5.2 Friction force measurements in liquids.....	78
3.11.6 Fluorescence Recovery After Photobleaching.....	79
3.11.7 Fluorescence Microscopy.....	81
Chapter 4: Conformational effect on tribological property of various patterned Poly(Cysteine methacrylate) brushes in different environments.....	84
4.1 Introduction.....	84
4.2 Experimental sections.....	87
4.2.1 Preparation of APTES-BIBB initiator.....	87
4.2.2 Micrometre and nanometre fabrications of ATRP initiator surfaces.....	87
4.2.3 Synthesis of cysteine methacrylate monomer and polymerization reaction.....	88
4.2.4 Surface analysis.....	88
4.3 Results and Discussion.....	88
4.3.1 Model surface reaction.....	88
4.3.2 Friction and scale behaviour of PolyCysMA brushes in water.....	96
4.3.3 PCysMA brushes in ethanol.....	100

4.4 Conclusion.....	103
Chapter 5: Effect of grafting density on the conformational and mechanical properties of PolyCysMA brushes	104
5.1 Introduction	104
5.2 Experimental Sections.....	106
5.2.1 Preparation of APTES-BIBB initiator	106
5.2.2 Gradient ATRP initiator.....	106
5.2.3 Synthesis of cysteine methacrylate monomer and polymerization reaction	106
5.2.4 Surface analysis.....	106
5.3 Results.....	106
5.3.1 Photodegradation and characterisation of ATRP initiator	106
5.3.2 The growth of PolyCysMA brushes and the effect of the initiator density	109
5.3.3 Frictional behaviour of brushes of varying grafting density	111
5.3.4 Effect of brush density on the friction-load relationships of the polymer brushes	117
5.4 Discussion.....	118
5.5 Conclusion.....	122
Chapter6: Investigation of the surface chemistry and morphology on the attachment of mesenchymal stem cells	123
6.1 Introduction	123
6.2 Experimental section.....	126
6.2.1 Preparation of silicon coated silane layer	126
6.2.2 Photodeprotection of NPPOC-APTES film and functionalisation with BIBB	126
6.2.3 Synthesis of Cysteine Methacrylate monomer (CysMA) and polymerization reactions.....	126
6.2.4 Surface analysis.....	127
6.2.5 Photolithography	127
6.2.6 Cell culture	127
6.3 Results and Discussion	128
6.3.1 Formation of SAMs.....	128
6.3.2 Photomodification of NPPOC-APTES and CMPTS films.....	132
6.4 Formation of PolyCysMA brushes on the patterned CMPTS and APTES-BIBB SAMs.....	137
6.5 Formation of PCysMA brushes on patterned NPPOC-APTES films	141
6.6 Culture of human mesenchymal stem cells (hMSC) on patterned polymer brushes	146
6.7 Conclusion.....	151

Chapter 7: Fabrication of Supported-lipid bilayers on the binary patterned gold nanodots/PCysMA brushes	152
7.1 Introduction	152
7.2 experimental section.....	155
7.2.1 Synthesis of 2-Bromo-2-methyl-N-(3-triethoxysilyl-propyl)-propionamide (BIBB-APTES)	155
7.2.2 Preparation of samples	156
7.2.3 Photoirradiation of the samples	156
7.2.4 Derivatization of Cr/Ti region with BIBB-APTES initiator molecules	157
7.2.5 Growing PCysMA brushes between gold features	157
7.2.6 Preparation of supported lipid bilayers.....	158
7.2.7 Surface characterization.....	158
7.3 Result and discussions	158
7.3.1 Photopatterning and etching of alkanethiolate functionalized gold films on Ti/Cr layer	158
7.3.2 Preparation of initiator silane-coated surfaces.....	163
7.3.3 Growing PCysMA brushes between gold nanodots.....	165
7.3.4 Formation of SLBs on the binary patterned gold nanodots/PCysMA brushes	167
7.4 Conclusion.....	171
Chapter 8: Summary of thesis	172
8.1 Fabrication of PCysMA micro – and nanostructures and characterisation of their behaviour as a function of feature size and grafting density	172
8.2 Mesenchymal stem cell cultivation on nanometer patterned PCysMA brushes	173
8.3 Formation of supported lipid bilayers on the binary patterned gold nanodots/PCysMA brushes.....	174
8.4 Future works	175
References.....	177

Abstract

The goal of this project was to develop a strategy to fabricate various nanometre and micrometre scale structures for biocompatible poly(Cysteine methacrylate) (PCysMA) brushes by photopatterning of 3-(2-bromoisobutyramido)propyl triethoxysilane (APTES-BIBB) film on a silicon surface. Micrometre scale structures were formed by exposure through a mask, and nanometre scale structures by Interference lithography. UV exposure causes debromination of the surfaces. Surface-initiated atom transfer radical polymerization (SI-ATRP) was used to grow the brushes from the ATRP initiators. Friction force microscopy (FFM) was used to investigate the conformations of the brushes as a function of footprint sizes in different environments. The friction - load relationship was found to be dependent on the conformation of the brushes, which is then was found to be influenced by the solvent medium. In a good solvent, sublinear friction-load relationships were acquired that were fitted with the Derjaguin-Muller-Toporov (DMT) model of contact mechanics, for nanostructured materials the contact mechanics were found to depend on the periodicity of the patterns. For large periods, the grafted polymer molecules exhibit a brush conformation, but this starts to collapse when the period is reduced below the critical value. In contrast, in poor solvent linear friction-load relationships were acquired and the friction coefficient increased as the period increased. In a poor solvent the polymer molecules collapse and form mushroom or pancake structures. These observations were rationalised by considering the friction values as a sum of an interfacial (shear) and plowing (load) dependent term.

Unpatterned brushes of controlled, but varying densities were fabricated by maskless UV exposure of brominated films followed by SI-ATRP. By varying the exposure, the density of initiator sites was changed. The contact mechanics were studied as a function of brush coverage. In a good solvent, sublinear friction-load relationships were observed at high density, but the relationship became linear as the density decreased. The change is attributed to a change in the conformation, from brushes at high grafting density to mushrooms and the pancakes as the density decreased. In a poor solvent, the friction-load relationship was linear regardless of grafting density. This means that energy dissipation by molecular ploughing was

dominate for poorly solvated brushes. The friction coefficient increased initially as the grafting density decreased, then started to decrease as the density further reduced.

The impact of nanotopography, chemistry and utility of non-biofouling of PCysMA brushes on the cultivation of mesenchymal stem cells (MSC) has been explored. AFM, ellipsometry, XPS, contact Angle goniometry, and fluorescence microscopy have been utilised to characterise the surfaces. Interference lithography (IL) was used to pattern three different types of SAM, including 2-nitrophenylpropyloxycarbonyl-protected aminosiloxane (NPPOC-APTES), (chloromethyl)phenyltrichlorosilane (CMPTS) and APTES-BIBB film. The patterned SAMs were used as templates to control SI-ATRP. Uniform polymer brush structures showed excellent resistance toward nonspecific adsorption of the cells, after 7 days of culture. The cells attached successfully on the patterned surfaces, but their alignments and organisations were different, depending on the feature sizes of grafted polymer lines and the chemistry of adhesive regions. Immunocytochemical methods were used to characterise the effect of nanoscale surface cues on cytoskeletal organisation in MSCs grown on these surfaces.

A method was developed for the fabrication of lipid bilayers supported on a PCysMA brush layer with integral gold nanostructures, to facilitate spectroscopic characterisation using plasmonic techniques. Gold nanostructures were formed using IL to pattern a resist consisting of SAM of octadecanethiol on gold. Regions between nanostructures were functionalised with an aminosilane which was brominated and used as an initiator for SI-ATRP. The polymer growth was controlled so that swollen brushes in water had heights identical to the heights of the Au nanostructures. Supported lipid bilayers were formed on these materials and lipid mobility was characterised using fluorescence recovery after photobleaching (FRAP). Mobilities were achieved that were similar to those obtained for positive control surfaces (glass).

Chapter 1: Introduction

1.1 General Introduction

In recent years there has been an increasing trend towards miniaturization in the replacement and repair of human organs and electronic devices. The advent of micro- and nanotechnology has accelerated this trend.

Surfaces have become increasingly important in technology as miniaturisation has progressed. Polymer brushes have shown great promise for regulating the surface characteristics of materials, leading to intriguing applications in fields including coating, sensing, biomaterials, catalysis and others¹. The major task in the development of grafted polymer brushes is to regulate, adjust and control the interaction forces between the brush and its environment, including liquid, vapour, solid, other brush and biological molecules. Properties such as friction coefficient, adhesion and wettability, mechanical stability, biocompatibility, antifouling and corrosion resistance of the brushes play a vital role in enhancing their potential applications. In addition, there are now comparatively simple ways to manipulate brush structures on small length scale, including soft lithography and photolithography. A wide range of monomers has been formed to be suitable for use on various substrates. The simplicity, low cost and versatility of popular brush formation makes it a very attractive strategy when compared to other surface modification techniques².

1.2 Self-assembled Monolayers (SAMs)

Self-assembled monolayers (SAMs) have become widely used for the fabrication micro- and nanostructures by various fabrication techniques³⁻⁶. SAMs are formed by the spontaneous adsorption of surfactants from solution on the surfaces of suitable substrates. Suitable adsorbates are composed of three different groups, each having specific functions. The reactive head group forms a strong, specific interaction with surface functional groups. The adsorbate-substrate interaction may involve either the formation of chemical bonds or physical interactions. The head group is linked to a hydrocarbon alkyl chain known as a spacer. The spacer is attached to a tail group that determines the functionality of the SAM surface (figure

1.1). The structure of the SAM is the result of a combination of factors, including the spontaneous formation of a strong bond to the surface, which tends to drive the formation of a dense surface layer, and lateral intermolecular interactions which cause the substrate to adopt an ordered structure.⁶⁻⁹

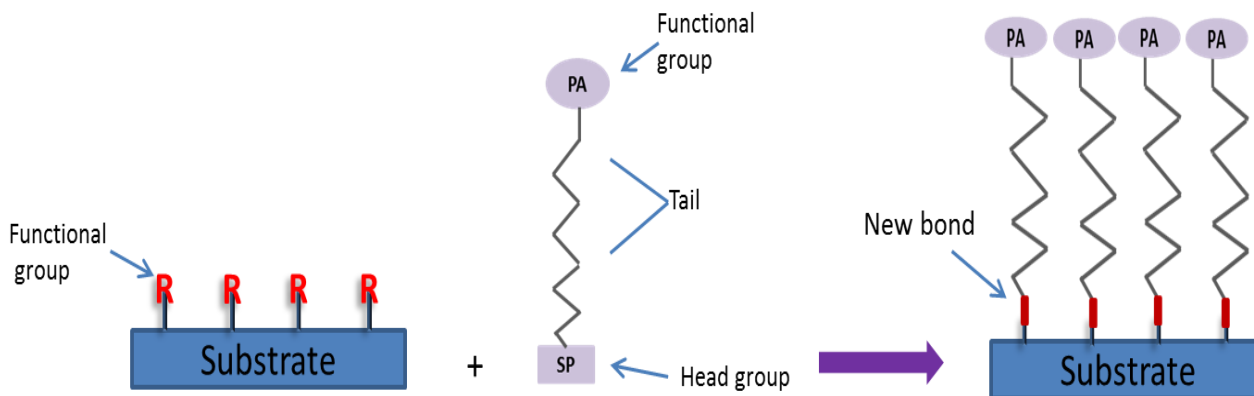


Figure1.1: Schematic diagram showing the self-assembly of molecules onto a surface.

The ability to tailor surface properties by both the head group and the reactivity of the functional group of the adsorbates makes SAMs ideal model systems for studying surface interfacial interaction. The role of intermolecular forces and interfacial forces in phenomena such as wetting, adhesion, transport, corrosion, and lubrication can be studied using SAMs as model surfaces⁶. In addition, due to several other advantageous properties of SAMs such as ease of preparation, not needing ultra-high vacuum and other specialised equipment and their flexibility, stability, and functionality SAMs have attracted widespread interest during the last three decades. However, it is interesting to reflect on the modest beginning of the field and vital efforts to develop it. The first recorded attempt of SAM formation was reported by Zisman in 1946. He reported forming monomolecular layers of long chain alcohol compounds on glass and platinum surfaces. The layers were not only hydrophobic, but also they were not wet with the solution and the solvent (oleophobic), due to the close-packing of the long chains on the surfaces⁹. Sagiv described a different oleophobic SAM system in 1980 that could be considered as a well-defined method for fabricating the monolayer films with controllable molecular organisations.

He revealed the possibility of fabrication of mixed silane SAMs on different substrates, by adsorption of a dilute solution and studied the kinetics of interaction between adsorbed molecules and those in the solution¹⁰. In 1983 Nuzzo et al. provided the foundation for the subsequent SAMs revolution when they modified gold surface by disulfides with a variety of molecular structures¹¹. This work was taken forward by Whitesides and co-workers in 1987, who prepared SAMs by the adsorption of long chain thiols on the evaporated gold. The resulting layers were characterized, using Ellipsometry, XPS, and contact angle measurements. The results indicated that the stability of the SAMs increased as long chains increased¹². Since then a very wide range of studies has been carried out on various SAMs formed on different substrates for numerous objects, including many fields in nanoscience and nanotechnology¹³⁻¹⁴. Potential applications of SAMs in different areas have been identified, including molecular electronics¹⁵, biosensors¹⁶, nanofabrication of protein and DNA¹⁷, adhesion, wetting, lubrication, and corrosion^{18,19}.

1.2.1 Kinetics of Monolayer Formation

Significant effort has been devoted to understanding the mechanism of formation of a self-assembled monolayer on a solid substrate. Three vital processes have been identified in this phenomenon. The first step involves the transport of adsorbates from the bulk solution onto the adsorbent surface (liquid-solid interface). The second is the adsorption process, which is determined by interactions between the head groups of the adsorbate molecules and the functional groups of the surfaces. This step depends on the physicochemical properties of both surfactant and surface components. The final step is the self-arrangement of the mobile adsorbed molecules to form 2-dimensional structures on the surface. These processes are considered to be critical to SAM stability and functionality²⁰. It has been shown that the kinetics of SAM formation can be modelled effectively using the Langmuir isotherom^{23,21}.

This model assumes that the rate of adsorption is directly proportional to the fraction of free space at the surface

$$d\theta/dt = k(1-\theta) \quad (1.1)$$

$d\theta/dt$ is the rate of change of the fractional coverage θ with time, $(1-\theta)$ is the fraction of unoccupied surface sites, and k is the adsorption rate constant. The coverage increases rapidly at first, and then more slowly as a monolayer coverage is approached²²⁻²⁵. The adsorption rate, depends on the temperature, concentration, solvent, surface contamination, and immersion time. Osamu et al. studied the effect of temperature on the growth mechanism of octadecyltrichlorosilane self-assembled monolayers on silica surfaces by using AFM, XPS, FT-IR and contact angle goniometry techniques. They showed that the density of adsorbed OTS molecules produced at low temperature was higher than the density of the molecule prepared at high temperature. In addition, the formation of a siloxane bond between silane molecules was vital for self-organization of the OTS monolayer.

The effect of the roughness of the substrate surface on the kinetics of the formation of a self-assembled layer of silane has been investigated. It has been revealed that silane island growth happens preferentially along grain boundaries in fingerlike architectures having molecular arrangements comparable to that observed on smooth silicon surfaces. The reason for preferential immobilization of the surfactants is likely because of the presence of thicker adsorbed layers of water at converging grains²⁸. Vijayamohan et al. reported an investigation of the kinetics and thermodynamics of adsorption of octadecyltrichlorosilane. Acquired data illustrated a rapid growth of the monolayer at the initial stage, decreasing as the fractional coverage increased²⁶. It has been suggested that OTS retains partial molecular order better than monolayers of alkylcarboxylic acid when it is subjected to thermal cycles²⁷. The other important factor is the effect of the concentration of the adsorption solution on the rate of the island growth and the rate of adsorption. If it is Langmuir-type adsorption, the dependence of the rate of adsorption on the concentration is defined by the adsorption isotherm²⁸⁻²⁹. Schwartz and coworkers studied the growth of the formation of SAMs as a function of the concentration of the surfactant solution. They found that the extracted diffusion parameters for the monolayer

formations did not actually scale with the solution concentration. Thus, the kinetics of island growth were controlled by a process follows diffusion-like kinetics (possibly a surface diffusion or assembly process) not by bulk transport or adsorption³⁰. A kinetic study of the growth of octadecanethiol (ODT) and p-nitrobenzenethiol from ethanol solutions was under taken. Contact angle, ellipsometry an angle-resolved XPS suggested that the density and the thickness of the monolayers depend on the immersion time of gold substrate into the organothiol solutions and the concentration of the solutions³¹.

The amount of water also plays a crucial role in the kinetics of growth of organosilane layers on oxide surfaces. High water content leads to the hydrolysis of large numbers of the adsorbates and the formation of a large number of silanol bonds. Thus, polymerization of organosilanes occurs in the bulk solution and instead of monolayers; multilayers are formed on the surface. On the other hand, too low a water content causes insufficient amounts of adsorbate hydrolysis, and an incomplete and inhomogeneous silane monolayer will result³²⁻³⁴. It is widely accepted for different kinds of monolayer formation that the rate of surface modification is increased initially as the exposure time of the surface the adsorption solution increased and then it decreases gradually. This is due to a large number of collisions between surfactants and adsorbent surfaces and a large area of free space on the substrate surfaces at the initial stage of the reaction. When the exposure time increases, the number of collisions and the amount of free space decreases gradually until they reach their limiting values³⁵.

1.2.2 Alkylsilane Films

Organosilane molecules have been widely utilised to fabricate self-assembled monolayers with various functional groups the different oxide surfaces³⁶⁻⁴⁰. The general formula of alkyl substituted silanes is $(X)_3\text{—Si—R}$, where X could be Cl, OCH_2 , OCH_3 or OEt and R is an alkyl chain, which may contain aromatic or heteroatoms. Due to the high reactivity of the head group of the organosilane a strong interaction occurs between the surface functional group (Si—OH) and the hydrolyzed silanol group of the head group. Subsequently, a covalent bond (Si—O—Si) is produced and a chemisorbed silane structure is formed on the surface.

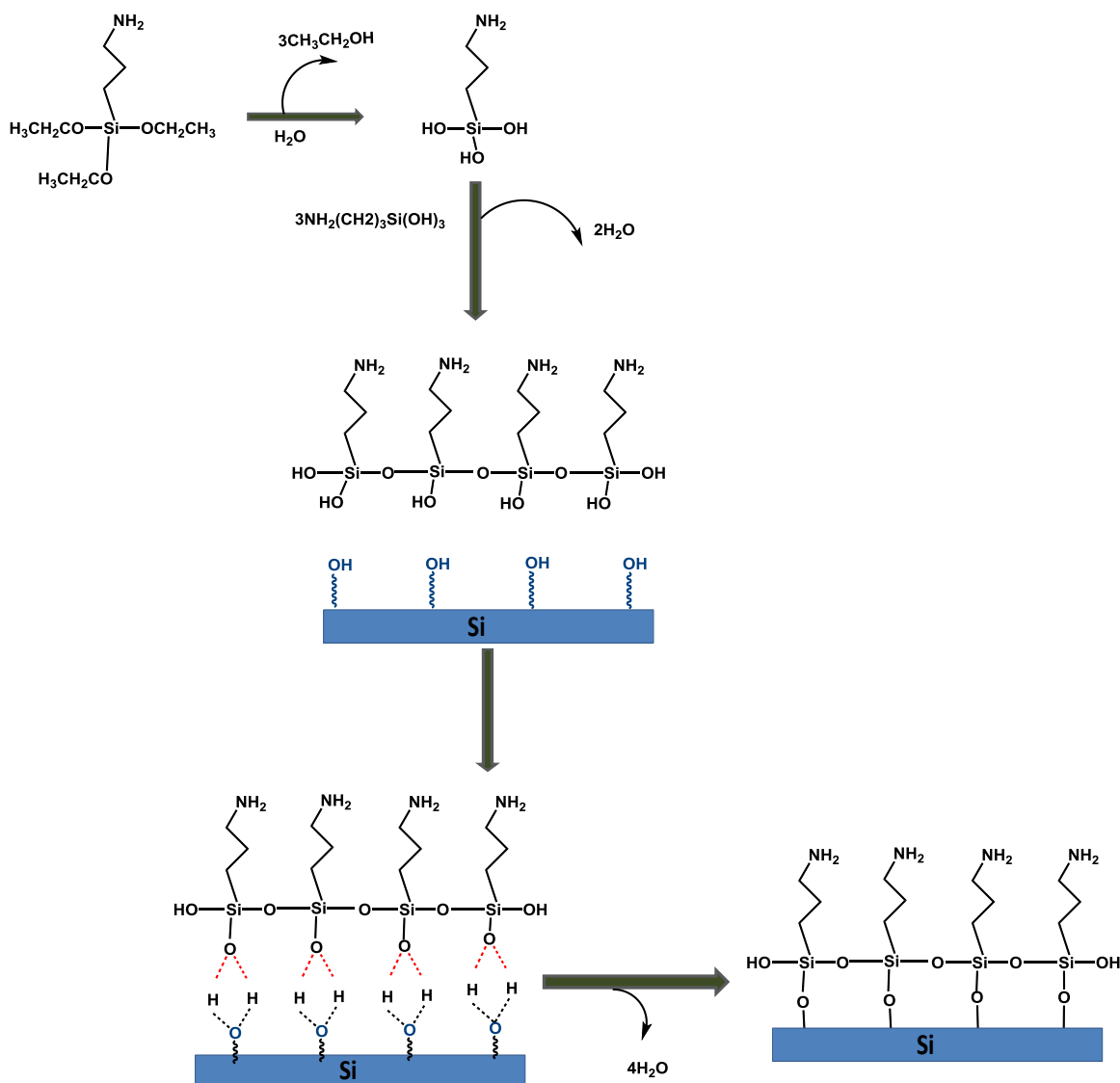


Figure 1.2: A reaction mechanism for the formation of alkylsilane monolayer⁴⁴.

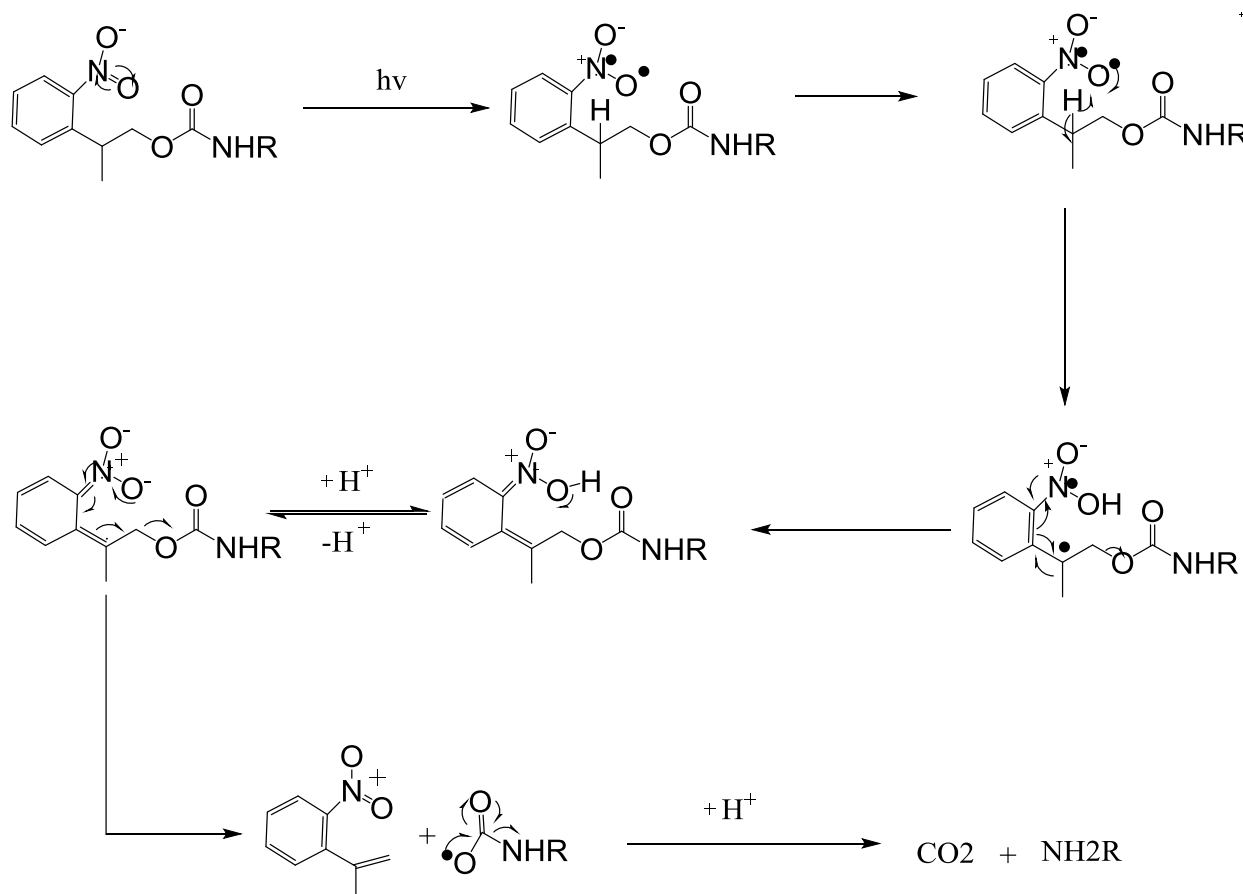
Intermolecular interactions between surfactants lead to the formation of cross-links bond between them and lateral dispersion interactions between the adsorbates provide further stabilisation. Consequently, a very stable monolayer is formed⁶. In 1992 Arkles et al. described the mechanism of self-assembly of alkylsilanes. The pathway includes three main steps (figure 1.2). Silanols are formed by hydrolysis of trialkoxysilanes in the presence of water, either present in the solvent or adsorbed on the substrate. The silanols condense with each other in

the second step of the pathway, an intermediate condensation step. Finally, the polymerised silanols start to form a hydrogen bond with hydroxyl functional groups of the substrates, followed by formation of a linkage between the surfactants and the solid surface⁴¹⁻⁴². It has been demonstrated that several important factors lead to the formation of a uniform surface, including the water content, type of solvent, immersion time, temperature, and the precise nature of both the self-assembled molecules and the surfaces⁴³. It appears that the amount of water is crucial in the reaction of silanol with hydroxyl surfaces because water acts as a catalyst and the head group is hydrolyzed by water. If the water content is high the polarisation of silanols occurs far away from the surface. As a consequence, a multilayer film will be produced⁴⁴.

In 1980, Sagiv showed that homogeneous and close-packed organosilane monolayers containing more than one component can be fabricated on the surfaces of different oxide substrates. It was demonstrated that the nature of the substrate and the surfactant components determine the type of interaction between them, whether physical or chemical or both¹³. Self-assembled layers of fluoroalkyl-functional silane with different chain lengths were prepared on silicon substrates. The high quality of the SAMs was confirmed by characterising the samples using contact angle, XPS, ellipsometry and coefficient of friction measurements⁴⁵. Moreover, the polarity of the solvent exerts a crucial influence on the reaction. A polar solvent tends to lead the formation of an increased number of silanol groups through hydrolysis reactions. These groups are condensed subsequently on the surface. In contrast, the number of silanols decreases with decreasing solvent polarity. In anhydrous conditions, the dominant mode of interaction is physisorption, in which van der Waals and dispersion forces hold the adsorbate on the surface instead of the covalent bonds⁴⁶.

Modification of oxide surfaces with organosilane self-assembled molecules has been widely investigated in a variety of applications. Organosilane molecules provide different functional groups at the surfaces such as -NH₂, -COOH, SH, -CN, which can be used to build up more complex systems⁴⁷. Recently, surface modification with silanes has been used in the development of the methods for the integration of top-down (lithographic) and bottom-up

(synthetic method) on the nanoscale. Silanes possessing a reactive (amino group) at the tail have been protected with a photocleavable group.



Scheme 1.1: Shows a proposed mechanism of photodeprotection of NPPOC.

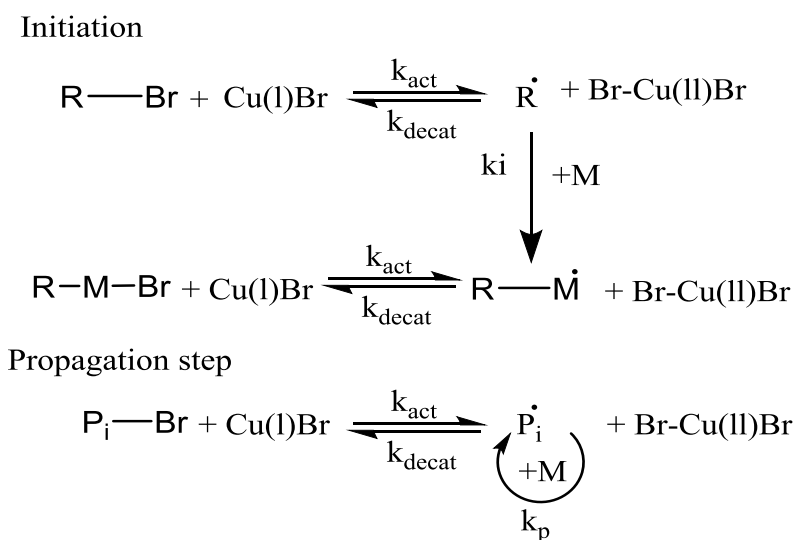
These have been used in the conjunction with nanofabrication techniques, which are capable of positioning and characterising nanostructures on the nanoscale⁴⁸⁻⁴⁹. The flexibility and reactivity of these groups once deprotected means that after patterning a wide range of molecules can be combined with the resulting template. Nitrobenzyl-based protecting group chemistries have been well established for such photodeprotection schemes, whether in solution^{50 51} or on surfaces. 2-Nitrophenylpropyloxycarbonyl (NPPOC) protecting group have been used to protect pyrimidine building blocks in photolithographic solid-phase DNA synthesis. The photodeprotection of NPPOC-protected amino acids by using UV light was found to be about twice as fast as corresponding *o*-nitroveratryloxycarbonyl (NVOC)-protected amino acids⁵⁴. One of the attractive features of NPPOC as a protecting group is that the

photodegradation process yields a free amine functionalized surface (scheme 1.1), which can be used as a site for derivatization by a suitable reaction. This enables the fabrication of various functionalized surfaces or biomaterials and offers a strategy for the immobilisation of biomolecules in the patterned structures⁵². NPPOC-protected aminosilanes were synthesised by Alang Ahmed et al. and immobilised on a glass substrate. The monolayer was irradiated to fabricate micrometre and nanometre structures, using a photomask and nearfield lithography techniques respectively. The photodeprotection pathway of NPPOC was proposed based on a conceptual mechanism proposed by Bierer et al.⁵³. They manipulated the photodeprotection processes by employing contact angle, ellipsometry and XPS techniques. Finally, the reactivity of the produced free amine surface was successfully tested by derivatizing it with trifluoroacetic anhydride (TFAA) and aldehyde-functionalized polymer nanoparticles³⁸.

1.3 Polymer Brushes

Polymer brushes are a class of surface modifier which consists of polymer chains tethered by one end to a solid surface with a sufficiently high packing density that steric hindrance causes them to stretch away from the substrate in order to avoid the formation of an overlapping conformation⁵⁴ (figure 1.3). There has been much interest in polymer brushes because of their potential applications in material science and nanotechnology. There has been a great deal of activity focussed on development of new synthetic strategies and more recently, techniques for forming patterned brush structures. There are two main approaches to brush formation. In the 'grafting to' technique, pre-synthesized polymer molecules are anchored onto the substrate.

However, this approach can be performed with a variety of the polymer molecules on a very wide range of substrates and also it can be implemented with almost all available polymerization methods such as nitroxide mediated polymerization (NMP)⁵⁷, ring opening metathesis polymerization (ROMP)⁵⁸, single electron transfer living radical polymerization (SET-LRP)⁵⁹, reversible addition fragmentation chain transfer (RAFT)⁶⁰, controlled radical polymerization (CRP)⁶¹ and surface-initiated atom transfer radical polymerization (SI-ATRP)⁶². The latter method reported by Matyjaszewski et al. for the first time in the mid of 1990s is considered among the most effective methods for controlled radical polymerization techniques (CRP). It allows researchers to prepare a material with well-defined, composition, architecture, and functionality at the molecular level.



Scheme 1.2: The mechanism of Atom Transfer Radical Polymerization (ATRP). In the initiation step, the radical (R•) is generated from the alkyl halide of the initiator and it reacts with a monomer, forming the radical monomer. The monomer is added to the intermediate polymer radical (Pi•) in the propagation step

The polymer brush is grafted via chemical bond formation the solid surface, initially functionalised with an initiator and the functional group of end-chain polymer in the presence of transition metal catalyst (which is the transition metal with any possible ligands). The controlled rate in SI-ATRP is the result of the reversible activation-deactivation reaction between the growing polymer molecule and the copper-ligand species⁶³⁻⁶⁵.

A general mechanism pathway is shown in a scheme 1.2; the radical is formed from through a reversible oxidation-reduction reaction in the presence of a transition metal catalyst.

Cu(I) undergoes a one electron oxidation with the abstraction of a halogen atom (Br) from the reactant species, R-Br. The radical species formed via reversible reaction with a rate constant of activation k_{act} and deactivation k_{deact} . The polymer chain is formed via adding the free radical to the monomer within the intermediate with a rate constant of propagation k_p . The polymerization rate is determined by the magnitude of the equilibrium constant $Keq = k_{act}/k_{deact}$. Polymerization will not happen or happen very slowly at a very small value of Keq . The rate increases with increasing Keq value. A high value of Keq will lead to an increase in the rate of termination, by generating a high radical concentration, which may accompany the formation of a large amount of deactivation complex ($CuBr_2$). This may shift the equilibrium toward the reactant species, yielding very slow reaction. It has been revealed that the thickness of the polymer brushes is related to the concentration of the free initiator, as the concentration decreased the thicker brushes result⁶³. Matyjaszewisky et al. have shown that adding a deactivator to the polymerization reaction causes increase in the concentration of Cu(II) and becomes equal in concentration with Cu(I), leading to control of polymerization reaction⁶⁶.

There have been many studies on the physio-chemical properties and mechanical stability of polymer brushes over the last few decades. There was slow progress initially, but this has dramatically increased over the last decade, because of the flexibility ATRP offers to form highly tailored thin films within which chemical composition, thickness, grafting density, wettability, and features of the macromolecule film can be precisely controlled by utilising rather simple experimental techniques. There has not been a lot of work on the nanofabrication of brushes. Besides their super lubrication properties, polymer brushes exhibit remarkable potential in biomedical technology. In particular, a number of polymer brushes have revealed high resistance toward biofouling¹.

1.3.1 Structural Definition of Polymer Brushes

The properties of polymer brushes are strongly dependent upon their conformations and on the way that the polymer changes its conformation in response to the external environment⁶⁷⁻⁶⁸.

Control the conformation of the brush is important to its usefulness, for example, control of biological interactions at the surface⁶⁹. It is generally recognised that the grafting density of the anchored polymer chains plays a vital role in controlling brush conformation and behaviour. The confirmation can be evaluated by measuring the distance between grafting points (D) figure (1.4) of two adjacent tethered polymer chains and it is called a transition parameter. When the size of the anchored polymer chain is larger than the D value, a stretched brush structure can be expected (figure 1.4a), while in the case of the larger value of D than the polymer chain the conformation could be mushroom or coil conformation figure 1.4b.

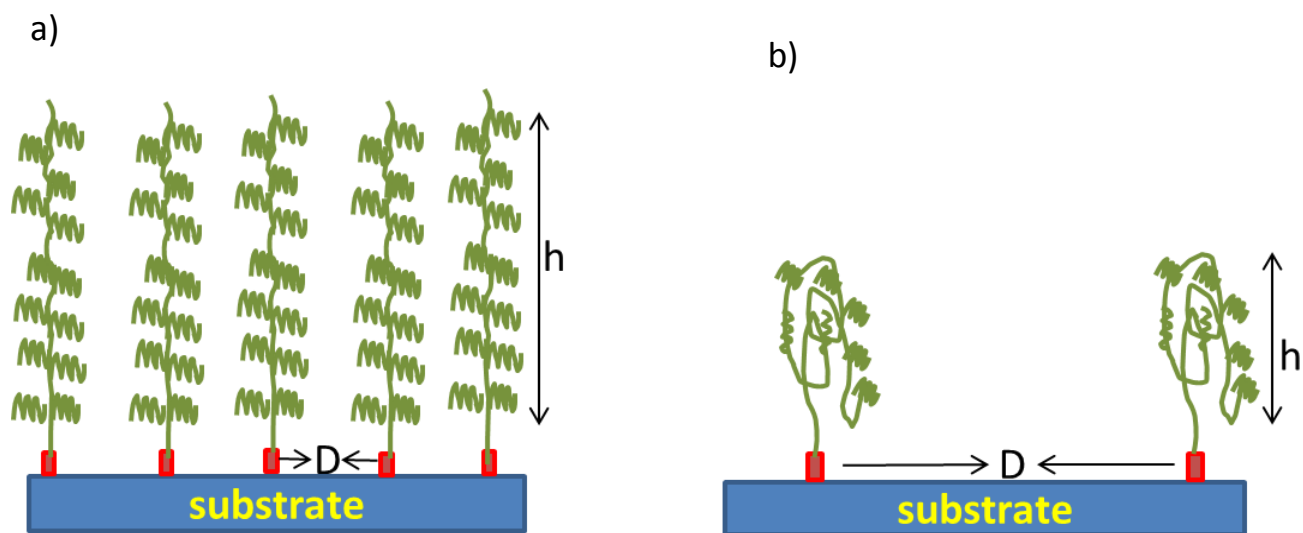


Figure 1.4: The characteristic parameter for end-grafted polymer chain, D is a distance between grafting points and h is the height of the brush. (a) $D < h$ for brush structure and (b) $D > h$ for mushroom structure.

The relationship between the transition parameter (D) and the grafting density (σ) is given by $\sigma = 1/D^2$. The reduced tethered density is given by

$$\Sigma = \left(\frac{R_g}{D}\right)^2 \quad (1.2)$$

Where R_g is the radius of gyration of a tethered chain at specific experimental conditions of solvent and temperature. There is a direct relationship between grafting density and the thickness of the polymer brush (h) and it is given by

$$\frac{M_n}{N_A} = h \rho D^2 \quad (1.3)$$

where ρ is the bulk density of the brush composition, N_A is the Avogadro number and M_n is the number average molecular weight. For characterization of all three grafted brush structures, the value of Σ parameter needs to be determined for mushrooms $\Sigma < 1$, and for brushes $\Sigma > 1$ ^{70,71}. Recently, Stamm et al. studied the influence of grafting density σ on swelling and adhesion of end-grafted poly(2-vinylpyridine) (P2VP). An AFM colloidal probe technique was used to investigate different grafted layers. D and σ values were determined and their relationships were studied. They found that the brush height increased with increasing grafting density and decreasing D values. Maximum adhesion was observed at intermediate grafting density and disappeared with denser brushes⁷². Due to the difficulty of the measurement of molecular weight of the end-grafted polymer chain on the surface, not all the researchers in literature tried to use this method in determining the grafting density. Molecular weight determination is particularly difficult when the “grafting from” approach is used to grow polymer brushes, for example ATRP. In literature, many research groups reported the possibility of determining grafting density when the “grafting to” was applied to form the brushes⁷³⁻⁷⁶. This is because of the possibility to determine the molecular weight of pre-synthesized polymer chains.

An alternative widely used technique is to systematically reduce the real density of active sites of the immobilised initiators. For this purpose, two main strategies have been considered. In the first strategy, the number of available initiator molecules on the surface is varied by controlling the concentration of the initiator or the length of the time that the initiator solution is in contact with the substrate⁷⁷. Genzer et al. formed a gradient density of polymerization initiator on a silicon substrate, using an evaporation process to generate a gradient density of 1-trichlorosilyl-2-(m-pchloromethylphenyl)ethane (CMPE) as an initiator. They found that the distance and the position of the CMPE molecular gradient can be tuned by varying the initiator diffusion time. Polyacrylamide (PAAm) was grown on the gradient surfaces via ATRP and they found a direct relationship between the brush thickness and the density of the initiator⁷⁸. The same group in another work reported the formation of a gradient of poly(acrylic acid) PAA brushes by controlling the molecular gradient of the polymerization initiator. The characterised

results showed that with increasing gradient density the height of the grafted brushes increased⁷⁹. In a work to investigate the relationship between the amount of initiator immobilised on a surface and the rate of grafted polymer layer formation. Luzinov and co-workers prepared different concentrations of bromoacetic acid initiator by varying the time and temperature of the initiator deposition. ATRP was used to grow poly(glycidyl methacrylate) (PGMA) brushes on the surfaces. It was found that an increasing surface density of initiator species led to an increase in the grafting rate⁸⁰. Despite many successes, this strategy suffered from difficulties because of the complexity of the kinetics of the attachment reaction and fine control of a very low concentration of the initiator molecule. The second strategy involves controlling the initiator density by using a mixture of the initiator and an inert analogue. Jones et al. reported the first systematic study of initiator density on surface-initiated polymerization. They used mixed monolayer of undecanethiol and ω -mercaptoundecyl bromoisobutyrate with different concentrations to control the initiator density over the substrate. The patterned surfaces were used to initiate the controlled radical polymerization of methyl methacrylate (MMA) and glycidyl methacrylate (GMA) polymers. Ellipsometry and AFM measurement revealed that the thickness of the brushes was linearly related to the population of the initiator molecules on the surfaces⁸¹. Very recently, Schönherr and coworkers reported the fabrication of poly(acrylamide) brushes with varied grafting density. The brushes were prepared by ATRP and mixtures of ω -mercaptoundecyl bromoisobutyrate and 16-mercaptohexadecanoic acid was used to prepare the surface, the former component being the initiator. Grafted polymer brushes with different densities were formed and characterized by using contact angle and XPS methods. The results showed that the brush thickness varied with the surface concentration of initiator, determining the transition from mushroom to brush regimes with increasing anchoring density. Cells were patterned on the surfaces and a change in the degree of cell adhesion was observed on the brushes⁸². This strategy involved the fabrication of many gradient brushes successfully, but the differences in the reactivity of the two SAMs toward the substrate may not have permitted the formation of an arbitrary concentration on the surface. In addition, identifying two components that do not interact with each other either in the solution or on the surface may not be easy. Thus, there is still a need for new strategies to fabricate gradient

polymer brushes. Genzer et al. used an attractive approach based on the degrafting of tethered poly(methyl methacrylate) (PMMA) brushes from flat silica substrates by using tetrabutylammonium fluoride (TBAF) solution. The degrafting rate was controlled by changing the concentration of TBAF, temperature and the sample incubation time in TBAF solution which resulted in formation different brush structures. X-ray photoelectron spectroscopy, ellipsometry, and time-of-flight secondary ion mass spectrometry were used to characterize the surfaces. It was found that the density σ of the grafted brushes decreased by either increasing the exposure time or concentration of TBAF solution⁸³.

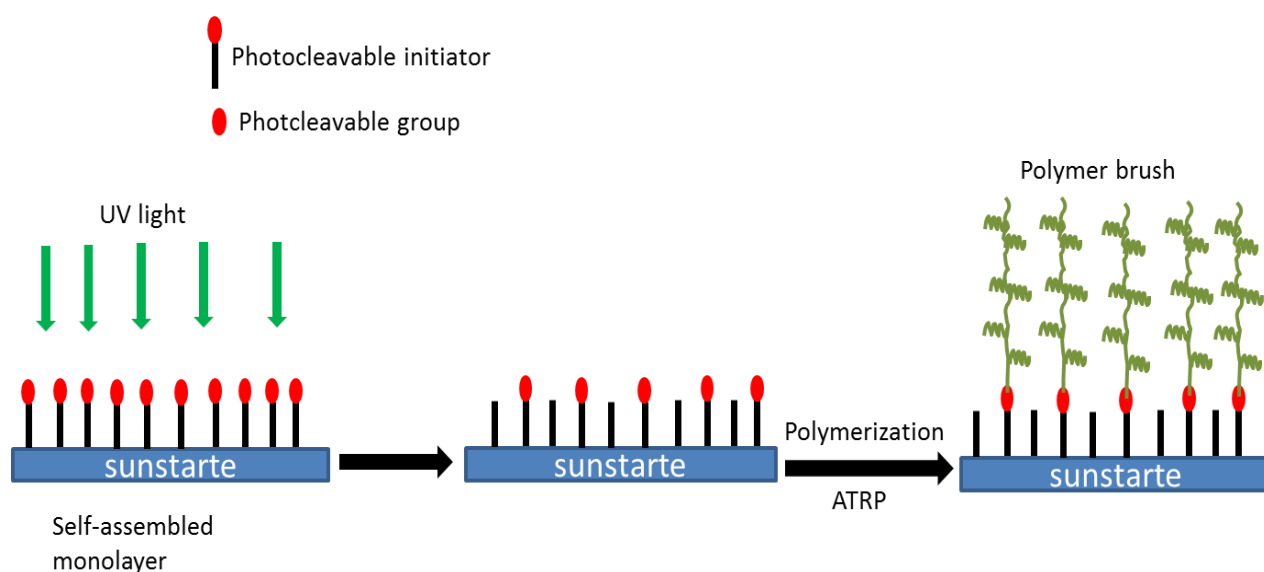


Figure 1.5: Schematic representation of photodegradation of a photosensitive self-assembled monolayer followed by a polymerization reaction by using a maskless lithography technique.

An alternative approach is illustrated in figure 1.5, based on the selective photolysis of the bond linking the initiator to the surface. While unexposed areas remain active toward polymerization reactions, the density of the photodegraded initiator is directly proportional to the UV exposure. Therefore, by controlling the photo irradiation period various patterns of the ATRP initiators could be generated. Fukuda et al. fabricated poly(methyl methacrylate) (PMMA) brushes with the same chain length but different grafted densities on a silicon substrate via ATRP method. The initiator was exposed for various periods of times to form surfaces with different densities. The impact of grafted density on the brush structure was explored, with

increasing brush density (σ) the brush height increased and the brush with a higher grafted density was more resistant to compression⁸⁴. The surface initiated photopolymerization (SIPP) of vinyl monomers on structured self-assembled monolayers was reported by Jordan et al., using photolithography. In the first step, a SAM of 4'-nitro-4-mercaptobiphenyl on an Au surface was irradiated with different dosages to form a gradient density of initiator 4'-amino-1,1'-biphenyl-4-thiol. Then, the patterned polymer brushes fabricated by using surface-initiated polymerization of vinyl monomer upon UV irradiation. A linear relationship observed between the photochemical conversion of the nitro group to amino group and the layer thickness of resulting polymer brushes⁸⁵.

1.3.2 Patterned Polymer Brushes

There has been a great deal of interest in the formation of patterned polymer brushes well-defined feature dimensions and controllable physicochemical properties. Patterned polymer brushes have proved to be a versatile role in the design of biomaterial and nanotechnological devices. A variety of fabrication techniques combined with appropriate synthetic methods can be used to form patterned brushes. The fabrication techniques can be classified into 3 major groups: a) mechanical contact, including nanoimprinting, scanning probe, and soft lithography; b) surface force based techniques, such as capillary force, and colloidal lithography; and c) irradiation methods including, photo- and interference lithography, and electron beam lithography⁸⁶⁻⁸⁷. Soft lithography involves either self-assembly or replica molding for the production of micro and nanometre patterned brushes, and allows polymer brushes grow via either 'grafting to' or 'grafting from'. Microcontact is the most widely used of this group of techniques attractive technique in this field, It relies on using a stamp (made from polydimethylsiloxane PDMS) to transfer either the initiator SAMs or the pre-prepared polymer chains onto the substrate. Recently, Ravoo et al. reported the formation of microstructured patterned brushes of polyethyleneimine (PEI), using photocatalytic microcontact with a stamp coated TiO₂ nanoparticles. It has been claimed that well-defined patterned PEI could be obtained either as a micrometre scale dots or lines on SAMs and cellulose surfaces, AFM and XPS supported their evidence⁸⁸. Zhou and coworkers have successfully prepared different patterns of various polymer brushes through combining μ CP with SI-ATRP. They prepared binary

polymer brushes structures from different brushes such as PINPAm, PDMEHMA, cationic and anionic polymer brushes⁸⁹. Although μ CP provides a pattern on a large area and it is a relatively simple and inexpensive, the diffusivity of the inks, contamination, resolution, and uniformity can be difficult to control.

Dip-pen lithography (DPN) is considered as a successful scanning probe lithography (SPL) approach which can provide nanometer-scale patterned polymer brushes with a great control and high resolution (approximately 15 nm). This method utilizes an AFM probe (as a pen) to transfer initiators or pre-prepared polymer chains (as an ink) onto the substrate. In addition to high resolution, it can be performed in ambient conditions, different solvents, and provides feature sizes below 50 nm⁹⁰. Mirkin et al. prepared nanometer patterned polymer brushes using a combination of Dip-pen lithography and ring opening metathesis polymerization (ROMP). The monomer was delivered through the AFM tip to the substrate. It has been shown that polymer brush nanostructures with different pattern sizes from micrometre to sub- 100nm can be generated with various architectures, such as dots, lines, and any other possible geometries⁹¹. Nanopatterned of Poly(N-isopropylacrylamide) (PINPAAM) was fabricated in a 'grafting from' approach on gold-coated silicon by integrating Dip-pen lithography with SI-ATRP technique⁹². Despite remarkable success and high resolution, DPN suffered from low-throughput. Demands in microelectronics and nanotechnology are still to fabricate architectures with a small dimension. Electron beam lithography (EBL) has been revealed to be an attractive method in this field. The main advantages is that by using electrons with wavelengths less than 0.1 nm, it can overcome the diffraction limit, which is the main limit to the use of photolithography.

A series of pre-synthesized polymer brushes of polymethyl methacrylate) (PMMA), poly(2-hydroxyethyl methacrylate) (PHEMA), poly(isobutyl methacrylate) (PIBMA), poly(neopentyl methacrylate) (PNMPA), and poly(2,2,2-trifluoroethyl methacrylate) (PTFEMA) was obtained with feature sizes smaller than 50 nm, using EBL to irradiate the brushes. In this work, the lithographic technique was used to "sculpt" a preformed brush layer. AFM images confirmed the well-defined patterns demonstrated that control had been achieved more effectively than when the brushes were grown on patterned initiators, particularly when the brush height is

bigger than the line widths. It has been rationalised that patterning of positive tone methacrylate photoresist by electron beam bombardment depends on the chain the scission reactions that occur in the polymer backbone⁹³. The reaction causes to degradation of the e-beam resist to some small fragments, which leads to a reduction in the molecular weight and intrinsic viscosity. In spite of high resolution and minimum contaminant pattern obtained by EBL, the high cost, need for a high vacuum, and low-throughput are considered as the main disadvantages associated with the development of EBL.

Photolithography has proved to be a remarkable place in the nanometre and micrometre patterning of the polymer brushes. It is a simple technique which is capable of patterning large areas with high resolution. This method has successfully combined top-down and bottom-up strategies to fabricate the polymer brushes with a high degree of control of polymer architecture. Top-down strategies, where polymer brush is irradiated by utilising UV light, offer patterns with well-defined features. However, such approaches are not applicable for all types of polymer brushes because the polymer must contain photolabile bonds⁹⁴.

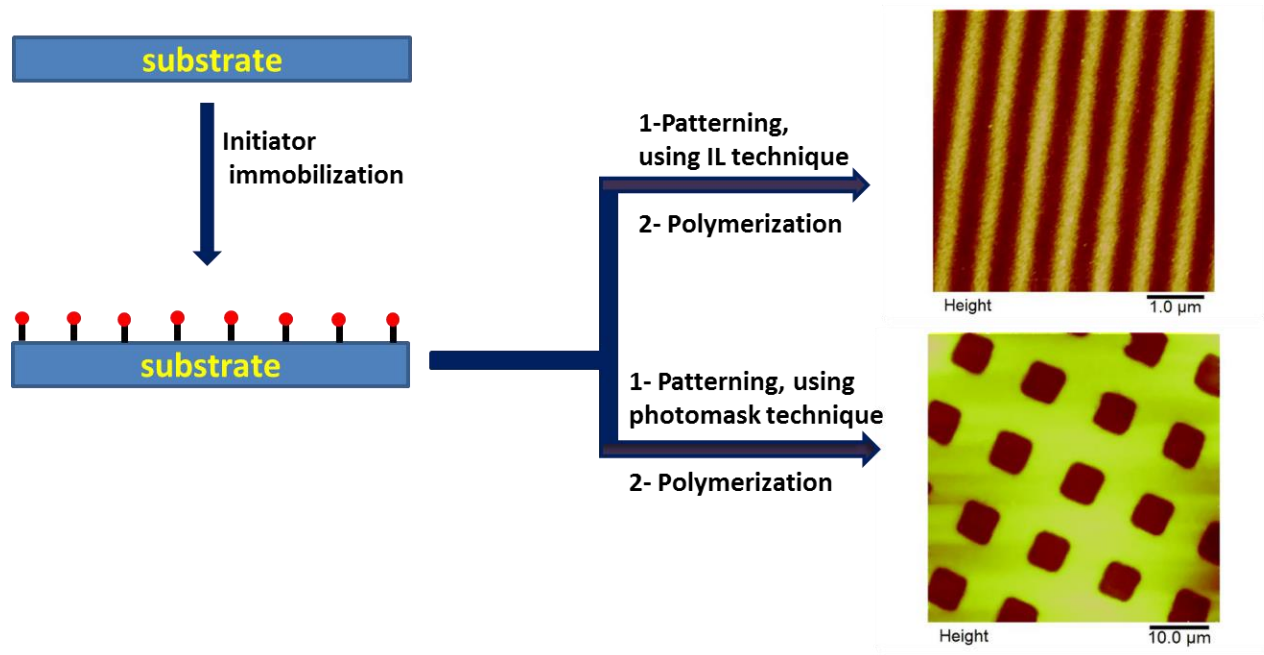


Figure 1.6: Schematic representation of patterning the micrometre and nanometre of polymer brush by using photomask and interference lithography techniques respectively.

Bottom-up approaches can overcome these drawbacks, where the immobilised light sensitive initiator photoresist is patterned by exposing to UV light and polymer brushes are grown via an appropriate technique such as SI-ATRP. In this field, Interference lithography (IL) and photomask techniques have been dramatically applied for fabricating nanometer and micrometre scale polymer brushes respectively Figure 1.6. Both methods involve either direct or indirect patterning strategies to create pattern brushes. In an indirect strategy poly[oligo(ethylene glycol) methacrylate] (POEGMA) have been patterned to create micrometre and nanometer polymer structures. In one study the irradiation of APTES-BIBB initiator surfaces through a mask to fabricate micrometre structures and by IL, to generate nanometer scale lines of initiator has been described. This was followed by polymer brush grown via SI-ATRP⁹⁵. Caykara et al. combined photolithography and RAFT techniques to fabricate micrometre and nanometre structures of 6-azidohexylmethacrylate (AHMA). Before immobilisation of DNA molecules on the patterned surface, the patterned structures were characterised by using AFM⁹⁶.

1.4 Biological Membrane

The biological membrane consists of lipid molecules and integral membrane proteins. The lipids form a bilayer. The common lipid molecules in most membranes are phospholipids, which are known as amphipathic molecules, meaning they have both hydrophilic and hydrophobic parts. In general, the hydrophobic tail, which consists of two long acyl chains esterified to two of the hydroxyl groups of a glycerol unit, while the third hydroxyl group is esterified with phosphate. The latter is also esterified to a hydroxyl group of another hydrophilic group that could be choline (figure 1.7b), serine, ethanolamine, and sphingosine to yield lipids phosphatidylcholine, phosphatidylserine, phosphatidylethanolamine and sphingophospholipids respectively. In lipid bilayers the hydrophilic heads point outward towards aqueous media, while the hydrophobic tails point inward towards each other⁹⁷ Figure 1.7a.

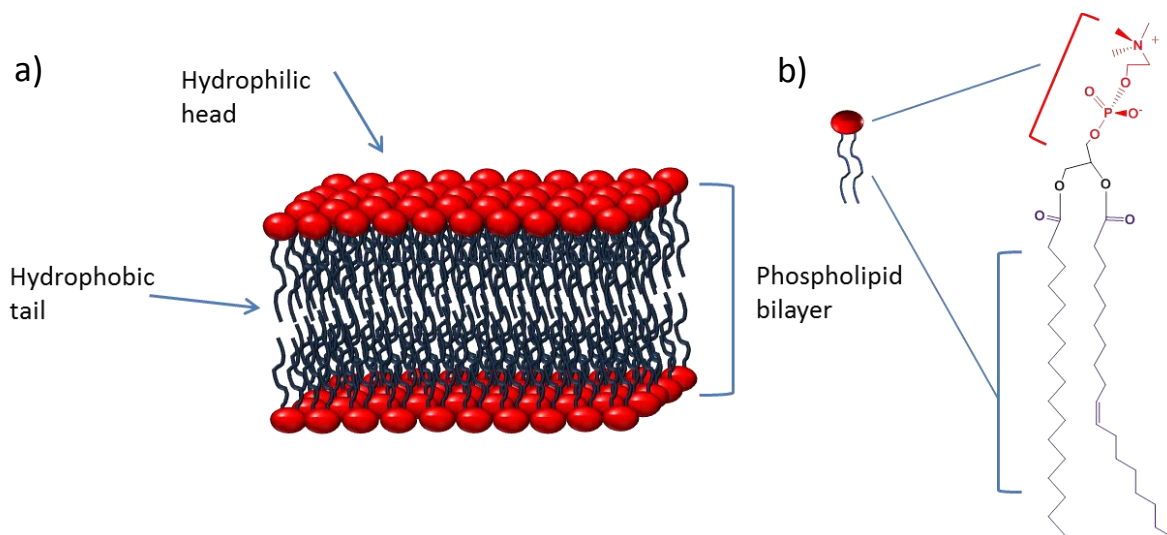


Figure 1.7: (a) Schematic representation of a lipid bilayer of phospholipids. (b) The molecular structure of a common phospholipid with a phosphatidylcholine.

Lipid bilayers are important structures in nature. They maintain many physical and biological properties of the cell membrane, such as its lateral fluidity. They also act as a very efficient barrier to proton transport, enabling the maintenance of the transmembrane proton gradients that are vital to the proton motive forces that are the driving force for life⁹⁸.

In the last few decades, there has been a great deal of interest in building model membrane system and in studying membrane biophysists. Lipid mobility is often studied by observing photobleaching of labelled lipids. In a small irradiated region the fluorescence of labelled lipid molecules is destroyed. Lipid diffusion causes fluorescence recovery if the bilayer is mobile, enabling the study of diffusion and mobility of the bilayer¹⁰¹. There has been a grow of interest in fabricating surface-confined membrane systems and numerous systems have been described, for example, solid-supported lipid bilayers⁹⁹, polymer-grafted lipid bilayers¹⁰⁰⁻¹⁰¹, hybrid bilayers¹⁰² and supported vesicular layers¹⁰³.

1.5 Supported-Lipid Bilayers (SLBs)

Lipid bilayers are two-dimensional films consisting of lipid molecules held together by hydrophilic interactions and self-assembled as a uniform bilayer in the solution.

They are called supported lipid bilayers (SLBs) when they are immobilised on either solid substrates such as mica, glass or substrates coated with hydrophilic soft surfactants such as polymers, forming a homogenous bilayer on the surface. Reconstituting the biological membrane on the surface has been an ongoing effort not only to explore basic membrane processes but also to enhance the development of biotechnological applications¹⁰⁴. One of the important advantages of SLBs is that they enable the use of a number of optical characterization techniques, typically total internal reflection fluorescence (TIRF)¹⁰⁵, fluorescence correlation spectroscopy (FCS), or fluorescence recovery after photobleaching (FRAP)¹⁰⁶. Such approaches typically require transfer of the pre-synthesized lipid bilayers onto a substrate. Three main methods have been reported, which all rely on using a Langmuir film balance¹⁰⁷. The first approach is the Langmuir-Blodgett method in which the lipids are formed as a monolayer at the air-water interface by adjusting the surface pressure between parallel barriers. The substrate is drawn vertically from the solution phase through the monolayer lipid phase and as it crosses interface a monolayer of lipids is deposited on the surface of the substrate (figure 1.8). It is then drawn back through the monolayer of lipid immobilise the second layer of lipid on top of the first layer, to form a bilayer¹⁰⁸⁻¹⁰⁹. The second method is the Langmuir-Schäfer technique, a first SLB monolayer is formed by using the Langmuir-Blodgett technique, but the second layer is formed by drawing the sample horizontally through the dispersed lipid molecules at air-water interface as shown in figure 2b. The latter method provides better quality SLBs in a more uniform bilayer and no adjusting pressure is required¹¹⁰. The third technique is known as adsorption, fusion, and rupture of vesicles from the solution, which is considered as one of the most convenient methods for producing SLBs. The first step of this method involves transferring vesicles into the substrate surface until a high density of the vesicles is formed on the surface. This is followed by fusion of vesicles and rupture at the end to create a uniform supported lipid bilayer as shown in figure 1.9.

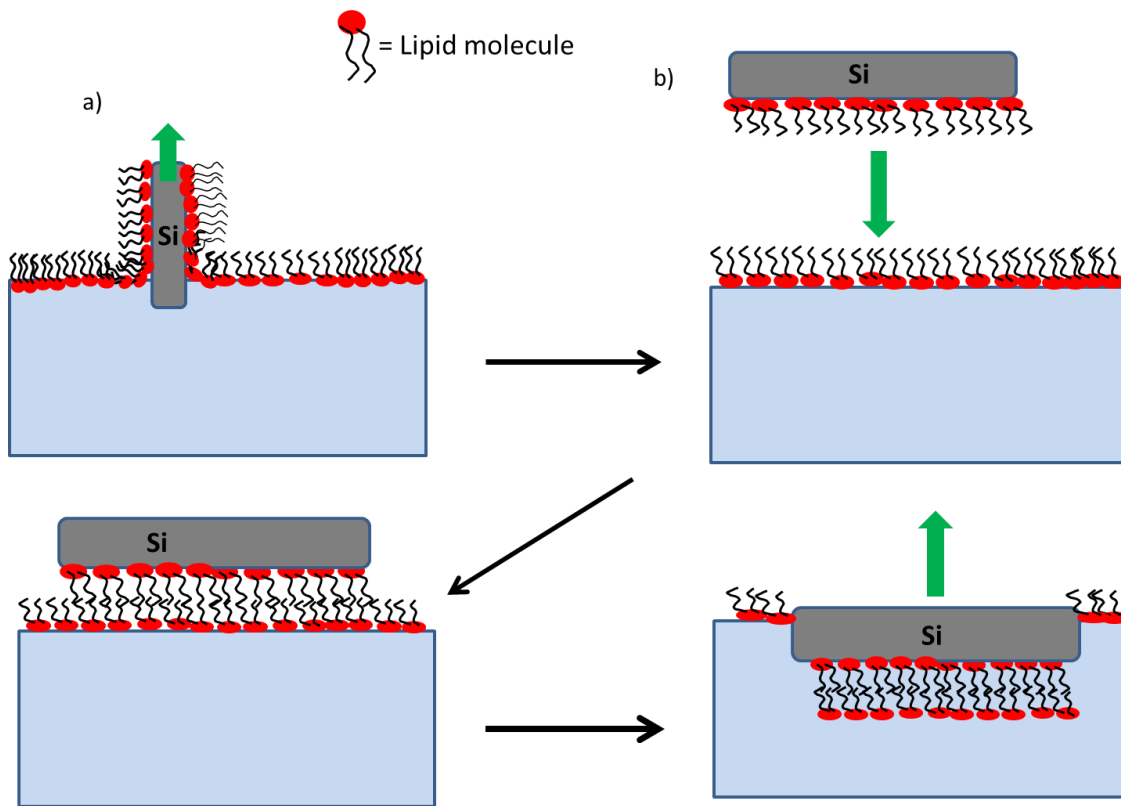


Figure 1.8: Schematic diagram showing the formation of the first monolayer of SLAB via (a) Langmuir-Blodgett method (b) and the second layer via Langmuir-Schäfer method.

The main advantages of this approach are that it is simpler, provides high-quality SLBs and offers a guide to a better understanding of the bilayer formation process¹¹¹. It would be fair to acknowledge that, in literature, there is a satisfactory explanation of the effect of the support on the mechanism, quality, and the nature of SLB formation. A number of the researchers investigated the possibility of forming SLBs on mica, silicon, and glass substrates¹¹². Rädler and co-workers reported these substrates (glass, silicon, and mica) influence the morphology and kinetics of spreading of SLB on the surface. Two different fundamental mechanisms of membrane spreading were observed. On the smooth surfaces like mica, the frictional coupling between the lipid membrane molecules and the solid substrate is dominated by shear flow of the thin water film at the interface. On rough surfaces (eg glass or silica) two-dimensional flow of the obstacles through the lipid bilayers controls the physical interaction at the interface¹¹³.

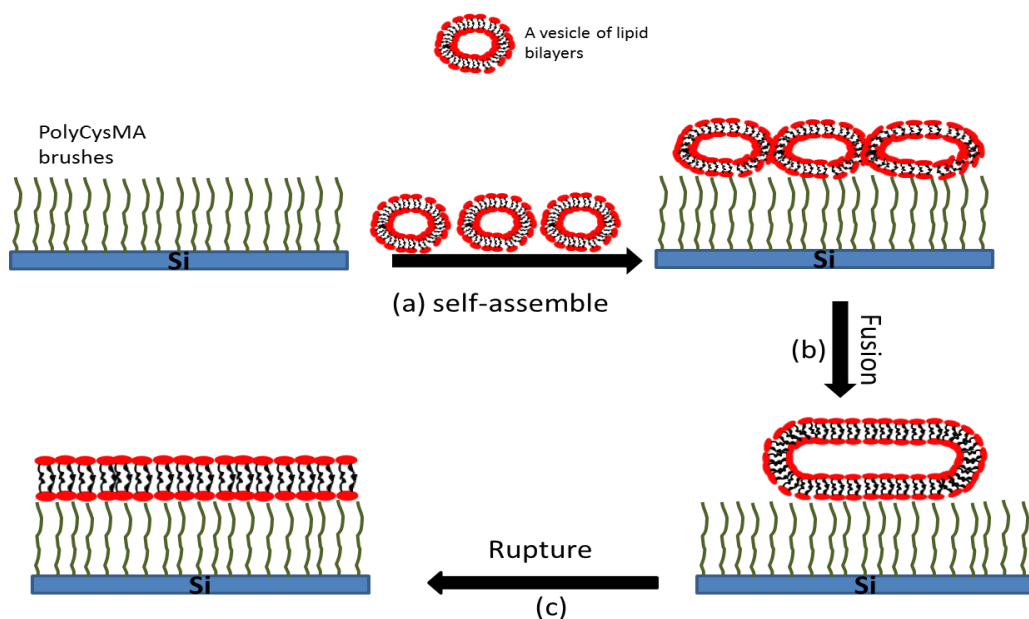


Figure 1.9: Schematic diagram showing the formation of polymer supported lipid bilayers via vesicle fusion approach, a) the lipid vesicles are adsorbed and self-assembled on the top of the polymer brushes, b) they are fused among themselves until a critical size is obtained, c) the fused vesicles are ruptured to form lipid bilayer on the surface.

The choice of solid supports is thus considered to be a vital step in the formation of SLBs, for example, bilayer membranes form on glass or mica while they cannot form on Au¹¹⁴ or TiO₂. In spite of the many successful applications of supported lipid bilayers in the study of nature and behaviour of the lipid membrane, there are significant unresolved problems. For example, when attempting to incorporate transmembrane proteins into the supported lipid bilayers, the proteins are denatured and deformed. This is because the bilayers are too thin (1-3 nm) and do not provide enough space for the cytosolic domain of the protein. As a result, the proteins interact with the substrate and denature. As a consequence, there has been interesting in using a polymeric layer as a cushion for the lipid bilayer to restore. The polymer would isolate the supported membrane from the support and would also provide low friction at the interface for both the artificial membrane and any embedded biological molecules¹¹¹. Ideally, the polymer brushes should have some specific properties, for instance, they should be of controlled thickness, homogenous with sufficient grafting density, very smooth, and they should be covalently anchored to the solid substrate.

In addition to their hydrophilic properties, the brushes must be chemically inert in order to avoid any unwanted reactions with either the attached molecules or the SLBs. Finally, brushes with high elastic modulus would be easier to be replicated in the every repeating process during the experiments¹¹¹. Various polymer brushes have been reported to be suitable for the formation SLBs. Very recently, a pH-responsive poly(2-dimethylamino)ethylmethacrylate) PDMA brush has been grown from a planar surface via ATRP. It has been reported that quaternization of the brushes, using 1-iodooctadecane in a poor solvent promoted the formation of SLBs and yielded a high diffusion coefficient with the high mobility of the SLBs confirmed, using fluorescence recovery after photobleaching (FRAP). These results provided evidence for the production of a good lipid membrane. It was also possible to fabricate lipid bilayers on non-quaternized brushes, but they had lower stability and flexibility compared to the quaternized surface¹¹⁰. Uniform SLBs has also been formed on a thin layer (12 nm) of a zwitterionic poly(cysteine methacrylate) brushes (PCysMA), formed by SI-ATRP. AFM and FRAP were used to evaluate the quality of the lipid bilayers. A very satisfactory diffusion coefficient of $\sim 1.5 \mu\text{m}^2 \text{s}^{-1}$ was recorded which indicates high mobility lipid and confirms the formation of a well-defined lipid membrane on the surface¹¹⁵. Cremer et al. investigated the relationship between poly(ethylene glycol) (PEG) brush thickness, conformation and supported the lipid membrane formation. At high sufficient density PEG forms brushes that promote the air stability of SLBs, while at the low density the mushroom conformation causes substantial damage and complete delamination of the lipid bilayer¹¹⁶.

In addition to the coformation of uniform SLBs, patterned phospholipid bilayers have been employed in fundamental studies that aim to understand how lipid organisation affects the composition and organisation of the cell membrane. These patterns are obtained by using either direct patterning, in which the pre-synthesized SLB is patterned or indirect patterning where the substrate is preliminary patterned. Groves and co-workers studied T cell receptor microcluster transport through molecular mazes, which consisted of 100 nm lines with 5.5 nm high of a chromium layer on a glass substrate. It was found the T cell receptor was driven by actin polymerization, and the distribution of F-actin was imaged at various time points during the synapse¹¹⁷.

In other work, they applied scanning probe lithography to fabricate SLBs by removing pre-patterned SLBs on the substrate followed by refilling with another lipid bilayer¹¹⁸. A micropatterned array was used to fabricate patterned DNA, immobilised on the glass substrate, which then served as a patterned support enable attachment of to giant unilamellar vesicles¹¹⁹. Craighead et al used photolithographically patterned polymer and a lift-off approach to prepare a patterned patch into which a lipid bilayers could be deposited. Polymer brushes were grafted onto a silicon wafer, then a photoresist applied to the brush selectively. The uncovered brushes were exposed and etched, using a normal lithography technique, forming patterned brushes. Fluorescence recovery after photobleaching confirmed the very good quality of the SLBs with high mobility and diffusion coefficient¹²⁰. Knoll et al. used a photomask technique to create a micrometre pattern in a polymer brush. The removed area was functionalized with a polymerised lipid, and its mobility was demonstrated using FRAP¹²¹. Despite providing a well multi-functional system and solving many problems associated with the use of solid substrates as described above, polymer supported lipid bilayers are not perfect systems. One of the main disadvantages is the many additional processes required to fabricate SLBs, compared to solid supports, highlighting the complexity of the production processes. Furthermore, the production of supported lipid bilayer is time consuming¹¹¹.

1.6 Cell Patterning

Transplantation of human organs is generally limited by donors, and there are hopes that tissue engineering may offer an alternative by providing implantable tissues. Currently, there has been a great deal of interest in using micro- and nanostructured materials to direct and enhance tissue formation.¹²²⁻¹²³. In this process, the important goal is focusing on fabricating a biomaterial with an architecture capable of guiding the adhesion, migration, proliferation and differentiation of cells at the right position and time^{124,125,126}. In addition, not all the available biomaterials have the same influence on the development of cell patterning. Polymer brush-based biomaterials have had a significant impact on this field, due to their biocompatibility and the capacity for control of their chemical configuration, density, architecture and thickness down to nanoscale resolution with simple patterning techniques¹²⁷⁻¹²⁹.

It has been shown, that the attached cell become elongated and aligned in the direction of ridges or grooves on the surface, a process known as guidance. However, the degree of the alignment and migration depends on the groove depth and width¹³⁰⁻¹³¹. The migration mechanism of the cell on the fabricated surfaces is complex, needing the cooperation of the cytoskeleton, membrane and signalling systems. Regarding the topographic or chemical stimuli, cells protrude their leading edge as shown in figure 1.10. The directional extension of the active membrane brings the attachment and thus the traction force to the substrate, lead to produce a counter force on the cell to promote cell migration. To move forward, the contraction of cytoskeleton filaments pulls the cell body towards the leading edge, then the tail retracts by releasing adhesion at the rear¹³⁵⁻¹³⁶.

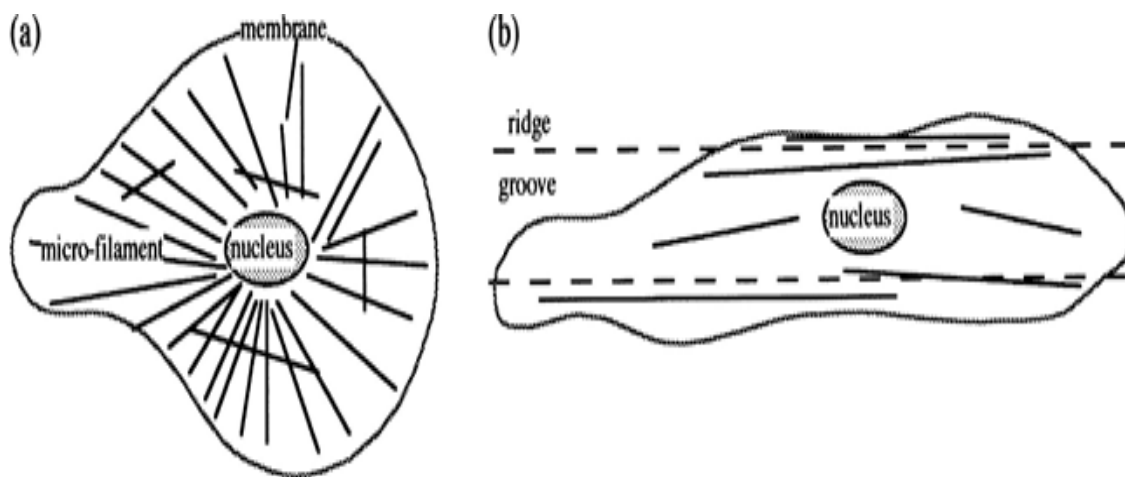


Figure 1.10: Demonstrates a schematic representation of cytoskeleton (a) shows a cell on a flat surface and (b) shows a cell on a patterned surface and reorganisation of micro-filament on that occurs on a grooved surface¹³².

There are many patterning techniques that have been applied to fabricate surfaces for the study of cell adhesion. Microcontact printing (μ Cp) lithography has been used widely to explore the topography and chemistry impact of the polymer brushes on the cell adhesion. To control cell adhesion and proliferation, microgroove structures of polymeric films of L-lactide/trimethylene carbonate copolymer (PLLA-TMC) and fibronectin on the planar polymer

film were prepared. μCp was used to transfer either the polymer ink onto the glass surface or fibronectin onto the polymer film. The cells were seeded onto the patterned samples, and light microscopy results showed that there was a possibility for aligning and growing cells in the patterned samples¹³³. Gautrot et al. fabricated micrometre scale arrays of poly(oligo(ethylene glycol methacrylate)) (POEGMA) brushes on glass or gold surface. μCp was used to transfer initiator molecules onto the surfaces, and then polymer brushes were grown via ATRP. The impact of morphology, chemistry and incubation protocol on cell adhesion was investigated by using AFM and fluorescence microscopy¹³⁴. A systematic study of cross-talk between stem cell behaviour and micropatterned polymer brush platform was carried out to control cell adhesion, spreading and shape independently on the other chemical and physical properties. For this purpose, a series of polymer brushes with different chemistries and geometries of 20 μm , 50 μm , 40 μm diameter rings and arc-shaped patterns were fabricated and the obtained data gave evidence for the cross-talk between the cell and the ridges¹³⁵. Nanotopographies of poly(L-lactic acid) were created by replication molding of the polymer film. Initial cell adhesion was improved on the nanopatterned surface compared to a smooth control surface, but subsequently, cell density was decreased on the patterned surface¹³⁶.

The ability of photolithography to pattern functional polymer over a range of length scales has prompted a variety of work aiming to integrate control of morphology with control of molecular functionality. Thus, biologically or photographically produced polymer patterns enable the precise manipulation and localization of cells and control of cell-cell and cell-substrate interactions. Poly(ethylene glycol) (PEG) is considered as one of the best polymer brushes for cell patterning associated with using photolithography technique¹³⁷⁻¹³⁸. In an attempt to precisely control cell-surface interactions, poly(ethylene glycol) (PEG) grafted on a glass surface was photopatterned to fabricate microstructures containing high-density hydrogel with cell-repellent and cell adhesive surfaces. AFM and fluorescence microscopy studies suggested that the fabricated structure was very effective in guiding and confining adhesion of 3T3 fibroblasts and primary rat hepatocytes to specific regions on the surface¹³⁹. Recently, a mask-less assisted laser was used to produce cell adhesive micro-domains delimited by the antiadhesive PEG microstructure.

The response of murine fibroblasts (L-929) toward the patterned structure was studied. It was found that the cell density and alignment in the cell adhesive region with surrounding walls of protein and nonbiofouling PEG was manipulated by the size and geometry of the micro features¹⁴⁰. Metters et al. reported the formation of a gradient of biocompatible poly(methacrylic acid) (PMAA) brushes by using a direct photolithography method; the brushes were functionalized with RGD-ligand. The ability to control the cell-adhesion across the patterned surface was investigated. The cell adhesion study was shown to preferentially increase in the direction of increasing RGD density until a limiting RGD density was reached¹⁴¹. In a study to explore the biomimetic polymer brushes in natural tissue fabrication, Ober et al. used photolithography to fabricate a specially designed polymer brush pattern. First, Biomimetic methacrylate polymer brushes containing tethered neurotransmitter acetylcholine functionalities in the form of dimethylaminoethyl methacrylate or free hydroxyl-terminated poly(ethylene glycol) units was grown, using ATRP technique. Then, photolithography method was used to create micropatterned structure with feature sizes varying from 2 to 20 μm . It was found that the structures can provide a simple and reliable way to guide protein and neuronal cells¹⁴².

Electron beam lithography (EBL) was also employed to fabricate polymer nanostructure with a feature size of depth: 5–350 nm and width: 20–1000 nm of polystyrene surface. The goal was to investigate the crosstalk between fibroblasts and nanopatterned and smooth surfaces of polystyrene. It was found that the cellular alignment was triggered by a combination of the feature width and groove depth. Cells did not migrate on the surfaces with groove depth below 30 nm and ridge widths smaller than 100 nm¹⁴³. The role of the biodegradable polymer in cell and tissue engineering was studied, by fabricating micrometre and nanometre-scale topographical features in polymer brushes, using EBL¹⁴⁴. Dalby et al. reported the formation of structures of 100 nm wide and 160 nm high of poly(methacrylic acid) (PMAA) brushes, using ion beam lithography. The result indicated a positive response from the ridges toward cell spreading¹⁴⁵.

1.7 Nanotribology

Tribology is the study of friction, wear, and lubrication at the contact between two surfaces in relative motion on a wide range of scales from the macroscopic to the nanometre scale. Nanotribology seeks to provide a fundamental description of the interaction between two sliding surfaces during mechanical motion. There has recently been a great deal of interest in the study of microscopic friction because of the development of microelectromechanical (MEM) and nanoelectromechanical (NEM) devices¹⁴⁶. The stability and lifetime of these devices depend on their tribological properties. Lubrication of small contacts in these systems requires solution different from those typically used in macroscopic systems.^{147,148,149,150,151,152}. These studies require very sophisticated tools to explore the interfacial properties at high spatial resolution. In this field, friction force microscopy (FFM) provides a means to study the frictional interaction between nanoscopic contacts. Because of difficulties with lubricating contacts in NEMS and MEMS using conventional methods, there has been interesting in using new approaches, including the formation of self-assembled monolayers as a means of controlling friction^{3, 6}. SAMs offer a large number of advantages such as low friction forces and friction coefficient, small thickness, low surface energy, etc.¹⁵³⁻¹⁵⁶. In addition, polymer brushes grown on a surface by tethering long polymer chains with sufficiently high density have been demonstrated to be an effective material to control surface properties including, surface wettability, adhesion, friction and composition¹⁵⁷⁻¹⁵⁹. Friction is a complex phenomenon, including both adhesion and plastic deformation as pathways for energy dissipation, hence is not simple to quantify it. However, many theories have been postulated to characterise the dependence of friction on other factors such as the normal load and the area of contact. Amontons' law can be considered the as first classical theory of friction. He assumed that the frictional force is directly proportional to the normally applied load in a micrometre contact.

$$F_F = \mu F_N \quad (1.4)$$

where F_F is the friction force, F_N is the normal force, and μ is the coefficient of friction, the constant proportionality between the friction force and load¹⁶⁰⁻¹⁶¹. According to this law, under zero applied load the friction is zero. In Amontons' second law of friction, under zero load the

friction may be finite and the friction coefficient can be determined from the slope of a graph of load versus friction. This law is purely phenomenological and does not provide any knowledge of why the friction coefficient is different for different material combinations¹⁶². After it was proposed numerous attempts have been made to justify this law either theoretically or experimentally, mostly by consideration the roughness and topographical properties of the sliding surfaces. However, Petra et al. showed that μ is not always influenced by just the surface geometry and roughness. They reported that the coefficient of friction is different for hydrophobic and hydrophilic nanostructured material deposited on the surface in aqueous media. There was no change in the coefficient of friction for all hydrophobic surfaces, and it was suggested that a bridging air cavity generated by a stored adhesion force during the measurements. However, measurement of hydrophilic samples yielded a different value of μ for different structures. It was suggested that this might be because of the restricted motion of the three-phase line of bridging cavity¹⁶⁶.

As a consequence of these uncertainties of friction, a second theory was postulated by Bowden and Tabor in 1950. They assumed the lateral friction F_L is linearly related to the real area of contact A and shear strength τ (the mean of the lateral force per unit area of interfacial atom)¹⁶³.

$$F_L = A \tau \quad (1.5)$$

This theory differs from Amontons' theory in that frictional relationship is not linear. Bowden and Tabor concluded that the real area of contact is related to the load between two sliding surfaces. Thus the apparent area of contact has not been taken into account. However, in the classical Hertz theory (total plastic deformation theory) the normal load is proportional to the contact area.

$$A(F_N) = \pi \left(\frac{R}{K}\right)^{\frac{2}{3}} F_N^{2/3} \quad (1.6)$$

where K is the elastic modulus. According to this theory $A \propto F_N^{2/3}$, in contrast with the prediction of Amonton's law. Moreover, in multi-asperity contact the normal force varies linearly with the lateral friction¹⁶⁴⁻¹⁶⁵. For single-asperity contact this relation is sub-linear. Numerous works have examined the friction-load relationships at both micrometer and nanometer scale by using FFM in different environments. It has been demonstrated that SAMs and polymer brushes provide a useful means to modify substrates and provide different surfaces with different functional groups (i.e multi-functionality surfaces). However, both linear and sub-linear friction-load relationships have been reported¹⁶⁶⁻¹⁷¹. In the present study these relationships have explored systematically in order to try and improve our understanding of the influence in molecular structure and composition on contact mechanics.

1.7.1 Chemical Force Microscopy (CFM)

At first sight, the applications of AFM in studying the chemical interactions of most multi-functional surfaces appear to be limited. Commercial AFM probes are manufactured from silicon or silicon nitride. These are also commonly used in the fabrication of miniaturised machines, such as MEMS, or NEMS. However, chemical modification of the AFM probe provides a means for the significantly understanding of the nature of molecular interactions on the nanoscale, which is required in many advanced systems such as in biology, nanobiosensors, tribology, adhesion, and catalysts¹⁷²⁻¹⁷⁵. The first process of AFM probe modification was reported by Nakagawa et al. who attached organosilane molecules with different chain lengths and compared interactions forces with surface layers containing adsorption with different chain lengths¹⁷⁶. But the term of CFM was used for the first time by Frisbie et al. when they tried to measure friction and adhesion between gold coated tips derivatized with alkylthiolates and surfaces functionalized with thiols and silane with different terminal groups¹. Since then, an abundance of papers has been published demonstrating that CFM or combined CFM with FFM can be used to describe numerous surface phenomena in different environments¹⁷⁷⁻¹⁸³.

To explore the effect of changes in the contact area and to measure the molecular interaction forces quantitatively by FFM or CFM, it is necessary to have a model of the contact mechanics that provides a proper understanding of adhesion and friction-load relationships or data.

The Amonton's law has been widely used to fit friction-load data, which in may cause do appear to exhibit linearity (equation 1.4)¹⁸⁴⁻¹⁸⁵

Leggett et al. characterised mixed SAMs of methyl- and carboxylic acid terminated thiols samples by utilising FFM. They found that friction data could be fitted with Amonton's law, and a relationship determined between surface composition and surface energies¹⁸⁶. These applications depended on the macroscopic theories for interpreting friction between multi-asperities at mechanical contact. However, sub-linear friction-load relationships also have been observed for single-asperity contacts and have been fitted using a single asperity contact mechanics approach (JKR, HRTZ, and DMT). Gao et al. reported some practical friction results acquired from the surface force tools SFA and FFM for a variety of adhesive and non-adhesive samples. They argued that a linear friction-load plot was normal and non-linearity represent a special case when the effect of adhesion is particularly strong¹⁸⁷. They argued that some factors which influences friction at nanoscale during sliding contact were not consistent with any of the single asperity contact mechanic theories. The frictional behaviour of end-grafted poly[2-(dimethylamino)ethyl methacrylate] films (brushes) as a function of pH in aqueous medium was investigated. The chemistry of the tip was controlled by either coating with gold or SAMs and FFM was employed to measure the friction forces. It was found that at low and very high pH the load-friction relationships were linear in agreement with the Amontons' law. However, at intermediate pH values, the relationship was sublinear and the data were fitted with single asperity contact mechanics model (DMT and JKR)¹⁸⁸. Until a few years ago the influence of te medium on the tip-sample interactions in which sliding occurs has not been realised. Recently, Legget and co-workers have demonstrated that the environment extremely important in determining the appropriate contact mechanics¹⁸⁹. The friction-load relationship depends on the nature of the interactions, for example, the ability to donate a hydrogen bond or to accept it) between surface adsorbates and solvent molecules. Commonly, for weak adhesion systems, the linear friction-load is dominant (where the energy is dissipated through molecular plowing) and data are in a good agreement with the Amonton's law. In contrast, with increasing adhesion the friction-load relationships become sublinear.

The results can be rationalised by treating friction as the sum of a load-dependent term (molecular plowing) determined by a frictional coefficient, and shear-dependent term characterised by shear strength τ ¹⁹⁰⁻¹⁹³.

$$F_F = \mu(F_N + F_a) + \pi\left(\frac{R}{K}\right)^{\frac{2}{3}} \tau(F_N + F_a)^{\frac{2}{3}} \quad (1.7)$$

where F_a is the pull-off force, μ is the “coefficient of friction”, R is the tip radius, K is the elastic modulus, and F_N the normal force. In the case of weak adhesion, DMT offers a good fit to the friction-load relationship, while in the case of a strong adhesion the JKR model may be dominant¹⁹⁴.

1.7.2 Contact Mechanics in AFM

In order to investigate the tribological properties of a single sliding asperity at mechanical contact, under a variety of applied load which is starting from negative to positive values, it is necessary to have a quantitative description of the contact area. FFM has proved to be a powerful means to study single asperity contacts, based on the assumption that a very sharp tip can be considered as a single asperity. Contact mechanics have been studied extensively for many years and it can play a crucial role in providing information on molecular interactions in the contact area, elastic indentation, contact stiffness, and both the strain and the stress of a mechanically loaded asperity¹⁹⁵⁻¹⁹⁶. Although many models have been developed, there is still debate about which is the appropriate model for particular situations. The first contact mechanic model was proposed by Hertz in 1880. In this theory, the circular contact area between two spheres was related to the elastic deformation of materials. This theory interpreted the property of single sliding contact in the absence of adhesion. The radius of the contact area (α) subjected to the normal load (L) as shown in this equation

$$\alpha = \left(\frac{LR}{K}\right)^{\frac{1}{3}} \quad (1.8)$$

where R is the sphere radius, and K is the elastic modulus

$$K = \frac{4}{3} \left(\frac{1 - \nu_1^2}{E_1} + \frac{1 - \nu_2^2}{E_2} \right)^{-1} \quad (1.9)$$

E_1 and E_2 are related to Young's modulus of sphere and flat plane, while the ν_1^2 and ν_2^2 are the Poissons ratios for the flat sphere and flat planes respectively. The Hertz model a fully elastic model in which the surface attraction was totally neglected¹⁹⁷. However, adhesion exists between the tip and the sample surface under many circumstances. An improvement of this theory was published by Johnson, Kendall and Roberts (JKR) in 1971, to take account of tip-sample attraction. The JKR model relates elastic properties to the surface energy. They suggested that a mechanical load is required to separate two solid surfaces in intimate contact. In addition, work must be done to overcome the adhesion energies to separate two contact bodies. Due to the action of attractive forces between the surfaces the contact radius of Hertz theory (equation 8) become

$$\alpha^3 = \frac{R}{K} (L + 3\pi\gamma R + \sqrt{6\gamma\pi RL + (3\gamma\pi R)^2}) \quad (1.10)$$

Where γ is the work of adhesion When $\gamma = 0$ this reverts to the Hertz equation

$$\alpha^3 = \frac{R L}{K} \quad (1.11)$$

At zero applied load the contact area is finite and given by¹⁹⁸

$$\alpha^3 = R \frac{6\pi\gamma R}{K} \quad (1.12)$$

The key assumption of this theory is that the adhesive interactions are infinitely short range, so the free energy of the system is only decreased by γ (the work of adhesion) units of energy per unit area in intimate contact. Therefore, no adhesion occurs in regions which are not in contact. Furthermore, in JKR model, there is a non-zero contact area at zero applied load caused by attractive forces. Hence a tensile load is required to separate two surfaces at zero external load. The minimum load that is required to separate two bodies exactly is known as a pull-off force, adhesion force or the critical load L_c ¹⁹⁹, which is given by

$$L_c = \frac{-3}{2} \pi R \gamma \quad (1.13)$$

Subsequently, an alternative theory was proposed by Derjaguin, Muller and Toporov. This model considers the effect of attracting forces (van der Waals Forces) outside the contact area. It has been shown that, although the van der Waals force does not increase the contact between the ball and the plane, the force that is needed to separate the two bodies (pull-off force) is nevertheless larger than expected based on a consideration of the contact area alone. In terms of the contact of stress and the deformation shape inside the contact area, both DMT and Hertz theories are in a good agreement, it is the van der Waals forces outside the contact area that are treated differently by the two models. In addition, DMT assumed that the applied load could be substituted by an “effective load”, which is the sum of the applied load and critical load. The DMT model reduces to the Hertz model in the limit that these effects are small. Thus the contact area in this case becomes

$$\alpha^3 = \frac{R}{K}(L + 2\pi\gamma R) \quad (1.14)$$

In DMT theory at pull-off force the contact area is zero, and in contrast with the JKR model, there is no stress distribution within the contact area, the pull-off force is given by²⁰⁰.

$$L_{c\ DMT} = -2\pi\gamma R \quad (1.15)$$

It is clear that the JKR and DMT models are using different parameters to describe the situation of the contact area when two surfaces are brought into contact. But the discrepancy between them was resolved by realising that they are both valid. For example, in the case of strong adhesion, short range, and soft materials the JKR model is accurate, while in the case of weak adhesion, long-range, and stiff materials the DMT model is dominant.

Then, limitations of these two models have been discussed by many researchers. For example, in 1977 Tabor has revealed his assumption, which focused on the importance of combining surface force concepts with the principle of contact mechanics. Therefore, this may reduce the limitation in JKR and DMT models. It has been suggested that the interaction forces between surfaces depend not only on the surface energies but also on the roughness of surfaces and degree of ductility of the solid surfaces. Furthermore, the roughness leads to decrease adhesion in the contact area²⁰¹.

Despite the differences in their description of the interaction potential, both the JKR and the DMT models can be valid at opposite ends of a spectrum of contact behaviour.

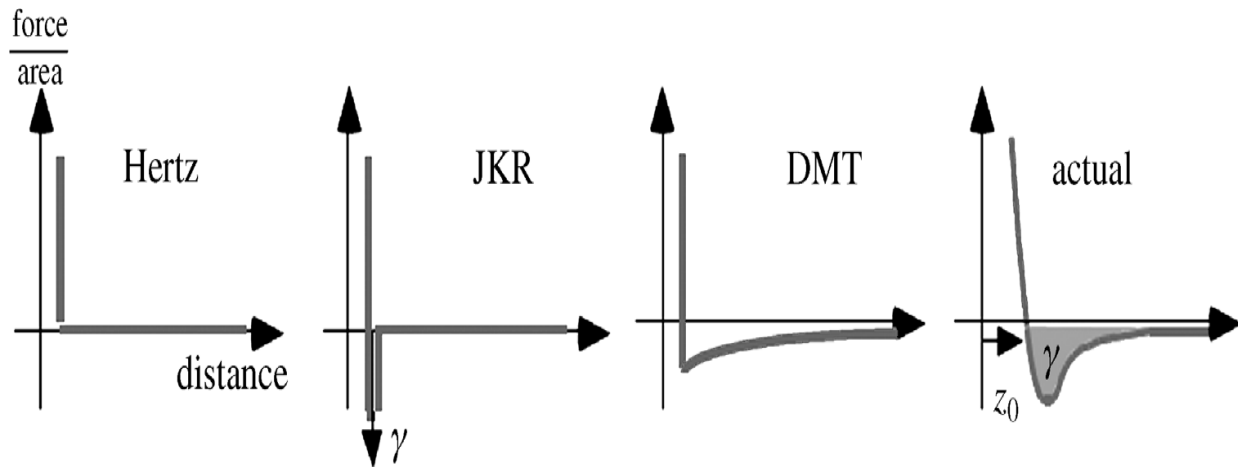


Figure 1.11: Schematic demonstration of attraction force between the AFM tip and the sample surface as a function of a distance between them for the Hertz, JKR, and DMT models with compression to actual interaction²⁰².

Figure 1.11 shows schematically the interaction force as a function of separation for all three models JKR, DMT, and Hertz. It is obvious that that adhesion is totally absent in the Hertz theory. In the JKR and DMT models the adhesion is present, but with different dependence on separation. In the JKR model, the attractive force is a strong, short range, one that causes deformation with respect to the elastic properties of substances. This means it is reasonable to apply JKR theory to the interaction between soft materials with strong adhesion. In contrast, the DMT theory treated adhesion as weak, with long range interaction forces; means in the case of the high stiffness and weak adhesion the DMT model is dominant²⁰⁶⁻²⁰³.

Tabor introduced a dimensionless parameter μ_T . In the case of a sphere in contact with a planar surface, the value of μ_T which is non-dimensional physical parameter as shown below

$$\mu_T = \left(\frac{16R\gamma^2}{9K^2Z_0^3} \right)^{1/3} \quad (1.16)$$

where R is the radius of the sphere, K is the combined modulus for the interacting materials, and Z_0 is the equilibrium separation of the surfaces, or in the atomistic picture is the equilibrium

bond length for the two materials²⁰³. This parameter μ_T has been used to select the appropriate model for the contact mechanics of particular systems.

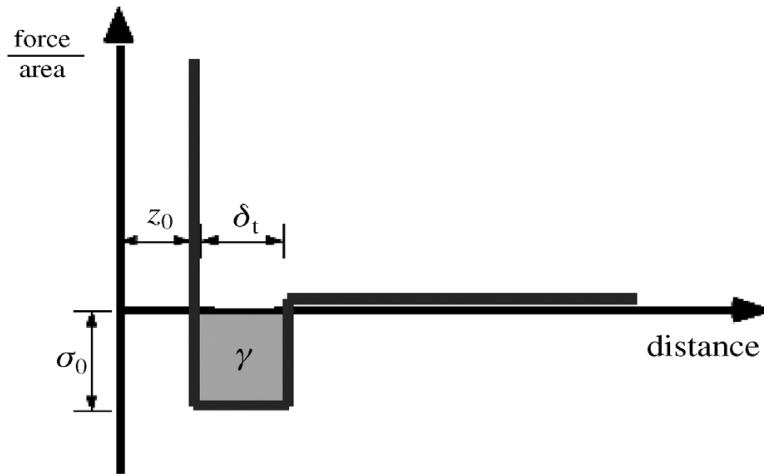


Figure 1.12: Schematic diagram showing the force-distance relationship predicted by Dugdale's model and utilised by Maugis²⁰⁶.

Maugis tried to connect JKR and DMT theory to find an intermediate model that could be used to predict the contact area and pull-off force at a given load (figure 1.12). The model used the Dugdale square-well potential to make the connection between the two models. A constant adhesion stress σ_o acts over a separation range δ_1 and then decreases to zero at larger separations. Thus, the work of adhesion is $\gamma = \sigma_o \delta_1$. Consequently, Maugis has driven a transition parameter equation which is similar to μ_T

$$\lambda = 2\sigma_o \left(\frac{R}{\pi\gamma K^2} \right)^{1/3} \quad (1.17)$$

where σ_o is set to be equal to the minimum adhesion stress in the Lennard-Jones potential. It follows that $\delta_1 = 0.97 Z_o$, and so $\lambda = 1.1570 \mu_T$ thus, they are approximately equivalent. The JKR model is valid when $\lambda > 5$, and the DMT model applies when $\lambda < 0.1$. Values between 0.5 and 0.1 correspond to a transition regime between the extremes represented by the JKR and DMT models. Maugis was able to choose a reasonable model for describing the contact area and pull-off force at a given load for intermediate values of the parameter λ (figure 1.13).

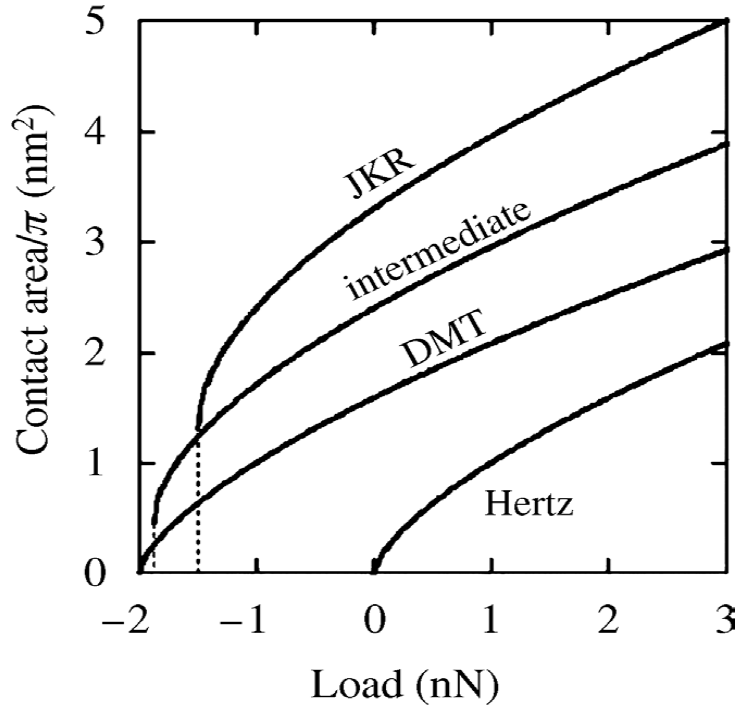


Figure 1.13: The predicted load depending on the contact area for some of some of contact mechanic models²⁰⁶.

It is clear that in the absence of attractive surface forces ($\gamma=0$) Hertz theory can be applied. The Maugis-Dugdale transition parameter has played a crucial role in the identifying the limits of different contact mechanics models, but it proved difficult to apply in any cases limiting its use. Thus, over a decade ago, another approach was provided by Carpick, Ologtree, and Salmeron (hereafter referred to as COS equation)²⁰⁴. They followed Maugis principles and they provided a simpler general equation to estimate a ‘transition parameter’: This equation relates the contact area and applied a load to the transition parameter.

$$a = a_{o(\alpha)} \left(\frac{\alpha + \sqrt{1 - L/L_C(\alpha)}}{1 + \alpha} \right)^{2/3} \quad (1.18)$$

$a_{o(\alpha)}$ is the contact area at zero load. If $\alpha = 1$, the JKR model applies exactly and if $\alpha = 0$, the DMT applies exactly.

Thus, the relationship between Maugis parameter and this parameter can be obtained

$$\lambda = -0.92 \ln(1 - 1.02\alpha_t) \quad (1.19)$$

1.7.3 Thin-film Contact Mechanics

In order to make FFM measurements on thin-coated films, it is necessary to have a reasonable contact mechanics model for interpreting the data. It is fair to say that until now there has been no unified model for the mechanics of tip-sample interactions in AFM. This is a reflection of the complexity of molecular interactions on the nanometer scale. Many factors are involved in the determination of the nature of contact mechanics such as the size, shape, and properties of the asperity and the nature of the sliding layers in the contact area. In addition, the molecular properties of the thin films in contact area are different from those of bulk and even thick layers. When two smooth surfaces slide against each other without plastic deformation and contact may occur at the single asperity level, the dissipative process is referred to as interfacial friction²⁰⁵. However, at the nanoscale elastic contact is usually dominant. Adhesion may also be very strong, and may provide the main dissipative pathway (shearing). In contrast, multi-asperity contacts more likely to behave plasticity. The nature of the contact area is different for the thin-coated film than is the case for bulk or thick films. Therefore, analysis of the behaviour of thin films in the contact area cannot rely on models that are used to characterise the contact mechanics in bulk or thick films. Some authors have used the Amontons' law to model FFM data, observing that in some circumstances the friction force is proportional to the load^{206,207}. However, using a single asperity mechanics approaches (JKR, or DMT) in which the friction-load relationships is sub-linear are needed more modifications to be fitted with experimental results²⁰⁸⁻²¹². Barthel et al. have illustrated that in order to fundamentally understand the surface mechanics of thin films, the geometrical shape of the systems, the mechanical properties of each single body, and the Physico-chemical response of the interfaces must be known²¹³. There was been a notable attempt to find out a solution for this conflict. Reedy has proposed a thin-coated contact mechanics (TCCM) postulate, which has been frequently and successfully applied to AFM to study the area depends on of the friction force as a function of load. The TCCM has developed both DMT and JKR approaches by finding a transition parameter. The model considered a rigid spherical indenter and a thin coated film that is bonded to a rigid substrate. The thin coat is assumed to be linearly elastic. In the TCCM the contact area is related to the square root of compressive load (L).

In contrast, it is related to the two-thirds over of one compressive load in Hertz theory. The thickness of the coat h , its elastic properties are defined by its Young's modulus E_c and Poisson's ratio ν , and R is the radius of the spherical indenter that is pushed into the elastic coating in a frictionless contact. Consequently, an equation has been driven for the compressive normal strain ϵ_z that relies on the geometry of the indenter and it is assumed to be uniform through the coating thickness:

$$\epsilon_z = \frac{a^2}{2Rh} \left[1 - \left(\frac{r}{a}\right)^2 \right] \quad (1.20)$$

where a is the contact radius and r is radial distance along the surface of the coating with the origin at the initial point of contact. With the postulation that R/h and a/R are much less than one, while a/h is greater than one, the compressive stress σ_z can be approximated to

$$\sigma_z = E_u \epsilon_z \quad (1.21)$$

where E_u is an axial strain modulus and it is $E_u = \frac{(1-\nu)E}{(1-\nu)(1-2\nu)}$. The relationship between L and A can be given as follows

$$L = \frac{E_u A^2}{4\pi R h} \quad (1.22)$$

Two years later Reedy expanded this development and introduced a transition parameter (ξ) in order to determine which contact model DMT or JKR is accurate to be applied in a given system. If $\xi \geq 0$ DMT is applied, while $\xi \leq 1$ JKR is more accurate to apply. Then he described the contact radius of interface as follows equation

$$\frac{L}{2E_u RT} = \frac{\pi}{4(2RT)^2} a^4 - \frac{\zeta \pi}{E_u T} \left(\frac{W}{E_u T}\right)^2 a^2 - \frac{\pi W}{E_u T} (1 - \zeta) \quad (1.23)$$

where W is the adhesion work and T is the total thickness²¹⁴.

Although this model has been applied by a number of researchers, particularly those using AFM. It cannot satisfy all problems arises in this area²¹⁵⁻²¹⁷. Recently, Leggett et al. have studied the relationship between contact mechanics and adhesion in pure liquids and mixtures.

They have found, that medium-medium interaction outside the contact area and the effect of hydrogen bond of the medium on adhesion has not been very good predicted by the models. Yang et al. have published an analytical method to study the elastic behaviour of a thin coated film. This is completely different from TCCM model, it depends on the scratching and bending resistance of polydopamine coated on PDMS sample when it is indented with a soft tip in nanoscale²¹⁸

1.7.4 Quantification of Friction in FFM

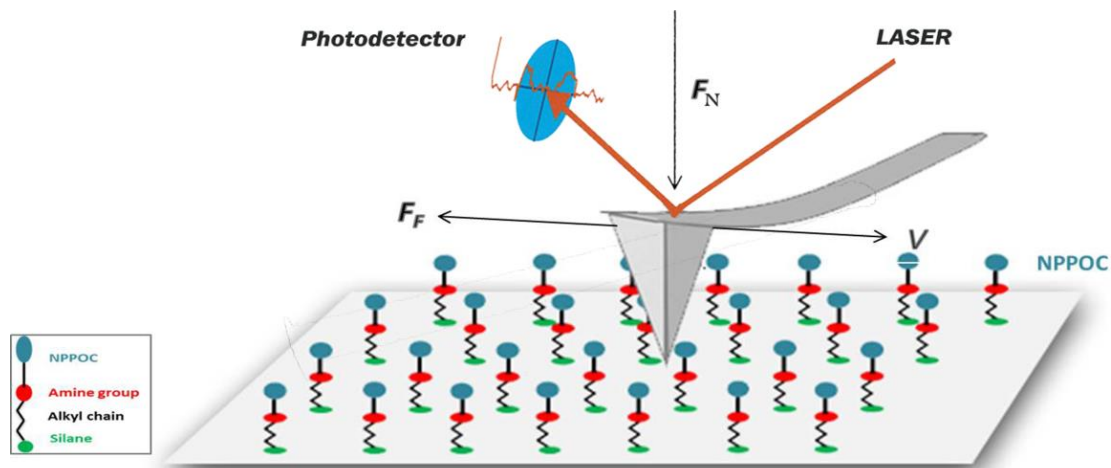


Figure 1.14: Demonstrates lateral scanning and twisting of a cantilever during its scanning across a thin coated film.

Forces generated by the tip-sample interaction act on the deflection of the cantilever. If the forces act at the apex of the tip in the vertical-direction, the cantilever is bent. However, if they act in the plane of the surface the lever is twisted. Torsional deflection and bending can be detected by utilising a laser beam, which is reflected on the back of the lever onto a photodetector. When the AFM operates in contact mode and the tip is scanned with constant Load, a lateral force results that act on the tip and as a result torsional force is generated that act on the cantilever (figure 1.14).

The lateral deflection, which is proportional to the friction force, can be measured from the lateral deflection of the cantilever if its lateral stiffness is known.

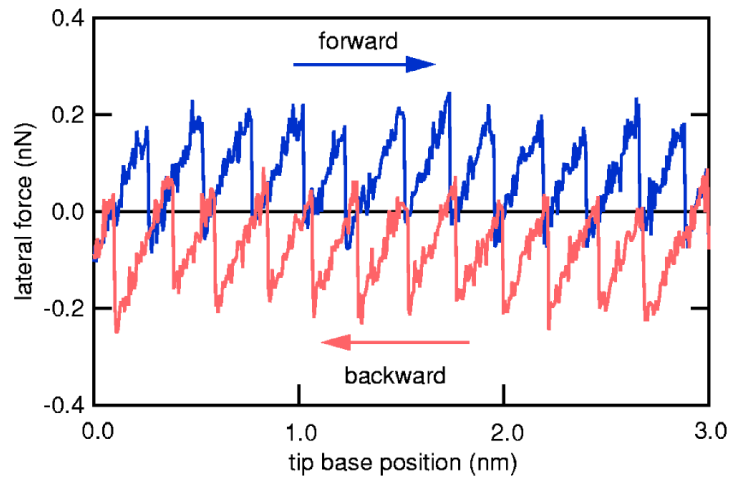


Figure 1.15: A friction loop for both forward and backwards scanning directions.

Frictional interactions between the tip-sample and the component of load resolved in the plane of the surface of the sloped substrate. Generally, the lateral deflection can be measured in two ways, first as a function of position to yield an image, and second, by scanning tip forward and backwards to generate a friction loop figure 1.15²¹⁹. Consequently, the absolute friction force can be quantitatively measured if the topographical contribution is removed by subtracting retrace from trace data and the photodetector outputs are halved. The lateral spring constant and tip profile at contact must be characterised to convert the photodetector signal into units of force²²⁰⁻²²⁴. Such quantitative investigation is not easy, due to the difficulty in the calibration of the torsional spring constant of the lever, the tip radius and sensitivity of the photodetector to the torsional deflection²²⁵.

To investigate the friction mechanism with multiple- and single asperity contact, many methods has been postulated under different conditions. Mate et al. For the first time in 1987 has observed not only a stick-slip mechanism but also hysteresis between forward and reverse scans (friction loops) as well. Stick-slip is obtained when the sample surface slides against the AFM tip, as a result, the tip is stuck at the beginning until it gains enough energy to be overcome for jumping from a position to another position on the surface²²⁶ figure 1.15. Then,

enough energy is stored in the spring after some movement that causes to slip into the neighbouring stable equilibrium position²²⁷. The Tomlison model can be considered as one of the most successful models to determine the friction force during atomic level stick-slip the main equation in this model is

$$f^* = \left(\frac{2E_o}{3Tk_B} \right)^{2/3} \frac{\Omega_k^2}{(1-\Omega_k^2)^{1/6}} \frac{4\pi}{ceff^a} (ceffR_c - F_m) \quad (1.24)$$

where, f^* is the radius bias, F_m the lateral force, E_o the surface potential, k_B The Boltzmann constant, T the absolute temperature, and Ω is the ratio of the resonance frequency of the tip in the surface potential to the torsional resonance frequency of the tip in contact²²⁸. A large number of models have been postulated to describe the friction force. Ogletree et al. have postulated a model based on comparison of the lateral force signal with different slopes to calculate the ratio of normal force into lateral forces. They assumed that the deflection of the laser beam is directly related to the slope of the lever In the X-Z plane and similarly, to the twist out of the probe at the point of reflection of laser. Assuming a Gaussian beam profile the photodiode signal S as a function of angular deflection φ can be derived:

$$S(\varphi) = \frac{(A-B)}{(A+B)} = 1 - \frac{1}{\Delta W} \sqrt{\frac{\pi}{8}} \int_{\varphi}^{\infty} e^{-2u^2/\Delta W^2} du \quad (1.25)$$

where ΔW is Gaussian half-width of the beam, A and B is the photocurrent of upper and lower two quadrants of respectively. If the cantilever twists because of the influence the tip-sample interaction in any direction, the angular displacement and resulting tip spring constant is

$$O(F_y, x) = F_y g(x), \quad K_y = 1/H_{tip} g(X_{Tip}) \quad (1.26)$$

where H is the tip height, O is angular displacement, and k_y is torsional spring constant. Thus, the ratio of angular deflection generated by normal and torsional can be calculated for a V - shape cantilever.

$$R(x) = \frac{2L-x}{H(1+\nu)} \quad \text{where } G = \frac{E}{2(1+\nu)} \quad (1.27)$$

E and G are the elastic hear modes of the lever and ν is poisson's ratio.

1.7.5 Calibration of Normal Force in AFM

In order to measure these forces accurately, it is necessary to calibrate the normal force. This can be done by measuring normal spring constant and normal deflection sensitivity of the probe. Hooke's law describes the dependence of the cantilever deflections on the force F :

$$F = -k x \quad (1.28)$$

Although manufacturers provide the spring constant for probes, they are subject to significant uncertainty^{229,230}. Many factors influence the spring constant, including the Young's modulus, Poisson's ratio, cantilever geometry, tip mass, and tilt angle. A number of different methods of cantilever calibration have been reported in the literature. In the present study, the method of Hutter and Bechhoefer based on measurement of the cantilever thermal noise has been used. This model has been widely used because it offers a number of advantages. It is rapidly implemented, non-destructive, independent of the shape, composition and coating of the cantilever and providing it is performed in situ, it is relatively easy to apply²³¹. Moreover, Matei et al. have revealed that the precision and accuracy of this method is 5% and 10%²³². In this thesis, the friction has been investigated as a function of normal load. The photodetector signal is in units of Volt, and must be converted to units of force. The basic principle of this theory is based on the equipartition theorem, according to which the total energy of each system at thermal equilibrium is $\frac{1}{2} k_B T$ (where, k_B is the Boltzmann constant and T is the absolute temperature). The total stored energy in the cantilever is presented as $\frac{1}{2} k d_c^2$, where k and d_c^2 are denoted the spring constant and the mean square of the cantilever deflection respectively. Hutter and Bechhoefer derived an equation by relating Brownian motion of the first oscillation mode to thermal energy^{233,234}

$$k = \frac{k_B T}{(d_c^2)} \quad (1.29)$$

From the theoretical point of view, for measuring the spring it is only necessary to know the mean square of the displacement of the cantilever and the temperature equation (1.27). Implementation is complicated by the contribution of environmental effects²³⁵, and the shape of the cantilever rectangular or V-shape²³⁶. In practice, the thermal spectrum is obtained from

the thermal vibrations of the free end of the cantilever, which is held far from the sample surface²³⁷. In the first step, the thermal fluctuations of the free cantilever are acquired by recording the photodetector voltage in time (V_t). This can then be Fourier transformed to the detector voltage power spectral density, P_v , that its relationship with the spectral power density P_d can be illustrated in the following

$$P_d = P_v \frac{1}{S^2} \frac{1}{\cos \alpha^2} X^2 \quad (1.30)$$

A correction factor X is required to convert between free ended and load-ended cantilevers. α is the cantilever tilt angle and S is the sensitivity of the cantilever. Consequently, the average power in the thermal vibration of the lever can be estimated. In the second step, the resonance peak is related to the simple harmonic oscillator, and then it is integrated to obtain a spring constant:

$$k_1 = \frac{2k_B T}{\pi A_1 F_1 Q_1} \quad (1.31)$$

where F_1 is the resonance frequency and Q_1 the quality factor of the lower peak. This spring constant is not a real spring constant k thus ETT found a correction factor between real spring constant and k_1

$$K = 0.97071k_1.$$

Initially, this method appeared to be independent in the shape of the cantilevers, but it is now clear that it is not²³⁵. The preceding analysis is appropriate for rectangular cantilevers, but a different approach is required for triangular levers. Stark et al. have taken advantage of the combination of thermal noise and finite element analysis method to calculate the V-shaped spring constant of a V-shaped lever. They noticed that the spectral density of thermomechanical noise for a V-shaped cantilever exhibits a systematic deviation from that observed for a rectangular cantilever. It has been noticed that the stiffness of the V-shaped cantilever is approximately 7% larger than the rectangular stiffness²³⁸. In spite of many successful experimental implementations, this method has some complications.

First, Butt et al. pointed out that the noise do not come from a single mode an assumption (an assumption implication in the use of the equipartition theorem). Includes all other possible vibration modes, they calculated the thermal noise from the deflection and fluctuations of the cantilever. Thus, they found out a correction factor that accounts for all other modes²³⁵. There is always a finite amplitude during stiffness measurements that involves as a resistance in front of other modes measurements. Also, the single mode amplitude appears larger than it really is because of the environment and electronic effects during applications. Walter et al. have reported the use of a simple harmonic oscillator model to resolve these complications. The simple harmonic oscillator was fitted with a single mode to describe the motion of the first vibration mode of the cantilever²³⁹. The effect of spot positions on the spring constant measurements has been investigated by Proksch et al in 2006, they noticed the systematic variation of the spring constant as a function of the spot position. They showed that by accounting for the spot diameter and position on the cantilever the gap between the thermally measured spring constant and other methods can be reduced²⁴⁰.

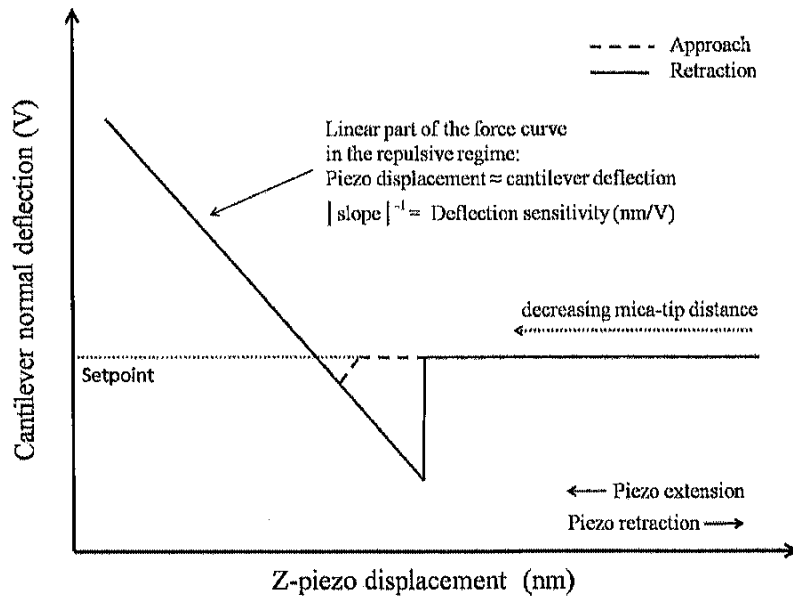


Figure 1.16: Schematic diagram showing a deflection sensitivity determination for a mica sheet against a silicon nitride probe.

A central goal of the present study is to quantify the friction force in nN as a function of supply load in nN as well, so it is necessary to convert voltage signals of both applied normal load (V) and also lateral force (photodetector's signal V) into a unit of force. The photodetector sensitivity is first determined to enable the deflection in V to be converted to deflection in nN; this is then combined with the stiffness to yield a force. The conversion parameter is known as the deflection sensitivity of the cantilever. Usually, hard samples (high stiffness) are used such as mica or silicon because the sample stiffness is much greater than that of the cantilever, the deflection may be assumed to occur only in the probe. Therefore, the z-piezo displacement Δz is equal to the normal deflection of the cantilever in the repulsive regime and the attraction regime²⁴¹. As a result of extension and retraction of the cantilever at the sample surface a force curve is generated (figure 1.16). The photodetector sensitivity is determined from the slope V/nm or the inversion slope (nm/V) of the linear part of the curve, depending on the definition needed. The inversion slope is called Inverse Optical Lever Sensitivity (InvOSL) sensitivity. Consequently, when the spring constant nN/nm, supplied load (V), and deflection in (nm/V) sensitivity is known as it is done in this study, the normal force can be calculated as follows

$$F_{N=} \text{Load (V)} \times \text{Deflection sensitivity} \frac{\text{nm}}{\text{V}} \times \text{normal spring constant nN/nm}$$

1.7.6 Calibration of Lateral Forces and Tip Radius of the Cantilever

Calibration of both the lateral stiffness and the tip radius are necessary in order to complete the process of friction measurements. The development of the reliable methods for the calibration of the lateral stiffness has proved challenging. Various methods have been proposed to characterise the tip profile and lateral stiffness²⁴²⁻²⁴⁴. In general, the term of contact stiffness can be defined as the force per unit of displacement which acts at a contact in a particular direction. The most common technique is called a Wedge Calibration method²⁴⁵. The attraction of this method is that it does not presuppose information about the probe dimensions or the tip height. Furthermore, not only it is able to work with any kind of deflection sensors, but also the profile of the lever can be determined.

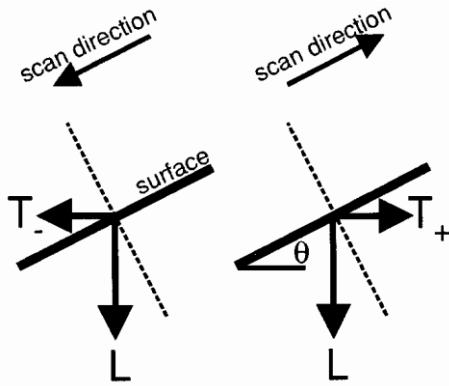


Figure 1.17: Demonstrates forces exist when the tip slides across a sliding surface²⁴⁹.

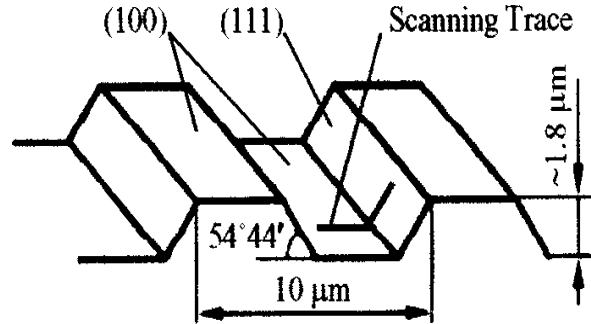


Figure 1.18: Shows the schematic diagram of feature of calibrating diagram TGF11, the pitch value is 10 μm , the edge angle is 54°44', and 1.8 μm step height²⁴⁹.

The calibration can be done by measuring the lateral photodetector response as a function of applied load, while the tip slides over a sample surface with a known slope. The authors showed a vector diagram to illustrate the forces acting on the tip during scanning up and down the sloped surface (figure 1.17). The tractive force (T) which acts in the scan direction must be in balance with the forces generated between the tip and the sample surfaces. The generated forces are a normal force (N) and a frictional force (F) acting in opposition to the scan direction. The direct calibration is done when the photodetector signals are measured as a function of lateral displacement and the sensor angular sensitivity to find a parameter (α) in (Newton/Volt). In 2003 Varenberg et al. reported an improved wedge calibration method, which is simpler than the origin postulate²⁴⁶. In this method a calibrated grating sample (TGF11) with a well-known slope and flat face (figure 1.18). They considered that it is possible to correct the measurement of the torsional loop offset Δ_o^* , by subtracting it from the torsional loop offset measured on the flat surface Δ_o^{flat} . Thus the accurate torsional loop offset Δ_o can be represented as follows

$$\Delta_o = \Delta_o^* - \Delta_o^{flat} \quad (1.32)$$

That means that topographical effect has been accounted for.

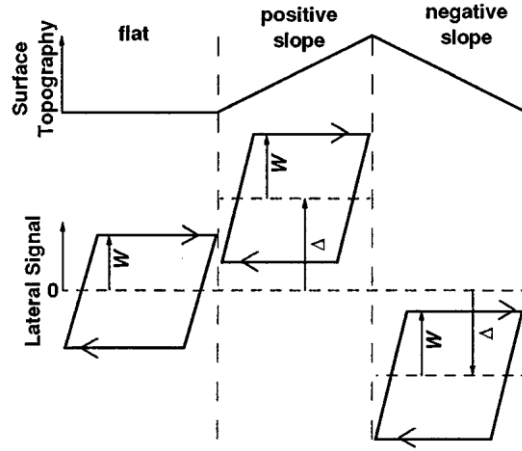


Figure 1.19: Schematic diagram showing the acquisition of frictional loops while the tip is scanned at forward and backwards direction on a calibration sample surface²⁴⁹.

They analysed the friction coefficient μ for both flat and sloped surface and a relationship was made between μ and the transition parameter α

$$\mu^{flat} = \frac{\alpha W_o^{flat}}{L + A} \quad (1.33)$$

where W_o^{flat} is the torsional loop half-surface of the flat surface, A is an adhesion force, and L is an applied load. The results showed similar values for the calibration factor α at both flat and slope surfaces figure (1.19). However, α is the required factor to convert the lateral deflection in Volt to force in Newton and can be obtained in the following equation.

$$\alpha = \frac{\mu (L + A \cos\theta)}{W_o (\cos^2\theta - \mu^2 \sin^2\theta)} \quad (1.34)$$

The reactions can be derived as follows

$$\sin\theta (L \cos\theta + A) \mu^2 - \frac{\Delta_o}{W_o} (L + A \cos\theta) + L \sin\theta \cos\theta = 0 \quad (1.35)$$

The values of W_o and Δ_o are acquired from the result of scanning both flat and slope surface of the grating sample TGF11.

$$W_o = \frac{(d-c)}{2}, \Delta_o^* = \frac{(d+c)}{2}, \Delta_o^{*flat} = \frac{(a+b)}{2} \quad (1.36)$$

1.8 Lithographic Techniques for Surface Patterning

There has been increasing interest in patterning surfaces during recent years, due to their importance in many research fields, including, nanoelectromechanical, microelectromechanical, biomedical, and in the development of optics and electronics (or nanotechnology). In general, all approaches involve either top-down or bottom-up strategy or both together in some occasions. They can be classified into three main groups soft lithography, particle beam lithography and photolithography, the latter one has involved vital application in fabricating micrometre and nanometer patterning structures.

1.8.1 Soft Lithography

Soft lithography can be considered as a branch in nanotechnology. It is an easy, inexpensive, and unconventional technique. The main strategy involves self-assembling and replica molding of the organic and polymeric molecule for manufacturing micrometre and nanometer structures of various chemicals on the surfaces. In general, four major methods can be seen in this field which are microcontact printing (μC_p), replica molding, micromolding in capillaries (MIMIC), and microtransfer molding (Mtm)²⁴⁷.

1.8.2 Microcontact Printing (μC_p)

This is the most common and successfully used soft lithography technique and it has found a broad range of applications in chemistry, physics, and biology. Typically, for the creation of functional surfaces, including self-assembled monolayer (SAMs) of organic and biological molecules, polymer brushes, nanoparticles, metal films and carbon nanotubes²⁴⁸. This technique is based on the use of an elastomeric stamp which is usually made from poly(dimethyl siloxane) (PDMS) to transfer the surfactants as an ink onto the targeted surface. After a few seconds of contact the stamp is removed from the surface very carefully, a chemical reaction between the adsorbent and adsorbate which results in a very stable functionalized surface²⁴⁹⁻²⁵⁰ figure (1.20b). The morphology of the patterned surface is dependent on the geometrical design of the stamp, which is transferred from a master onto the stamp figure (1.20a)²⁵¹.

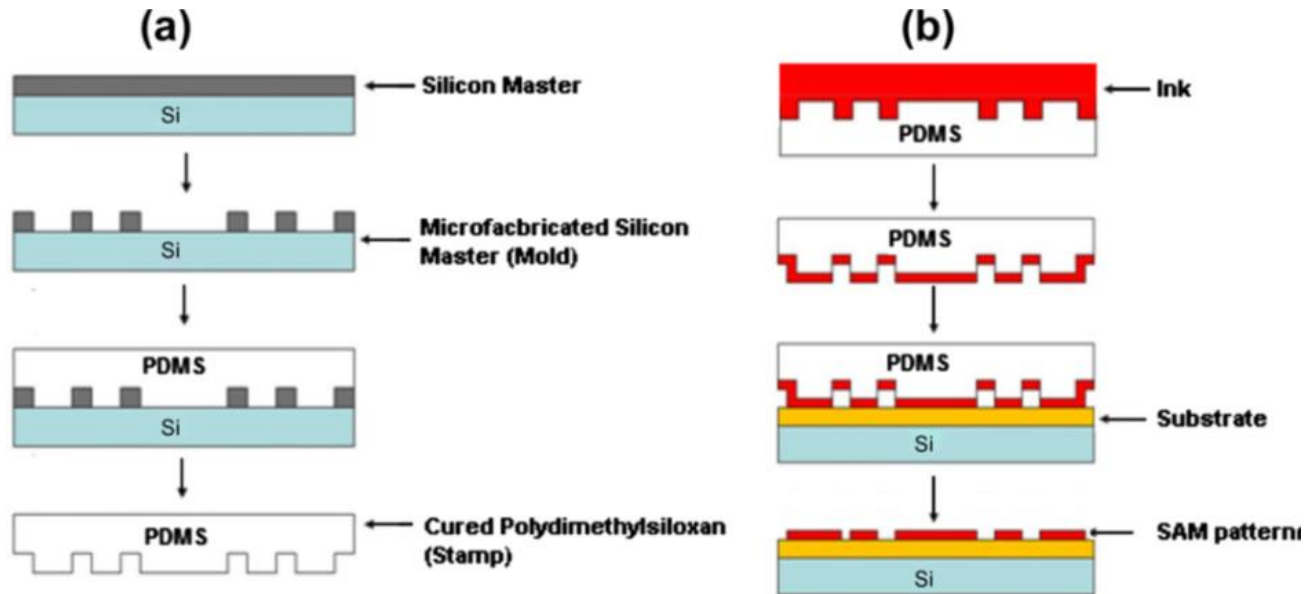


Figure 1.20: Demonstrates schematic representation of fabrication of a) the PDMS stamp from the master and b) the self-assembled layer from the stamp.

It is believed that the mechanism of spreading and transfer of the ink from the stamp to the surface is controlled by the gradient concentration and the affinity of the substrate toward the surfactant which supposed to be higher than the affinity from the stamp. Many parameters like electrostatic interactions, hydrogen bonding and even hydrophobic interaction play a role in enhancing the affinity of the substrate. PDMS is used as a stamp because of its inert to most solvents and chemicals. Its elastic properties also mean that PDMS can be easily removed from the surface after molding and because of its low surface free energy it is thermally and oxidatively stable²⁵². Combination of the μ CP with the SI-ATRP provides a new route to fabricate complex polymer brush structures. Zauscher with co-workers have prepared different micrometre scale structures from poly(N-isopropylacrylamide) (PNIPAAm) brush by printing thiol initiator on gold surface and using surface-initiated atom transfer radical polymerisation to grow the polymer. It has been revealed that size and the shape of the polymer brush microstructures can be controlled by the condition of μ CP, for example, changing physical deformation of the stamp by using force or solvent swelling, and UV-Ozone chemical modification of the stamp²⁵³.

Zhou et al. reported the preparation of patterned bilayer brushes. They prepared the first brush on a silicon surface via SI-ATRP. It was then derivatised, using the μC to transfer initiator integrated polydopamine (PDOPBr) onto the surface of the grafted polymer. This step was followed by growth of a second brush on the patterned initiator through SI-ATRP. They found that the surface energy plays a key role in transfer efficiency of the PDOPBr initiator from the stamp onto the grafted polymer surface which dominates the initiator stability and the quality of the second brush²⁵⁴. Despite the extraordinary success of the μCP in the many fields, there are still some noticeable drawbacks related to this technique, including difficulties that limit the high quality of the patterned surface including swelling, stretching, inappropriate geometrical shape of the stamp, and the result of compression of the stamp with load of force when it is in contact with the surface results in collapsing the stamp and damaging the pattern. In addition because of higher affinity of the stamp to the surfactants rather than the substrate, the molecular crystals of materials remain on the mold surfaces and cause to contamination²⁵⁵.

1.8.3 Particle Beam Lithography (PBL)

Focused beams of energetic particles, including electrons, ions, and electrically neutral metastable atoms offer proper approaches for fabricating patterns in a targeted substrate. The main methods in this field are known as electron beam lithography (EBL) and Focused ion beam lithography (FIBL). From the methodological point of view, these techniques share the same protocol, in which a focused spot is scanned over the surface of the targeted substrate²⁵⁶. One of the main advantages of these methods is the extremely high resolution, due to their short wavelengths ($> 0.1 \text{ nm}$) combined with an accurate control of size²⁵⁷. Thus, they have been used in many applications. For example, EBL has been applied for fabrication of sub-10 nm electrode gaps for nanoelectronic applications²⁵⁸. In addition to the high-resolution these techniques could be high throughput, easy, and fast. N. Nagy and co-workers prepared nanopatterns with different periods and properties on a large area of the silicon surface, exposed to either Ar^+ or Xe^{2+} in a masked ion irradiation technique²⁵⁹.

Although high cost and problematic byproducts have become the main challenges in the developments of these techniques compared to the others, they have been used to fabricate nanometre and micrometre structures in a variety of Self-assembled monolayer (SAMs) and

polymer brushes²⁶⁰. Nanometer structures of 4'-methylbiphenyl-4-thiol on the gold surface have been reported. AFM topography images revealed features with 100 nm that was used as a template for Cu electrodeposition and lift-off²⁶¹. EBL has been used by Ohdomari et al. to fabricate nanometer and micrometre architecture of perfluorodecyltriethoxysilane (FDTES) immobilised on the silicon wafer. The exposed area was functionalized with 2-[methoxy(polyethylenoxy)propyl] trichlorosilane, which was used as a template for patterning proteins²⁶². The patterning of the polymer brush is a multiple setp processes and complicated, but this could be done in a single step using particle beam lithography, provided just the polymer is the beam sensitive. A series of polymer brushes including poly(methyl methacrylate) (PMMA), poly(2-hydroxyethyl methacrylate) (PHEMA), poly(isobutyl methacrylate) (PIBMA), poly(neopentyl methacrylate)(PNPMA), and poly(2,2,2-trifluoroethyl methacrylate) (PTFEMA) brushes were grown on silicon via SI-ATRP. Then, the nanopatterned polymer brushes were generated, using EBL and AFM tapping mode images confirmed the architectures of the patterned brushes²⁶³.

1.8.4 Photolithography

Photolithography is one of the most widely-used, convenient, and useful technique for the fabricating nanometer and micrometer-sized patterns²⁶⁴. There are a number of different variats, including mask based and maskless methods, such as interference lithography (IL) and scanning near-field optical microscopy (SNOM). Photolithography techniques can bused to create a variety of micrometres and nanometre scale architectures, which are useful in many biological²⁶⁵ and industrial applications²⁶⁶. A long-standing goal has been to integrate top-down and bottom-up fabrication methods²⁶⁷. This goal cannot be achieved without having a proper photoresist material deposited on a surface. This material plays an important role in improvement of resolution, proximity, diffraction limit, high aspect ratio, and structural stability. Which are considered as the most common challenges in conventional lithography. In general, photoresists are organic and light-sensitive materials that their chemical and physical properties are changed after they are illuminated with a UV light.

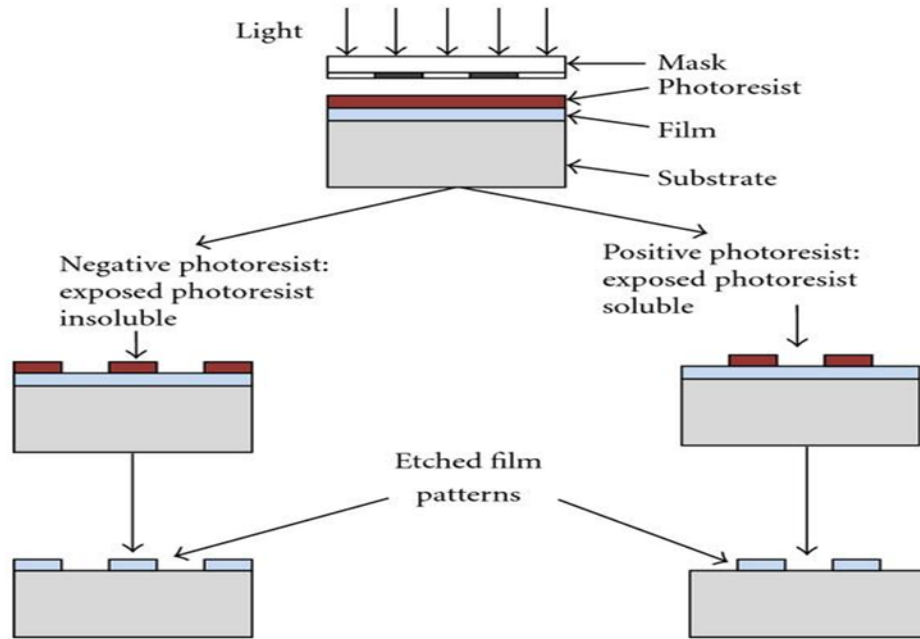


Figure 1.21: Schematic diagram of photolithography process utilising positive and negative mode.

There are two main types of resistant: negative and positive tone. In positive mode, the irradiated part of the resist is dissolved in the developer, while the masked area remained. As a result, the mask is replicated after the etching process. The negative mode involves removal of the non-exposed part of the resist in the developer as shown in²⁶⁸, the resulting pattern is the negative of the mask (figure 1.21)²⁶⁹.

Nanometer patterns can be fabricated by using either IL²⁷⁰ or SNOM²⁷¹. The latter technique has been applied to improve the proximity effect and resolution. Azuma et al. demonstrated that the reducing the thickness of the photoresist could successfully improve the proximity effect in the photolithography which leads to increase the resolution as well²⁷¹. Since then, self-assembled monolayer and polymer have been most widely-used chemicals in these fields.

1.8.5 Interference Lithography (IL)

Today's nanolithographic techniques such as electron beam lithography (EBL), Ion beam lithography (IBL), and those based on atomic force microscopy have witnessed significant progress. However, each of these methods has faced some limitations, including, high

throughput, cost, resolution, and capability to the pattern over a large area, therefore, none of these has able to become a dominant tool. Interference lithography (IL) has overcome some of these limitations. It can be regarded as simple, fast, inexpensive, high throughput technique that causes minimal surface contamination. It is also capable of fabricating nanometer structures with different shapes and periodicity over a large area^{272,273}. Interference occurs when two or more coherent beams overlap to cause an interferogram. Their intensity distribution is recorded in a photosensitive film figure 1.22.

In general, two different strategies are used to generate an interference pattern by utilising laser beams. The first involves utilising optics to split the amplitude of a coherent beam into two beams (which is known two-beam IL) or more beams (which is called multiple-beam IL) which are then made to interfere with each other. The second relies on passing light from a single coherent source through an optical element to form an interference pattern.

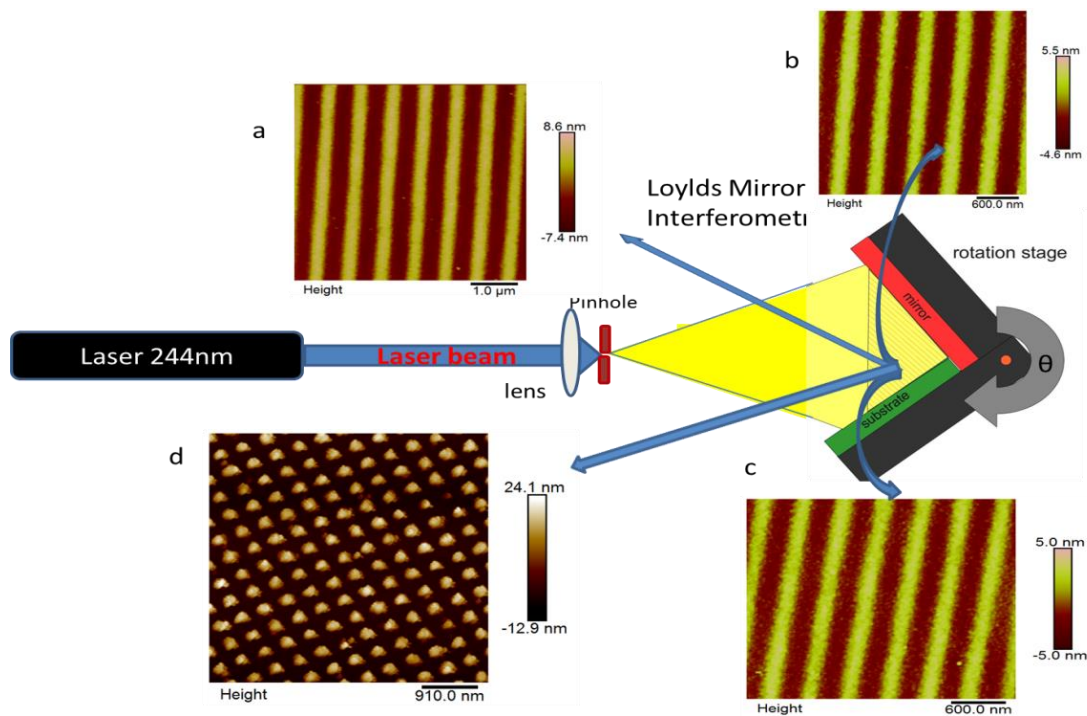


Figure 1.22: Schematic diagram of interference lithography based two-beam system with some patterning resultants which have different periods and shapes a) 586 nm period, b) 470 nm, c) 360 nm made via single exposure and d) gold nanodots on silicon surface via multiple exposures.

Young's double slit experiment can be considered as the most common example of the latter method, in which a light of a coherent beam is used to illuminate two slits placed a fixed distance apart. As a consequence of interfering the diffracted lights from the slits a one-dimensional (1D) pattern is produced in the far field. There are some key parameters which involve an important role in controlling and manipulating the desired nanostructures, including exposure dosage ($J \cdot \text{cm}^{-2}$), the angle (θ) between the two beams, the wavelength of the laser beam, and the number and time of the exposure²⁷⁴⁻²⁷⁶. However, the period (d) of the resultant nanopatterns can be varied as a function of the exposure angles (figure 1.22a, 1.22b and 1.22c), and also relies on the wavelength (λ) of the coherent beam used.

$$d = \frac{\lambda}{2n \cdot \sin \theta} \quad (1.37)$$

where n is the index of refraction of the photoresist film.

Hunter et al. have reported that the periodicity and the linewidth of 1D amine terminated self-assembled monolayer on the gold surface can be controlled by varying the angle between interfering beams and exposure time, using the single exposure pathway. They found that the full width half maximum (FWHM) of the patterned lines dramatically decreased as a function of exposure time, and also by increasing the θ the periodicity of the pattern decreased. AFM Lateral force microscopy images showed 1200 nm, 550 nm, 400 nm, and 240 nm period obtained by exposing the film with the angle of 6° , 13° , 18° , and 30° respectively. On the other hand, the 600 nm FWHM obtained with a period of 1200 nm, required 2 min exposure, the line width was reduced to 170 nm after 15 min exposure, while the period was not changed²⁷⁷. Smith with co-workers reported a model which showed the linewidth relies on the exposure power in IL²⁷⁸. IL can be used to fabricate nanodot and hole patterns with 2D or 3D structures on the surfaces through multiple-exposure²⁷⁹ as shown in figure 7d. Technically, the sample is placed in the normal position on the stage, which is in 90° with the mirror, and then it is rotated with a certain degree during the second exposure. A multiple-exposure process has been used to fabricate a microlens array, using IL followed by reflow and reactive ion etching. After the first exposure, the photoresist was rotated at 90° to perform the second exposure.

AFM images revealed 2D and 3D structures of the microlens array, which they were in excellent uniformity and good quality surface²⁸⁰. IL has been widely used to fabricate periodic architectures in polymer brushes, for use as building blocks in the formation of many biomedical devices²⁸¹.

Despite numerous applications and its flexibility for performing on a large number of photoresists to fabricate nanostructures in various fields, the high resolution and diffraction limit are the most important issues concerning IL. The minimum period that can be fabricated by IL is equal to the half of the wavelength of the coherent beam and it is given by $d = \lambda/2$. Therefore, improving the resolution has been targeted by many researchers; all strategies can be concluded in two ways. The first strategy involves reducing the wavelength of the coherent beam by using either x-ray or extreme ultraviolet (EUV) and soft X-ray which they provide very short wavelength, By using these techniques sub-50 nm period pattern has been reported²⁸². However, two main challenges have terminated the development in these fields which are the high cost related to the generation of these light sources and high absorption coefficient of the photocleavable material in the short wavelengths. The second strategy was the immersion lithography, in which the photoresist is immersed in a proper liquid and the period size of the pattern is reduced as a function of the refractive index of the medium. Rothschild et al. used immersion IL to fabricate 20-nm half-pitch, this achieved by combining two-beam interference, very short wavelength 157 nm, and application immersion lithography²⁸³.

Chapter 2: Aims

Membrane biochemistry occurs in two dimensions. The formation of synthetic biocompatible surfaces provides a means to recreate the membrane environment under systematically controlled conditions. Cellular attachment to artificial materials is controlled by the interaction of membrane receptors with the artificial surface. In this thesis, a novel polymer polymer, poly (cysteine methacrylate), PCysMA, is used to design structures to study membrane biochemistry and stem cell-material interactions.

Chapter 4 and 5 describe fundamental studies of the structures and properties of PCysMA brushes, and of nanostructured materials formed by interferometric lithography.

The goal of the Chapter 6 is to examine how nanostructured materials based on PCysMA can be used to control and direct stem cell attachment. The goal of Chapter 7 is to explore whether PCysMA may be used as a support for lipid bilayers and whether they can be designed in such a way as to incorporate gold nanostructures for plasmonic analysis.

Chapter 3: Experimental

3.1 Materials

Silicon wafers <100> orientation, boron doped, test grade, 380 nm thick were supplied by Compart Technology (Peterborough, UK). Electron microscope grids (1000-2000 Mesh Cu) used for micron-scale patterning, (3-aminopropyl) triethoxysilane (APTES) ($\geq 99\%$), triethylamine ($\geq 99\%$), α -bromoisobutyryl bromide (BIBB) (98%), copper (I) bromide ($\geq 99\%$), copper (II) bromide (99.9999%), 2,2'-bipyridyl (>99%) and dimethylphenyl phosphine (DMPP) (99%) were purchased from Agar Scientific (Stansted, UK). Titanium wire (99.9%), gold wire (99.99%) and tungsten boats were purchased from Testbourne (Basingstoke, UK). L-Cysteine (98%), 3-(Acryloyloxy)-2-hydroxypropyl methacrylate, 11-mercaptoundecanoic acid (MUA, 95%), octadecanethiol (ODT) (97%), paraformaldehyde (>95%), 3-(triethoxysilyl)propyl isocyanate (95%), benzyltrimethylammonium hydroxide (Triton B) (40 wt. % in methanol) (>99%), and potassium dihydrogenphosphate (>99%) were obtained from Sigma-Aldrich (Gillingham, UK). Sulfuric acid ($\geq 95\%$), hydrochloric acid (>30%), hydrogen peroxide (30% v/v), ethanol (HPLC grade), toluene (HPLC grade), dichloromethane (DCM, HPLC grade), ammonia solution (s.g. 35%), ethyl acetate (HPLC grade), hexane (HPLC grade), diethylether (HPLC grade), methanol (HPLC grade) were supplied by Fisher Scientific (Loughborough, UK). Dry toluene was collected from an onsite Grubbs dry solvent system. Deionized water was obtained from an Elga PURELAB operates system and had a resistivity of 15 M Ω cm. Cysteine methacrylate (CysMA) was synthesized according to the previously reported protocol²⁸⁴. 4-(chloromethyl)trichlorosilane (CMPTS, 97%) was purchased from Alfa Aesar (Heysham, UK). Msenchymal stem cells (MSC) were supplied by Lonza Lonza, UK), T75 tissue culture flasks from Corning, UK and trypsin from Sigma, UK. 1-palmitoyl-2-oleoyl-sn-glycero-3-phosphocholine (POPC) and 1,2-dioleoyl-3-trimethylammonium-propane (DOTAP) (99%) were purchased from Avanti Polar Lipids (Alabaster, AL).

3.2 Cleaning Glassware and Silicon Wafers

Glassware and silicon wafers in glass tubes were cleaned thoroughly by immersion in a mixture (50% each) of ethanol-acetone for 30 min with sonication, followed by sonicating with water for another 30 min. The substrates were immersed in piranha solution sulfuric acid (70%) and hydrogen peroxide (30%) for CA. 40 min. *Warning! Piranha solution is a mixture of an extremely strong oxidizing agent that has been known detonate spontaneously upon contact with organic materials*). After removal from the piranha solution they were rinsed seven times in deionized water and cleaned further by immersing in RCA (Radio Corporation of America) solution (70% deionized water, 15% hydrogen peroxide, and 15% ammonia) which was heated and left boiling for approximately 40 min. The substrate underwent a further clean by rinsing seven times with deionized water and sonicating for 15 min. The cleaned substrates were placed in a dry oven (120 °C) overnight.

3.3 Surface Self-assembled layer Formation and Subsequent Surface Initiation

Silane films were made by immersing the dry silicon wafers in 2% v/v APTES solution in ethanol, which had already aged for 5 min. The reaction proceeded for 30 min and the samples were sonicated during the first 5 min of the period. After film formation the wafers were rinsed with ethanol for 5-10 min and blown dry with nitrogen. Subsequently, the samples were annealed by placing them into the vacuum oven (120 °C) for 40 min. Prior to performing atom-transfer radical polymerization, the functionalized silane substrates were derivatized by immersion a solution of 2-bromoisobutryl bromide (BIBB) (0.37 ml, 3 mmol) and triethylamine (0.41 ml, 4 mmol) in dichloromethane (DCM; 60 ml) for 40 min. Finally, the samples were sonicated in DCM and ethanol for 5 min and then dried under nitrogen.

3.4 Formation of MUA and ODT Self-assembled Monolayers on a Gold

The substrates were prepared by depositing of 3.5-5 nm of an adhesive layer of either chromium (Cr) or titanium (Ti) onto a clean silicon surface at a rate of 0.03 nm s⁻¹, using an Edwards Auto306 vacuum coating system. The samples were allowed to cool before depositing 18-20 nm of gold at a rate of no more than 0.03 nm s⁻¹. The samples were cooled and vented

cool to dry nitrogen. Self-assembled monolayers were prepared via immersing the slides in a solution of 1 mM 11-mercaptoundecanoic acid (MUA) or octadecanethiol (ODT) in degassed ethanol. The reaction was allowed to proceed for 24 h, after which the SAM coated slide was sonicated and rinsed with ethanol and finally dried under a stream of nitrogen. The slides were kept in the same solvent and far away from UV light during the entire period of the experiments, to avoid the adsorbed alkanethiolate SAMs from the oxidation reaction.

3.5 Synthesis

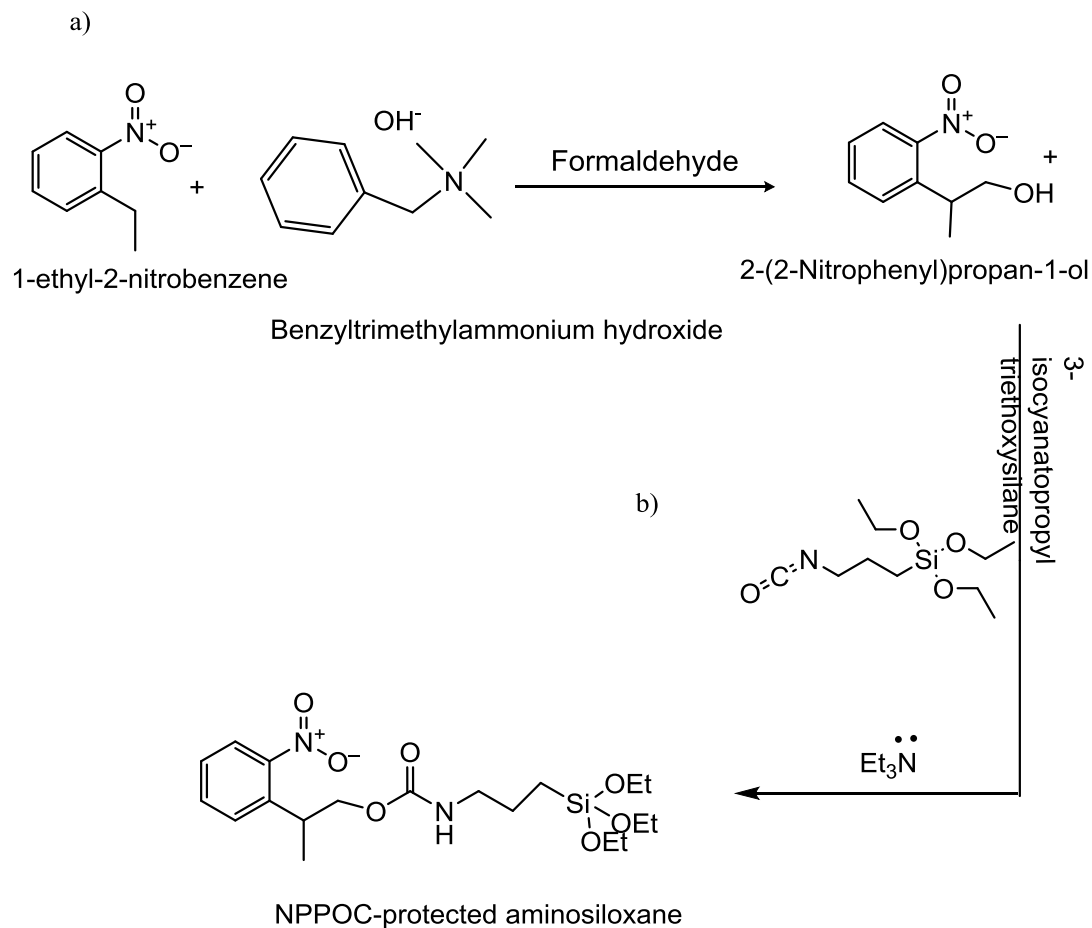
3.5.1 Synthesis of Cysteine Methacrylate Monomer (CysMA)

Cysteine methacrylate was synthesized as described previously. L-cysteine (15.13 g, 124.88 mmol) was dissolved in 100 mL deionized water, then transferred to a 250 mL round-bottomed flask. 3-Acryloxy-2-hydroxy methacrylate (29.43 g, 137.36 mmol) was added slowly to the stirred aqueous solution, followed by addition of dimethylphenyl phosphine (20 μ L, 147 μ mol) as a catalyst. The mixture was stirred for 2 h at room temperature. The product was washed twice with ethyl acetate (2 x 50 mL) and dichloromethane (2 x 50 mL) and excess solvent removed in a rotary evaporator. The concentrated aqueous solution of CysMA monomer was collected and the product crystallized in a freezer before drying for 48 h. The resulting white solid powder (39.6 g, 94% yield) was stored under nitrogen in the fridge.

3.5.2 Synthesis of 2-nitrophenylpropylloxycarbonyl-3-aminopropyltriethoxysilane (NPPOC-APTES)

2-Nitrophenylpropylloxycarbonyl-3-aminotriethoxysilane (NPPOC-APTES) was synthesized following the previously reported procedure²⁸⁵. The synthesis consisted of two main steps. In the first step, 2-(2-nitrophenyl) propan-1-ol was prepared via adding 2- ethylnitrobenzene (5400 μ L, 40.0 mmol) to a 40% of benzyltrimethylammonium hydroxide (triton B) solution in methanol (7 g, of solution 40.6 mmol) followed by paraformaldehyde (183 mg, 61 mmol) scheme 2.1. The mixture was refluxed at 80 $^{\circ}$ C for 24 h, then it was allowed to cool and evaporated under reduced pressure to remove extra solvents. The mixture adjusted to PH 7, using 1M aqueous HCl, then it was extracted thrice by utilizing EtOAc 60 mL each, before filtering and evaporating

under reduced pressure to yield a brown oil. The separated organic layer was dried using MgSO_4 .



Scheme 3.1: demonstrates a schematic representation of the synthesis of APTES-NPPOC, a) preparation of 2-(2-Nitrophenyl) propan-1-ol and b) the reaction between first yielded product and isocyanatopropyltriethoxysilane to yield NPPOC-APTES.

The brown oil was purified using flash column chromatography (mixture of hexane/ETOAc 4:2 or 2:1) to yield the product as a deep orange oil (3.524 mg); R_f 0.11(hexane/ETOAc 2:1); δ_H (400 MHz, CDCl_3) 1.34 (3H, d, J 7, CH_3CH), 1.70 (1H, s(br), OH), 3.52 (1H, m, CH_3CH), 3.81 (2H, m, CHCH_2O), 7.39 (1H, dd, J 8 and 8, 5-Ph), 7.50(1H, d, J 8, 3-Ph), 7.59 (1H, dd, J 8 and 8, 4-Ph), 7.76 (1H, d, J 8, 6-Ph).

In the last step, 2-nitrophenylpropyloxycarbonyl-3-aminopropyl triethoxysilane (scheme 3.1 b) was synthesized by adding 15 mL of dichloromethane to 3518 mg, 19.42 mmol of 2-(2-nitrophenyl) propan-1-ol, followed by 5 mL (20.2 mmol) of 3-isocyanatopropyltriethoxysilane and (235 μ L, 1.7 mmol) of Et₃N.

The mixture was refluxed at 60 °C for 24 h, after which 20 mL of Et₂O was added to the mixture before extracting the product thrice using 0.1 M potassium buffer PH 7 (50 mL each). The separated organic layer was dried with MgSO₄ and the solvent evaporated under reduced pressure. The desired product (residual oil) was purified, using flash column chromatography. TLC was used to separate the desired fractions, and evaporated under reduced pressure to remove all solvent. The flash column chromatography and the evaporation process were carried out in the dark place to protect the photosensitive yellow oily product (5.324 g) from UV light and the product stored under N₂ in a dark place. R_f 0.50 (hexanes/EtOAc, 1:1); $\nu_{\max}(\text{neat})/\text{cm}^{-1}$ 3337 (CONH), 2971 (alkyl), 2928 (alkyl), 2881(alkyl), 1718 (CONH), 1526 (NO₂), 1356 (NO₂), 1074 (SiOEt), 954 (SiOEt); δ H (300 MHz, CDCl₃) 0.59 (2H, t, *J* 8, CH₂Si), 1.21(9H, t, *J* 7, OCH₂CH₃), 1.34 (3H, d, *J* 7, CH₃CH), 1.58 (2H, tt, *J* 7 and 8, CH₂CH₂CH₂), 3.12 (2H, td, *J* 7 and 6, NHCH₂), 3.70 (1H, m, CH₃CH), 3.81 (6H, q, *J* 7, SiOCH₂), 4.10 (1H, m, CHCH₂O), 4.23 (1H, m, CHCH₂O), 4.85 (1H, s(br), CONHCH₂), 7.36 (1H, dd, *J* 8 and 8, 5-Ph), 7.47 (1H, d, *J* 8, 3-Ph), 7.56 (1H, dd, *J* 8 and 8, 4-Ph), 7.73 (1H, d, *J* 8, 6-Ph); δ C (100 MHz, CDCl₃) 7.9 (CH₂Si), 17.8 (CH₃CH), 18.7 (OCH₂CH₃), 23.6 (CH₂CH₂CH₂), 33.6(CH₃CH), 43.7 (NHCH₂), 58.8 (OCH₂CH₃), 68.9 (CHCH₂O), 124.4(6-Ph), 127.6 (5-Ph), 128.3 (3-Ph), 132.9 (4-Ph), 137.9 (2-Ph), 151.1(1-Ph), 156.5 (CONH); m/z (ES⁺) 451 (100%, [M + Na]⁺); HRMS found 451.1875 [M + Na]⁺, requires 451.1871, δ 0.9 ppm.

3.6 Formation of NPPOC-APTES Film

A 2 cm X 3 cm piece of a cleaned silicon slide was placed in a dry, clean Schlenk tube. The tube was evacuated and refilled more than three times with dry nitrogen to purge moisture. The Schlenk tube was filled with nitrogen and sealed with a septum. The tube was wrapped with foil to exclude light. 1.0 mM of NPPOC-APTES in dry toluene solution was added into the schlenk tube. The reaction proceeded under nitrogen for about 48 h.

The substrate was rinsed and sonicated in toluene, ethanol/toluene (1:1), and then ethanol and blown dry under a stream of nitrogen to remove all physisorbed surfactants. The silane coated film was annealed by placing it in the evacuated Schlenk tube, which was wrapped with foil and fitted with a septum, and then placed in a vacuum oven at 120 °C for 30 min. After that, the annealed sample was rinsed with ethanol, wrapped with foil, and stored in a dark place.

3.7 Photolithpgraphy

3.7.1 Nanometre and Micrometre Scale Patterns of APTES-BIBB Film

Micrometre and nanometre photopatterning of BIBB-APTES initiated samples was carried out using a Coherent Innova 300 C FreD Frequency-doubled argon ion laser (coherent U. K, Ely, UK) with an emission wavelength of 244 nm. The laser power was maintained at 100 mW. Micrometre photopatterned ATRP initiators were obtained by irradiation of the samples through a copper electron microscopy grid (1000-2000 mesh, Agar, Cambridge, UK), using a dose of 3.0 J cm⁻². The diameter of the illuminated area was 0.5 cm². Interferometric Lithography (IL) was carried out using a Lloyd's mirror two-beam interferometer. A coherent beam passes through a pinhole. Half of the beam is pointed onto the mirror, while the other half is placed onto the photoresist. The reflected beam and the direct beam interfere on the substrate surface and forming a sinusoidal pattern of intensity that can be recorded by the film. To form nanopatterned ATRP initiator films, a dose of 1.8 J cm⁻² was used. The angle between the two beams at the intersection was controlled by the rotation stage (which holds the mirror and sample at an orientation of 2θ to each other) to fabricate different periodic structures using angles of θ, 10°, 15°, 20°, and 30° during exposure to obtain patterns with periods of 690, 511, 450, 307 nm respectively. The irradiated samples were subsequently rinsed with ethanol and blown under a stream of nitrogen, in order to remove all photodegraded byproducts. A micrometre, nanometer patterned and unpattern samples were fabricated together using portions of a single Br-terminated sample (1 cm wide and 4 cm length) patterned samples were immersed in polymerization solution in a carousel tube under nitrogen.

3.7.2 Gradient PCysMA brushes

Gradient of initiator density on silicon surfaces were prepared by photodegradation of the samples, using the a photolithography technique. The samples were cut into 1 cm x 1cm sizes by using a diamond cutter and they were quickly washed with ethanol and dried under a stream of N₂. Samples were irradiated at 244 nm. The laser power was adjusted in the exposed area by controlling the size of the irradiated area, using an aperture, and by varying the exposure time. Doses of zero, 0.2, 0.5, 0.8, 1.0, 1.5, 2.0, 2.5, 4.0, 7.0, and 10 J cm⁻² were used to creat a gradient of exposure. Upon the completion of the photodegradation process, the surface was flushed with a sufficient amount of ethanol and dried under a stream of nitrogen to remove all the byproducts of the irradiation reactions. After that the samples were saved in a very clean well-plate and immediately transferred to the polymerization reaction.

3.7.3 Photodegradation of 2-nitrophenylpropyloxycarbonyl-3-aminotriethoxysilane NPPOC-APTES

A sample of NPPOC-APTES coated film was exposed at 244nm through a copper electron microscopy grid (1000-2000 mesh, Agar, Cambridge, UK) at a dose of 5.0 J cm⁻². Nanometre patterning was carried out by employing IL with a power of 1.2 J cm⁻². The angle between the two interfered beams was adjusted to be 10° and 30° to form periodic structures of 630 nm and 317 nm, respectively, the FWHM of the polymer lines was 473 nm for 10° and 175 nm for 30° exposure. The photodegraded surfaces were subsequently rinsed with ethanol and dried under a stream of nitrogen to remove the irradiation byproducts.

3.7.4 Preparation of nanodot and micrometer structures of gold films by photolithography

Gold nanostructures were formed using IL, with two orthogonal exposures of a SAM of either ODT or MUA SAMs on a gold surface. The samples were placed on the stage, exposed to the interferogram, then rotated by 90° and exposed a second time. The exposed samples were rinsed with ethanol and dried under a stream of nitrogen straight after the exposure processes, then they were stored in the same solvent. For MUA-coated films, the first exposure was 10 J cm⁻² at 10°, while the second exposure dose was reduced to 8.3 J cm⁻² with keeping the same exposure degree. The ODT-coated samples were exposed to a dose of 25 J cm⁻², before rotating

by 90° and exposing again to a dose of 25 J cm⁻². After that, the patterned samples were immersed in an etching solution, which consisted of a solution of 0.2 M cystamine hydrochloride in 8% v/v of 35 % of ammonia in ethanol. The etched samples were washed with ethanol and blown under nitrogen and the completion of etching process was manipulated by using AFM. To remove the remaining SAMs and gold clusters on the patterned gold structures, the samples were exposed to UV light and washed very quickly with a cold piranha solution for no more than 5 min.

3.8 polymerization reaction

Patterned and unpatterned samples were loaded into the carousel tubes, which underwent three nitrogen-vacuum cycles before filling with nitrogen. The CysMA monomer (5.0 g, 15.0 mmol) was placed in a round-bottom flask before adding deionized water (12 mL). The solution was degassed under nitrogen for 30 min, before addition of copper (I) bromide (71.4 mg, 0.5 mmol), copper (II) bromide (55.6 mg, 0.25 mmol), and 2-2' bipyridyl (234 mg, 1.50 mmol). After being sufficiently mixed and degassed for 10 min the mixture was quickly sonicated for 2-3min. Subsequently, to commence the surface ATRP of CysMA, an amount (2-5 mL depending on the sample size) of the monomer-catalyst solution was transferred to the carousel tube to cover the sample, the carousel was shaken well and left for 1.5 h. Once the polymerization time finished the polymerized samples were sonicated in water, rinsed in water and ethanol, and finally they were blown dry with nitrogen, prior to use.

3.9 SLB Formation

In a 50:50 mixture of HPLC-grade chloroform and methanol an amount of dried lipids was dissolved and transferred to a glass vial. Depending on the experiment the following molar ratios of the lipid/ proteins were used: 99.5:0.5 POPC/Atto598, 24.9:74.6:0.5 DOTAP/POPC/Atto598, or 24.9:75:0.1 DOTAP/POPC/ pR-Alexa568. Before re-hydrating by using phosphate buffer, which is a 10 mM mixture of sodium dihydrogen phosphate and disodium hydrogen phosphate in Milli-Q water (18.2 MΩ cm MilliPore Ltd, Watford, U.K.) adjusted to pH 7.1 with NaOH or HCl, the prepared lipids were dried under a stream of nitrogen

for about 1h. In order to create multilamellar vesicles as a cloudy suspension, the vesicle solution was prepared by vortex mixing of the lipid solution for 1 min (Vortex Genie2, Jencons Ltd., Leighton Buzzard, U.K.). Small unilamellar vesicles were prepared by tip sonication (Branson Sonifier 750, Branson Ultrasonics Corp., Danbury, CT) of the suspension at 4 °C for 20 min, during which time the suspension became clear. After centrifuging (Heraeus Fresco 17, Thermo Fisher Scientific, Loughborough, UK) the suspension for 1 min at 14500g, the supernatant was removed and retained. d. The suspension was diluted with buffer to 0.5 mg mL⁻¹ prior to use and stored at 4 °C in the dark for no longer than 5 days.

SLBs were formed in a custom-built flow cell. For the polymer brush patterns, the samples were first soaked with buffer solution for 10 min, subsequently, the vesicles were injected and incubated for 24 h at 50 °C. Finally, the samples were rinsed for 20 min with degassed Milli-Q water at a flow rate of 2.6 ml min⁻¹.

3.10 Cell Fabrications

Frozen Mesenchymal stem (MSC) cells were defrosted rapidly in a 37 °C water bath and seeded into a T75 tissue culture flask (Corning, UK) with a 10 ml medium (Lonza's MSC media with the Lonza Bullet kit, which includes L-Glutamine, Fetal bovine serum and an antibiotic). The medium was changed after 24 h and the cells were allowed to become confluent (takes 2-3 days). When confluent finished they were passaged, which involved removal of the media, washing with PBS, and then the cells were removed from the flask by using 5 ml of trypsin (Sigma, UK). The cell suspension was then split between 3 flasks with adding more media about (10 mL) for the each, this process was repeated until the required cell number for the experiment reached.

The patterned and unapptterend PCysMA brushes were placed at the bottom of the well, using 24 well plates. 20,000 cells were seeded onto the patterned side of the polymer brush samples and incubated for 2 h. Finally, the well was flooded with 2 mL of the medium and incubated for 24 h.

3.11 Surface Characterization Techniques

3.11.1 Contact Angle Measurements

The surface free energy or surface tension of a chemically modified solid surface can be characterized by considering its interaction with a droplet of water at the interface. The liquid drop spreads across the surface, and at its permits, solid, liquid and vapor are in equilibrium¹⁴⁴. The relationship between these interfacial tensions (surface energy) and the contact angle is given by the Young's equation

$$\gamma_{SG} = \gamma_{SL} + \gamma_{LG} \cos\theta \quad (3.1)$$

Where γ_{SG} , γ_{SL} , and γ_{LG} is the interfacial tension between the solid-gas (air), solid-liquid, and liquid-air respectively, while θ is an equilibrium contact angle located between the solid-liquid and liquid-air lines figure 3.1a. Surfaces for which $\theta < 90^\circ$ are said to be hydrophilic, while for $\theta > 90^\circ$ the surface is said to be hydrophobic surfaces. When the θ increases to 150° the surface is describing as being super-hydrophobic surface.

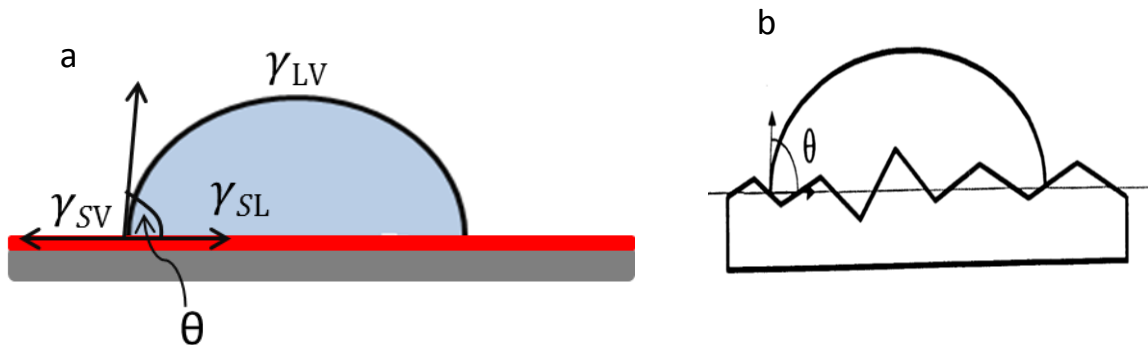


Figure 3.1: Illustrates (a) the three interface lines of a drop of water on a surface and apparent contact angle on the rough surface (b).

The young's equation is applicable for contact angles measured on ideal surfaces, which are smooth, rigid, chemically homogeneous, and inert. In contrast, real surfaces such as polymer brushes and SAMs surfaces may be chemically heterogeneous and rough As a consequence, the real and apparent contact areas may differ and the advancing and receding contact angles, known as contact angle hysteresis²⁸⁶⁻²⁸⁷ (figure 3.1b).

Experimental procedure

A Rame Hart sessile-drop model 100-00 goniometer was used to measure advancing sessile drop water contact angles. The instrument was fitted with a micro-litre syringe. A 2 μL drop of deionised water (18.2 $\text{M}\Omega\text{ cm}$) was expelled at the syringe tip. The syringe was lowered until the sample surface touched the released water drop. The syringe was gently lifted to detach the drop. Any acquired values are the average of a minimum of five different positions per sample and over typically three samples.

3.11.2 Ellipsometry

Ellipsometry is an optical surface analytical techniques that plays a crucial role in the characterization of molecular film structures. In addition to its ease, the ellipsometry is a non-damage surface tool; either thin or thick film can be characterized with high accuracy and precision about 0.01 nm. In principle, the ellipsometer measures the change in polarization of the linearly polarized light upon reflection or transmission through a film or an interface. The change is characterized by the variation in amplitude ψ and phase Δ of the polarized light which are sensitive to the thickness and the refractive index of all the films²⁸⁸⁻²⁸⁹.

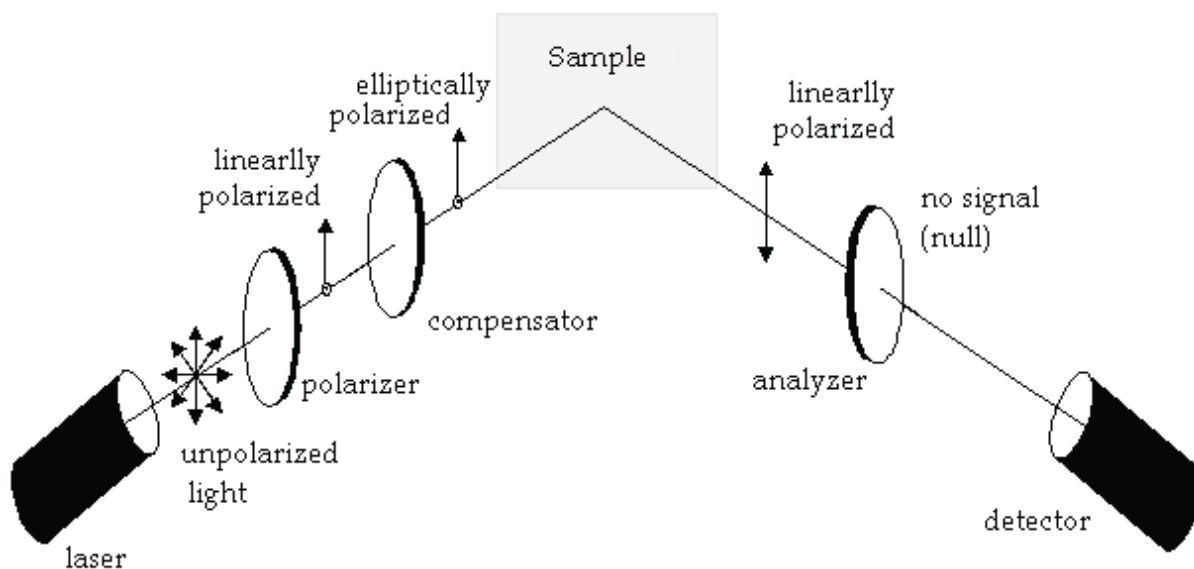


Figure 3.2: It is demonstrating the schematic diagram for an ellipsometer¹².

Experimentally, unpolarised light is polarized by being passed through a polarizer, and then becomes elliptically polarized before hitting the sample surface via a compensator figure (3.2). The reflected polarized light is collected by another analyzer and directed to a photosensitive detector¹². The technique has recently attracted a great deal for measuring polymer brush growth thickness¹, responsive polymer thickness²⁹⁰, and gradient polymer brush thickness²⁹¹⁻²⁹².

Experimental Procedure

The thickness of the various grafted densities of PCysMA brushes grown from the ATRP initiators on the planar silicon wafers was measured, using an M-2000 V ellipsometer (J.A. Woollam Co., Inc.) with a white light source (370.5–998.7 nm) at a 70° incidence angle. Multi-measurements were carried for any given sample (at least two samples for each given exposure) under ambient conditions, and the obtained ellipsometric data were fit using a model comprising PCysMA brushes at a variable thickness on a planar silicon substrate, utilizing WVASE32 software (J. A. Woolam Co., USA). The model consisted of a single layer Cauchy for a polymer brush with $n = 1.5$ and $k = 0$ with a silicon substrate ($n = 0.3.875$ and $k = 0.015$). The actually grafted polymer brush thickness was calculated by subtracting the combined silicon dioxide and initiator layer thickness from the fitted layer thickness. The mean value of the brush thickness was taken from the multiple measurements across the two polymer-coated surfaces, the data gave an indication on the brush uniformity.

3.11.3 X-ray Photoelectron Spectroscopy (XPS)

X-ray Photoelectron Spectroscopy (XPS), also known as Electron Spectroscopy for Chemical Analyses (ESCA) and it has become one of the most important surface analysis technique. It fascinates compositional analysis and provides some chemical structural information with a sampling depth of only several nanometers. XPS provides both qualitative and quantitative information on the surface structures non-destructively²⁹³⁻²⁹⁴.

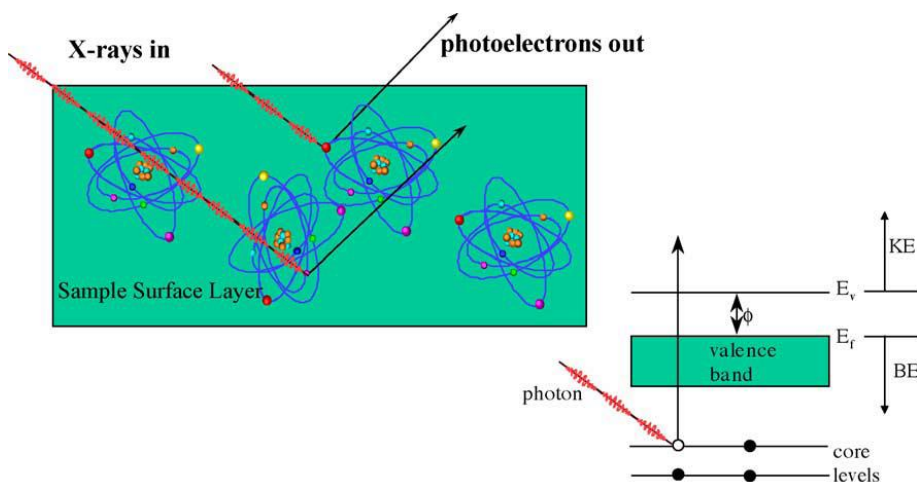


Figure 3.3: It is showing the mechanism of photoelectron emission on a sample surface²⁹⁵.

The target surface is bombarded by X-ray photons, which eject the core shell electrons. These photoelectrons are collected and analysed according to their kinetic energies. XPS relies predominating on the ejection of core shell electrons (C1s, O1s, N1s, S2p....). The binding energy can be calculated by

$$BE = hv - KE - \phi \quad (3.2)$$

Where ϕ is the electron spectrometer work function and hv is the X-ray photon energy.

The BE is effectively the ionisation potential of the atom of interest. Its value is influenced by the chemical environment of the atom, so that small shifts “chemical shifts” are observed in the BE as a consequence of changes in chemical bonding. The width of the photoemission peaks provides information on the non-homogeneity of the sample-surface¹⁸. The mean distance which is traveled by the photoelectron inside the solid before it is scattered is called the inelastic mean free path (λ). It is proportional to the kinetic energy: the inelastic mean free path is larger for electrons with larger kinetic energy. As a consequence of this the depth of the sampled region can be calculated:

$$I_d = I_\infty \left(1 - e^{-\frac{d}{\lambda} \sin\theta} \right) \quad (3.3)$$

Where I_d is the XPS peak intensity, I_∞ is the intensity of the electron from the thick film. The λ is known for most of solid surfaces¹⁸.

There is a direct relationship between the peak intensity and the concentration of the surface element (C_A) and the relationship given by

$$I_A = F K S \sigma_A C_A L(\theta) \quad (3.4)$$

Where F is the intensity of the incident photons, K is an instrumental factor, and S is the sample analyzed area. These three factors are constant for a given spectrometer. σ_A is the cross-section for the emission of the photoelectron, and L (θ) is the angular symmetry factor²⁹⁶⁻²⁹⁷.

Experimental procedure

X-ray photoelectron spectroscopy (XPS) was carried out with a Kratos Axis Ultra DLD x-ray photoelectron spectrometer. The instrument had a monochromatic Al K α x-ray source with an ultra-high vacuum environment. Survey and wide scans had acquisition pass energies of 160 eV and 20 eV respectively. The XPS data were analyzed using Casa XPS software (UK). All binding energies were calibrated with respect to the C 1s saturated hydrocarbon peak at 285.0 eV. Data is presented as intensity in counts per second (cps) against binding energy in eV. XPS sample loading and data collection were carried out by Dr Claire Hurley, Charlie Smith and Deborah B Hammond. All XPS data analysis were undertaken by the author.

3.11.4 Atomic Force Microscopy (AFM)

The Atomic force microscopy (AFM) is a member of the family of scanning probe microscopy and near field techniques. In which the interaction force between a sharp tip and a surface is measured by observing the deflection of a flexible cantilever²⁹⁸⁻²⁹⁹. It was first developed by Binnig and Greber in 1985 as an extension of scanning tunneling microscopy³⁰⁰. In general, an AFM consists of four main parts: (i) a probe, (ii) a piezo electric scanner, (iii) a control software, and (IV) a feedback system. The AFM tip mounted at the end of a cantilever is scanned over the sample surface. As a result of the repulsive and adhesive forces acting between the tip and sample, the cantilever is deflected.

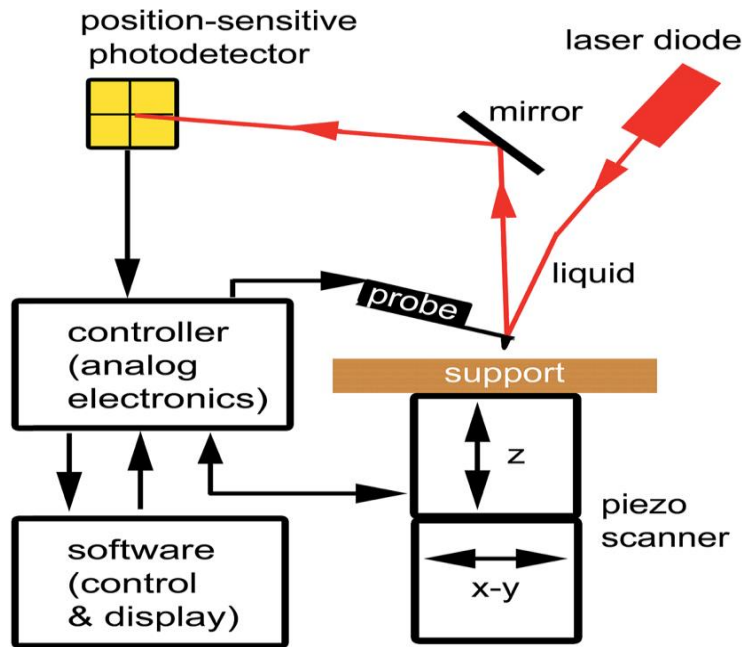


Figure 3.4: Demonstrates a schematic representation of AFM instrument³⁰¹.

The deflection is measured by observing the reflection of a laser beam, from the back of the cantilever onto a photo-sensitive detector (figure 3.4). A feedback loop utilizes the signal to control the probe position both vertically and laterally using the piezoelectric stage that extends or retracts as the applied voltages are changed³⁰²⁻³⁰³. The AFM may be operated in three different modes: non-contact, contact and tapping modes. Each one can provide different information on the surface. In non-contact operation the probe oscillates close to the surface and it is oscillating at or near its natural resonance frequency. In contact mode, the tip touches the surface and it is moved with free amplitude over the surface. However, it is operating in the repulsive regime the mechanical contact between the tip and the surface may cause damage to soft surfaces or yielding misleading height information for very soft surfaces such as polymer brushes. Tapping mode combines qualities of the two other modes by scanning the tip to oscillate close to the surface, making intermittent contact with the sample once per cycle^{304,305,306}. This has the effect of removing the lateral drag forces that contribute to damage in contact mode. Non contact mode is hard to do, experimentally, although it can yield exceptional resolution.

Due to its capability to measure intermolecular forces with atomic resolution and AFM works in air, liquid and there is no requirement for special sample preparation. AFM has evolved as a technique with broad utility that has been employed in applications, including, fabrication polymer science, adhesive, electronics, semi-conductor industry, biology and biomaterials. To date, It has been widely applied to either qualitatively or quantitatively characterize self-assembled organic molecules and polymer brush-coated samples in different environments. Tapping mode is the most commonly used imaging mode for physisorbed or soft surfaces such as polymer brush³⁰⁷⁻³⁰⁸, protein³⁰⁹⁻³¹⁰, cells³¹¹, DNA³¹²⁻³¹³, and supporting lipid bilayers³¹⁴. The height image can be used to analyze the surface morphology, patterns, and the roughness of the characterized materials.

Experimental procedure

In this work, a Dimension Icon atomic force microscope with Nanoscope V controller (Bruker, UK) was used to collect contact and tapping mode scans of patterned and unpatterned samples under ambient conditions in the air. The cantilevers used for tapping in the air were Bruker silicon TESPA (nominal spring constant of 42 N m⁻¹). The topographical tapping mode images were acquired with a scan angle of 0°, the scan rate of 1.0 Hz and typical gain setting of 25 for the integral and 50 for the proportional.

3.11.5 Friction Force Microscopy (FFM)

3.11.5.1 Modification of AFM probes

Commercial V-shape silicon nitride (Si₃N₄) probes (model NP, with a nominal normal force constant 0.06 N m⁻¹) were cleaned using cold Piranha solution (sulfuric acid (70%) and hydrogen peroxide (30%) for ca. 40 min. Warning! Piranha solution is an extremely strong oxidizing agent that has been known detonates spontaneously upon contact with organic materials). The probes were immersed in the cold piranha solution for about 15-20 min, rinsed seven times by immersion in deionized water, then flooded with water using a wash bottle and finally rinsed in HPLC ethanol and blown dry under a very slow stream of nitrogen. The cleaned probes were stored overnight to dry at room temperature prior to gold deposition. They were coated with 1-2 nm Chromium layer (Cr chips, 99.99% purity, Agar, Scientific) deposited at a rate

of 0.01 nm s^{-1} , followed by 10 nm gold (Au wire, 99.99%, Advent Research Materials Ltd) at a rate of 0.02 nm s^{-1} using Edwards Auto 306 bell jar vacuum system. Subsequently, the AFM coated probes were immersed in 1.0 mM of 11-mercaptoundecanoic acid (MUA) in degassed HPLC ethanol for approximately 24 h. The acid functionalized cantilevers were stored in ethanol and far away from the UV light through the entire period of the experiments to prevent the thiol monolayer on the tips from the oxidation reaction.

3.11.5.2 Friction Force Measurements in Liquids

Friction forces were made by using a Digital Nanoscope VIII multi-mode Atomic force microscope (Multimode VIII, Bruker, UK) operating in contact mode, using an E-scanner, gold coated tips functionalized with and the 11-mercaptoundecanoic acid was used. An improved and newly designed glass liquid cell (MTFML-V2, higher performance measurement with lower noise, Bruker, UK) with an O-ring plastic (Bruker, UK) were used for performing friction measurement in different media. The friction forces were acquired from the friction loop which was obtained from forward-reverse scanning along a single line. The friction signal was calculated by subtracting the signal of pick maximum from the signal of peak minimum for micrometer and nanometer patterns, while for unpatterned brushes the mean signal of forward subtracted from the main signal of the reverse ward, and subsequently halved. Then, the acquired friction of completely patterned surface subtracted from the friction of polymer samples to get the final friction forces. For the gradient brushes the acquired frictional forces were analyzed by subtracting the average friction value of the trace image from the mean value of the retrace image. It is important to notice that, all analyzation processes have been carried out manually.

The measurements were performed at a scan rate of 1.4 Hz with 256 samples per line and 90° scan angle. The scan size was maintained at $3.0 \mu\text{m}^2$ and the friction behavior of the samples was examined by using V-shape carboxylic acid functionalized contact mode probes (model DNP, non-conductive Silicon Nitride, with a nominal normal spring constant 0.06 or 0.12 N m^{-1}) with tip radii in the range 20-60 nm. The normal load was reduced stepwise in increments of 0.2 V from 2.0 V down till the probe separated from the brush surfaces. Four to six locations were examined on each sample, at least two different samples were examined, using two

different cantilevers, in each experiment. Normal calibration of the cantilevers was carried out in two ways. In the first attempt the deflection sensitivity (nm V^{-1}) of the probes was acquired from the slope of a linear part of the force curve at the repulsive regime, acquired on the flat surface of mica. Secondly, the actual spring constant of the cantilever was calculated from the power spectral density of its thermal spectra at room temperature, using multi-mode VIII AFM, following the method introduced by Hutter and Bechhofer³¹⁵.

Lateral stiffness was achieved by using the wedge calibration method introduced by Ogletree et al.³¹⁶ and developed by Vandenberg et al.³¹⁷. In which the cantilever is scanned across a commercially available silicon grating TGF11 (MikroMasch, Tallinn, Estonia) and the friction signals were obtained as a function of the applied loads. The lateral force was calibrated in each solution which was used for the measurements. The tip radius was measured by imaging a calibration grating TGG01 (MikroMasch, Tallinn, Estonia) at 0.0 and 90° scanning angles. The profile of the tip was determined using the Zenhausen model of deconvolution³¹⁸. To avoid the contamination and losing the tips all the calibrations were done straight after each experiment in the same solution which the friction measurement experiments were being performed.

3.11.6 Fluorescence Recovery After Photobleaching

Fluorescence recovery after photobleaching (FRAP) is a quantitative microscopic technique that can be used to investigate the dynamics of molecular mobility of a fluorophore within the two-dimensional structure. By taking advantage of the fact that the fluorophores are irreversibly bleached (which is a photochemical destruction of the fluorophore) when they are exposed to the high intensity of a light³¹⁹. Instrumentally, FRAP consists of three main parts, an optical microscope, a single laser light source, which is used for both bleaching and monitoring processes, and finally, a fluorescent probe which is coupled with a molecule of interest³²⁰. In a simple system, a neutral density filter is placed in the beam path to modulate the intensity of the laser source, a high intensity pulse is produced upon brief withdrawal of the filter from the beam path. While, in other systems a dual beam splitter is utilized to split the laser beam into a low and high intensity beam, the latter beam is controlled by a shutter.

To perform the FRAP, a targeted surface which includes fluorescence labelled molecules is illuminated with a low intensity beam to determine the initial fluorescence intensity. Subsequently, an intense laser beam is used to flash an interesting region of the sample, which quenches the fluorescent probes in the defined region (such as a circular spot with a Gaussian and uniform intensity). After bleaching, a low intensity laser beam is used for monitoring the recovery of the fluorescence caused by the diffusion of the neighboring (non-bleached) molecules into the bleached area and the outward diffusion of the bleached molecules. Plotting the fluorescence recovery as a function of time results in a recovery curve (figure 3.5), which yields the recovery times that can be used to calculate the diffusion coefficient of the diffusion species²⁵. The diffusion coefficient (D) is given by²⁵

$$D = \frac{r^2}{4\tau} \quad (3.5)$$

Where r is the radius of the circular beam and τ is the time at which half of the fluorescence recovery also, known as a characteristic diffusion time.

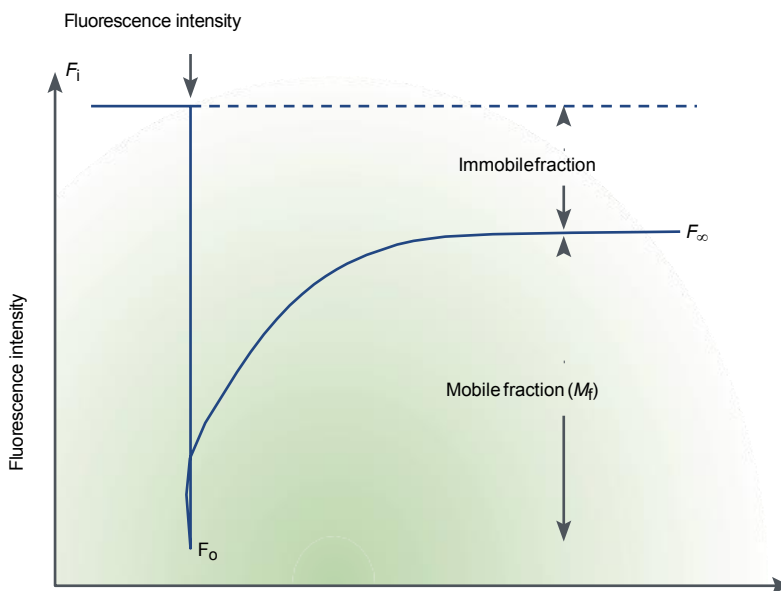


Figure 3.5: The plot of fluorescence intensity in a region of interest as a function of time after a photobleaching process. The prebleach (F_i) is compared with the asymptote of the recovery (F_∞) to calculate the mobile and immobile fractions. Information from the recovery curve (from F_0 to F_∞) can be used to determine the diffusion constant of a fluorescent molecule.

Not all the fluorescences are recovered to its initial intensity after photobleaching, they actually partially recovered, due to physical or chemical interactions. The difference between the initial fluorescence F_i and the fluorescence after recovering F_∞ is attributed to the proportion of immobile fluorescent probes, while the proportion of mobile probes obtained from the difference between the fluorescence after photobleaching F_o and the fluorescence after recovery F_∞ . The mobile fraction, which is the percentage of mobile probes to non-mobile probes, can be calculated by comparing these two values in the recovery graph³²¹.

Experimental procedure

FRAP was performed using an Epifluorescence Microscope (E600 Nikon, USA). The samples were illuminated and bleached by a high-pressure mercury arc lamp. The bleached spot radius was 14 μm when using a 40 \times objective lens. Fluorescence images were collected using Zyla sCMOS CCD (Andor Technology Ltd., Belfast, U.K.) with 2 \times 2 binning and recorded in the NIS elements software. Images were collected until complete fluorescence recovery was observed. The Axelrod approach of analysis was employed, which can provide both the diffusion coefficient and the mobile fraction.

3.11.7 Fluorescence Microscopy

Fluorescence microscopy is a versatile optical imaging technique capable of varying of modes of operation, ranging from relatively straightforward wide-field microscopy to highly specialized spectral-imaging confocal microscopes³²²⁻³²³. The microscopes that can be used for investigation of cell dynamics and functions involve a vital role in the development of biological science³²⁴. Most live cells and tissues are not normally illuminated by light during their life cycle, and it has been revealed that UV light destroys DNA and fluorescence excitation causes to phototoxicity to the live cells and tissues. The main reason for occurring phototoxicity is the oxygen-dependent reaction of free radical species, which are produced during the excitation of protein and dye molecules. Therefore, it is very important to microscopic devices to minimize the intensity of the exposure light, meanwhile, they must be optimized to collect emitted light as much as possible. This can be obtained by using high quality optical components and detectors³²⁵⁻³⁷.

It is really important to understand the meaning and main concept of fluorescence during the study of cell and molecular biology. Fluorescence is the emission of the light that caused by adsorption of the incident light (with shorter wavelength) by a fluorophore. It is vital to be able to separate excited and emitted light to obtain a powerful emission spectrum. In the principle of working of fluorescence microscopy devices, the fluorophore is illuminated by an excited light, which obtained by filtering the main light from a light source, using excitation filter. In general, the wavelength of the excited light is shorter than the wavelength of the emitted light. The main technical issue with such device is that the excited beam and emitted fluorescence beam overlap in the light path, Thus, a special kind of beam splitter (Dichroic mirror or filter) is required to separate the excitation from the emission beam.

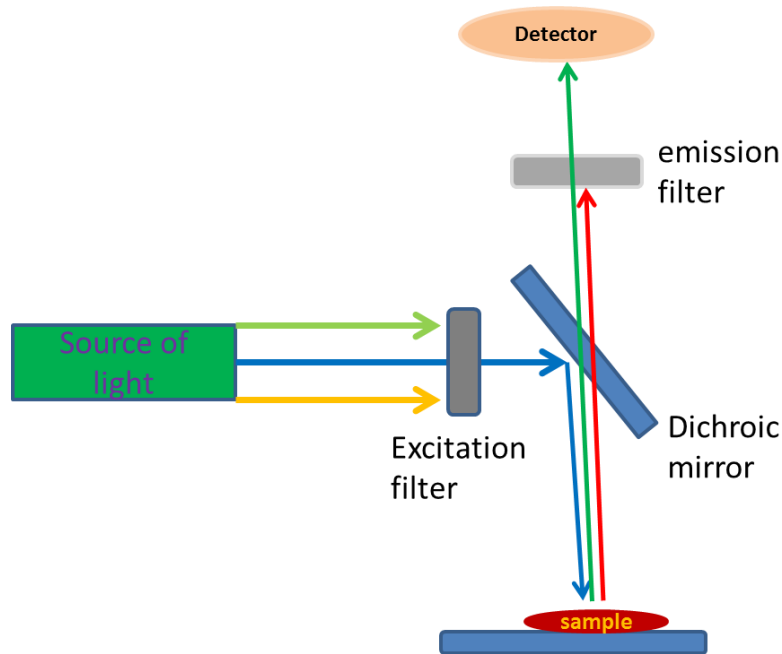


Figure 3.6: Schematic diagram for fluorescence microscopy.

The Dichroic splitter reflects the shorter wavelength of the excited light and allows the longer wavelength of the emitted fluorescence to transmit toward the detector³²⁶ (figure 3.6).

Experimental procedure

All culture media were removed from culture plates, the Cells were washed with Dulbecco's PBS (Sigma, UK) and fixed using a 2% formaldehyde (Sigma, UK) and 4% sucrose (Sigma, UK) fixative. After that, The samples were washed in PBS and blocked/permeabilised using a solution of 1% bovine serum albumin (BSA) in PBS with 0.1% triton X100 (Sigma, UK) and 10% normal horse serum (Vector, UK), for 45 minutes at 37°C. To detect actin cytoskeleton, the samples stained using Oregon green (Life technologies, UK) for 1 hour at room temperature. Finally, they were then washed with PBS and examined using an Axiocam fluorescent microscope (Zeiss, Germany) after being mounted using Vecta shield with Dapi (Vector UK).

Chapter 4: Conformational effect on tribological property of various patterned Poly(Cysteine methacrylate) brushes in different environments

4.1 Introduction

There has been a great deal of interest in the use of patterned polymer brushes in manufacturing, nanotechnology and biomedical devices³²⁷⁻³²⁸ such as biosensors, cell-based devices³²⁹⁻³³⁰, protein-based devices³³¹⁻³³², and actuators³³³. The main strategy for the creation of such systems is the integration of top-down lithography, which provides a molecular patterning with bottom-up synthesis through surface-initiated atom transfer radical polymerization (SI-ATRP). Lithographic techniques such as Interference lithography, photomask lithography, electron beam and scanning probe lithography have been used to form patterned polymer brushes with controllable feature dimensions ranging from the macroscopic to the nanometre scales³³⁴⁻³³⁶. The grafted polymer chain properties, such as conformation, stimuli-responsiveness, and tribological characteristics in various environments, may be controlled via the selection of appropriate polymerisation conditions. It is believed that the elastic free energy and entropy penalty have a strong influence on the behaviour and responsiveness of the polymer chains in patterned architectures, for example, polymer brushes could be collapsed laterally at the periphery of a patterned structure and may overlap the “polymer free” regions. In addition to the environmental effect, the size of grafting footprint and the non-grafted surface area is expected to have a significant impact on the conformation of a nanopatterned polymer brush. As the size of the footprint decreases the brush thickness is decreased and less crowding of the chains results³³⁷⁻³³⁹. A variety of approaches have been used to characterise the conformations of the polymer brushes, including the study of brush behaviour as a function of its thickness and the characteristics of the surrounding environment such as solvent quality, ionic strength, pH, and temperature³⁴⁰. FFM is one approach that is proven capable of providing quantitative data. Lateral deflections of the cantilevers are recorded while scanning a sample. Analysis of the AFM contact mechanics may provide information on the basic conformation. The

chemical nature of the probe may additionally be modified to information on specific interactions between the brush and its environment³⁴¹⁻³⁴³.

Leggett et al. examined the influence of solvent composition and brush thickness on the frictional properties of PMPC brushes. They found that the friction coefficient decreased with increasing brush thickness for thick brushes, but it became thickness independent at low thicknesses. In a good solvent, PMPC is solvated and swells from the surface to form brushes. In contrast, a collapsed film is obtained in a poor solvent³⁴⁴. Takahara et al. reported that the structure and the frictional behaviour of Poly(2-methacryloyloxyethylphosphorylcholine) are largely dependent on the solvent quality and the affinity between the brush and probe. Swollen brushes were formed in an aqueous medium, while collapsed polymer chains were observed in toluene³⁴⁵. It has also been shown that the coefficient of friction is highly dependent on the grafting density. At a low polymer grafting density the friction force is relatively large compared to highly covered surfaces³⁴⁶. Continuum mechanics models, in particular Derjaguin- Muller- Toporov (DMT) Johnson–Kendall-Roberts (JKR) models have been applied to characterise the probe-brush interaction. It has also been reported by many groups that the medium and tip chemistry have a significant influence on the energy dissipation pathway and the nature of contact area between the self-assembled monolayers^{347-348,191}. Recently, it has been proposed that the friction force is treated as a sum of the load-dependent term, associated with molecular ploughing and a shear-dependent term resulting from the dissipation of energy through the shearing of adhesive interactions^{191,195,349-350}. The friction can be described by

$$F_F = \mu(F_N + F_a) + \pi\left(\frac{R}{K}\right)^{2/3} \tau(F_N + F_a)^{2/3} \quad 4.1$$

Where F_a is the pull-off force, R is the tip radius, and K is the elastic modulus of the film. μ , the “coefficient of friction”, characterises energy dissipation in ploughing, while τ , the surface shear strength, characterises energy dissipation in shearing. In the limit of very small contact area with extensively weak adhesion, the shear stress is negligible and eq. 5.1 becomes

$$F_F = \mu(F_N + F_a) \quad 4.2$$

In which friction force linearly varies with the applied load, consistent with the microscopic law of adhesion which demonstrated by Amontons.

There have been many attempts in the last few decades to understand the tribological properties of polymer brush surfaces. There is still a lack of agreement in this field and a comprehensive picture of brush nanomechanics has yet to be established. Herein, we try to address this challenge by examining the tribological properties of polymer films of controlled grafting density and using nanostructured polymers formed by interference lithography.

In the present work, the surfaces of silicon wafers have been functionalised by adsorption of APTES and reaction with 2-bromoisobutyryl bromide (BIBB) to yield a brominated layer as shown in figure 4.1. Surfaces were photopatterned using a photomask and by interference lithography, forming micrometre and nanometre patterns respectively. This was followed by polymerization of PolyCysMA onto the patterned surfaces via 'grafting from' using SI-ATRP. The grafted brushes were characterised using contact angle, XPS, ellipsometry and AFM. The tribological properties of the brushes were investigated using friction force microscopy (FFM) with a chemically modified probe.

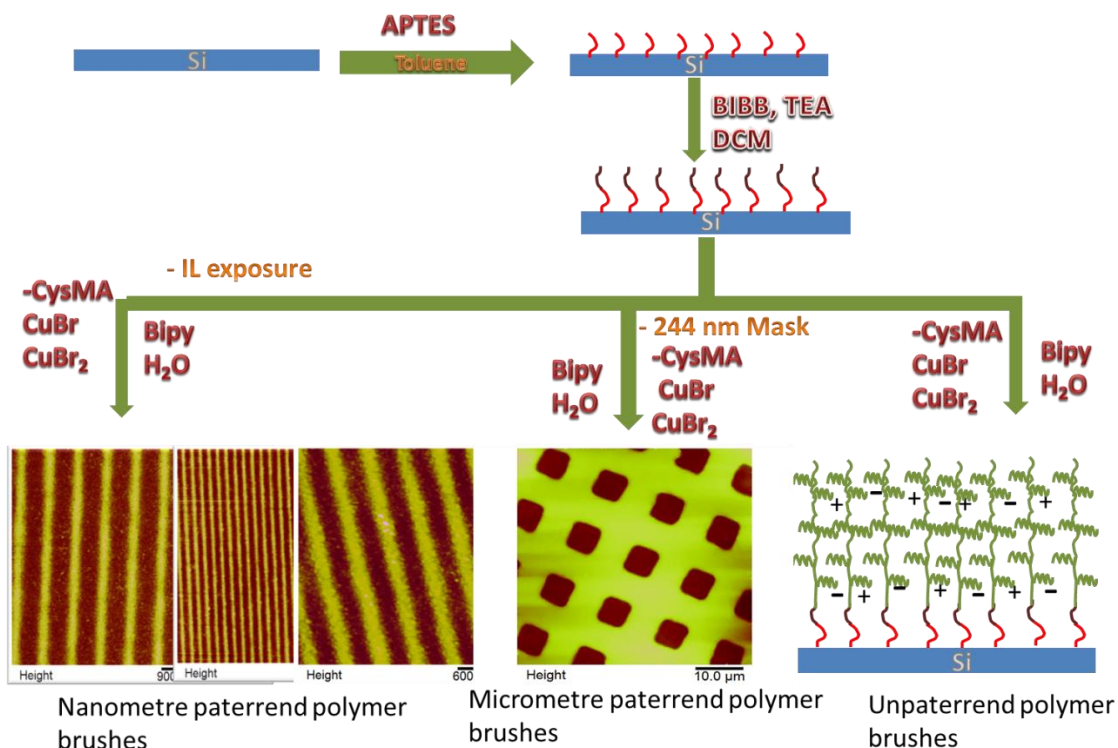


Figure 4.1: Schematic representation of the methods used for fabrication of macro, micro and nanometre scale structures of PolyCysMA brushes by using photolithography and SI-ATRP techniques.

4.2 Experimental section

4.2.1 Preparation of APTES-BIBB initiator

A silicon surface was functionalised by adsorption of APTES molecule and then derivatised by reaction with BIBB molecules according to the procedure written in section 3.3.

4.2.2 Micrometre and nanometre fabrications of ATRP initiator surfaces

A micrometre structure of APTES-BIBB film was prepared by photodebromination of the sample through a microscopic grid using UV light with a dose of 3.0 J cm^{-2} . Interference lithography was used to fabricate nanometre patterned samples, a dose of 1.8 J cm^{-2} was used.

The angle between the two beams at the intersection was controlled to be 10°, 15°, 20° and 30° during exposure to obtain patterns with periods of 690, 511, 450, 307 nm respectively (more details is written in the experimental section 3.7.1).

4.2.3 Synthesis of cysteine methacrylate monomer and polymerization reaction

The procedure for the synthesis of cysteine methacrylate (CysMA) monomer and the growth of PCysMA brushes on the patterned ATRP initiator samples written in the experimental section 3.5.1 and 3.8, respectively. To fabricate the uniform brush the polymerization conditions such as the monomer to catalyst ([CysMA]: [CuBr]: [CuBr₂]: [Bipy] molar ratio = 30: 1.0: 0.5: 3.0) ratio, which is the best ratio to control the thickness of the grown brushes, temperature, solvent type, initiator density and the polymerization times have been kept constant during the polymerization reaction and all samples were prepared together. To facilitate composition of the properties of patterned and unpatterned polymers, samples were prepared that consisted of large (1 cm–4 cm) unpatterned regions, micropatterned structures and nanostructures on a single substrate. This enabled polymers to grow under identical conditions for all types of structures.

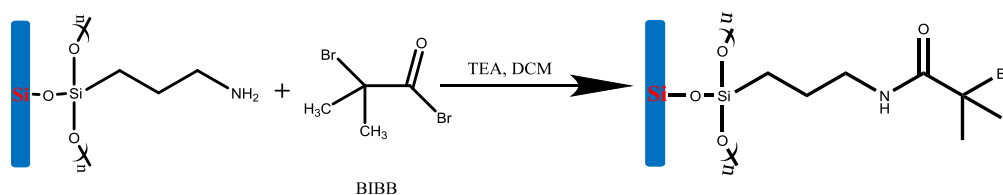
4.2.4 Surface analysis

XPS, ellipsometry, contact angle goniometry and Friction force microscopy (FFM) were carried out according to the procedures presented in the experimental section 3.11.

4.3 Results and Discussion

4.3.1 Model surface reaction

Initiator-functionalised surfaces were produced by the reaction of the acyl bromide BIBB with a surface coupled amine functionalized APTES:



The resulting APTES and APTES-BIBB surfaces were characterised using contact angle goniometry and X-ray photoelectron spectroscopy (XPS). High-resolution C1s and N1s are shown in figure 4.2.

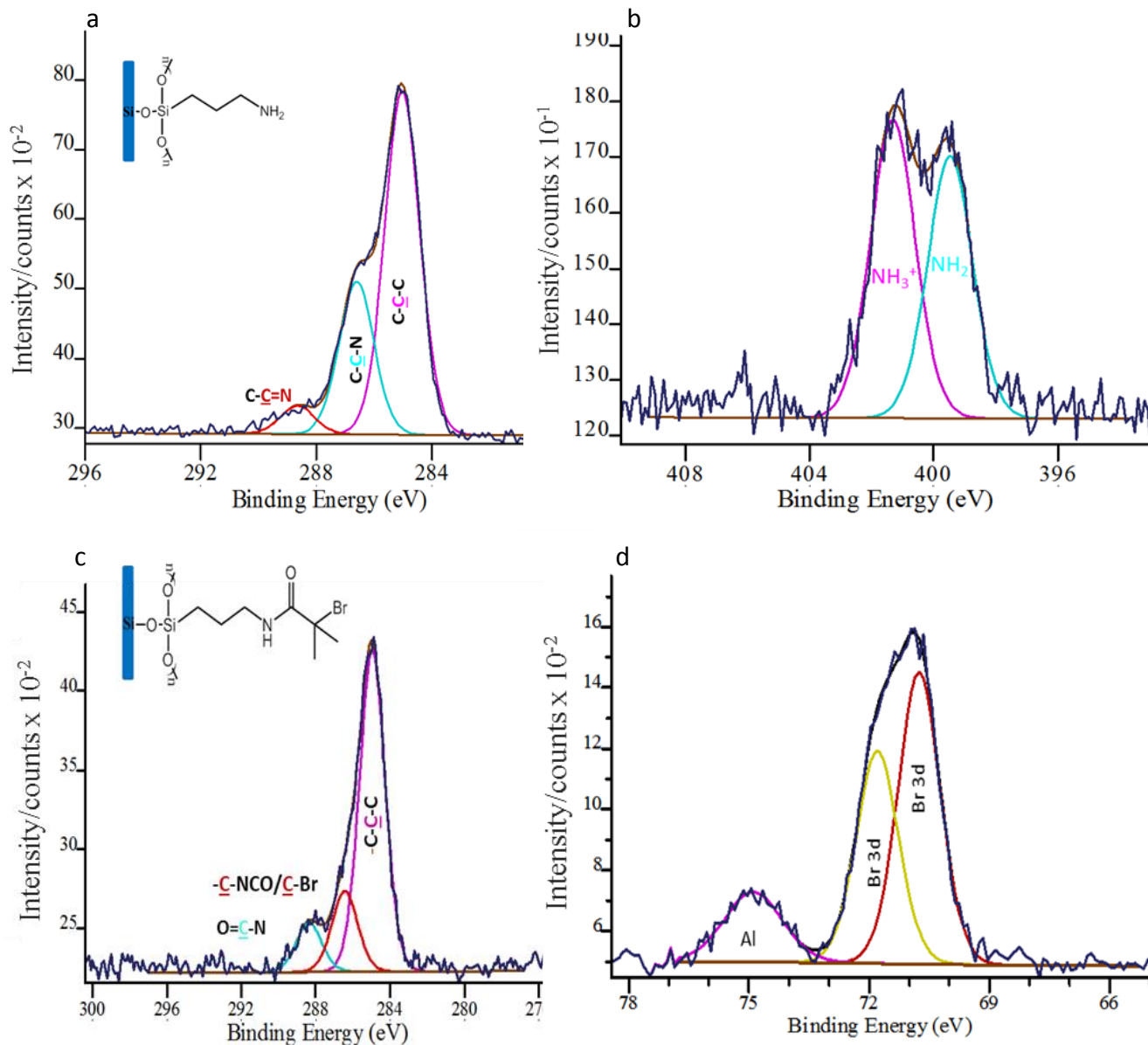
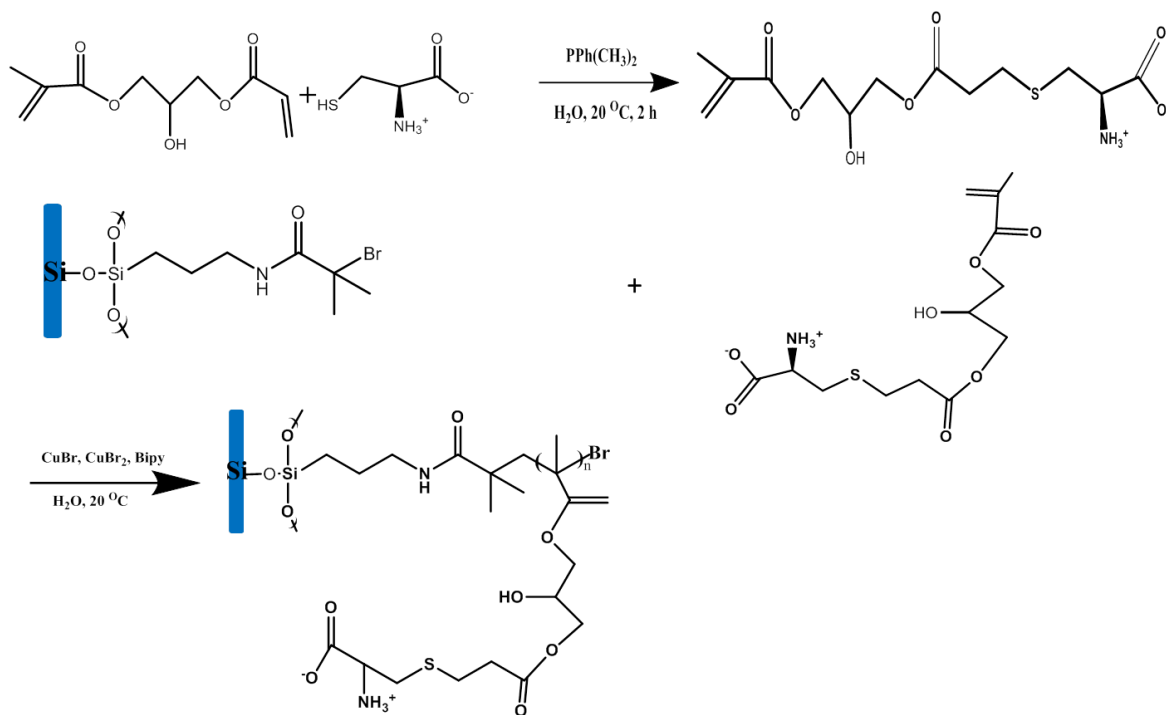


Figure 4.2: The high-resolution XPS spectra obtained from the initiator surface. (a) The C1s spectra from the APTES layer, (b) N1s spectrum from the APTES layer, (c) C 1s spectra from the APTES-BIBB surface and (d) Br 3d spectra from the APTES-BIBB layer.

The C1s spectrum for an APTES film exhibited two peaks at 285.0 eV and 286.6131 eV (figure 4.2a), which are attributed to saturated carbon and carbon adjacent to the amino group,

Respectively, as expected. The experimental ratio obtained here between saturated carbon and carbon linked to nitrogen was 2.24:1.0, which is close to the calculated ratio 2:1. A peak was also observed at 288.56 eV which is most likely due to the presence of the imide group (C=N) formed as a result of multilayer generation in the silane films. This is supported by the presence of a protonated amine group (NH₃⁺) peak next to the N1s of free amine peak at the 399.774 eV. The N 1s spectrum of an APTES layer shows at 399.786 eV as expected (figure 4.2b). The C1s core level spectrum for an APTES-BIBB layer (figure 4.2c) was fitted using three components with binding energies of 285.0, 286.729 and 288.763 eV, corresponding to C-C-C, C-Br/C-NCO and O=C-N respectively. The ratio of the C-C-C, C-Br/C-NCO and O=C-N components was 3.91:1.95:1, in a close agreement with the calculated ratio of 4:2:1. The characteristic Br 3d doublet is observed at 70 and 74 eV confirming successful incorporation of Br into the film (figure 4.2d). The contact angle of the surface was 70±3° consistent with expectations for a smooth, high-density brominated surface.



Scheme 4.1: Schematic representation of the formation of cysteine methacrylate monomer and its reaction with the APTES-BIBB molecule as an initiator.

PCysMA brushes were grown from the unpatterned bromine initiator, using surface-initiated atom transfer radical polymerization (SI-ATRP). The expected chemical reactions in the synthesis of the cysteine methacrylate monomer and also the polymerization reaction are shown in scheme 4.1.

The kinetics of growth of the polymer brushes were studied using ellipsometry to measure the dry thickness of the polymer layer as a function of the polymerisation time (figure 4.3). The polymerisation conditions, including the monomer to catalyst ([CysMA]: [CuBr]: [CuBr₂]: [Bipy] molar ratio = 30: 1.0: 0.5: 3.0) ratio, temperature, solvent type, initiator density were kept constant.

The thickness of the polymer chains increased with the polymerisation time, reaching 7.0 nm after 1.5 h of reaction. Up to this time, the rate of increase in thickness was approximately linear but thereafter, the rate of the growth slowed and a maximum thickness of ca. 8 nm was reached.

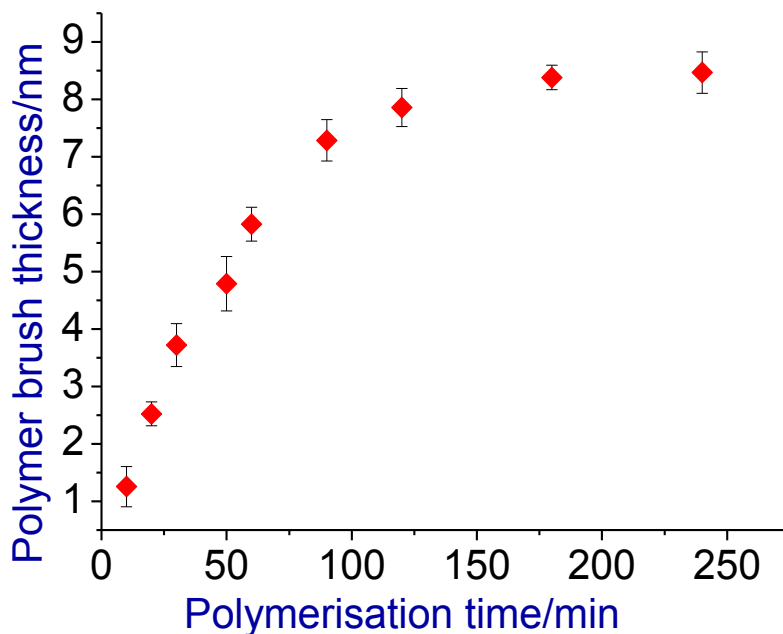


Figure 4.3: Variation of the ellipsometric dry thickness of the PCysMA brushes grown by SI-ATRP with the polymerisation time.

The static water contact angle increased from 0° for the unmodified silicon surface to 37° after 1.5 h of polymerisation. High-resolution C1s, N1s, and S2p XPS spectra were obtained for 7nm thick of PCysMA brushes (figure 4.4). The XPS C1s spectra were fitted using three components with binding energies of 285.0 eV, 286.3 eV, and 288.7 eV which are attributed to the C-C-C, -C-C-O/C-C-N, and O=C-O respectively. The calculated atomic ratios of C-C-C, C-C-O/C-C-N, and O=C-O were 2.07:1.32:1, which is in a very good agreement with the theoretical ratio 2:1.3:1.

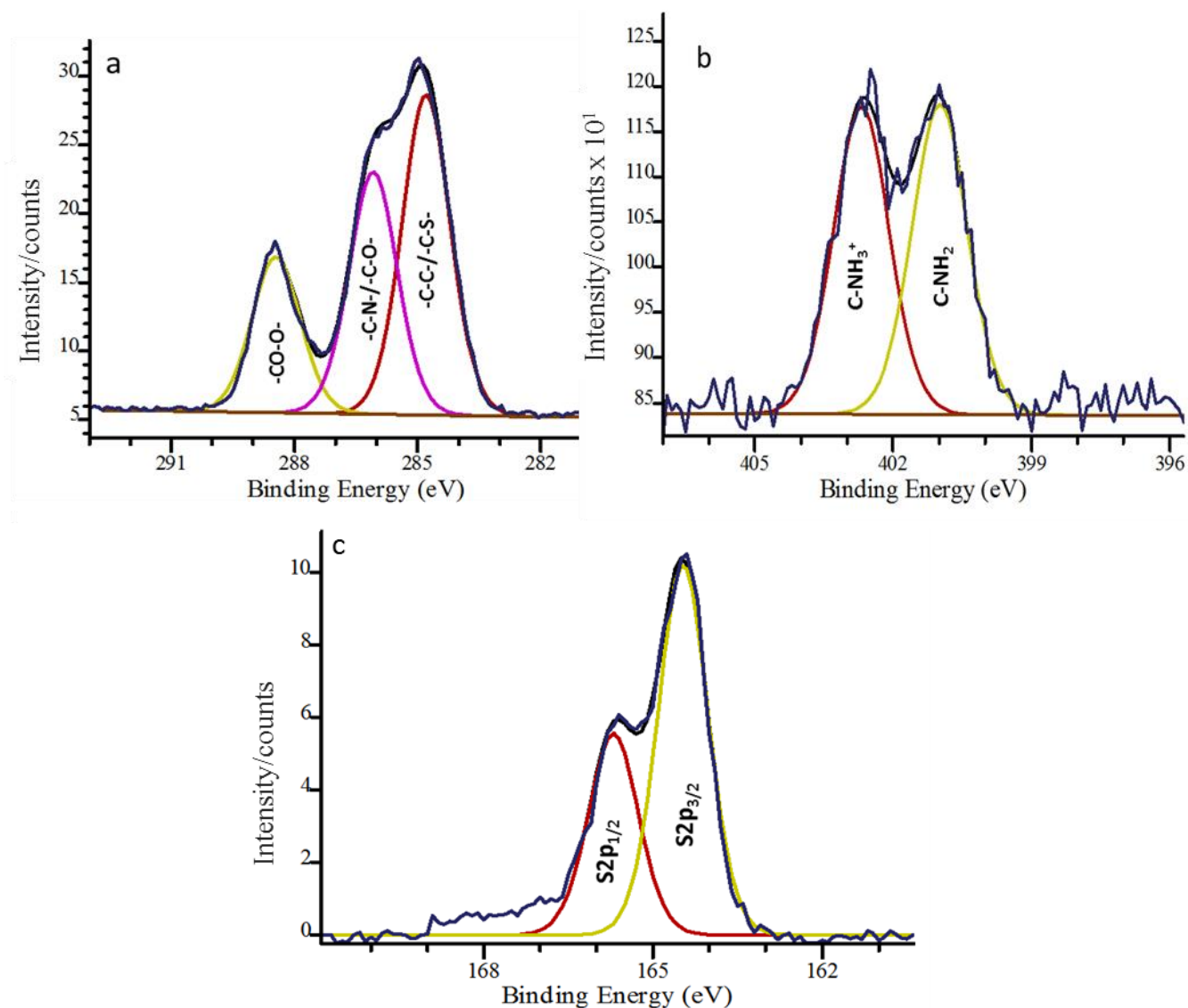


Figure 4.4: High resolution X-ray Photoelectron Spectroscopy spectra obtained for PCysMA brush of 12 nm dry thickness (a) C1s spectrum, (b) N1s spectrum, and (c) S2p spectrum.

The N1s spectra were fitted with two components centered at 399.0 and 401.5 eV, assigned to C-NH₂ and C-NH₃⁺. This means that about 50% of the free amine was protonated, and thus, the brush provides both positive (NH₃⁺) and negative charges (COO⁻) equally at intermediate pH. The high resolution S2p spectrum was fitted with both S2p_{3/2} and S 2p_{1/2} components with a binding energy of 164.47 and 165.7 eV (figure 4.4c). The intensity ratio between these two peaks was 2:1, as expected for 2J+1 spin-orbit coupling³⁵¹.

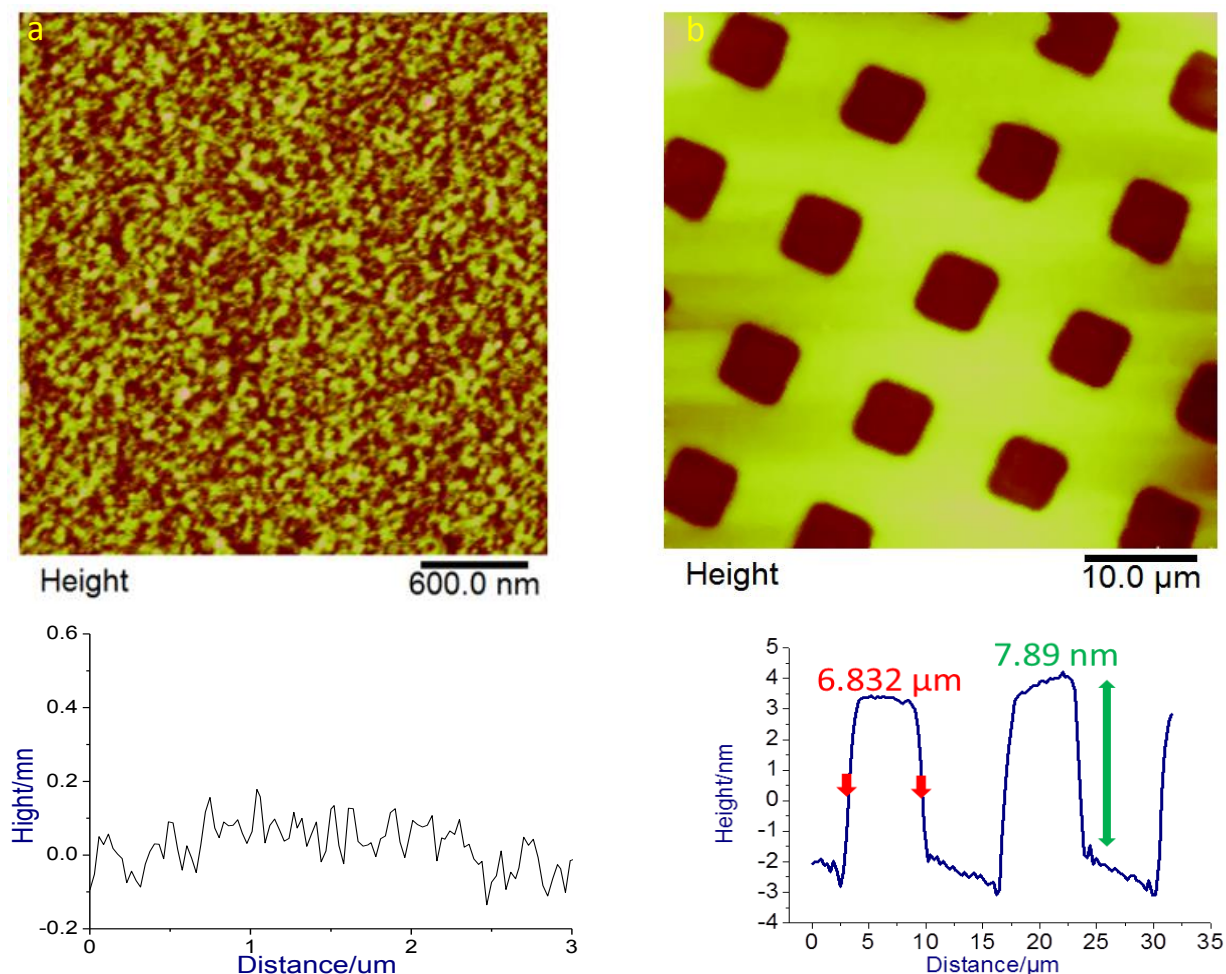


Figure 4.5: Tapping mode AFM topographical images and cross-sectional analysis for a) an unpatterned PCysMA brush and b) a micrometre scale patterned brush formed on a planar silicon oxide surface.

Figure 4.5a shows a tapping mode AFM image of the polymer brush surface (after 1.5 h polymerization). The surface exhibits a low roughness confirming the uniform growth of the

polymer across the surface. The estimated roughness was approximately R_q/R_a 0.355 nm/0.252 nm, which also confirmed a smooth and high grafted density of the grafted polymer brushes.

The dry thickness of the brush was further studied by fabricating micrometer scale patterned structure. Initiator-functionalised surfaces were exposed to UV light through a copper electron microscopy grid (2000 mesh, Agar, Cambridge, UK). The diameter of the illuminated area was 0.5 cm^2 and the exposure power was 2.6 J cm^{-2} . PCysMA brushes were grown from the patterned surface and characterised by tapping mode AFM (figure 4.5b). The image exhibits dark squares, which are attributed to the exposed regions in which the Br initiator was removed by UV exposure. Bright regions are attributed to the grafted polymer brushes, which are grown from the initiator intact at the unexposed area on the surface. Cross-section analysis of the image revealed that the dry thickness was approximately 7.89 nm. Exposure of brominated surfaces to UV light leads to elimination of Br, as previously reported³⁵².

Interferometric Lithography (IL) was used to fabricate nanometre scale patterns, using Lloyd's mirror two beam interferometer. The angle between the two beams was controlled by the rotation stage to fabricate different periodical structures. Subsequently, PCysMA brushes were grown from the unexposed bromine areas via SI-ATRP. Figure 4.6 shows the topographical tapping mode AFM images and their cross-sectional analyses obtained from the nanometer patterned polymer samples. The samples were fabricated by using a fixed exposure of 1.6 J cm^{-2} , while varying the period by changing the angle between the sample and the mirror in the interferometer, angle of 10° , 15° , 20° , and 30° were used. In the patterned figures, the highest points correspond to regions exposed to a minimum in the interferogram, while the dark regions exposed to intensity maxima. The periods of the samples were approximately of 690 nm, 511 nm, 450 nm, and 307 nm for 10° , 15° , 20° , and 30° respectively, and the widths (FWHM) of the polymer structures were 270 nm, 210 nm, 180 nm, and 145 nm respectively. Thus increasing the angle between the mirror and the sample led to a decrease in both the period and the width of the resulting structures.

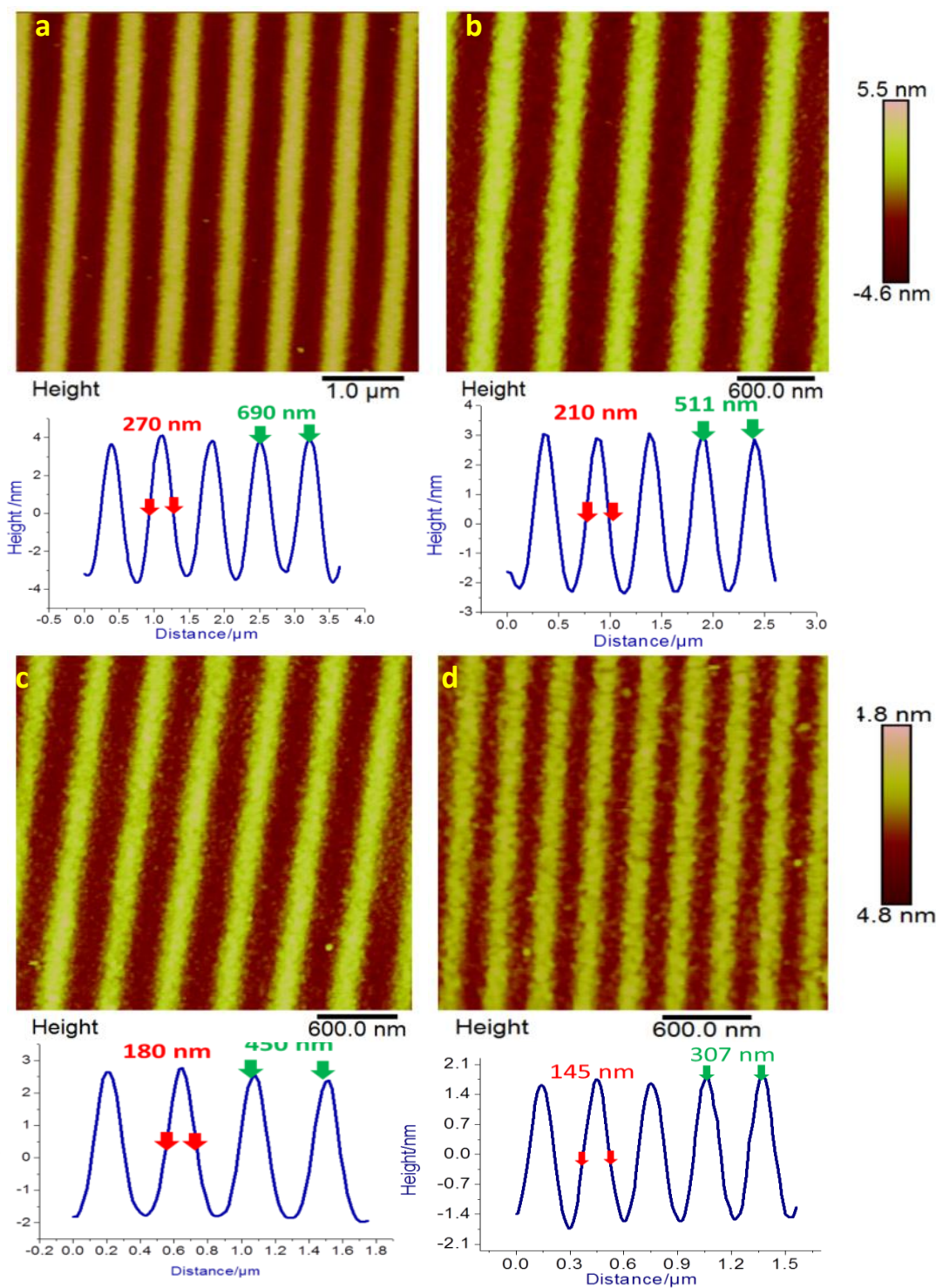
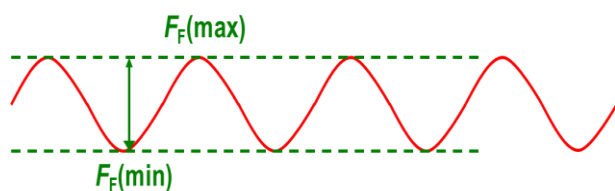


Figure 4.6: AFM topographical images of patterned PCysMA brushes with periods of (a) 690 nm, (b) 511 nm, (c) 450 nm, (d) 307 nm, and the strip width of (a) 270 nm FWHM, (b) 210 nm FWHM, (c) 180 nm FWHM and (d) 145 nm FWHM respectively. Cross section analyses obtained from the AFM images are shown below each image.

4.3.2 Friction and scale behaviour of PolyCysMA brushes in water

Friction force microscopy was performed to investigate the frictional behaviour of the PolyCysMA brushes as a function of the pitch. The chemistry of the tip was controlled by coating it with gold and functionalising it with a carboxylic acid terminated SAM. The measurements were carried out in water, which is thought to be a good solvent for the PolyCysMA brushes. As a result, the polymer molecules are expected to be solvated by water molecules coordinated to the surface via hydrogen bond interactions. The bound water causes an increase in osmotic pressure and the steric hindrance between the polymer chains^{188, 344-347}.

To analyse the data quantitatively, trace and retrace images were acquired. Line sections were measured at different loads, and the difference between the peak friction force and the minimum friction force was determined.



For the subtracted image the friction is given by

$$F_F = F_F(\max)_T - F_F(\min)_T$$

Where $F_F(\max)$ is the friction force at peak maximum and $F_F(\min)$ is the friction force at peak minimum.

To determine the friction value for unpatterned samples, the friction force of completely debrominated (fully debrominated surface) sample was acquired, and then it was subtracted from the friction obtained for completely covered brush surface. All measurements were done manually.

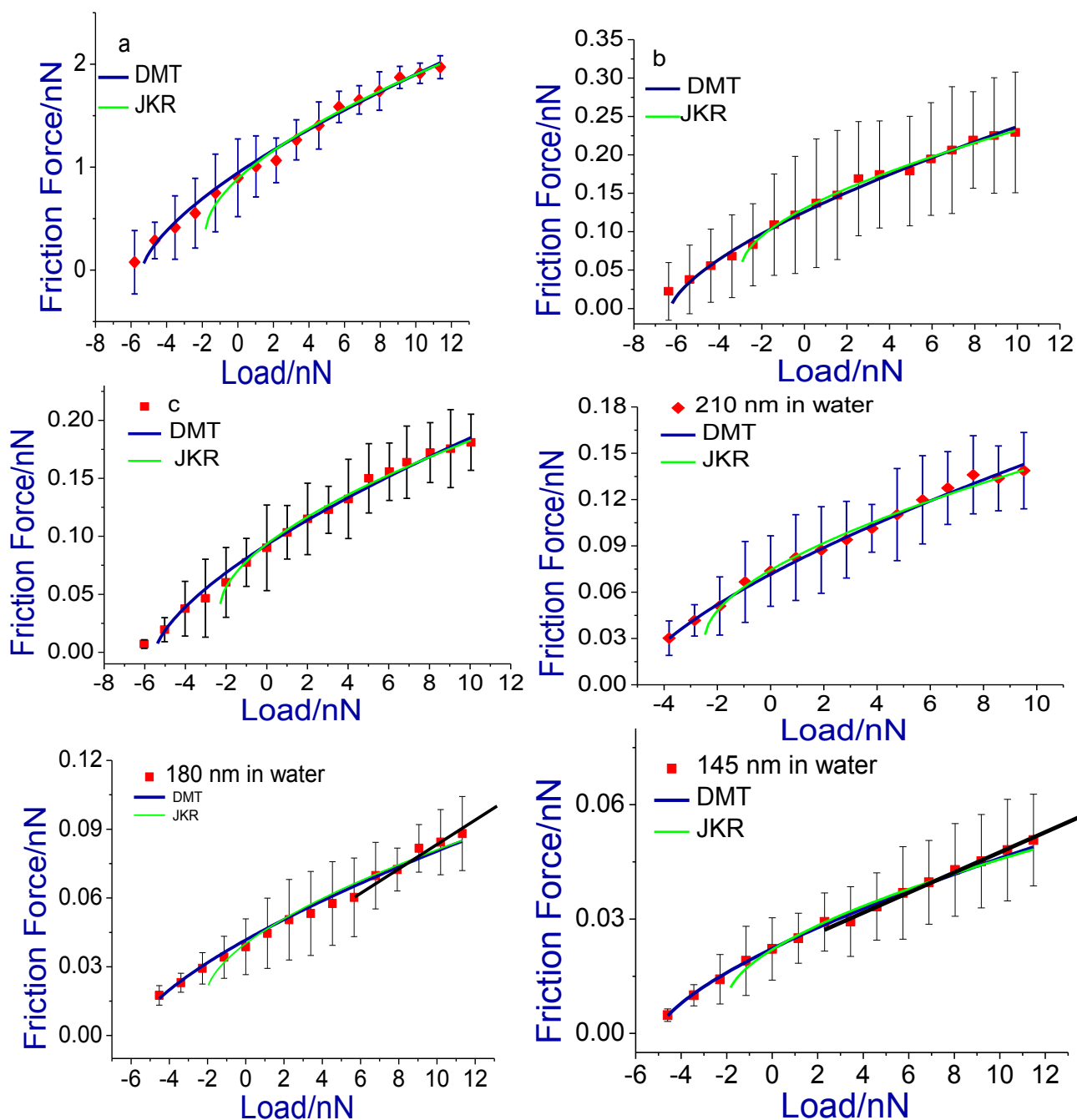


Figure 4.7: Variation in the friction force obtained by FFM as a function of the applied load for patterned PCysMA brushes in water. The samples consist of (a) unpatterned brush, (b) micrometre patterned sample, (c-f) nanometre patterned samples with FWHM of (c) 270 nm, (d) 210 nm, (e) 180 nm and (f) 145 nm brushes.

To rationalise the resulting friction-load data, it was assumed that the friction force is the sum of a load-dependent term, associated with molecular ploughing and a shear term, due to tip-sample adhesive interaction. It was found that for all of the samples studied here, the friction-load relationship in water was non-linear (figure 4.7). It is also believed that due to the solvation state at the interface the work of adhesion is reduced. However, because of the swell modulus of the polymer, the tip deforms the sample causing a large contact area. Thus, weak adhesion of a large contact area causes a significant adhesion force and leads to a non-zero shear term in equation 4.1.

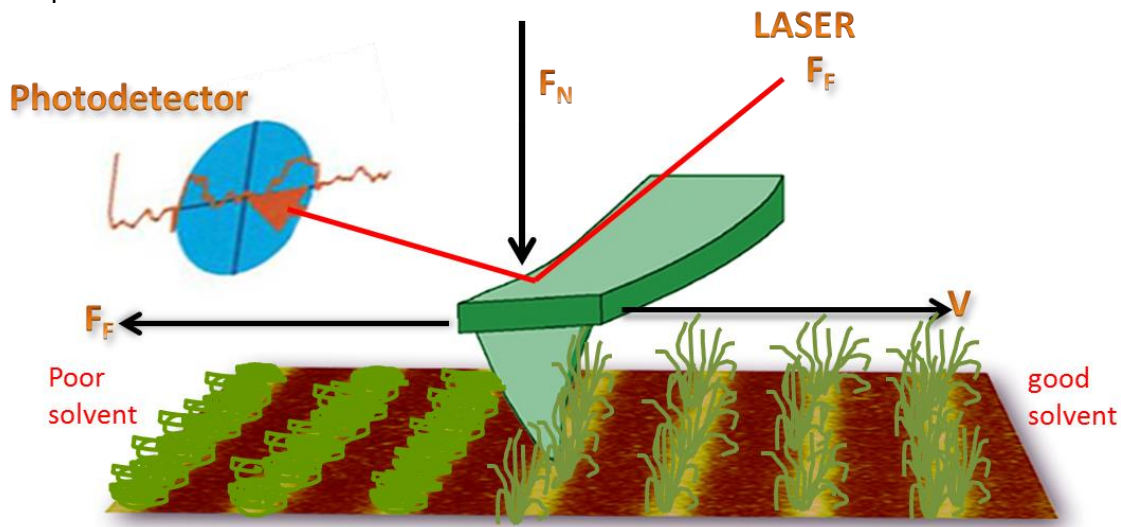


Figure 4.8: Demonstrates the expected the conformation of the polymer chains in a good and poor solvents.

The data were fitted using the DMT model (blue curves in figure 4.7) a good fit was achieved. However, when the data were fitted using the JKR model (green curve in figure 4.7) the fit was less good. The peak value of the friction force decreased as the size of the polymer structures decreased. The highest friction value was recorded for the unpatterned brushes. The relationship between the friction formed to the feature size is in the order of F_F unpattern > F_F micrometer pattern > F_F 270 nm FWHM > F_F 210 nm FWHM > F_F 180 nm FWHM > 145 nm FWHM. This is thought to reflect a change in the brush conformation as a function of the

pattern dimensions. It can be seen from figure 4.7 that the frictional force values are directly related to the sizes of the features. It is believed that the contact area between tip-sample surface decreased as the density of the grafted polymer chain or the scale size of the footprint decreased. The most reasonable explanation for this case is that the grafted chains on the edge of the polymer lines tend to be collapsed or extended over the ungrafted area as shown in figure (4.8). This has led to a decrease polymer density at the centre of the footprints, and as a result, the contact area is decreased so that the strength of interaction between the tip and the grafted polymer chains is reduced. In addition, there could be a physical interaction between the segments of the overlapped brush with polymer-free regions of the surface. This may lead to an additional factor which may have an impact on the tip sample contact and the rate of energy dissipation. As the distance between the polymer chains increases (due to collapsing of chains at the edges of the lines) that may cause to less crowding occur on the polymer brush regions, specifically at the periphery pattern.

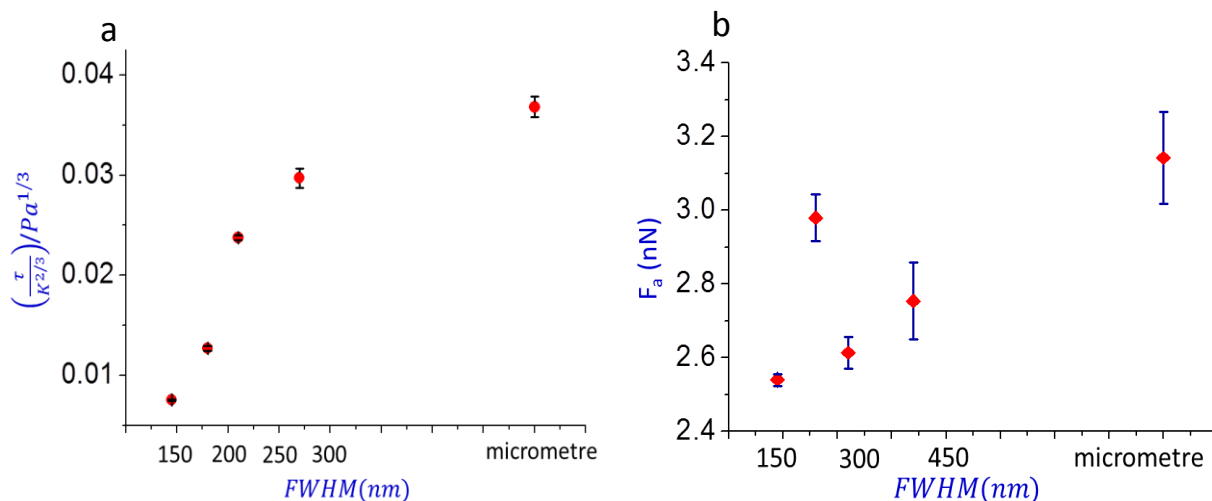


Figure 4.9: Results of fitting of friction-load data to DMT equation, Variation of (a) shear stress and (b) adhesion as a function of scale size (or FWHM of brushes line) for patterned poly (cysteine methacrylate) brushes in contact with a carboxylic acid functionalized cantilever in water solvent, the scale sizes, including 150 nm, 180 nm, 210 nm, 270 nm and a micrometre scale.

This phenomenon increases as the size of the brush lines decreases, and thus the tip may face less number of polymer molecules on the small scales compared to the bigger scale during its scanning over the sample surfaces.

The contact mechanics were modelled for each of the systems in figure 4.9 and the value of the surface shear stress and adhesion force were determined using the DMT model for the micrometre and nanometre patterned samples. Figure 4.9a shows the variation in the surface shear strength with the dimensions of the polymer structures. It can be seen that the shear strength increases with feature size up to Ca 270 nm. There is comparatively little difference in the values obtained for the 270 nm structures and micrometre-patterned samples. It is hypothesised that for narrow features, the density of the polymer chains, even in regions exposed to a minimum in the interferogram, is comparatively low. The feature sizes increases, the width of the densest part of the nanostructures increases, leading to an increase in the density of immobilized polymer molecules. Eventually, at 270 nm, the density of the polymers at the peak point in the nanostructures is close to that formed in the polymer regions of the micropatterned material. A direct relationship is observed between the calculated adhesion force and the dimensions of the polymer structures as shown in figure 4.9b.

4.3.3 PCysMA brushes in ethanol

Similar measurements were also made in ethanol. Friction-load relationships were obtained for all the samples and the results are shown in figure 4.10. The solvent is considered as a poor solvent to the PCysMA chains and the polymer molecules are expected to be collapsed as a consequence of the reduced amount of bound solvent. Therefore, the energy dissipation pathway in the contact area is dominated by molecular deformation rather than the adhesion. Consequently, the value of τ is negligible, and the energy dissipation is dominated by molecular ploughing. The friction force is linearly related to the applied load and the friction data obey the equation 4.2.

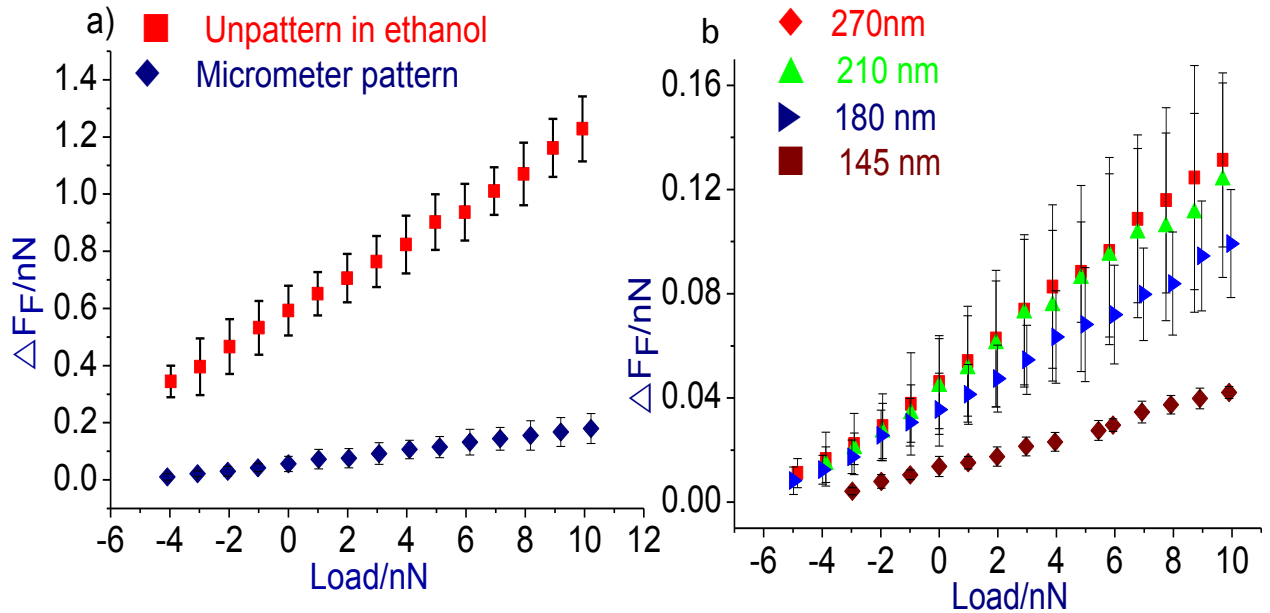


Figure 4.10: Variation in the friction force obtained by FFM as a function of the applied load for patterned PCysMA brushes in ethanol. The samples consist of (a) unpatterned and micrometre patterned samples (b) nanometre pattern samples with FWHM of 270 nm, 210 nm, 180 nm and 145nm.

The friction coefficients (μ) were calculated from the slopes of the friction-load plots as shown in figure 4.11. It was found that μ is directly related to the size of the features in the patterned samples. This is attributed to the fact that as the size of the scales decreased the amount of the collapsed polymer chains contributed in the ploughing process decreased. It is also suggested that the amount of the overlapping and interaction between polymer free regions and grafted polymer molecules on the patterned structures is diminished and the polymers molecules exhibit less stretching at the pattern periphery as shown in figure 4.8. In this case, the main reason behind the decreasing of the μ values as a function of the size of the features is related to the grafting density of the polymer chains.

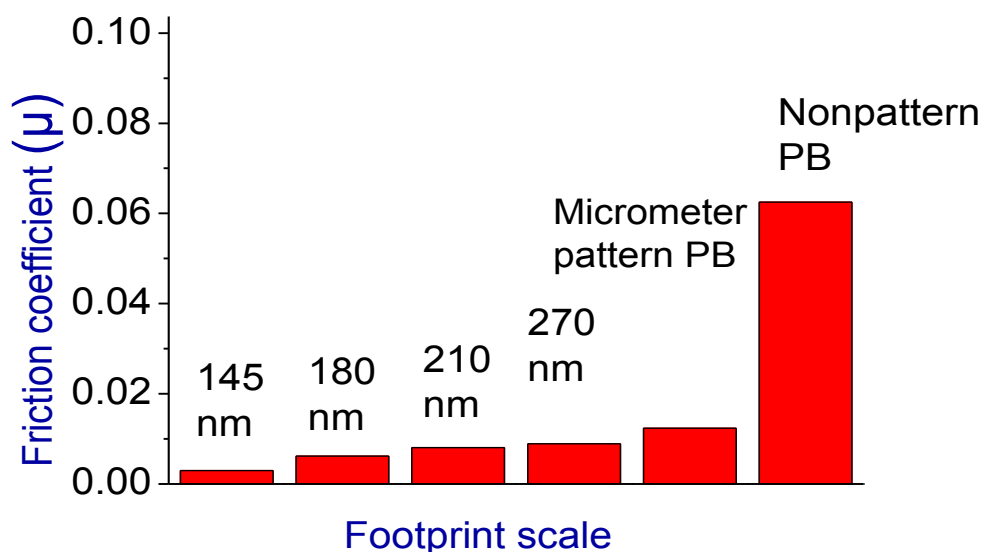


Figure 4.11: Coefficient of friction (μ) obtained for various patterns of PolyCysMA brushes as a function of scale sizes in ethanol.

As can be seen, the minimum value was recorded for the smallest grafting density and the maximum value was recorded for the highest grafting density of the samples. Qualitatively, the magnitude of molecular ploughing in the dissipation energy between the tip and PolyCysMA brushes can be represented in the order of Friction for unpattern > Friction for micrometre pattern > friction for 270 nm FWHM > friction for 210 nm FWHM > friction for 180 nm FWHM > 145 nm FWHM.

4.4 Conclusion

A series of patterned zwitterionic PCysMA brushes was formed with dimensions ranging from the 145 nm up to macroscopic scale. The frictional behaviour of the brushes as a function of feature size and solvent has been investigated by FFM. The friction force was treated as the sum of a load-dependent term, which is attributed to molecular ploughing, and an area dependent- shear term, which is assigned to adhesive interaction. In water, which is a good solvent for the PolyCysMA brushes, adhesion controls the interaction at the interface, providing a sublinear friction-load relationship which is consistent with the DMT model. The calculated contact mechanics parameters have supported this hypothesis. In addition, the work of adhesion decreases as the size of the feature reduces. In the case of the reduction of the sizes down to 180 nm and 145 nm FWHM, which contain a very small number of polymer chains, intermediate behaviour was observed, shear stress initially dominates the energy pathway, then it becomes ploughing dependent at high loads. These results indicate that in addition to the solvent effect the response of the polymer brush is affected by lateral stretching and elastic free energy of polymer chains in the patterned area. A completely different behaviour was observed in a poor solvent (ethanol). The brush is collapsed and the friction-load relationships are linear across the entire range of the applied loads. This is attributed to the fact that the shear stress is so small and negligible; the ploughing has become a considerable mechanism at the sliding contact area. The friction coefficient, μ , directly related to the footprint size and the grafted density of the brushes, as the period or density decreased the μ decreased. It is suggested that in the poor solvent the PolyCysMA chains would neither extend nor overlap with non-polymer regions at the periphery and chain contraction is further expected than stretching.

Chapter 5: Effect of grafting density on the conformational and mechanical properties of PolyCysMA brushes

5.1 Introduction

The conformations of the polymers in a brush must be precisely controlled to be useful in the development of many devices or smart-surfaces, including biomedical, sensing and polymer-coated devices³⁵³. The structure and behaviour of polymer brushes depend on the way in which the polymer chains are anchored, the grafting density, formula weight, and the local environmental conditions (e.g. type of solvent, ionic strength, pH, and temperature) of the surface³⁵⁴⁻³⁵⁹. The grafted polymer chains are said to be brush at high grafting densities, such that the separation between adjacent polymer chains is smaller than the height of the polymer. Consequently, steric repulsion forces the chains to stretch normal to the surface, forming a brush architecture. In contrast, a mushroom or pancake (or coil) morphology is formed at low grafting density, where the separation between neighbouring chains is larger than the polymer height so that the chains grow laterally and overlap the non-grafted area³⁶⁰⁻³⁶³. Moya et al. found a direct relationship between the thickness of poly {[2-(methacryloyloxy)ethyl] trimethylammonium chloride} (PMETAC) brushes and the density of an initiator (ω – mercaptoundecyl bromoisobutyrate thiol) using ellipsometry and QCM-D to characterise the surfaces. At a low grafting density collapsed brushes were identified, but a brush structure was achieved at high density³⁶⁴. Surface-initiated atom transfer radical polymerization (SI-ATRP) a widely used method that facilitates the fabrication of polymer systems with highly controlled conformation. One of the most important advantages of this synthetic method is the ability to use bottom-up and top-down strategies together or separately, providing a way to fabricate well-defined brush structures that could be useful in many biological applications³⁶⁵⁻³⁶⁶. Many groups have tried to control the grafting density of brushes using approaches that include the formation of mixed monolayers³⁶⁷⁻³⁶⁹, hydrolysis of ester-linked polymer brushes³⁷⁰, controlling polymerization conditions (such as reaction time and concentration of the monomer)³⁷¹⁻³⁷³, formation of a gradient density of ATRP initiator³⁷⁴⁻³⁷⁵, hydrolysis of grafted polymer chains³⁷⁶ and photodegradation of grafted polymer³⁷⁷. However, these methods have suffered from a

number of limitations, and there is still a need for better approaches. Photolithography is an attractive tool because it enables the fabrication of structures across a range of length scales, from the macroscopic to nanometre scale³⁷⁸⁻³⁷⁹. Yamamoto et al. used photolithography to irradiate 2-(4-chlorosulfonylphenyl)-ethyltrichlorosilane (CTCS) initiator to generate surfaces with different densities. Poly(methyl methacrylate) (PMMA) was grown from the unpatterned sites of the initiator using ATRP. It was found that the thickness of the brush decreased with increasing photodegradation. AFM force-distance measurements showed that the resistance to compression decreased as the grafted density of the brushes decreased³⁸⁰. Recently, Friction force microscopy (FFM) has attracted interest for the investigation of the structures of brushes by measuring friction forces and shear stress of end-grafted polymer brushes in different environments^{188, 381-387}. Friction forces are commonly attributed to the energy dissipation pathways which arise from either the molecular adhesion or molecular deformation at interfaces between the tip and sample surfaces. These pathways are influenced by the environment that surrounds both surfaces. In a good solvent, polymer chain forms a brush conformation due to the steric repulsion between solvated polymer molecules. In a poor solvent, a collapsed polymer structure is most likely to occur. Therefore, the mechanism of the energy dissipation is controlled by molecular plowing at the contact area between tip-sample surfaces which makes the friction force to be load-dominated term³⁸⁸⁻³⁸⁹. For swollen brushes the relationship between the tribological behaviour and the brush conformation may be more complex.

Here a new approach is investigated to the study of the relationship between brush properties and grafting density, by using controlled photolysis of brominated surfaces to form brushes with systematically varying densities of attachment. As a surface is progressively debrominated the density of grafting decreases, leading to a change in the polymer properties. The conformation and behaviour of the fabricated brushes were investigated using FFM with either SAMs or gold coated cantilevers in different environments. The friction data have been rationalised based on the approach developed by Zhang et al.³⁹⁰, who postulated that the friction force could be treated as the sum of a shear surface term and a load-dependent term. This was further supported by using contact mechanic models to analyse the data.

5.2 Experimental Sections

5.2.1 Preparation of APTES-BIBB initiator

A silicon surface was functionalised by adsorption of APTES molecule and then derivatised by reaction with BIBB molecules according to the procedure written in section 3.3.

5.2.2 Gradient ATRP initiator

The ATRP-initiated samples were irradiated using maskless lithography, gradient density of the initiator sample was prepared by varying the exposure times according to the experimental procedure written in section 3.7.2.

5.2.3 Synthesis of cysteine methacrylate monomer and polymerization reaction

The procedure for the synthesis of cysteine methacrylate (CysMA) monomer and for the growth of brushes using SI-ATRP can be found in the section 3.5.1 and 5.7.2 respectively. The polymerisation conditions were held constant throughout the work described in this chapter and all samples were prepared together to ensure that the brushes were grown from polymers of equal molecular weight. The dry thickness of a complete brush layer was 7 nm.

5.2.4 Surface analysis

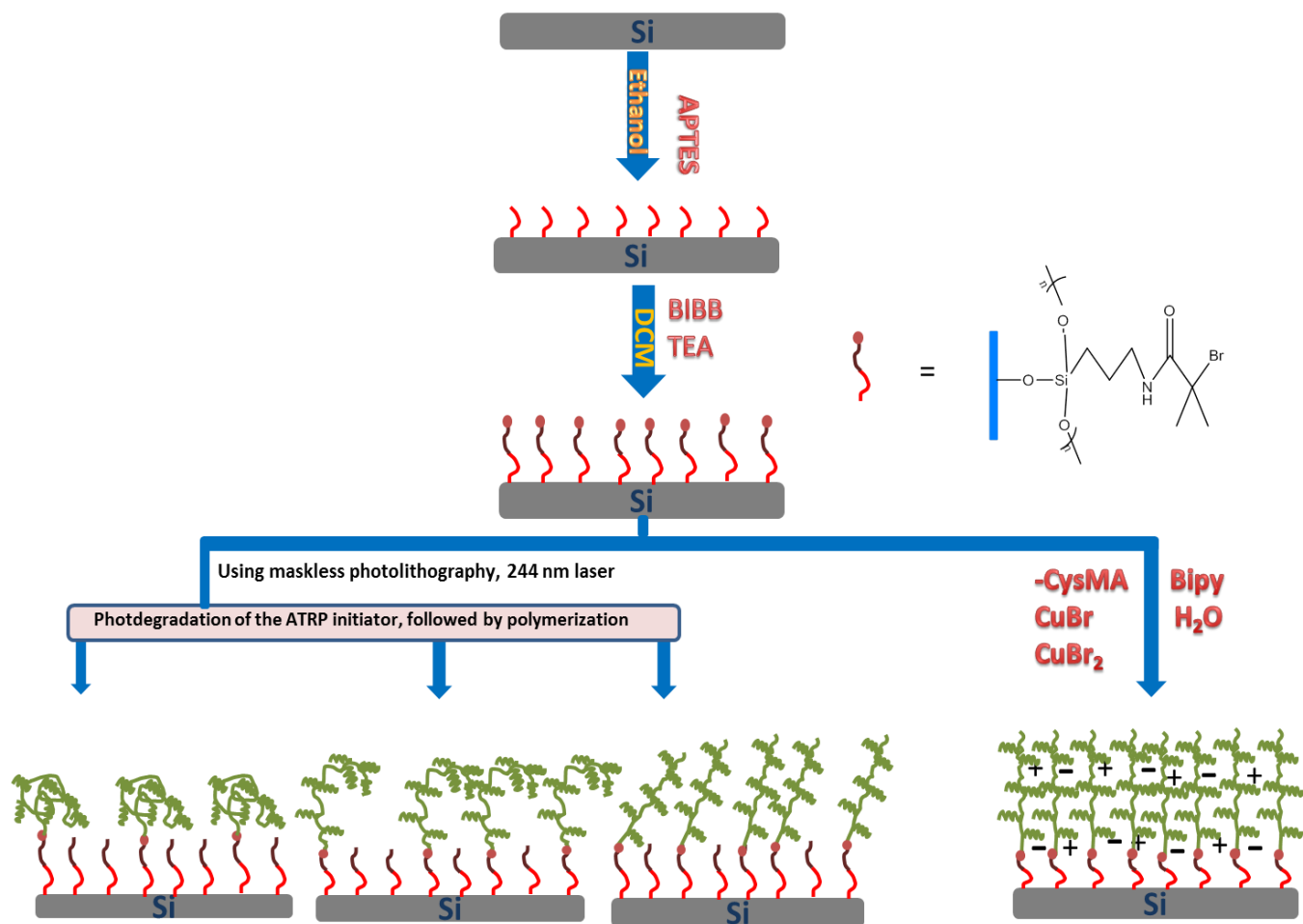
XPS, ellipsometry, contact angle goniometry and Friction force microscopy (FFM) were carried out according to the procedures presented in the experimental section of 3.11.

5.3 Results

5.3.1 Photodegradation and characterisation of ATRP initiator

An ATRP initiator surface was fabricated reacting a 3-aminopropyl triethoxysilane (APTES) functionalised silicon surface with bromoisobutyryl bromide (BIBB), forming an APTES-BIBB structure on the surface. Scheme 5.1 shows typical fabrication processes to create an initiator film and a gradient PCysMA brush. To fabricate a surface with varying grafting density, a maskless photolithography was used to selectively remove Br from the surface by UV photolysis. The composition of photopatterned and unpatterned surfaces was characterised using XPS. High-resolution C 1s, N 1s and Br 3d peaks were observed in the spectrum of an

unmodified sample. The C1s core level spectra (figure 5.1a) were fitted with three components, as seen at 285.0, 286.729 and 288.7632 eV, corresponding to C-C-C, C-Br/C-NCO and O=C-N respectively



Scheme: 5.1: Schematic diagram showing the formation of an APTES-BIBB layer on a silicon substrate, the preparation of PCysMA layers of varying grafting density using maskless photolithography.

The peak area for C-C-C, C-Br/C-NCO and O=C-N was 3.81:1.93:1, which is in a close agreement with the calculated ratio of 4:2:1, Br 3d peaks were observed at 70.0 and 72.0 eV as shown in figure 5.1b, which is consistent with the components of the BIBB-APTES initiator. High-resolution XPS Br 3d peaks were acquired to characterise the patterned initiators. It was

observed that as the intensity of the photodegradation increased the concentration of bromine decreased on the surface.

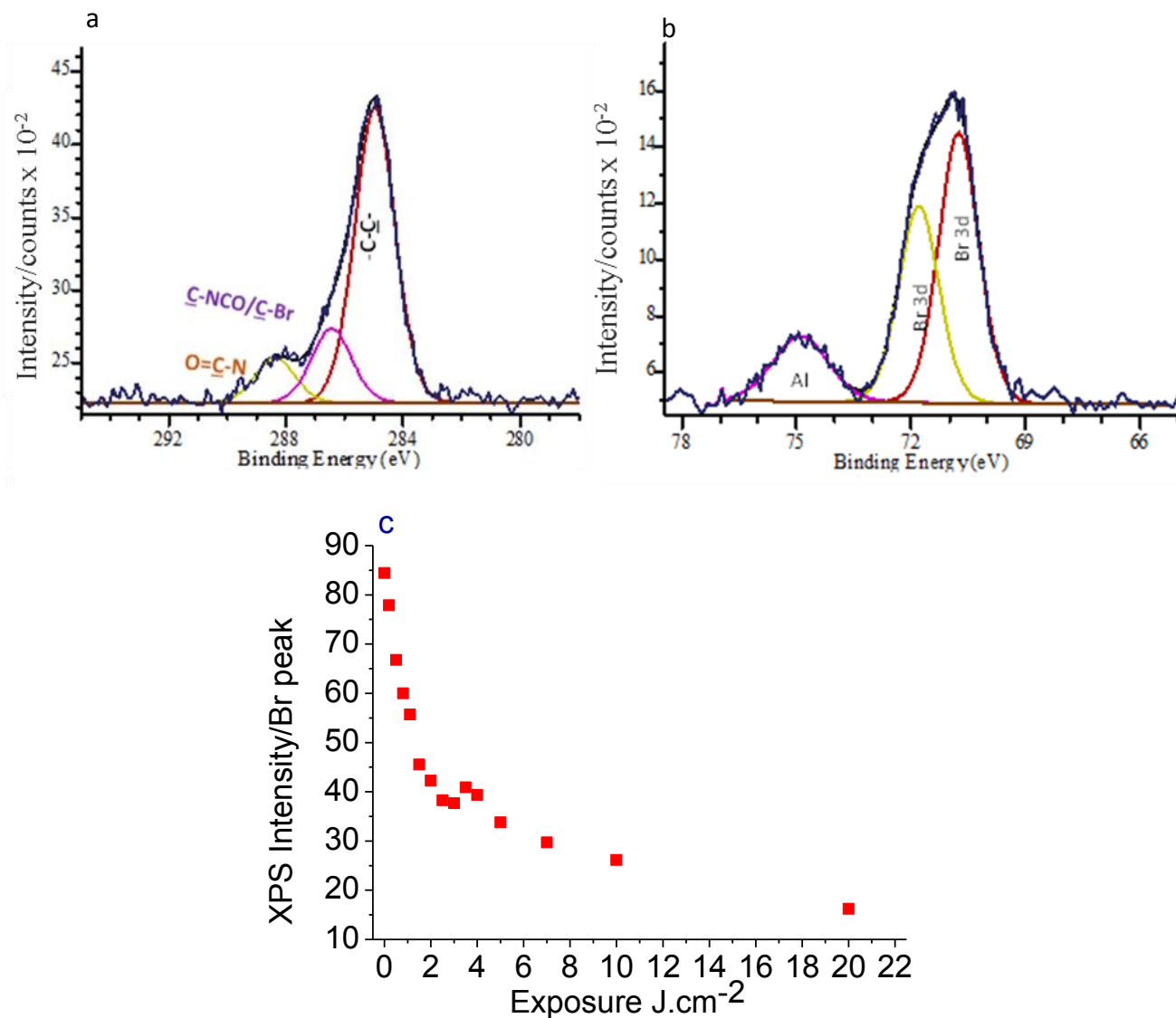


Figure 51: a) High-resolution C 1s and b) high-resolution Br 3d XPS spectra for unmodified APTES-BIBB film. c) Variation in the intensity of the Br peak as a function of the UV exposure for APTES-BIBB film.

Figure (5.1c) shows the sum of the areas of the two components to the Br 3d peaks obtained for the initiator film exposed to 244 nm UV light for various times. It can be seen from the XPS data that there was an initial dramatic decrease in the concentration of the bromine film until it a dose of 3.0 J cm⁻², after which, the rate of the change was much slower, and began to approach

a limiting value. It is also observed that the density of bromine was not reduced to zero even after very large exposure. One explanation, for this is that adsorption of APTES onto the surface leads to bilayer formation. If BIBB molecules are able to penetrate the upper most APTES layers, the Br may be incorporated that is less reading lost after photolysis. It is likely that upon photodebromination, the top layer of the initiator is fully debrominated, but some bromine remains intact under the underlying layer of the film. The XPS sampling depth would be greater than the SAMs thickness. Only the photodebromination of the top layer of the film is required to create an inactive region, which will prevent the polymer from growing. After a dose of 20.0 J cm^{-2} the Br 3d signal is indistinguishable from the background signal. This may explain by assuming that the high power exposure caused to degrade the main parts of the surfactants.

5.3.2 The growth of PolyCysMA brushes and the effect of the initiator density

PolyCysMA brushes grown by SI-ATRP on various graft densities of APTES-BIBB initiator, regarding the polymerization time and conditions. To ensure the success of the polymerization reaction, a control sample was characterised using XPS, ellipsometry, and contact angle goniometry. High-resolution C 1s, N 1s, and S 2p XPS spectra were obtained for 7nm dry thickness of PolyCysMA brush on a silicon surface. The high-resolution C 1s spectra fitted using three components at binding energies of 285.0 eV, 286.3 eV, and 288.7 eV which are attributed to C-C-C, C-O/C-N, and O=C-O bond respectively (figure 5.2a). The peak area of C-C-C, C-O/ C-N and O=C-O was 2.07:1.32:1, which is in a good agreement with the calculated ratio 2:1.3:1 for these atoms in the brush component. The N 1s spectra were fitted with two components centred at 399.0 and 401.5 eV, and assigned to C-NH₂ and C-NH₃⁺ groups and the peak ratio was 1:1 (figure 5.2b). This means that 50% of the free amine groups were protonated. At a neutral pH (2-9.5) the brush is expected to be zwitterionic, with equal numbers of positive (NH₃⁺) and negative charges (COO⁻).

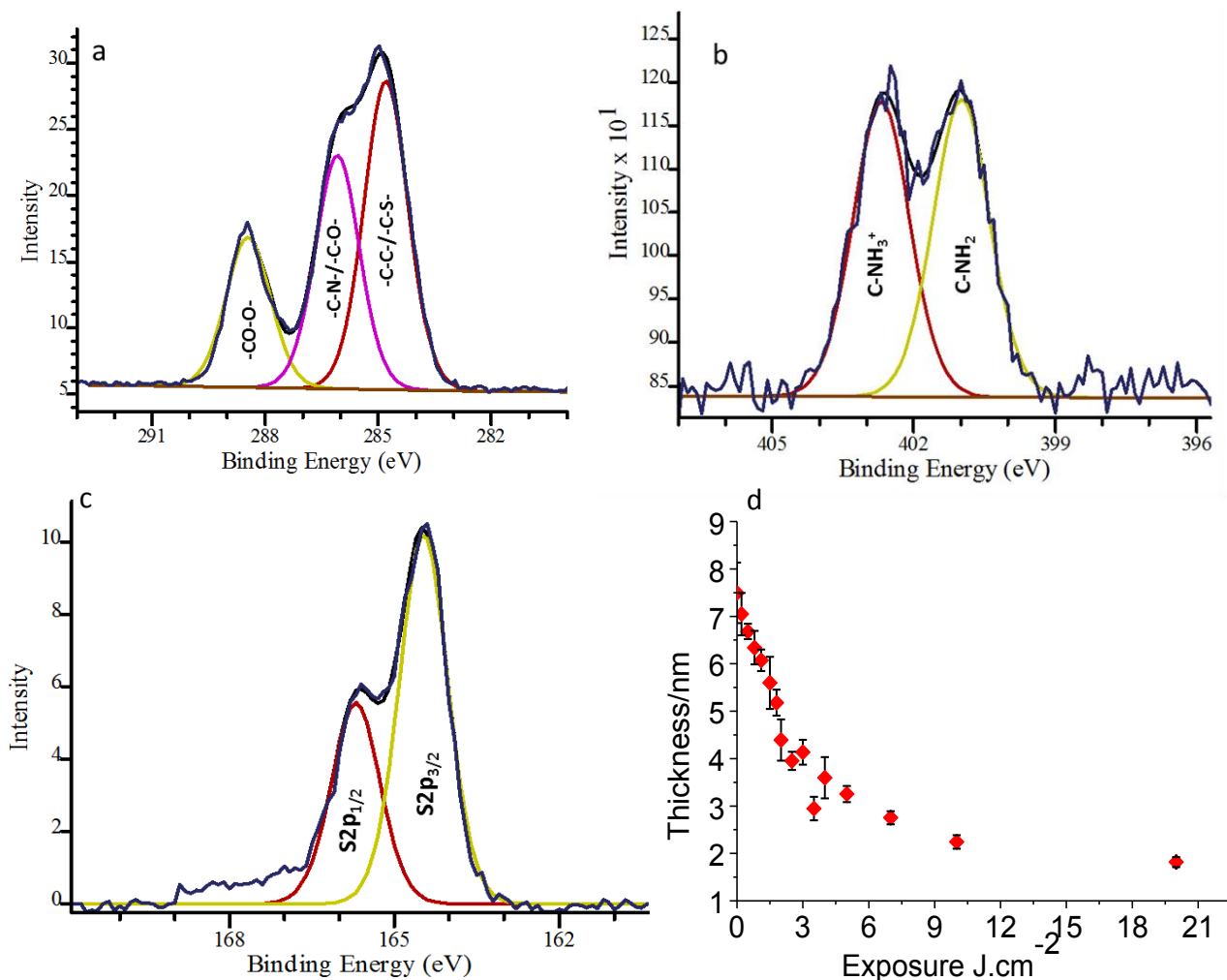


Figure 5.2: Shows high-resolution XPS spectra for PolyCysMA brush grown on a silicon surface, (a) C 1s spectra, (b) N 1s spectra, (c) S 2p spectra and (d) the variation in the thickness of PCysMA brushes grown from surfaces subjected to varying UV exposures.

The high resolution S 2p spectrum was fitted with S 2p_{3/2} and S 2p_{1/2} components with binding energies of 164.47 and 165.7 eV. The intensity ratio between these two peaks was 2:1, as expected for 2J+1 spin-orbit coupling (figure 5.2c). The brush thickness was measured as a function of exposure using ellipsometry as shown in figure 5.2d. A non-linear relationship was observed between them. The ellipsometry data are in a good agreement with the XPS results. It can be seen that as the exposure increased the thickness of the brushes decreased. The thickness dramatically decreased at the beginning of the exposure to 2.5 and 3.0 doses, then the rate of the change decreased slowly and became constant at 10 - 20 J cm⁻². This is attributed

to the fact that the number of Br atom decreased as the exposure increased. As a result, the distance (D) between the adjacent end-grafted polymer chains increased. Leading to an increasing tendency for the brushes to adopt a mushroom conformation.

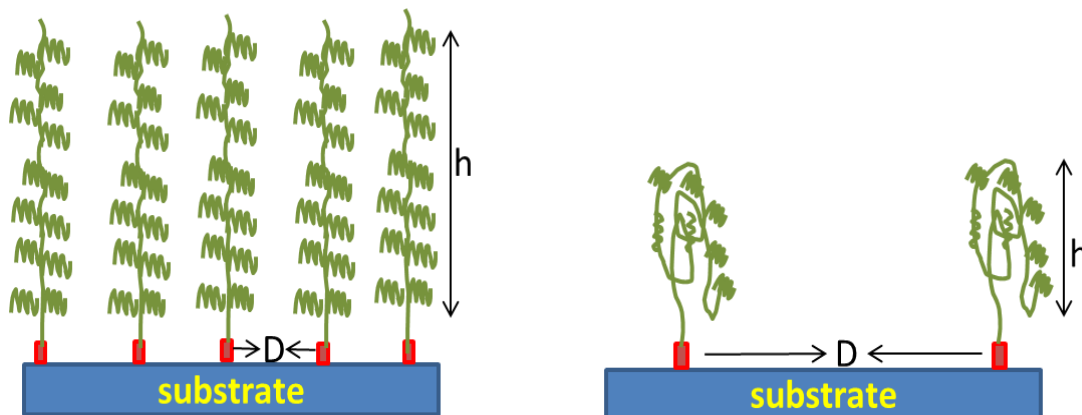


Figure 5.3: The transition from a brush to a mushroom conformation for polymer brushes on a surface. D is the distance between two grafting points and h is the brush height. (a) $D < h$ for brush structure and (b) $D > h$ for mushroom structure.

This observation is in a very good agreement with expectations based on other work in the literature, such as that by Britain et al.³⁹¹, Hess et al.³⁹² and Penn et al.

5.3.3 Frictional Behaviour of Brushes of Varying Grafting Density

Friction forces were measured as a function of the load for PCysMA brushes grown from surfaces subjected to varying exposures, and with varying degrees of debromination, while immersed in either water or ethanol, using carboxylic acid and gold coated tips. It can be seen that for polymer films grown from substrates subject to small UV exposure, the friction-load relationship is sublinear and fitted with DMT model.

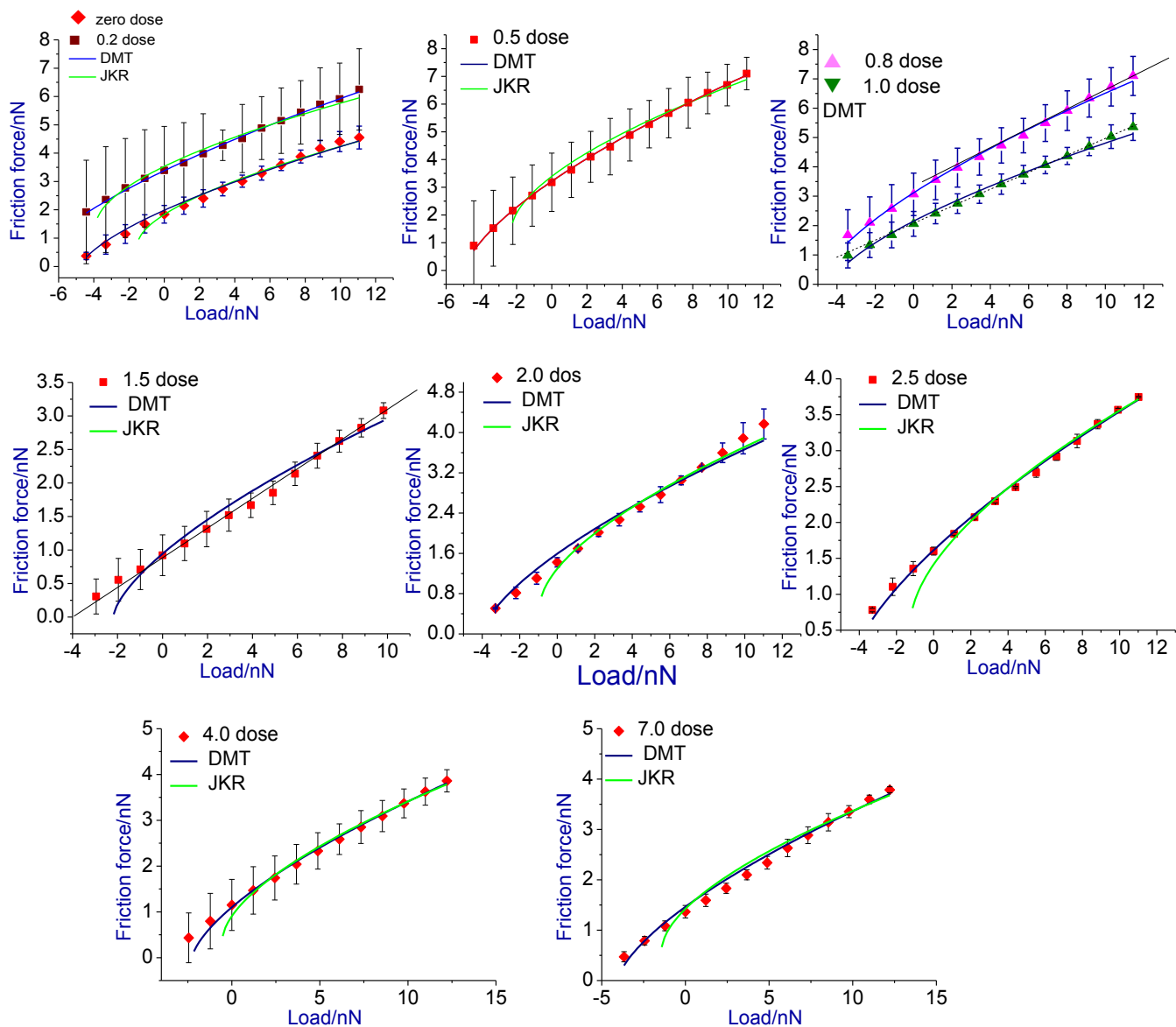


Figure 5.4: Typical friction-load plots acquired for brushes grown from the APTES-BIBB films subjected to varying UV exposures, the scan distance was $3\mu\text{m} \times 3\mu\text{m}$. The data were fitted using contact mechanic model.

As the exposure increases, the friction force decreases and the friction-load relationship becomes linear. It has been shown that PCysMA brushes form zwitterionic structures in the range of pH 2.5-9.0. Under these conditions, the polymer is solvated strongly by water, creating steric repulsion between neighboring chains and causing them to swell away from the surface.

The COOH terminated tip is also solvated by the solvent molecules, reducing the adhesive interaction between the tip and brush surfaces. Because of the high compressibility of the brushes (due to their small elastic moduli) the sharp tip penetrates the brush film and generate a large contact area. Although the solvated polymer is expected to yield a small work of adhesion, the small modulus of the polymer leads to a large contact area and consequently a net adhesive interaction that is significant. Therefore, the friction force is sublinearly related to the applied load through the entire range of the applied load as shown in figure 5.4. It was possible to fit the friction-load relationship using the DMT model. However, this relationship was changed as the density of the grafted brushes decreased. It can be seen that the relationships were nonlinear for the samples exposed to zero, 0.2, 0.5, 0.8 and 1.0 doses, but it became linear for the samples exposed to 1.5 and 2.0 doses, and then it turned to be sublinear for the rest of the samples. As the polymer density decreases, the net interaction strength also decreases. In contrast, in a poor solvent (ethanol) the possibility of H-bond interaction between the brush and the solvent on one side and the tip-solvent on the other side is reduced, and thus, the non-solvated brush is tended to be collapsed which may lead to the formation of mushroom structures. The mechanism of the tip-sample interaction is controlled by plowing and the friction force is identified as a load-dependent term. Therefore, a linear relationship between friction-load is expected for the entire measurements in the ethanol as shown as shown in figure 5.5.

Further investigations were carried out by using gold coated tip in a similar way to the MUA coated tip. The friction forces were nonlinearly proportional to the applied loads for the measurements obtained in water, regardless of the grafted density of the polymer brushes. This further supports the hypothesis that the non-linear friction-load relationships result from a large contact area, resulting from the small modulus of the polymer, rather than the formation of specific interactions.

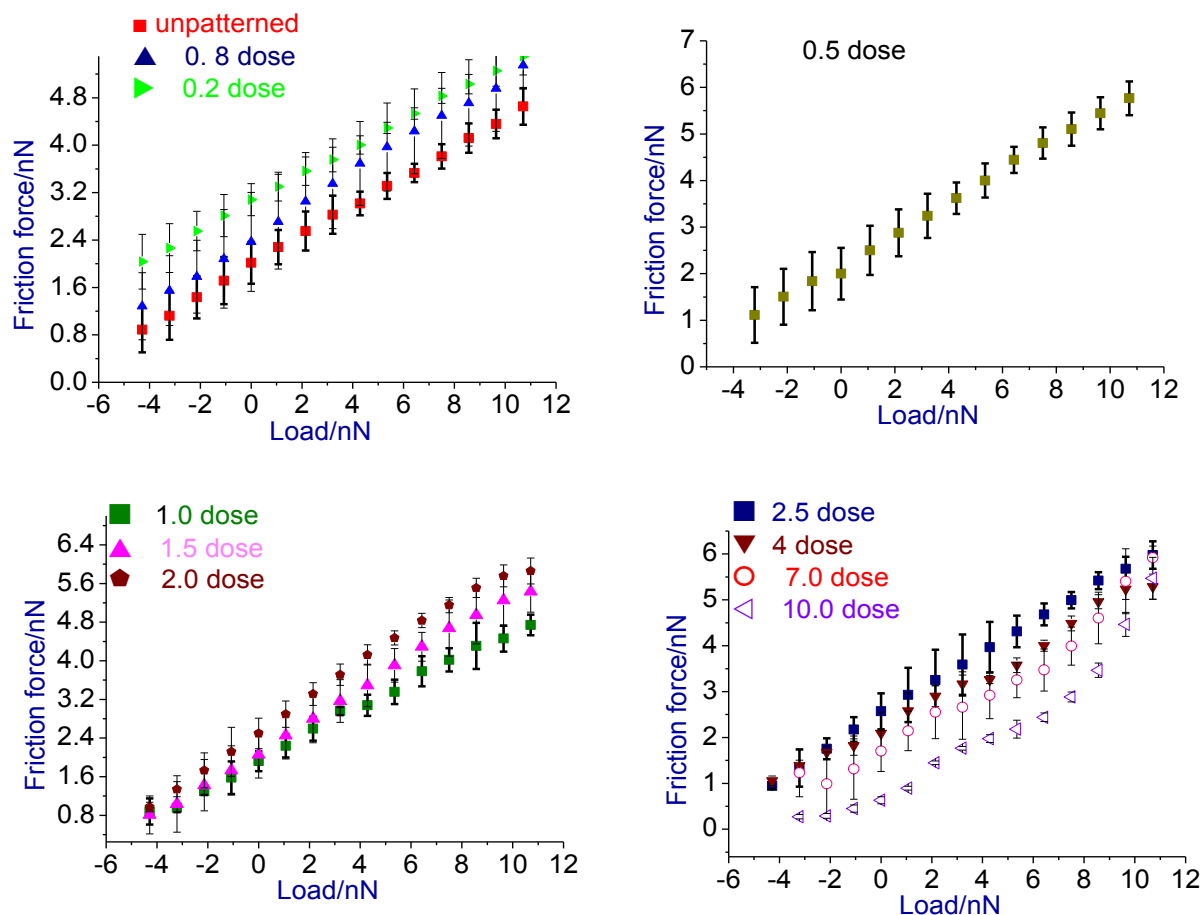


Figure 5.5: Typical friction-load plots obtained using SAM coated probe in ethanol for PCysMA brushes of varying densities.

Variation in the friction forces as a function of applied loads was also studied for PCysMA brushes with varying grafting densities immersed in ethanol using gold coated tip (figure 5.6). The friction forces were linearly related to the applied loads, meaning that molecular deformation controlled the energy dissipation at the interface, due to the formation of a mushroom conformation in this solvent.

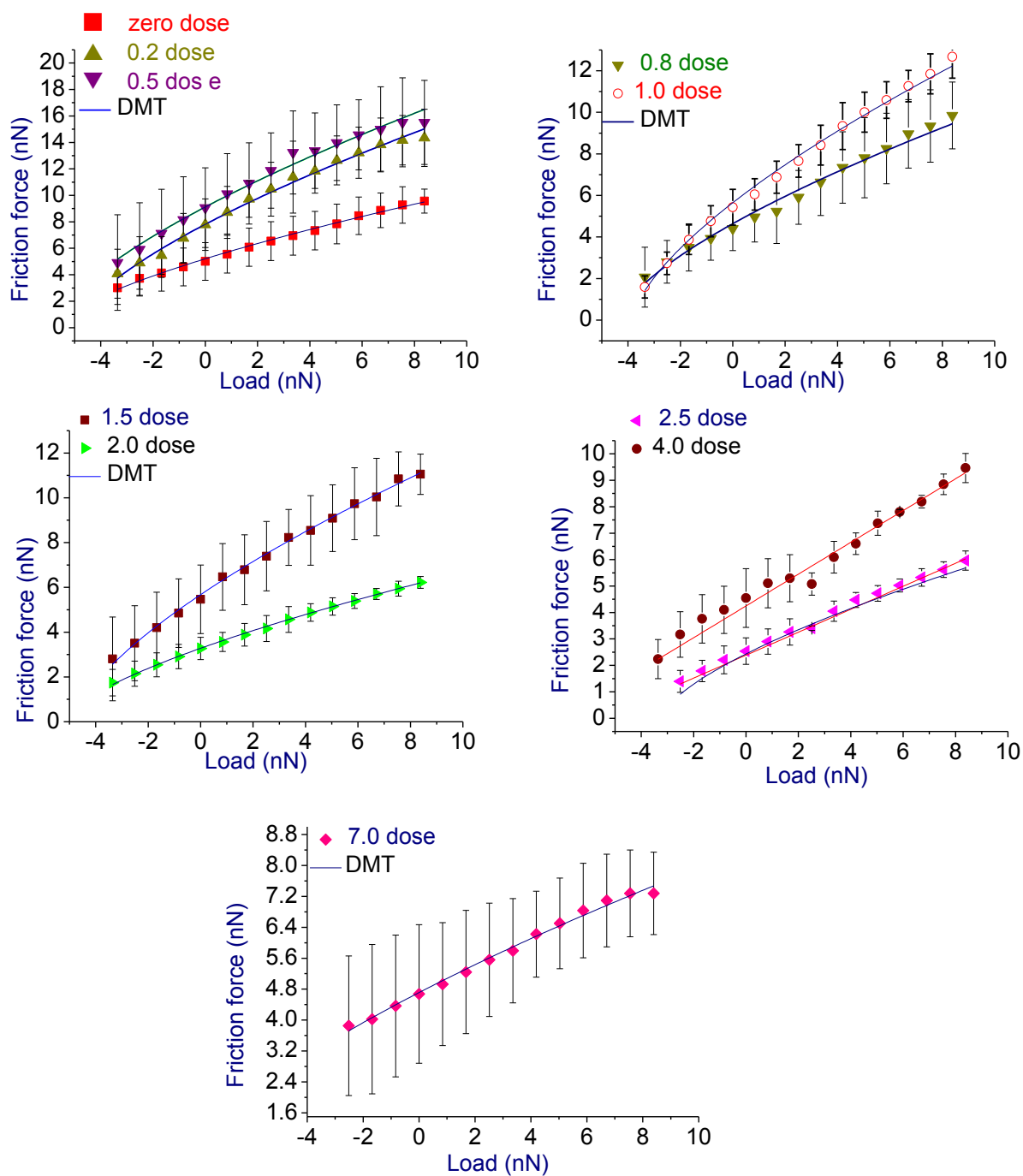


Figure 5.6: Typical friction-load plots obtained using gold coated probe in water for PCyMA brushes of varying densities. The friction data were fitted with contact mechanic models.

The data in figure 5.7 are noticeably similar to those obtained using an MUA coated tip.

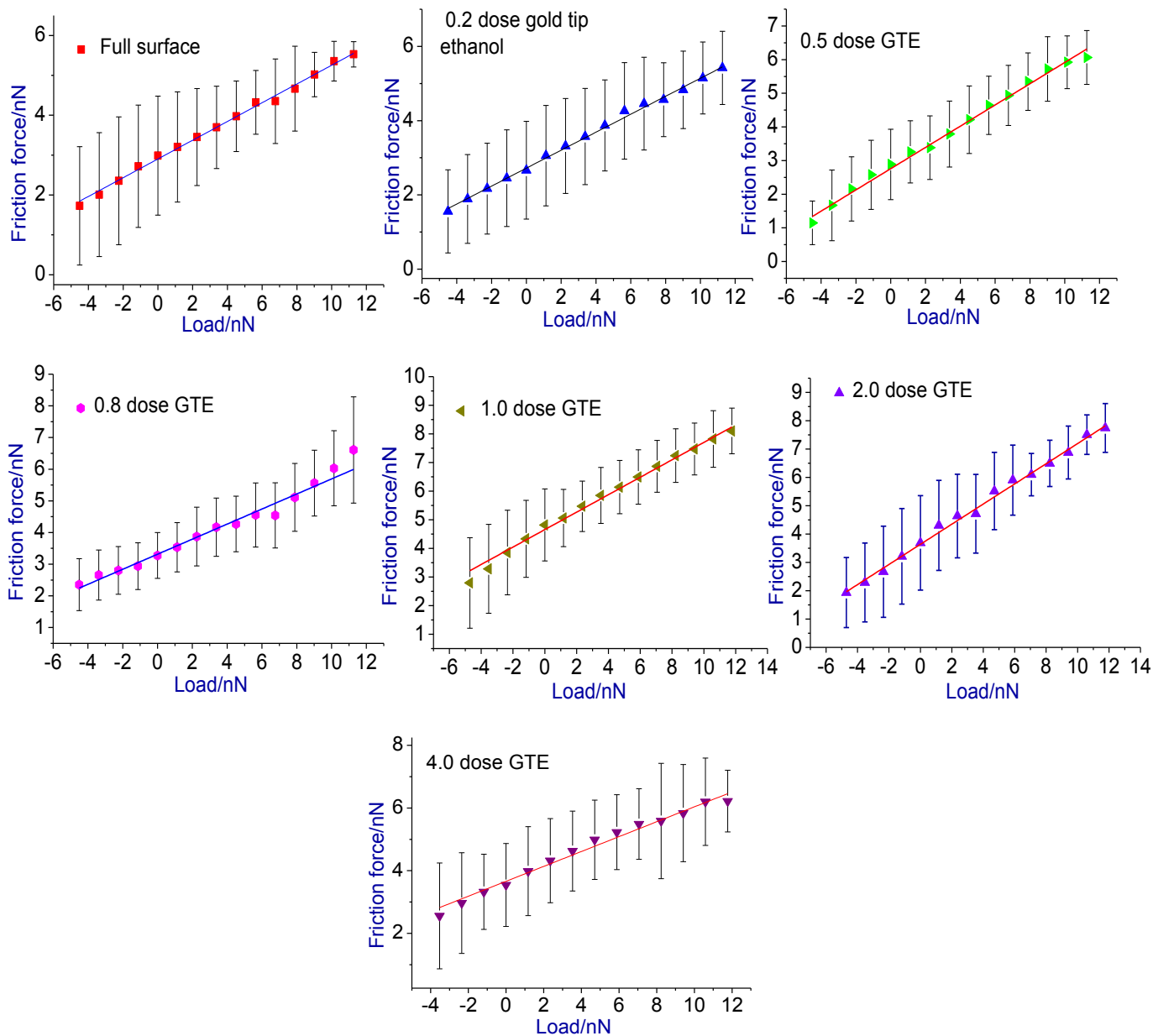


Figure 5.7: Variation in friction forces as a function of applied loads for various grafted PolyCysMA brushes in ethanol using gold coated tip and FFM. The data were fitted to a general linear equation.

5.3.4 Effect of Brush Density on The Friction-load Relationships of The Polymer Brushes

It is widely believed that the conformation of a polymer brush depends on the grafting density of the anchored polymer chains. The transition from a brush structure to a mushroom conformation occurs as the grafting density is reduced^{30-34,37}. In this work, both environmental and grafting density effects on the response and mechanical properties of a PolyCysMA brush were investigated, using FFM and AFM tips with controlled chemistry. The polymerisation time and conditions remained constant. Hence, differences in behaviour are attributable to differences in grafting density of the brushes. Based on previous results, an exposure of 3.5 J cm⁻² is sufficient for complete debromination of the initiator. It was found that as the exposure increased the density of grafted brushes decreased and the distance between two adjacent polymer chains increased. From figures, it is inferred that for samples exposed to zero, 0.2, 0.5 and 0.8 J cm⁻² polymer adopted a brush conformation. These samples yielded sublinear friction-load relationships. However, for the samples were exposed to 1.0, 1.5 and 2.0 doses, a linear friction-load relationship resulted. This is best explained by a transition to a mushroom conformation. Because of a large distance formed between grafting points ($D > h$), the polymer chains started to grow laterally and overlapped with the ungrafted area, collapsed brushes were formed. For the samples exposed to 2.5 doses and more, the friction load relationships tended to be sublinear again. This may be because the grafting density was now very low and the friction-load relationship was dominated by the interaction with the underlying substrate.

In ethanol, the friction-load relationship was observed under all conditions. A transition in the friction behaviour of the polymer brushes was not observed, despite changing the grafting density of the brushes.

5.4 Discussion

The data presented here clearly illustrate that the conformation of the PolyCysMA brush depends on the grafting density of the polymer chains on the surfaces. However, the role of the environment in controlling brushes behaviour cannot be ignored. The transition in the structure of the PolyCysMA brushes from the brush to the mushroom or coil structure was observed in a good solvent, as the density of end-grafted brushes reduced. The brush conformation of the polymer is most likely to be occurring, due to the degree of the solvation and small distance between grafted points of the polymer chains. This means small exposures are not enough to create a distance between grafting points larger than the brush height. The sublinear friction-load relationship, in this case, is related to the pathway of the energy dissipation, which is controlled by the adhesion. Adhesion reduced due to the solvation state, but the small elastic modulus of the polymer leads to a large contact area. Consequently, the DMT contact mechanics model provided a good fit to the data (figure 5.4). The data were fitted using the DMT model and the surface shear strength was calculated as a function of the exposure (figure 5.8a). It is observed that the shear stress τ increased initially as the grafting density decreased and maximum value was recorded for a sample exposed to 0.5 J cm^{-2} . After that point, τ started to decrease. After 2.0 J cm^{-2} no further decrease was observed, and the tip-sample interaction is though to be dominated by ploughing. The distance between grafting points became bigger than the brush height, thus the polymer chains were collapsed and overlapped the nongrafting area. The friction forces were directly related to the applied loads as shown in figure 6 (sample 1.5 and 2.0 doses). The calculated shear stresses (τ) were small enough to be ignored (figure 9a).

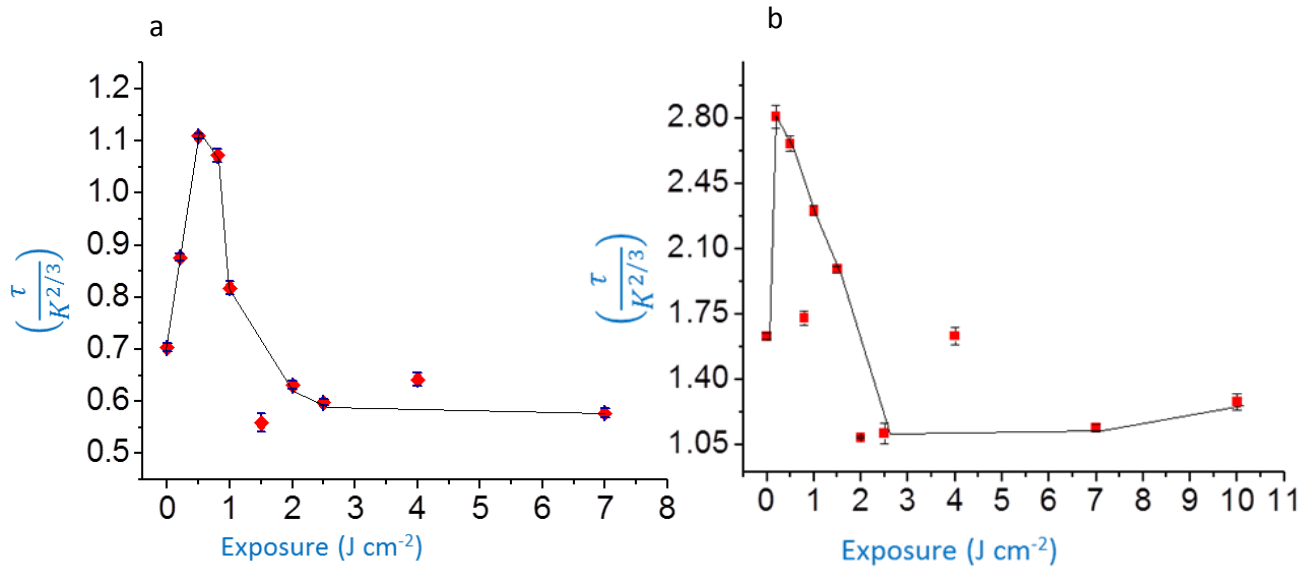


Figure 5.8: The variation in the surface shear strength τ with exposure, (a) shear stress τ as a function of exposure obtained for the gradient brushes in water by using the MUA coated tip. (b) Shear stress τ as a function of exposure obtained for the gradient brushes in water by using gold coated tip. K = elastic modulus.

As the exposure increased above $2.5\ J\ cm^{-2}$ the friction load relationship became nonlinear again. At the large exposure the polymer grafting density is very and the tip-sample contact begins to be dominated by the properties of the underlying substrate.

The results were similar when gold coated tips were applied to measure the friction of the gradient polymer brushes in the same condition. The friction-load relationships were nonlinear for all measurements, regardless of the changing in the grafting density and the data were fitted with the DMT model. Figure 5.8b shows the variation in τ as a function of exposure in which the τ dramatically increased at low exposure regime, after 0.5 dose it sharply decreased and became constant at the high exposure regime. It can be noticed that the values of τ obtained here are twice as big as the τ values for the SAM coated tip. The gold-coated tip has a slightly larger radius so that the area of contact is larger, leads to higher friction force. This could be a reason why adhesion was controlling the tip-sample interaction for measurements.

A linear friction-load relationship was observed in ethanol regardless of the grafting density. This is attributed to collapse brushes and the dissipation energy pathway controlled by molecular deformation. In this case, environmental effects were more considered than the grafting density and chemistry of the surfaces. However, the friction coefficients (μ) were not identical for all the measurements.

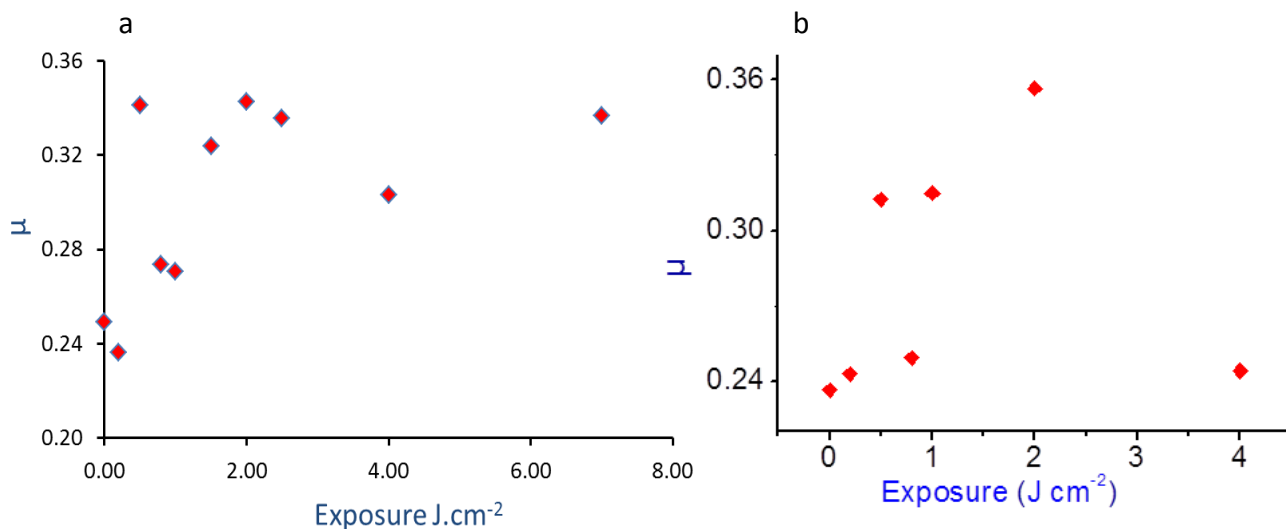


Figure 5.9: Shows variation in the friction coefficients as a function of the exposure for a gradient grafting density of PCysMA brushes in ethanol using a) MUA coated tip and b) gold coated tip.

For PCysMA brushes the coefficient of friction was determined as a function of exposure (figure 5.9a and 5.9b). The value of μ increased as the grafting density decreased until it arrives in 2.0 J cm^{-2} , then it started to decrease at high exposure. Similar results were obtained by using SAM and gold coated tips. We hypothesise that the amount of collapse brush increased as the grafting density decreased, causing a reduced tendency for the brush layers to deform under applied loads. For sample 2.5 -7 J cm^{-2} the μ decreased and then increased, It is believed that 2.5 -3.0 dose was enough to remove most of the active sites on the ATRP initiator. This means that the population of the polymer chains on these samples was almost reduced to zero percent. Consequently, the derbrominated molecules, which remained after the exposure process was contributed in the friction forces and this contribution was increased at the end.

Because of the complexity of the photodegradation processes, the structures of the exposed molecules will not be easy to work out.

5.5 Conclusion

For zwitterionic PCysMA brush prepared with various grafting densities using SI-ATRP and lithographic methods. FFM was used to study the conformational effect on polymer conformation of the grafting densities, using gold and SAM coated AFM tips. It was found that the conformation of the brush is dependent on the grafting density and their local environments. Sublinear friction load relationships were acquired in a good solvent, but this relationship became linear at a very low grafting density. These results suggest that for high coverages, the grafted polymer adopts a brush conformation and the small modulus of the polymer leads to a large area of contact giving rise to adhesive sliding, there is a significant contribution to friction from energy dissipated in shearing. In contrast, as the grafting density decreases the brushes are collapsed and ploughing dominates. This conclusion is supported by modelling the friction-load relationship using DMT model, which provided a good fit to the sub-linear friction-load relationships, while it deviated from the linear relationships. The value of the surface shear strength τ was found to vary with grafting density, initially increasing as the grafting density decreased but decreasing at very low grafting densities. This hypothesis suggests that a transition in the conformation of the polymer chains was occurring from brush to mushroom or coil structures as the grafting density decreases. For the gold coated tip, sublinear friction-load relationships were acquired regardless of the grafting density, and the DMT model provided a good fit to the data.

FFM has also been used to investigate the effect of grafting density on the brush conformation in a poor solvent (ethanol). Linear friction load relationships were observed for all the measurements, regardless of grafting density and the chemistry of the AFM tips. This was rationalised by assuming that the brushes adopt collapsed structures when immersed in ethanol, thus molecular deformation manipulated the contact area between the tip and brush surfaces.

Chapter 6: Investigation of the surface chemistry and morphology on the attachment of mesenchymal stem cells

6.1 Introduction

Advances in molecular patterning have provided researchers with new tools that enable them to design materials with which to study the influence of micrometre and nanometre-scale structure on biological interfacial phenomena such as cellular attachment³⁹³⁻³⁹⁴. It is believed, that when a cell interacts with a surface, membrane receptors sense the properties of the surface, triggering biochemical responses within the cell that influence its behaviour including fundamental cell functions, such as migration, differentiation, proliferation and survival. To facilitate the investigation of these phenomena, the fabrication of model materials with well-defined nanometre scale structure has attracted a great deal of interest. Many researchers have attempted to optimise the cellular response by engineering a spatial pattern or switchable surface, which contains patterned cell adhesive regions surrounded by regions that are non-adhesive to cells^{395,396}. For example, it has been found that cells can be elongated and aligned in the direction of grooves and that cellular migration may be guided³⁹⁷⁻⁴⁰⁰.

Organic thin films have been widely used as a biomaterial suitable to control cell adhesion⁴⁰¹⁻⁴⁰⁴. Jing et al. reported an effective method for cell patterning using self-assembled monolayers. A micrometre scale gold structure was fabricated using a photomask technique. The gold microstructure was functionalized using a monolayer of 1-hexadecanethiol in an aim to create a non-adhesive region, while the glass bars were coated with 3-trimethoxysilyl propyl-diethylenetriamine to promote cell growth. Four different types of cells were successfully patterned on the fabricated surfaces⁴⁰⁵. Mesenchymal stem Cells (MSCs) were patterned on an array of peptides (Arg-Gly-Asp-Ser-Pro), which was created by patterned replacement of the monolayer⁴⁰⁶. Gohara and coworkers investigated cell patterning on a template consisting of micrometre structured of organosilane layer, using photolithography⁴⁰⁷. Despite the potential ease of implementation, widespread application of this strategy may be questionable because of the stability of SAMs is not high, degradation of SAMs may occur upon incubation in a serum-free media at 37 °C⁴⁰⁸. Therefore, a search for alternative strategies has become a major goal for

a number of research groups. Because of the wide range of compositions, they exhibit the availability, processing techniques, their high stability in relatively harsh biological conditions and also their potential for straightforward modification peptides, polymer brushes are attractive materials for applications in which control of biofouling is required⁴⁰⁹⁻⁴¹³. In one study, Klok et al. investigated the stability of non-biofouling poly(ethylene glycol) methacrylate and its effect on cell adhesion and proliferation. SI-ATRP was used to grow the brush on a substrate. The polymer brush showed high stability after being immersed in water/ethanol and PBS for one month, and in culture medium for 10 days. There was no evidence for brush detachment. After modification by attachment of peptide molecules, the brush showed excellent responses toward cell adhesion and spreading⁴¹⁴. To study the change in the differentiation behaviour of the human mesenchymal stem cell (hMSC), various grafting densities of poly[poly(ethylene glycol) methacrylate] (PPEGMA) were prepared using SI-ATRP. The targeted cells were seeded on the surface of polymer brushes to which collagen was immobilised. Due to the change in the grafting density of the brushes the surface elasticity was changed that potentially having an extensive impact on the spreading and adhesion of the cells⁴¹⁵. It has been discovered that most zwitterionic polymer brushes can be considered as biocompatible materials. The antifouling properties in such polymer brushes strongly depend on the control of both uniformity of charge distribution and charge neutrality of two opposite charge moieties on the surface⁴¹⁶⁻⁴¹⁷. Up to 10 nm of a zwitterionic Poly(sulfobetaine methacrylate) (PSBMA) brush was grafted on a substrate using ATRP. After human mesenchymal stem cells (hMSCs) were cultured on the surface, it was found that the rate of the cell proliferation was inhibited by the charged polymeric brush surface⁴¹⁸.

It is widely known that to design a cell-based system, precise control of the features of the polymer brushes at the micrometre and nanometre scale is required⁴¹⁹. The difference in morphological behaviour between fibroblasts cultured on nanogrooved (groove depth: 5–350 nm, width: 20–1000 nm) and smooth polystyrene substrates has been investigated. It was found the cells do not align on a surface with a groove depth of below 35 nm or ridge widths smaller than 100 nm⁴²⁰. Laser interference lithography was used to fabricate periodic line and point micropatterns on a polycarbonate surface.

AFM and XPS were used to characterise the fabricated surfaces. Human pulmonary fibroblasts cultured on micrometre scale patterns consisting of lines showed elongation and orientation along lines with different widths, while no orientation was observed on point-patterned surfaces⁴²¹. Revzin et al. studied the impact of nanotopography and heparin hydrogel microstructure on the cultivation of primary hepatocyte cells. The features were 300 nm deep with pitches of either 400, 1400, or 4000 nm. To create a complex biological cellular microenvironment, the microstructure of the hydrogel was fabricated on the top of the nanopatterned structure. Cell attachment and function were better on 400 nm features than on surfaces consisting of features with larger pitches. Also, cells cultured on complex structures were more functional than the cells attached to the patterned surfaces without the hydrogel⁴²². The influence of the surface morphology and chemistry of polyoligo(ethylene glycol) methacrylate brushes on the adhesion and spreading of hMSC was investigated by Vancso et al. The brushes were grown using ATRP on a poly(ϵ -caprolactone) (PCL) substrate, which heated to the formation of micrometre and sub 100-nanometer structures. The stem cells attached to these patterned brushes adopted different morphologies, responding to the variation in the brushes feature sizes⁴²³. The same cells were cultured on nanopatterned polymethylmethacrylate (pMMA) brushes by Biggs and coworkers. Differences in the adhesion and density of the cells were observed⁴²⁴.

Much work has sought to develop materials capable of directing and controlling cellular behaviour for applications in regenerative medicine and tissue engineering. However, most existing materials exhibit limitations in supporting cell adhesion and growth⁴²⁵. After implantation, most biomaterials exhibit limitations to inflammation and the lack of functional remodelling of the delivered cells⁴²⁶. The mechanisms of interaction between the cells and biomaterials are still not yet fully understood. The present examines a new approach to the design of artificial surfaces for the study of biomaterial-tissue interactions. Interferometric lithography is used to generate periodic nanometre-scale structures for the biocompatible poly(cysteine methacrylate) brush. SI-ATRP was used to grow the polymer brushes from patterned surfaces presenting different initiators. The effect of the surface morphology and chemistry on adhesion, differentiation and proliferation of mesenchymal stem cells (MSCs) are

investigated. The cell type was chosen because MSCs-based therapy is a promising strategy for regenerative medicine and tissue engineering⁴²⁷.

6.2 Experimental Section

6.2.1 Preparation of Silicon Coated Silane Layer

BIBB-APTES ATRP initiator was immobilised on silicon substrates as described in section 3.3. The Synthesis and immobilisation of APTES-NPPOC molecules were described in section 3.5.2 and 3.6 respectively. 4-(chloromethyl)phenyl trichlorosilane self-assembled monolayers (CMPTS) are prepared on a silicon oxide according to the previously recorded procedure⁴²⁸. A clean silicon substrate was immersed in a 2.5 mM solution of CMPTS in dry toluene in a Schlenk tube under a stream of nitrogen for 40 min. After film formation, the wafers were rinsed in toluene and ethanol for 5-10 min and blown dry under nitrogen. Subsequently, the samples were annealed by placing them into the vacuum oven (120 °C) for 40 min. After annealing, the samples were rinsed with ethanol and dried under a stream of nitrogen to remove any contamination.

6.2.2 Photodeprotection of NPPOC-APTES Film and Functionalisation with BIBB

Photodeprotection of NPPOC- APTES- films was carried out as described in section 3.7.3. Prior to performing atom-transfer radical polymerization, the patterned silane substrates were derivatized by immersion a solution of 2-bromoisobutyryl bromide (0.37 mL, 3 mmol) and triethylamine (0.41 mL, 4 mmol) in dichloromethane (DCM; 60 mL) for 40 min. Finally, the samples were sonicated in DCM and ethanol for 5 min and dried under nitrogen.

6.2.3 Synthesis of Cysteine Methacrylate Monomer (CysMA) and Polymerization Reactions

Cysteine methacrylate monomer (CysMA) and PCysMA brushes were prepared according to the procedure in sections 3.5.1 and 3.8, respectively. The polymerization reaction was very slow for CMPTS initiator surface, and a longer reaction time (overnight) was required to yield 7 nm thick brushes.

6.2.4 Surface Analysis

Contact angle measurement, AFM, XPS, and fluorescence microscopy were employed to characterise the prepared surfaces. The details of each method have been described in chapter 3.0.

6.2.5 Photolithography

Micrometre and nanometre-scale photopatterning of the three initiator samples were carried out using a Coherent Innova 300 C FreD Frequency-doubled argon ion laser (coherent U. K, Ely, UK) with an emission wavelength of 244 nm. The laser power was maintained at 100 mW. Micrometre-scale photopatterned ATRP initiators were obtained by irradiation of the samples through a copper electron microscopy grid (2000 mesh, Agar, Cambridge, UK), using doses of 3.5 J cm^{-2} , 4.5 J cm^{-2} and 5.0 J cm^{-2} for BIBB-APTES, CMPTS and APTES-NPPOC surface respectively. The diameter of the illuminated area was 0.5 cm^2 . Nanometre-scale patterns were fabricated by employing Interferometric Lithography (IL) with a power of 1.2 J cm^{-2} , 1.8 J cm^{-2} and 2.0 J cm^{-2} for NPPOC-APTES, APTES-BIBB and CMPTS films respectively. The angle between the two interfered beams was adjusted to be 10° and 30° to form periodic structures, the feature sizes depended on the initiator types. Details of the feature sizes of the structures fabricated can be found in section 3.7.1 and 3.7.3.

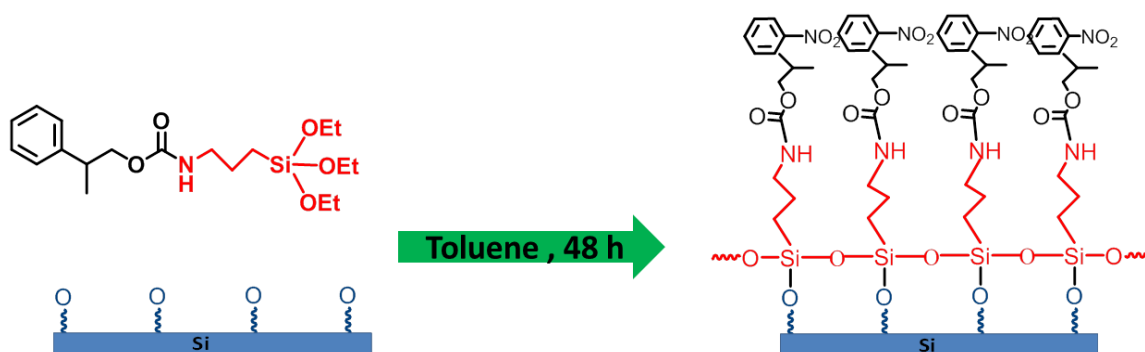
6.2.6 Cell culture

The experimental methodology used to culture mesenchymal stem cells on a patterned surface is described in section 3.10.

6.3 Results and Discussion

6.3.1 Formation of SAMs

2-nitrophenylpropyloxycarbonyl-3-aminotriethoxy silane (NPPOC-APTES) was synthesised (section 3.5.2) then immobilised on a flat silicon dioxide surface (scheme 6.1). To confirm the formation of an APTES-NPPOC film, the functionalized surface was characterised using contact angle measurement, XPS, ellipsometry and AFM.



Scheme 6.1: Schematic diagram showing the formation of an NPPOC-APTES monolayer on a silicon dioxide surface.

The growth of the NPPOC-protected silane film was studied using contact angle measurement and ellipsometry. Figure 6.1a shows the variation in the contact angle as a function of immersion time of the substrate into 1.0 mM of the silane solution. The contact angle dramatically increased at the beginning of the study, reaching $64^{\circ} \pm 3$ after 5h. After that time the rate of change decreased slowly as the immersion time was increased further.

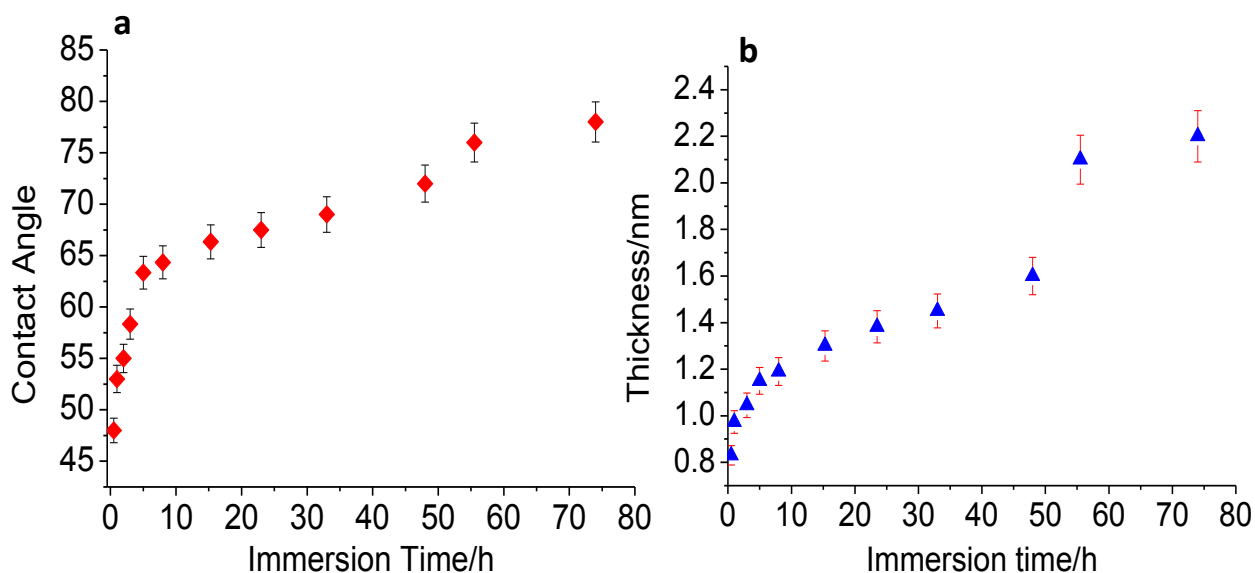


Figure 6.1: (a) Variation in the advancing water contact angle as a function of immersion time of the substrate in the NPPOC-protected silane solution. (b) Variation in the ellipsometric thickness as a function of immersion time of the substrate in a solution of NPPOC-APTES.

A contact angle of $75^{\circ} \pm 3$ was obtained after 48 h immersion time. The change in film thickness was measured as a function of the immersion time by ellipsometry. As shown in figure 6.1b, the thickness increased rapidly at first, but more slowly after 5h. A thickness 1.6 nm was recorded at 48 h, corresponding to the expected thickness of a monolayer. After this point, a significant increase was observed in both the thickness and the contact angle suggesting that a bilayer is formed after longer immersion times.

Following the formation of NPPOC-APTES films, the surface roughness was measured using AFM. The roughness of a complete NPPOC-APTES monolayer after annealing was 0.16/0.18 nm (Ra/Rq), indicating the formation of a smooth continuous silane layer. NPPOC-APTES films were characterised using XPS. The high-resolution C1s spectrum was fitted with three components at binding energies of 285.0 eV, 286.7 eV and 289.15 eV, corresponding to $-\text{C}-\text{C}-$, $-\text{C}-\text{N}-$ / $-\text{C}-\text{O}$ and NCOOR group respectively (figure 6.2a).

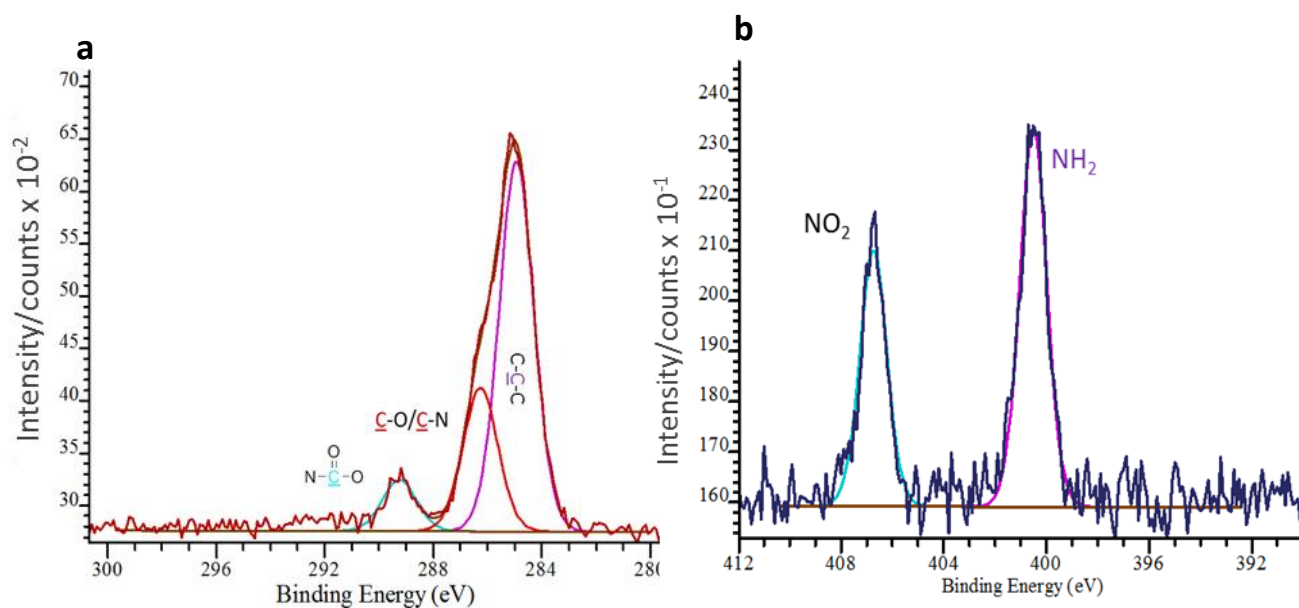


Figure 6.2: High resolution XPS spectra for NPPOC-protected silane surface (a) C1s and (b) N1s spectrum.

The N1s spectrum was fitted with two components at 400.5 eV and 406.78 eV, corresponding to an amino and nitro group respectively figure 6.2b. The calculated ratio of the amino and nitro groups should be 1:1, due to the equal number of these atoms in the silane structure. However, the ratio in the spectrum was measured to be 1:0.89. The most reasonable explanation for this is that some of NPPOC groups were deprotected, due to X-ray exposure within the XPS instrument.

To ensure the formation of high-quality silane film, the CMPTS surface was characterised using contact angle measurement, XPS, ellipsometry and AFM. The contact angle rose from $\leq 3^{\circ} \pm 3$ for a clean silicon wafer to $69^{\circ} \pm 3$ after the formation of a CMPTS monolayer. The result is in close agreement with data found in literature³⁶⁻⁴²⁹ and it is consistent with the formation of the high-quality CMPTS film. Figure 6.3 shows an AFM tapping mode image of a CMPTS monolayer. The roughness was 0.204/0.228 (Ra/Rq). This smooth morphology is consistent with the formation of a well-organized CMPTS monolayer. XPS for C1s and Cl2p spectra are shown in figure 6.4. The high resolution C1s spectrum was fitted with two components at 285.0 eV and 286.858 eV, corresponding to $-\text{C}-\underline{\text{C}}-\text{C}-$ and $-\text{C}-\underline{\text{C}}-\text{Cl}$ respectively (figure 7.4 a).

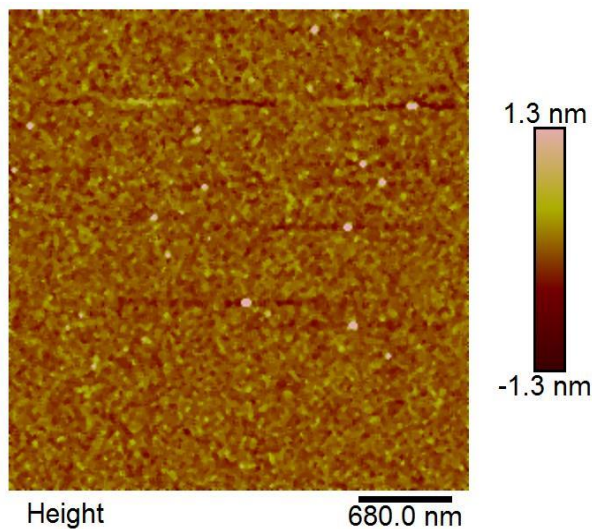


Figure 6.3: AFM tapping mode morphology image for a CMPTS monolayer

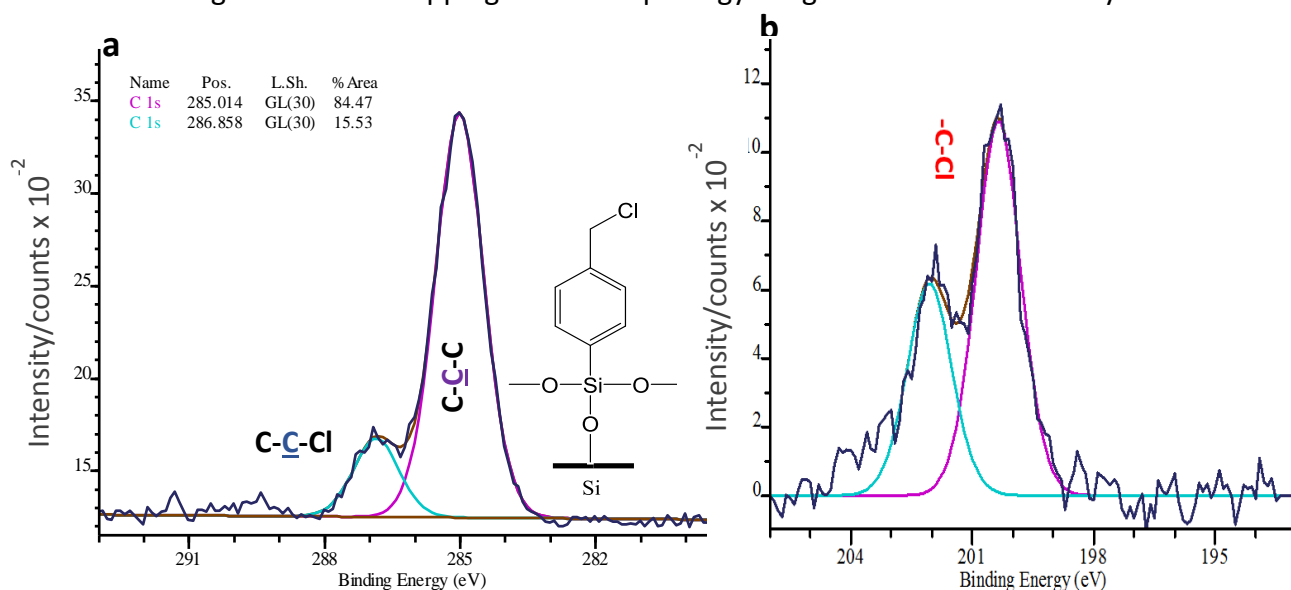


Figure 6.4: (a) The high resolution XPS C1s spectrum and (b) XPS Cl2p high resolution spectrum for a CMPTS film on a silicon dioxide surface.

The percentage area of these peaks was calculated to be 84.47% and 15.53%, in close agreement with the calculated values of 85.72% and 14.28%. Two overlapping components were observed in the Cl2p spectra, because of spin-orbit coupling. The peak was fitted with two components at 200.347 eV and 202.064 eV, which are assigning to $\text{Cl}_{2p_{3/2}}$ and $\text{Cl}_{2p_{1/2}}$ respectively (figure 6.4b).

The characterisation of APTES-BIBB film is described in chapter 4.0.

6.3.2 Photomodification of NPPOC-APTES and CMPTS Films

A study of the kinetics of the photodeprotection of NPPOC-APTES films on silicon surfaces was previously reported by Alang Ahmed et al. at wavelengths of 325 and 365 nm³⁵. Here, 244 nm was used and contact angle measurements were used to monitor the photodeprotection process. Figure 6.5 shows the relationship between contact angle and exposure for an NPPOC-APTES layer exposed to irradiation at 244 nm as a function of dose. It was observed that the contact angle decreased as exposure increased.

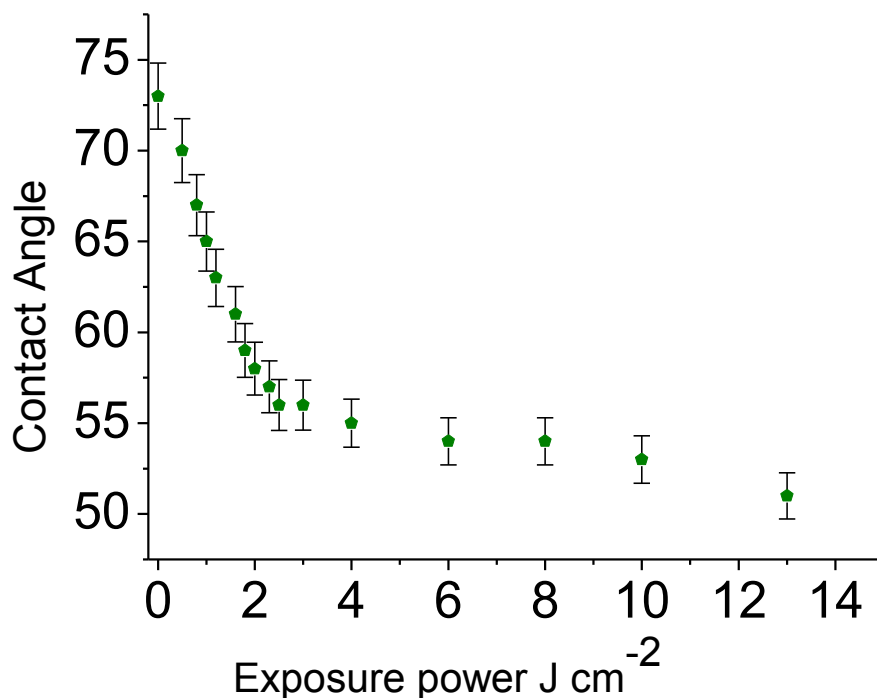
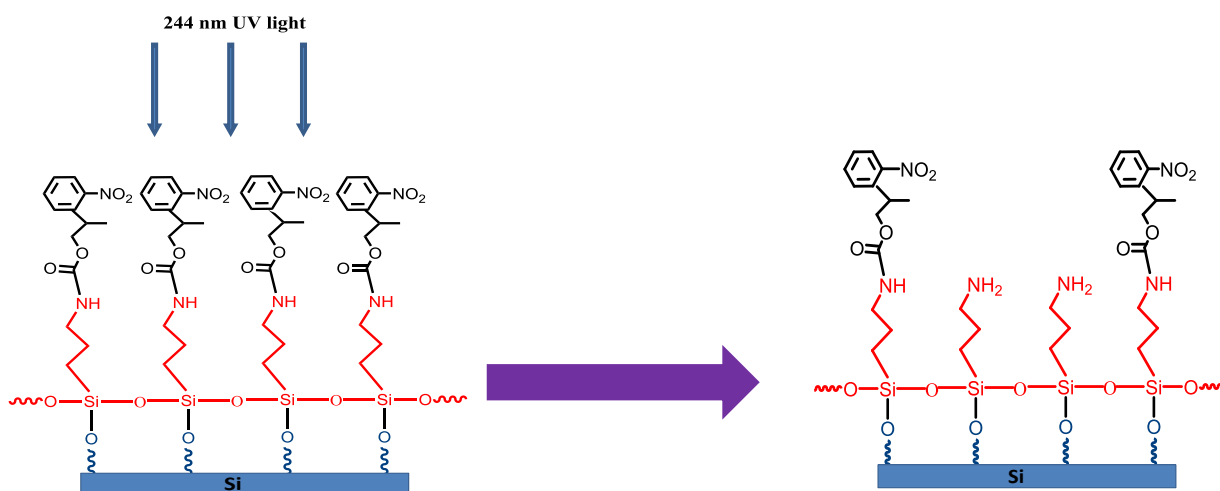


Figure 6.5: The variation in the contact angle as a function of exposure power of 244 nm UV light for an APTES-NPPOC film functionalized on a silicon surface.

This is consistent with the photodeprotection of NPPOC group and the formation of free amine at the surface as shown in the scheme 6.2. The contact angle reached a limiting value at 3.0 J cm⁻², indicating that most of NPPOC group was removed at this point by the exposure, similar to the dose reported by Alang-Ahmed et al. at longer wavelengths.



Scheme 6.2: Schematic diagram showing the photodeprotection of NPPOC-APTES films by exposure to UV light.

XPS was used to characterise a sample of NPPOC-APTES film which exposed at a dose of 3.0 J cm^{-2} (figure 6.6). It can be seen that the NO_2 peak has been lost for the N1s spectrum, leaving a single component at 400.5 eV corresponding to NH_2 species. This confirms completion of the photolysis reaction at that dose.

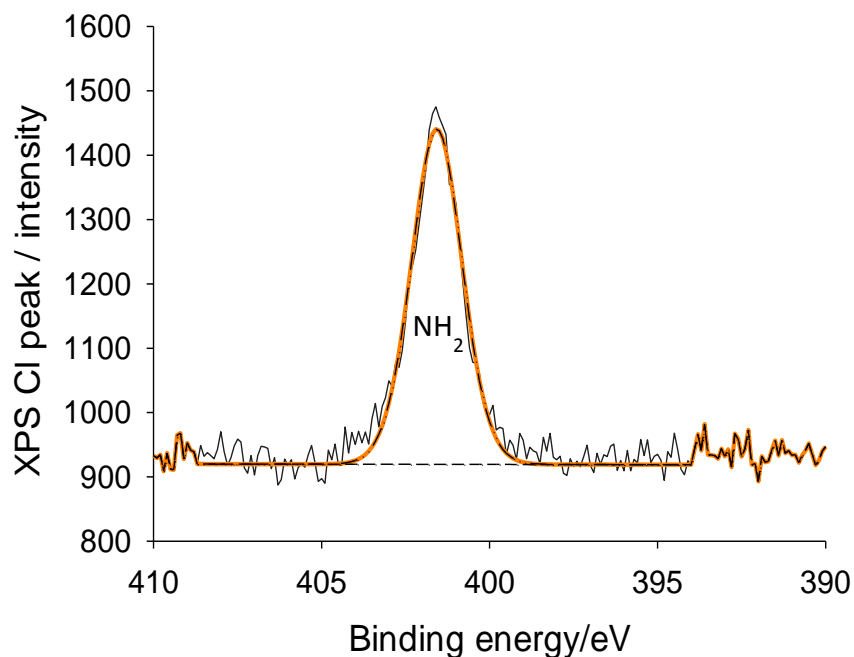
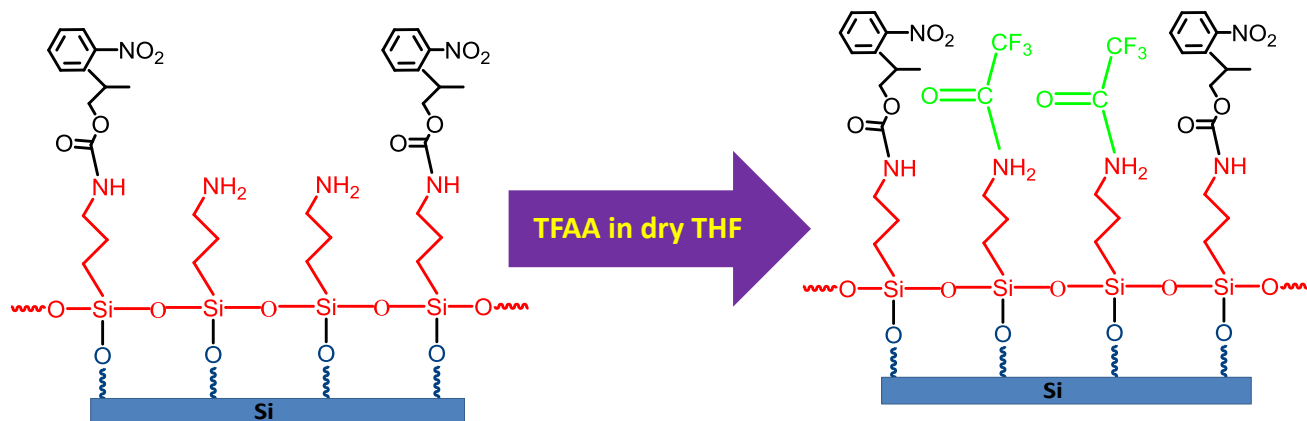


Figure 6.6: XPS N1s XPS spectrum for an APTES-NPPOC monolayer after exposure to a dose of 3.0 J cm^{-2} at 244 nm.

The free amine surface formed by deprotection of NPPOC-APTES film was derivatized by immersing them into a solution of trifluoroacetic anhydride (TFAA) in dry THF (scheme 6.3).



Scheme 6.3: Derivatization of deprotected NPPOC protected aminosilane film by trifluoroacetic anhydride in THF.

The derivatized surface was analysed by contact angle measurement and XPS. The contact angle increased from $55^{\circ} \pm 3$ to $87^{\circ} \pm 3$ after reaction with TFAA, consistent with the derivatisation of a high fraction of the adsorbates, confirming that extensive deprotection had occurred. The high resolution C1s spectrum was fitted with four components at 285.0 eV, 286.45 eV, 288.946 eV and 293.23 eV, corresponding to $\text{-}\underline{\text{C}}\text{-C-C-}$, $\text{-}\underline{\text{C}}\text{-N-}$, $\text{N}\underline{\text{C}}\text{O-C-}$ and F-C-F bonds, respectively (figure 6.7). The peak ratio of the area of the C-N and F-C-F peaks was 1: 0.84, close to the atomic ratio 1:1 expected for a complete monolayer of derivatised adsorbates. These data confirmed the formation of a free amine surface after UV exposure of NPPOC-APTES.

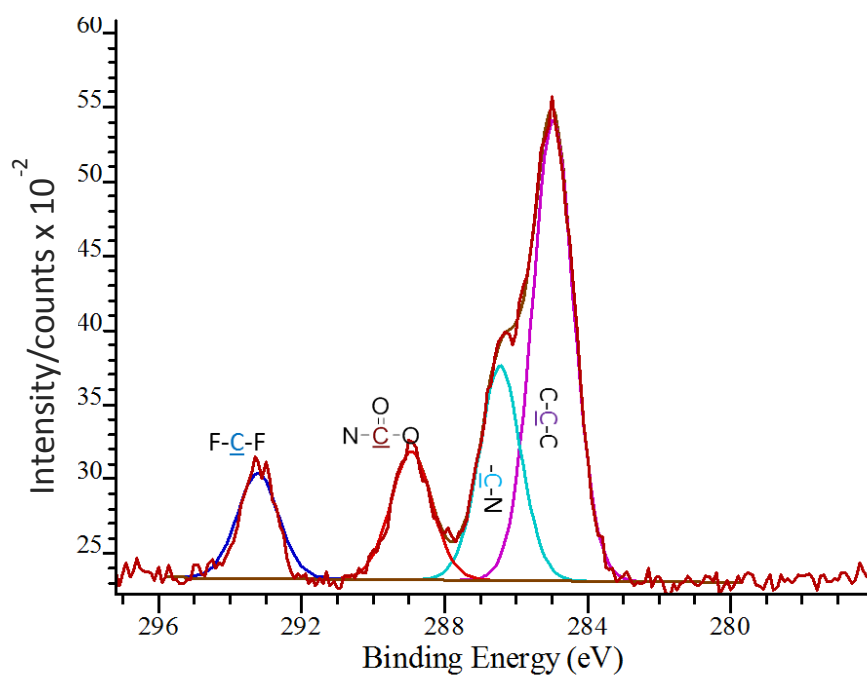
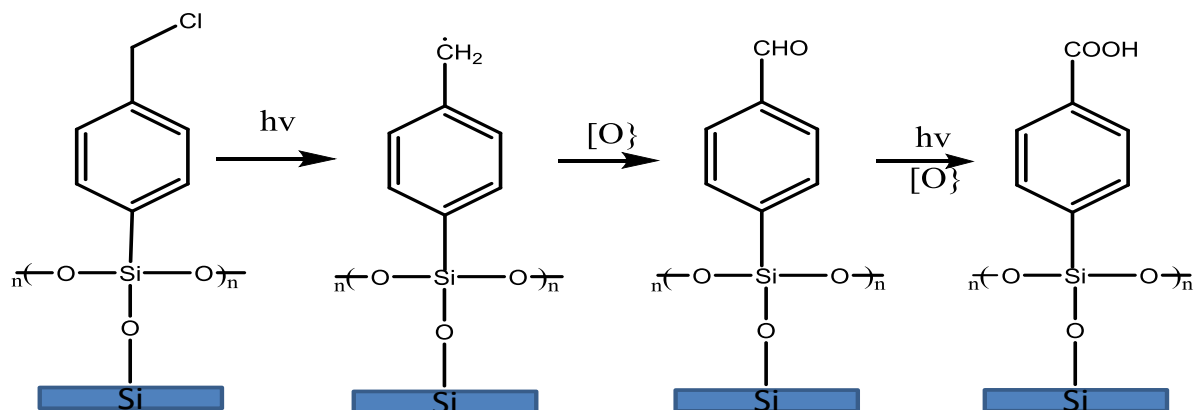


Figure 6.7: Shows high resolution XPS C1s spectra obtained for the TFAA functionalized deprotected NPPOC silane film.

A film formed by the adsorption of CMPTS was exposed to 244 nm UV light at a dose of 4.0 J cm^{-2} according to the previously described procedure. The samples were characterised by contact angle measurement and XPS, to ensure on the formation of high quality CMPTS monolayer.



Scheme 6.4: Mechanism for the radical photo-oxidation reaction of CMPTS monolayers under exposure to UV light where the terminal chlorine groups were oxidised to aldehyde and carboxylic acid groups.

The contact angle was reduced from $70^{\circ} \pm 3$ to $8.0^{\circ} \pm 3$ after exposure, indicating conversion of hydrophobic chlorophenyl terminal groups to hydrophilic groups probably carboxylic acids. Scheme 6.4 shows a mechanism for the photo-oxidation of the chlorophenyl functionalized surface to carboxylic acid surface after exposure to 244 nm UV light, Sun et al⁴³⁰. As seen from the XPS C 1s spectra, a peak appeared at 289.26 eV, attributed to the formation of a carboxylic acid group following photo-oxidation of chlorine atom (figure 6.8). As seen a new peak was also observed at 286.7, which is attributed to $\text{-}\underline{\text{C}}\text{-C-O}$ bond.

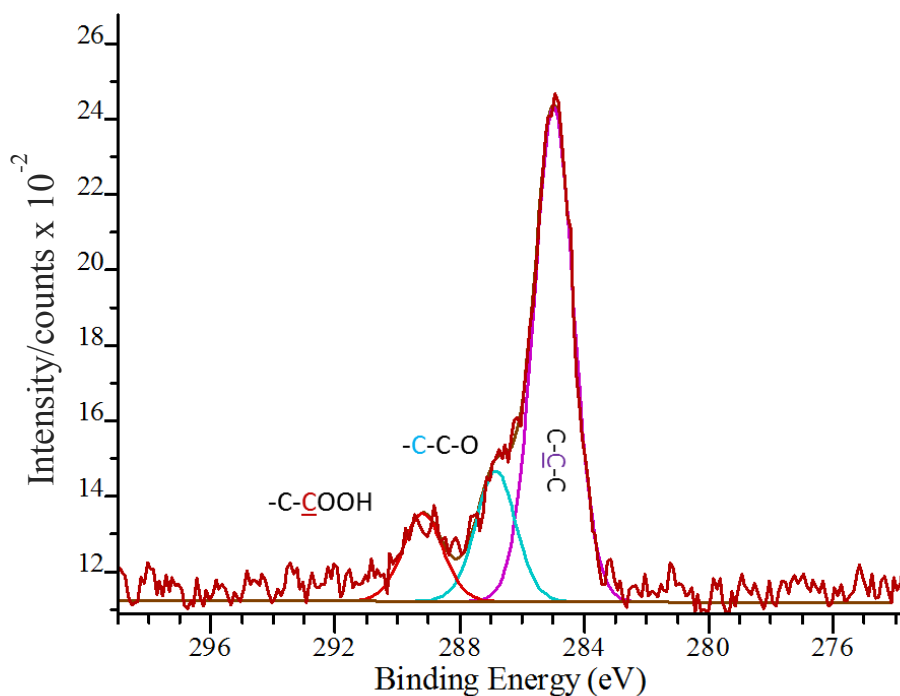


Figure 6.8: High resolution XPS C1s spectrum obtained for photo-oxidised CMPTS film after an exposure of 4.0 J cm^{-2} .

This was further confirmed by the absence of a Cl 2p peak as shown in figure 6.9.

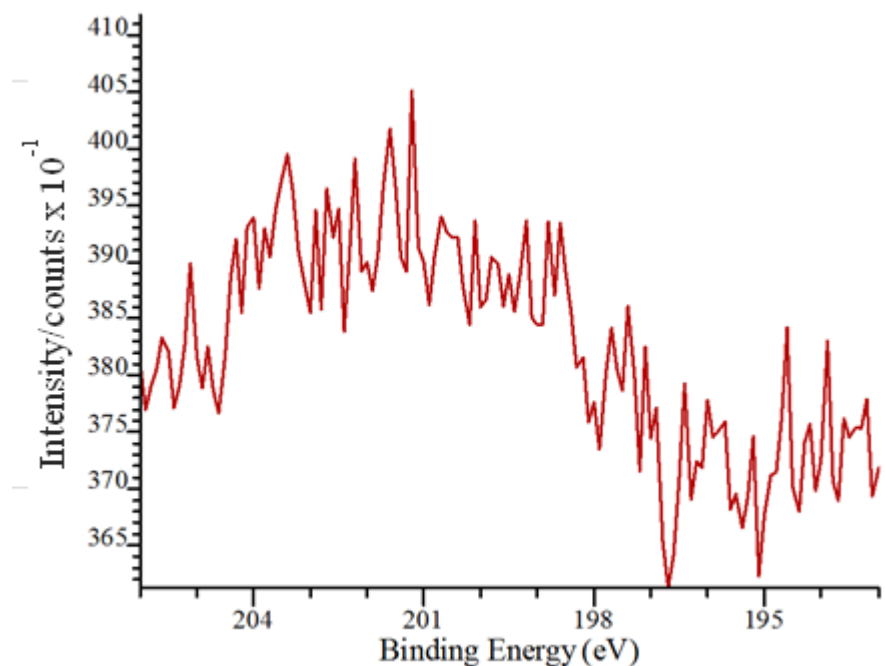
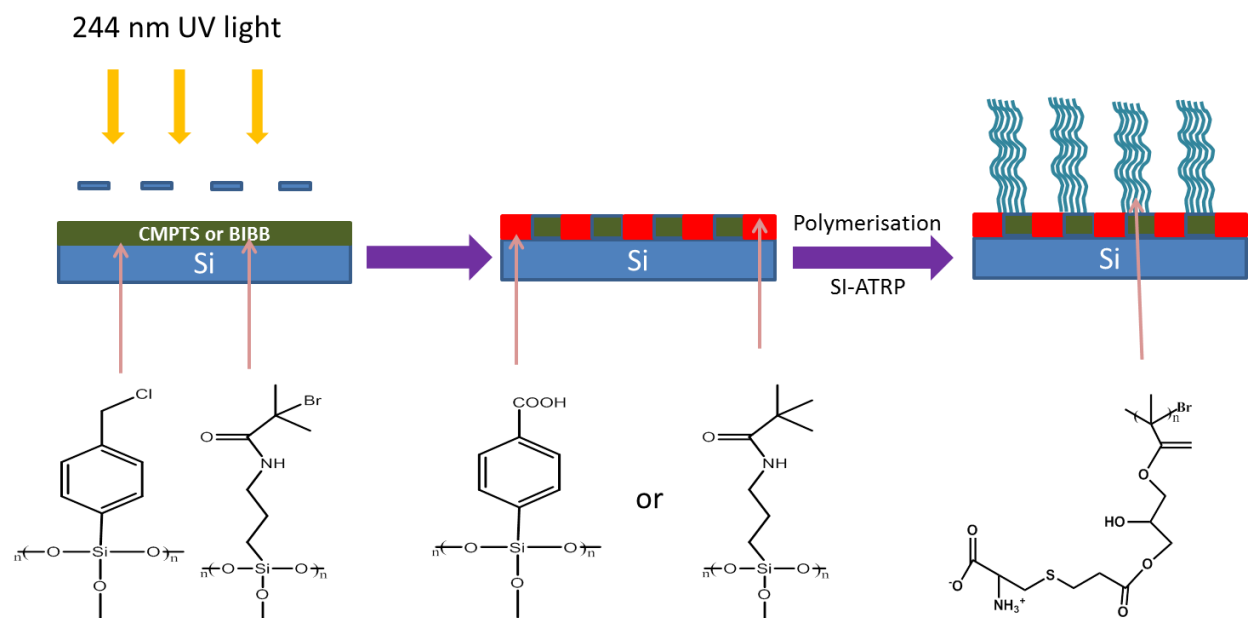


Figure 6.9: XPS Cl_{2p} peak after exposure of a CMPTS film to 4.0 J cm⁻² of UV irradiation.

Photo-debromination of an APTES-BIBB film using 244 nm of UV light was also carried out as described in chapter 4 and 5.

6.4 Formation of PolyCysMA brushes on the patterned CMPTS and APTES-BIBB SAMs



Scheme 6.5: Schematic diagram showing the growth of PCysMA brushes from a template formed by photopatterning either a CMPTS or an APTES-BIBB film.

PCysMA brushes were grown from the unexposed regions of patterned CMPTS films using SI-ATRP. The terminal chlorine group may be used as an initiator for ATRP. In contrast, polymer does not grow from carboxylic acid terminal groups in exposed regions because there is no initiator there. Figure 6.10 shows an AFM tapping mode image of a micrometre-scale PCysMA brush pattern which was formed on a patterned CMPTS template using SI-ATRP.

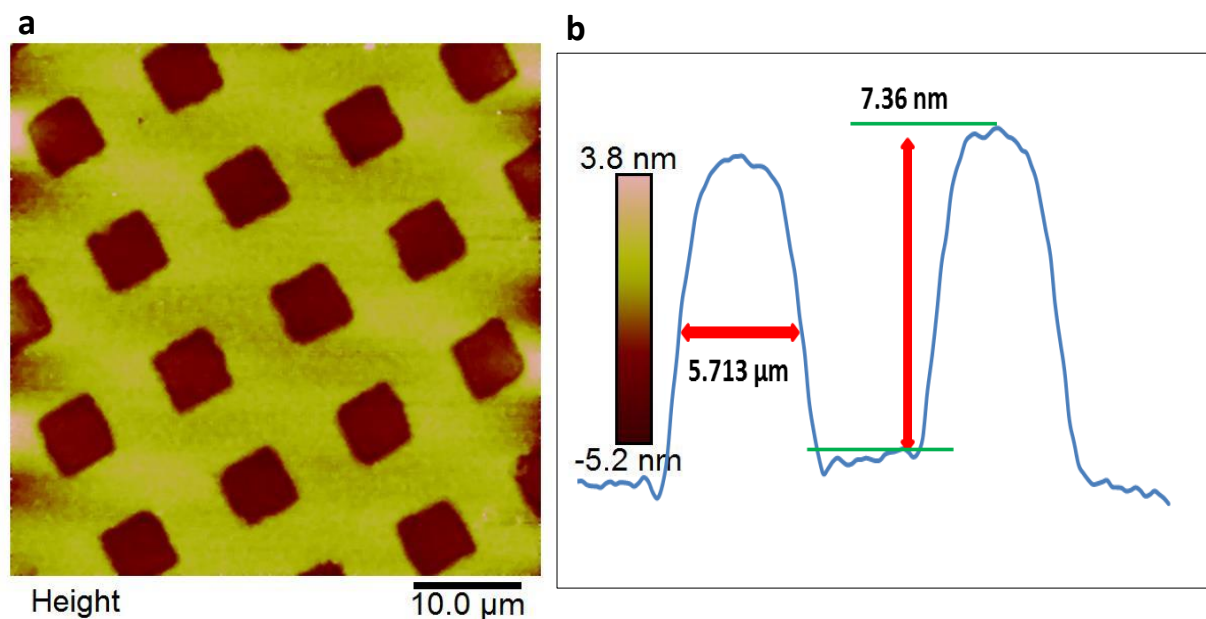


Figure 6.10: (a) AFM tapping mode height image of a micrometre-scale PolyCysMA brush pattern grown from a micropatterned CMPTS film and (b) corresponding line section was taken at the centre of the image.

From the line section, the height difference between the exposed and masked regions (bars and squares respectively) was found to be 7.36 nm, the same as the thickness of a continuous, unpatterned brush grown under the same conditions, confirming complete removal of initiator for the exposed regions.

Nanometre-scale PolyCysMA brushes were also fabricated using CMPTS films. Interference lithography (IL) was used to expose the SAM. Photolysis of the terminal chlorophenyl group to the carboxylic acid group was expected to occur in the regions that were exposed to maxima in the interferogram. In contrast, in the regions were exposed to the minima in the interferogram the chlorine groups were expected to be retained. Polymer brushes were selectively grown on

the chlorinated regions. Figure 6.11 shows AFM tapping mode topography images after ATRP on IL-patterned CMPTS films where the angle in the interference was set to 10° (a) and 30° (b).

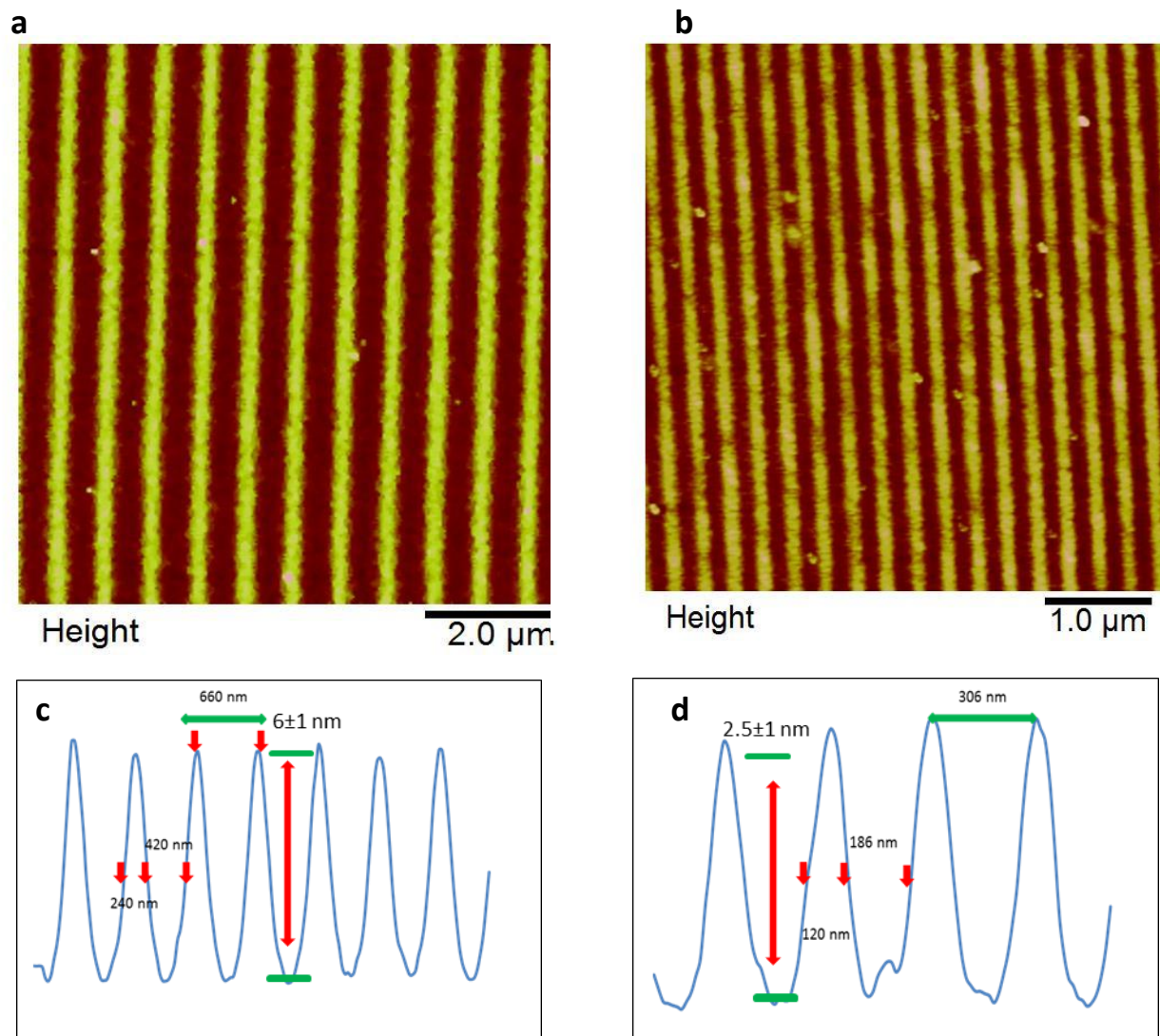


Figure 6.11: AFM tapping mode topographical images obtained from nanometre-scale patterned PCysMA brushes grown from CMPTS exposed to a dose of 1.8 J cm^{-2} using an angle of (a) 10° and (b) 30° . Corresponding line-sections are shown beneath each image.

The period of the polymer lines was measured to be 660 nm and 306 nm for 10° and 30° samples, respectively. The FWHM for the polymer features was 240 nm for 10° and 120 nm for 30° samples. Thus reducing the angle from 10° to 30° effectively doubles the period and halves the width of the resulting brush structures.

Micrometre-scale patterns were also formed by exposing an APTES-BIBB sample through a 2000 mesh copper grid. Debromination occurred in the illuminated regions (squares), while in the masked regions (bars), the bromine remained largely intact at the surface (figure 7.12). After lithography PCysMA brushes were grown by ATRP

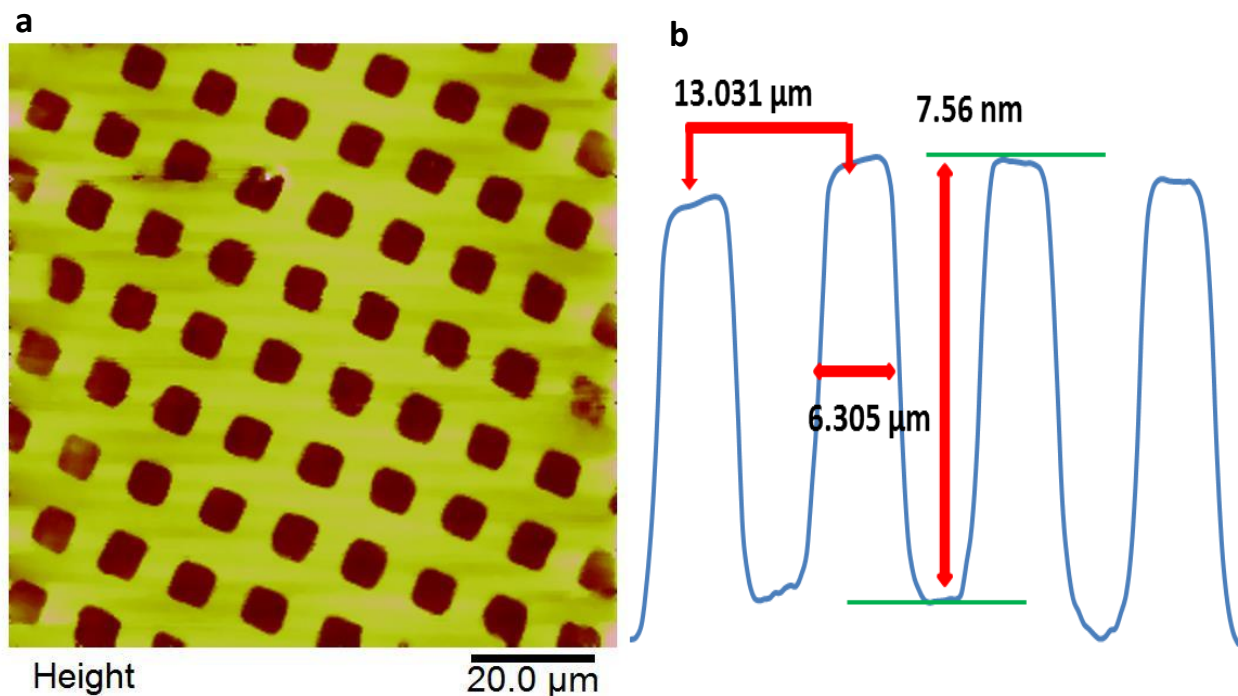


Figure 6.12: (a) AFM tapping mode height image of a micrometre-scale PCysMA brush pattern using an exposure of 3.5 J cm^{-2} through a mask. (b) Corresponding line section was taken at the centre of the image.

The height between masked and unmasked regions was 7.56 nm, confirming that a complete brush film was formed in the masked regions while polymerisation was prevented in the exposed areas. For nanometre fabrications two beam interferometer was used to expose the APTES-BIBB film, using angles of 10° and 30° (figure 6.13). It can be seen that as the angle increased the feature sizes decreased. For the smaller angle, the period was 663 nm while it was reduced to 296 nm for the larger angle (figure 6.13c and d). At 10° the FWHM of the polymer structures was 270 nm, and this decreased to 137 nm, with a period of 296 nm, at the larger angle.

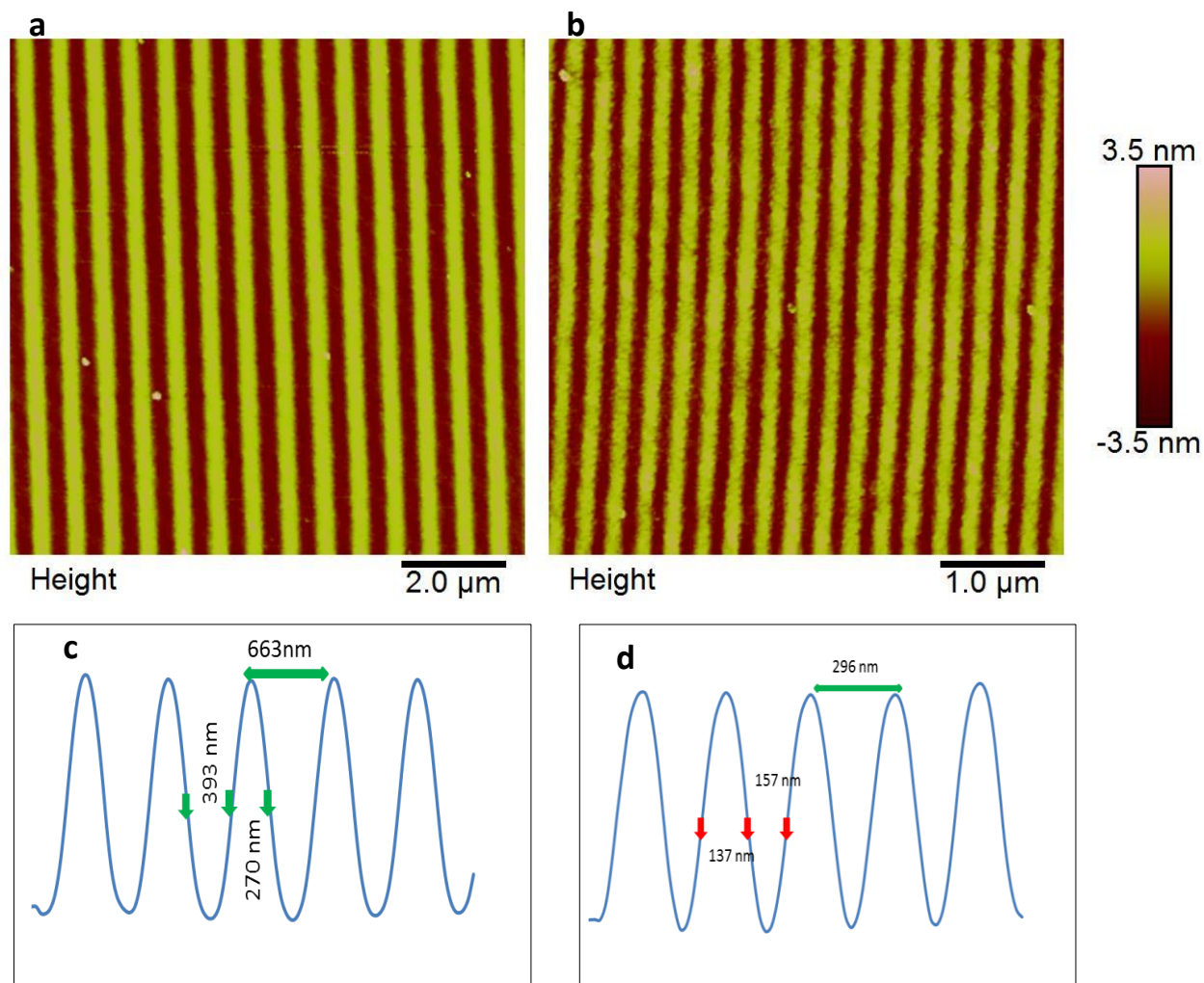
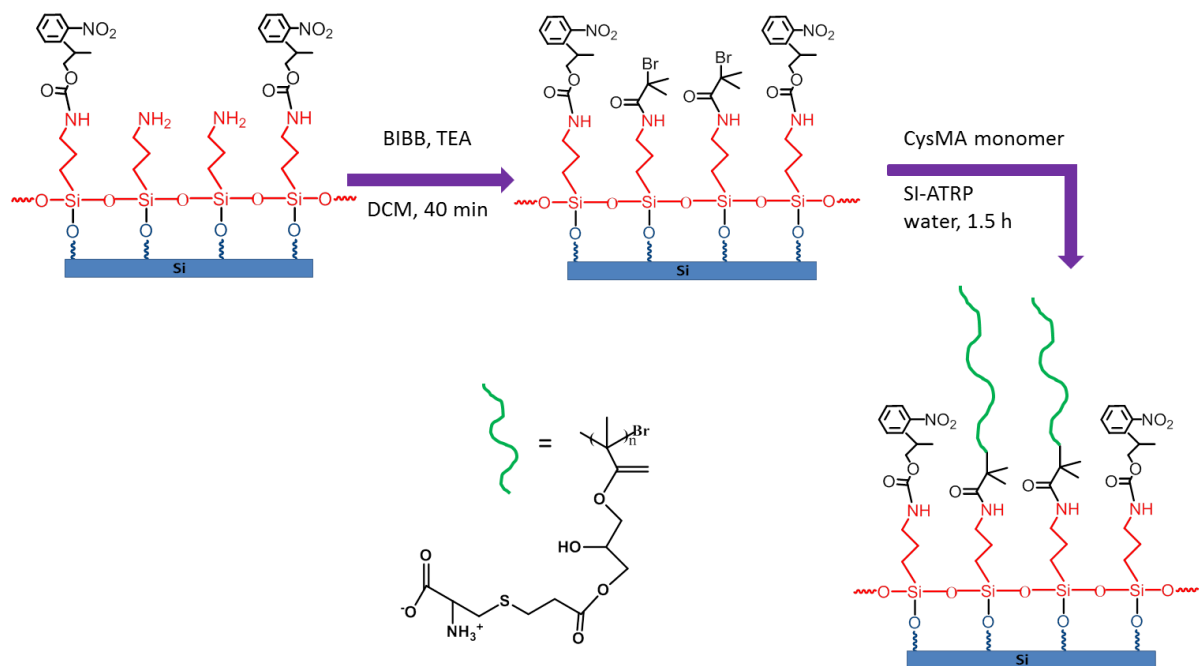


Figure 6.13: AFM tapping mode topographical images obtained from nanometre-scale patterned PCysMA brushes grown from BIBB initiator surface exposed to a dose of 1.8 J cm^{-2} using an angle of (a) 10° and (b) 30° . Corresponding line-sections are shown under each image.

6.5 Formation of PCysMA brushes on patterned NPPOC-APTES films

NPPOC-APTES films were deprotected by exposure to UV light through a mask or IL. The terminal amine groups in the exposed regions were functionalised with 2-bromoisobutyryl bromide to form a halogen terminated surface that could be used as an ATRP initiator (scheme 6.6).



Scheme 6.6: Schematic diagram showing the growth of PCysMA from a patterned NPOOC-protected aminosilane film. The SAM was exposed to UV light through a mask, causing the removal of the NPOOC groups from the exposed regions. After derivatisation of exposed amines by reaction with BIBB, brushes were grown from the exposed areas.

To confirm that the free amine groups were successfully functionalized with BIBB molecules, an NPOOC-APTES film was fully deprotected using 244 nm UV light at a dose of 3.0 J cm^{-2} . The deprotected surface was derivatized with BIBB molecules and analysed by contact angle measurements and XPS. The contact angle of 75.0 ± 3 for a uniform surface was reduced to 56.0 ± 3 after photodeprotection, and then it was increased to 67.0 ± 3 following the halogenation reaction.

The high resolution C1s spectra were fitted with three components at binding energies of 285.0 eV, 286.75 eV and 288.78 eV, corresponding to $-\text{C}-\text{C}-\text{C}$, $\text{C}-\text{N}/\text{C}-\text{Br}$ and NCO bonds (figure 6.14). The observation for a new C-Br component is evidence of derivatisation by BIBB. A PCysMA brush was grown on the fully modified for 2 h, and a thickness of 7.0 nm was determined by ellipsometry.

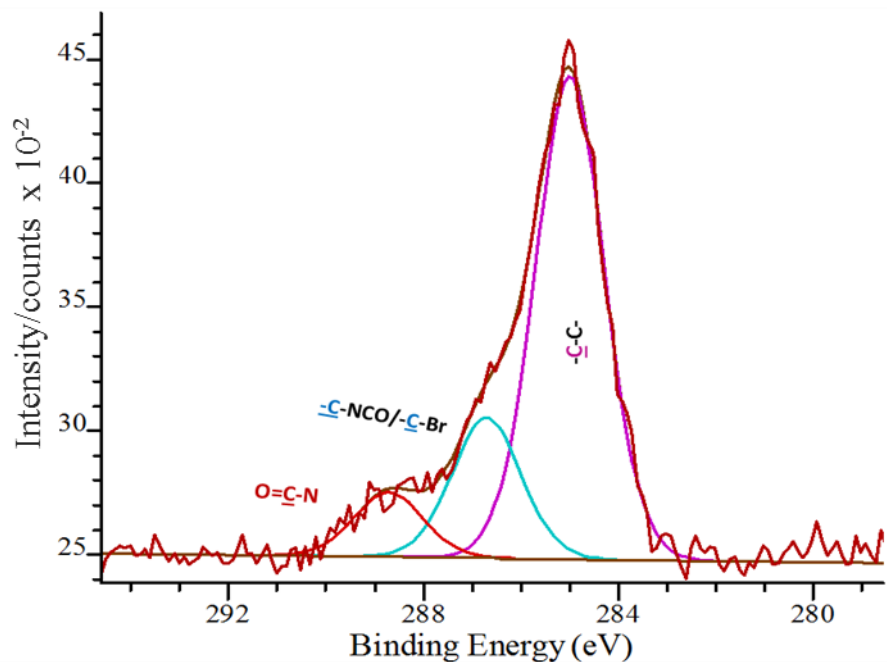


Figure 6.14: High resolution C1s spectra obtained for a photodeprotected NPPOC aminosilane film after being functionalized with BIBB molecules.

Micrometre-scale patterns were formed by carrying out exposure through a 2000 mesh grid using photomask. The exposed (square) regions were derivatised with BIBB and SI-ATRP was performed to grow PolyCysMA brush. The patterned sample was characterised using tapping mode AFM (figure 6.15). Cross-sectional analysis revealed a clear height contrast between the brush regions (squares) and NPPOC regions (bars), confirming the spatially selective growth of the polymer brushes.

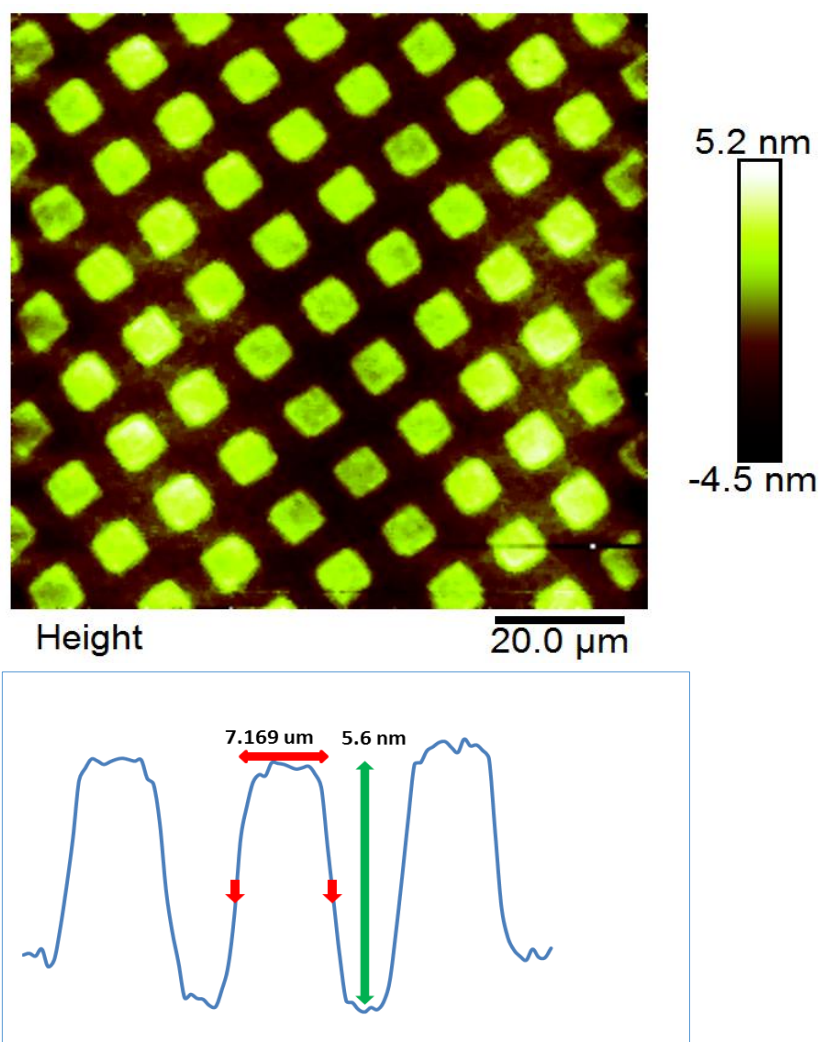


Figure 6.15: AFM tapping mode topographical image of a micropatterned PCysMA brush grown on a patterned NPPOC-APTES film via SI-ATRP.

To form nanometre structures a two beam interferometer was used to expose NPPOC films at angles of 10° and 30° . Figure 6.16 shows AFM tapping mode height images obtained for these patterns. In regions exposed to a maximum in the interferometer, deprotection of the terminal NPPOC group occurred and after halogenation polymer brushes were grown from these regions. In regions were exposed to a minimum in the interferometer, the protecting group remained intact and inhibited growth of the polymer brush. Cross-section analysis showed that the polymeric regions in these patterns were wider than the unmodified regions.

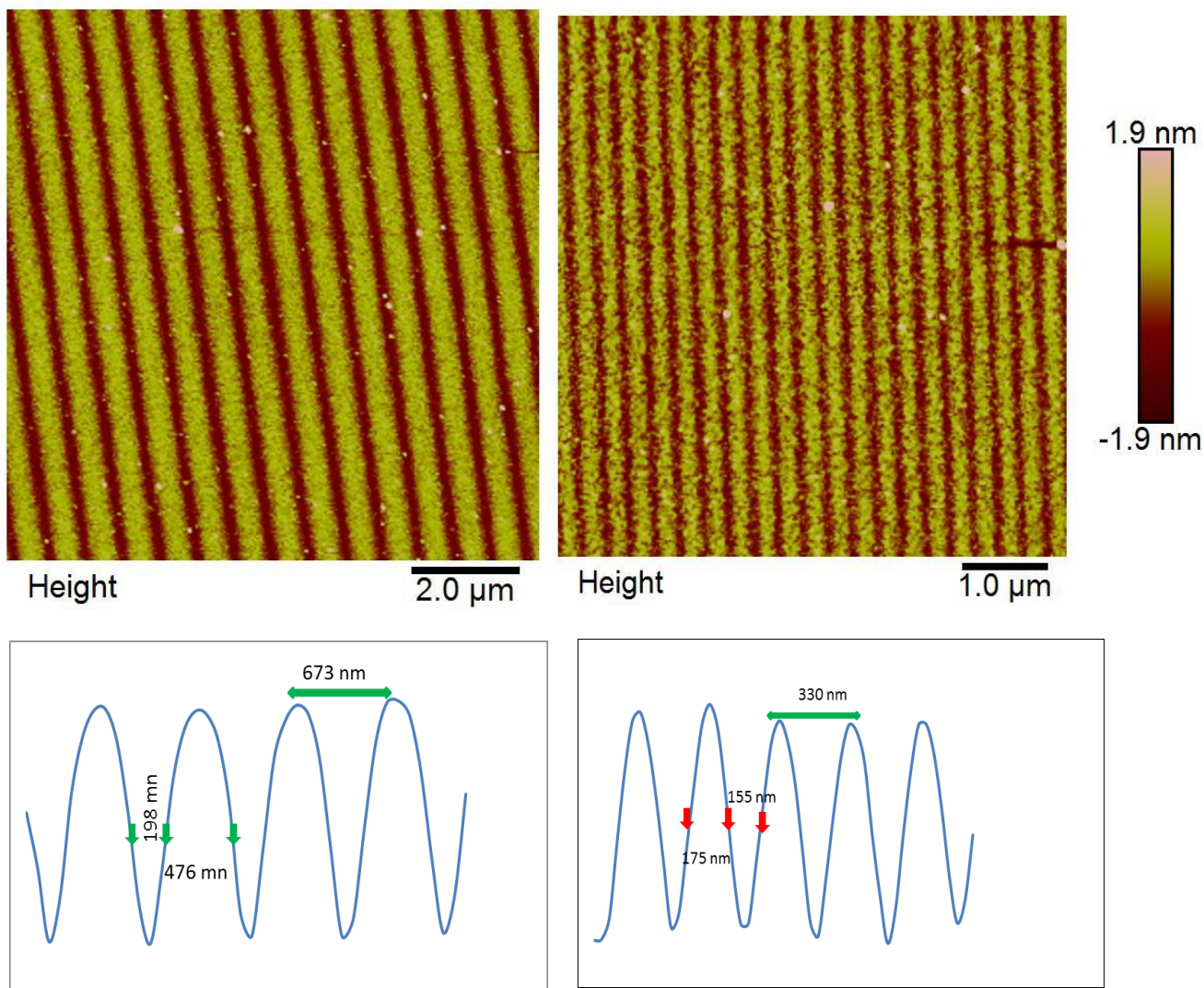


Figure 6.16: AFM tapping mode topographical images obtained from nanopatterned PCysMA brushes on NPPOC-protected silane surfaces exposed to 244 nm UV light with a dose of 1.2 J cm^{-2} using an angle of (a) 10° and (b) 30° . Corresponding line sections are shown beneath each image.

The periods of the features were 673 nm and 330 nm for films patterned at 10° and 30° respectively. At 10° the FWHM of the brush line is 476 nm, more than twice the width of the polymer free region 198 nm FWHM. However, such big difference was not observed in the 30° feature sizes, for which the FWHM of both polymer and nonpolymer lines are almost identical.

6.6 Culture of human mesenchymal stem cells (hMSC) on patterned polymer brushes

MSCs were seeded on the homogenous polymer brushes grown from BIBB-APTES, CMPTS and brominated deprotected-NPPOC films. After 7 days of cultivation, no cells were observed on any of the three polymer surfaces (figure 6.17), demonstrating the excellent nonbiofouling property of the brush. These results are consistent with those of Alswieleh et al²⁸⁴.

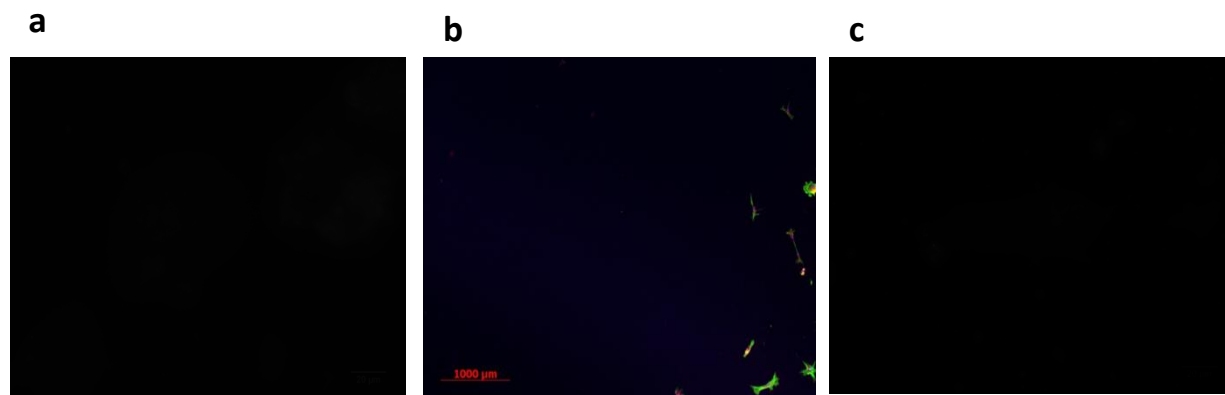


Figure 6.17: Fluorescence microscopy images obtained for PolyCysMA brushes subjected to a stem cell challenge. The brushes were grown on (a) APTES-BIBB, (b) CMPTS and (d) deprotected-NPPOC silane film.

MSCs were also cultivated on nanopatterned brushes. The patterned samples consisted of regions occupied by PCysMA brushes, which are protein and cell resistant, separated by adhesive regions. It is expected that cells will not attach to the brushes, but they may attach to the regions between the brush features. The culture medium contained serum proteins that would be expected to adsorb to polymer free regions. Membrane receptors will interact with these proteins. The particular importance in cell attachment is the integrin receptors⁴³¹, which bind to cell adhesion molecules, especially fibronectin and vitronectin but also other serum proteins. The mechanistic relationship between the serum proteins and cell attachment has been investigated before⁴³². It was found that there is no simple correlation between the amount of adsorbed proteins and the mechanism of cell attachment, but there must be enough of serum proteins in the medium the cell attachment process to be successful.

Successful attachment is followed by the formation of focal contacts and the polymerisation of actin to form filaments that are anchored at their ends by focal adhesions. Thus, the thickness and directions of these actin stress fibres can be used to characterise the response of the cells to the polymer morphology and to the chemistry of the adhesive regions.

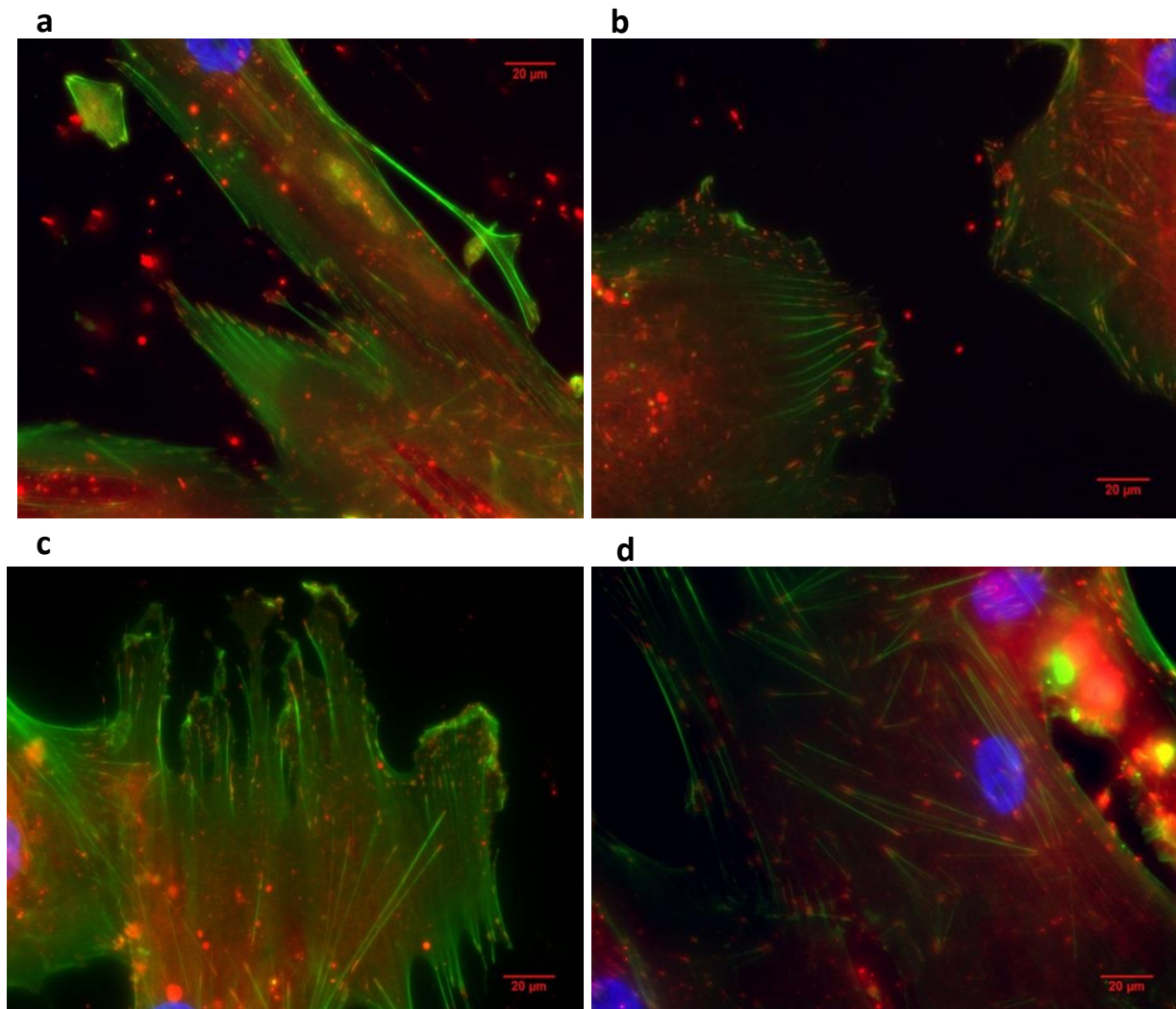


Figure 6.18: Fluorescence microscopy images obtained for nanopatterned PCysMA brush grown from patterned BIBB-APTES initiator. It was carried out at 10° (a) and (b) and at 30° (c) and (d).

Figure 6.18 shows fluorescence microscopy images obtained for MSCs grown on nanopatterned PCysMA brushes formed by IL at angles of 10° and 30° after 7 days culture.

The cells attach successfully on the both samples. Actin is stained green and long stress fibres may be seen in all images.

For the 30° sample, the stress fibres appear in general to align parallel to the direction of the features in the underlying nanostructures. This suggests that the patterning of the surface is influencing the way that the cells attach. Vinculin, a protein that is recruited into focal adhesions during the attachment process is stained red using a labelled monoclonal antibody. The focal adhesions are in many cases needle-like.

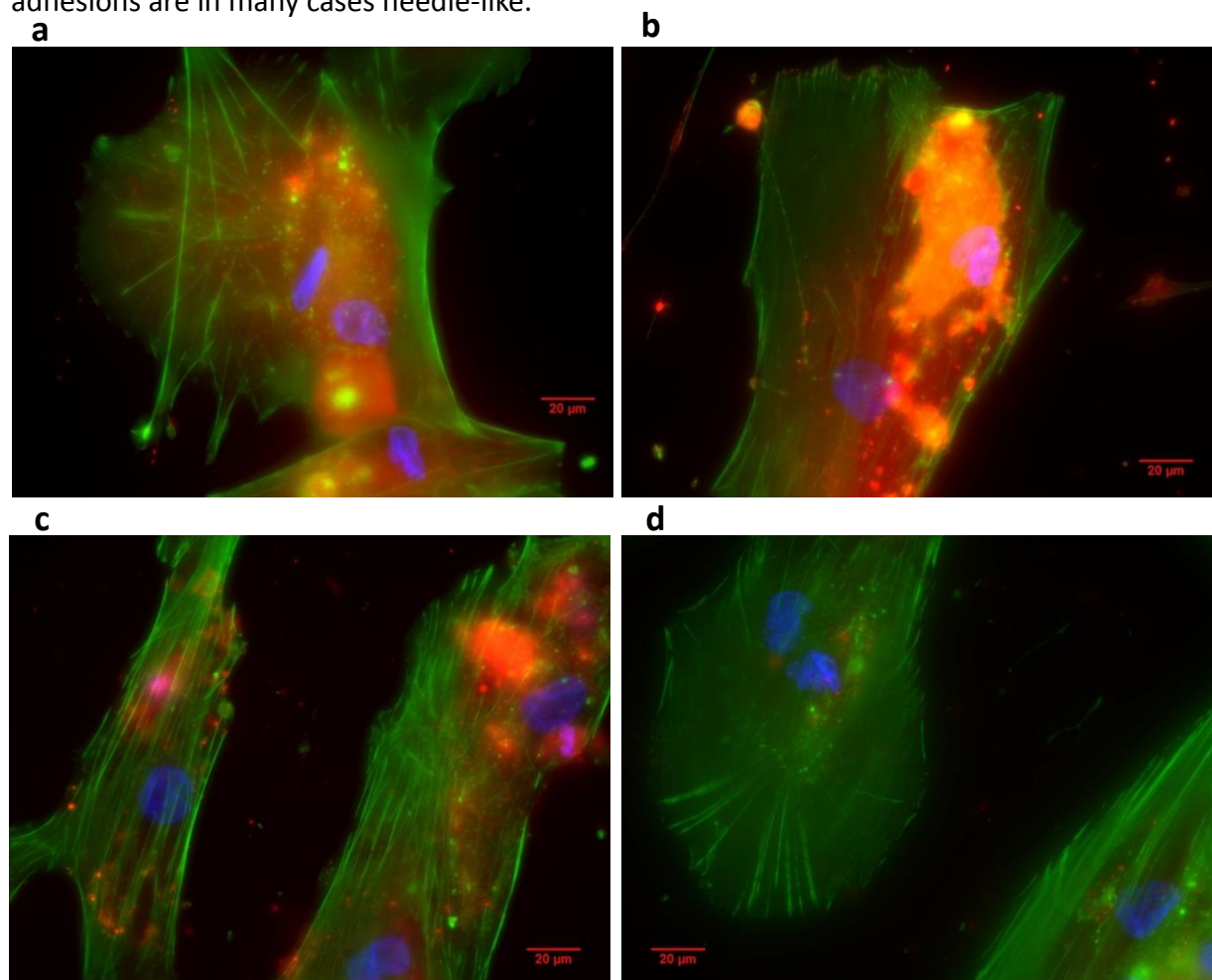


Figure 6.19: Fluorescence microscopy images obtained for nanopatterned PCysMA brushes grown from patterned CMPTS films. It was carried out at 10° (a) and (b) and at 30° (c) and (d). There is much more directional in the 30° samples.

They are observed at the leading edges of the cytoplasm, suggesting that the cells are still motile that the degree of alignment increases with increasing time.

However, the alignment and organisation of the cells on 10o sample are less pronounced that is the case at 30o sample. Clearly the structures formed at 10° are significantly broader (in terms of the period at the FWHM of the polymer structures) and this appears to lead to a reduction in the influence of the surface morphology.

For brushes grown from CMPTS samples patterned at 10° and 30° the orientation and distribution of the focal adhesion is different, labelling of vinculin suggests that they are rounder and less well-defined, but the cells attach successfully and there are pronounced actin filaments (figure 6.19).

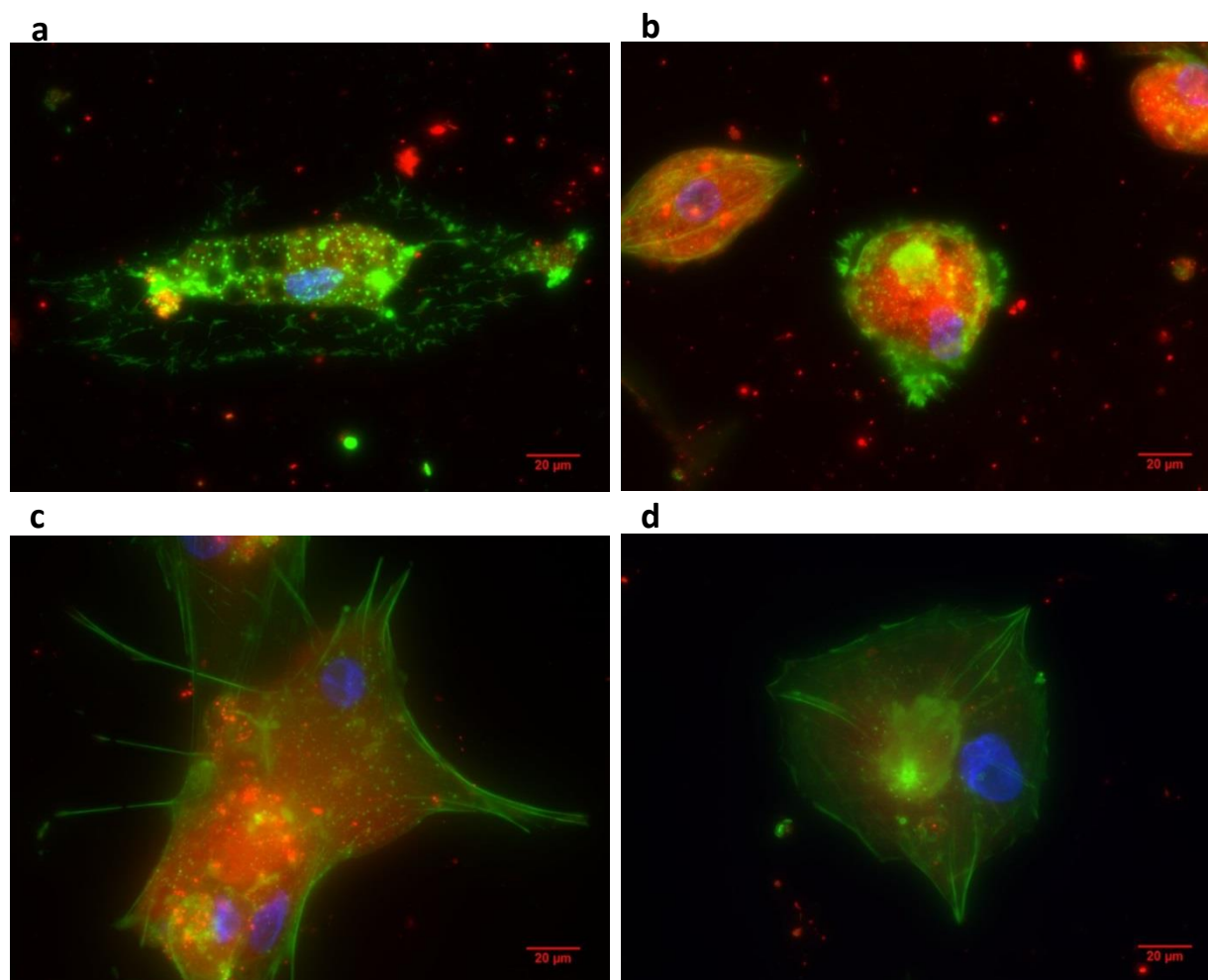


Figure 6.20: Fluorescence microscopy images obtained for nanpatterned PCysMA brushes grown from the deprotected NPPOC-APTES film. It was carried out at 10° (a) and (b) and at 30° (c) and (d).

For these samples, the surface chemistry of the brush-free regions is highly polar (dehalogenation of CMPTS leads to the formation of carboxylic acid groups). This may yield a difference in the composition of the layer of adsorbed protein and hence to the cellular response. The width of the carboxylic acid (hydrophilic) region is twice that of the polymer region, suggesting that the membrane receptors recognize a large number of adhesive molecules, which guiding the focal adhesions into different directions.

As can be seen from figures 6.19 and 6.20, the size of the focal adhesions depends on the sizes of the adhesion zones. On the small adhesion zones (30°) the focal adhesions are small and point-like, and polymerised actin filaments are finger-like with a high concentration which follow the direction of the cell growth. For these samples there is a large number of narrow nonpolymer lines, which allowed the cell to form a large number small closely spaced focal adhesions. Consequently, there is a high concentration of the filaments that follows on the direction of the patterned lines. In contrast, on samples with a larger period (10°), the adhesive zones are much wider and further apart which leads the cells to distribute the filaments randomly, rather than following the direction of the patterned lines.

On deprotected-NPPOC samples, the chemistry and morphology of the nanostructured surfaces are different from the other samples. The widths of the polymer lines are larger than the width of the adhesive regions (figure 6.20). The cells attach less successfully, and it is clear that there is a difference in the size and shape of the focal adhesions

As shown in the figure 6.20, the focal contacts are much rounder and fewer especially on 10° NPPOC compared to other samples.

6.7 Conclusion

NPPOC-protected aminosilane, CMPTS and APTES-BIBB films were fabricated and characterised using contact angle and XPS. The photodeprotection kinetics of NPPOC-APTES, photo-oxidation of CMPTS and photodebromination of APTES-BIBB layers were studied using contact angle measurements and XPS. The reactivity of photodeprotected NPPOC-APTES surface was studied, it was reacted with TFAA molecules, the contact angle and XPS revealed high quality of the functionalised surface. The results were found to be in close agreement with those found in the literature. Nanometre and micrometre-scale patterns were successfully formed using IL and photomask lithography. The patterned regions of NPPOC-protected silane film were functionalised with BIBB molecules in order to be used as ATRP initiators. PCysMA brushes were grown on the patterned surfaces using SI-ATRP, the polymerised surfaces were characterised using AFM and Ellipsometry. It was found that CMPTS can be used as an ATRP initiator and both the width of the lines and the periodicity of the patterns were shown to be easily controlled by changing the angle in the Lloyd's mirror. Mesenchymal stem cells were seeded onto nanometre patterned PCysMA brushes and cultured for seven days. Fluorescence microscopy was used to characterise the alignment and organisation of MSCs on the nanostructured and uniform brushes. It was found that both chemistry and morphology play an important role in changes in the distribution of focal adhesions and in the directionality of the actin filaments. No cells were found to attach to the uniform brushes, suggesting a high resistance of the brushes to cells. For 30° BIBB and CMPTS samples cells successfully attached, forming long and thin stress fibres that followed the direction of the features of the BIBB sample. For nanostructured brushes grafting from BIBB-APTES and CMPTS exposed at 10° there was evidence of attachment and organisation of the cells, but the focal adhesions were less well defined and randomly distributed on the surfaces. For NPPOC-APTES exposed at 30° and especially 10° patterned samples the cells attached less successfully suggesting that the wider cell resistant brush structures made it harder for cells to attach and form focal adhesions.

Chapter 7: Fabrication of Supported-lipid bilayers on the binary patterned gold nanodots/PCysMA brushes

7.1 Introduction

During the last few decades, considerable attention has been focused on the development and manufacturing of smart, functional materials usable in a wide range of applications. Gold nanodots deposited on silicon substrates has attracted interest for use in new functional nanodevices, including subwavelength antennas in plasmonic applications⁴³³, electronic devices⁴³⁴, and biological applications⁴³⁵⁻⁴³⁶. The popularity of gold substrate in such applications is because of its high electrical and thermal conductivity, corrosion resistance, stability, solderability and bondability². Fabrication of periodic nanodot arrays demands precise control of the gold film structure and a high-resolution nanolithography tool. Nanolithography techniques such as electron-beam and focused ion-beam lithography enable the formation of well-defined nanodot arrays, but they suffer from high cost, low throughput and small area production which limits their potential utility⁴³⁷. Photolithographic techniques are simple, low-cost, and high-throughput techniques that can be used for fabricating patterns on a large area⁴³⁸⁻⁴⁴⁰. By taking the advantage of photoresist Self-assembled monolayers (alkanthiolate), which can serve either as a resist for photo patterning or chemical etching processes⁴⁴¹⁻⁴⁴³ photolithography techniques can be used to produce micrometre and nanometre features of gold structures. The whole patterning process simply consists of two main steps: (i) the immobilized thiolate on the gold surface is selectively photo-irradiated and (ii) the subsequent development of the resist in an etch process⁴⁴⁴. Both dry and wet etches may be used. Simple wet etches exist for gold. They utilize an etching solution, which contains a ligand that will coordinate to gold to form a stable Au(I) complex and an oxidant to establish the potential of the surface at a value when gold dissolution can occur⁴⁴⁵. Oh et al. have functionalized gold surfaces, using an aromaticthiol and alkanethiols. The SAMs have been patterned by using a UV light, and sulfonates in the illuminated areas developed with pure water. The patterned surfaces were characterized using AFM and STM. Cytochrome c molecules were adsorbed on the patterned gold surfaces and they were characterised using cyclic Voltammetry⁴⁴⁶. Two-beam

Interference Lithography (IL) was implemented to form periodic structures covering large areas. They generated structures with diameters of 140-350 nm separated at an average pitch of 304-750 nm. The gold arrays were functionalized with a protein-resistant oligoethylene glycol (OEG) and then immersed in a solution of the protein fibronectin to form cell adhesive domains for the study of the cell attachment. Giessen et al. reported the formation of gold lines with a width of 135 nm and a period of 395 nm on an area of $5 \times 5 \text{ mm}^2$, using IL to expose a photoresist first and then a dry etchant to remove the gold from the exposed area, forming gold patterns⁴⁴⁷.

One of the main issues of the gold thin films is their weak adhesion to inert and commonly used glass and silica substrates. To address this problem, a very thin layer of either chromium (Cr)⁴⁴⁸ or Titanium (Ti)⁴⁴⁹ is introduced between the gold thin film and the main substrate, forming a very stable gold thin film. However, these adhesive layers can be modified using a bottom-up approach that can enable the system to be used in a range of applications. Many studies have described the formation of self-assembled organic silane films on the Ti surface⁴⁵⁰⁻⁴⁵². Sigrist and co-workers used the formation of films of 3-aminopropyltriethoxysilane (APTES) on planar titanium surface in dry toluene, The thickness of the APTES film and its composition were characterised using ellipsometry and XPS⁴⁵³. To study Chitosan on Ti surfaces, the APTES molecules were first immobilized on the titanium surface followed by functionalization of the free amine of immobilized APTES with glutaraldehyde and the reactions were confirmed by using XPS⁴⁵⁴. By combination of the modification process with photocatalytic lithographic techniques, polymer brushes were grown on the titanium surface. (3-(2-Bromoisobutyramido)propyl)triethoxysilane (BIB-APTES) initiator-functionalized titanium dioxide surfaces were exposed through a mask to form a micrometer pattern, which was followed by growing poly(methyl methacrylate) (PMMA) brushes via SI-ATRP method⁴⁵⁵. Collard et al. reported the fabrication of patterned proteins and cells on Ti surface after it was modified with initiating APTES-BIBB molecules that followed by grafting 2-gluconamidoethyl methacrylate (GAMA), which resists protein adsorption and cell adhesion⁴⁵⁶.

The fabrication of soft biofunctional and biocompatible interfaces by grafting polymer brushes to the surfaces has potential applications in the design and development of a supported lipid membrane (SLB) system. Due to their importance as a model system in membrane biophysics,

the SLBs have attracted a great deal of attention⁴⁵⁷⁻⁴⁶⁰. Recently, supported lipid bilayers (SLBs) have been fabricated on quaternized and non-quaternized Poly(2-dimethylamino)ethyl methacrylate) (PDMA) brushes, which was grown from planar substrates via SI-ATRP. The quaternized brushes yielded more stable and better protocol for the formation of SLBs than non-quaternized brushes. Fluorescence recovery after photobleaching (FRAP) studies of such SLBs indicate ideal diffusion coefficients ($2.8 \pm 0.3 \mu\text{m}^2 \text{s}^{-1}$) and mobile fractions ($98 \pm 2\%$)⁴⁶¹. Poly(Cysteine methacrylate) brush has also been used recently as a support for SLBs. FRAP studies of lipid mobility provided a diffusion coefficient of $\sim 1.5 \mu\text{m}^2 \text{s}^{-1}$, which is comparable with those obtained for SLBs on a planar of the glass substrate¹¹⁵. Van Oijen et al. presented a rapid method for the formation of the polymer-supported lipid bilayer that displays complete lateral mobility of both leaflets. They showed that fabricated SLBs provide a lipid environment which is similar to those found in physiologically relevant environments. The FRAP suggested that full recovery of lipid membrane obtained on polymer-supported LB after photobleaching, while in the case of using a glass substrate that partial recovery as lipid molecules acquired⁴⁶².

The goal of the present work was to build on these studies by integrating gold nanostructures into a system consisting of an SLB formed on a brush support. The process is shown schematically in figure 6.1. An array of gold nanoparticles is formed by using IL to expose a SAM of alkylthiolates on a film of gold on Cr- or Ti – primed silicon oxide. After etching a PCysMA brush is grown from the oxide regions between the gold nanostructures and a supported lipid bilayer is formed by vesicle fusion on the brush regions. Ultimately, it would be the goal to deposit membrane proteins on the gold nanostructures.

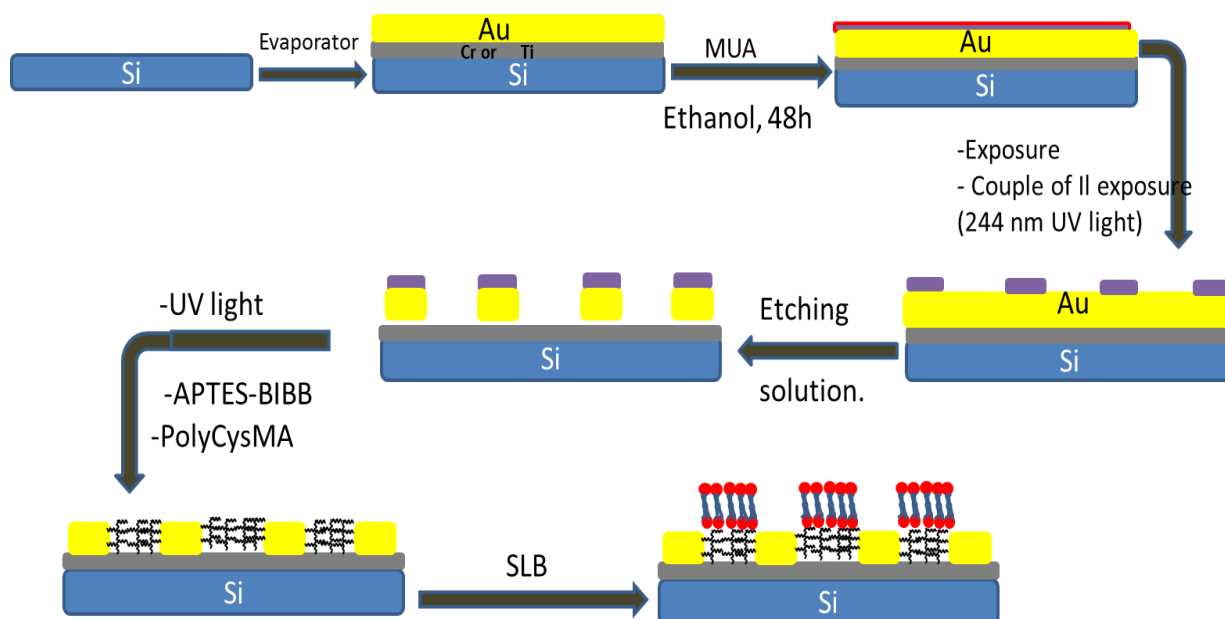


Figure 7.1: A schematic representation of the formation of supported lipid bilayers on PCysMA brushes grown on gold nanostructures.

7.2 experimental Section

7.2.1 Synthesis of 2-Bromo-2-methyl-N-(3-triethoxysilyl-propyl)-propionamide (BIBB-APTES)

2-Bromo-2-methyl-N-(3-triethoxysilyl-propyl)-propionamide was synthesized depended on the previously recorded procedure⁴⁶³. 1.5 mL (2.79 g, 12.1 mmol) of 2-bromo-2-methyl-propionyl bromide was added dropwise to 100 mL of dry THF, which already contained 4.0 mL (3.8 g, 17.1 mmol) of (3-aminopropyl)triethoxysilane and 3.60 mL of triethylamine (2.62 g, 25.8 mmol). The mixture was stirred under a stream of nitrogen for 12 h, the precipitate was filtered off and the solvent was removed. Then, the product was dissolved in 20 mL of dichloromethane (HPLC-grade) and washed twice with 0.01 N of HCl and twice with deionized water. The organic phase was dried with magnesium sulfate and filtered again. The flash column chromatography with silica gel was used to purify the final product, using a mixture of n-hexane and ethyl acetate with a ratio of 2:1. The desired fragments were collected and a rotary evaporator was used to remove the solvent and produce a colourless oil with a yield of 86.4 % (5.43 g).

Product was characterized by using NMR spectroscopy. ^1H NMR (250 MHz, CDCl_3): δ 6.9 (s, 1H, NH), 3.82 (q, 6H, SiOCH_2), 3.28 (t, 2H, CH_2N), 1.95 (s, 6H, CH_3), 1.68 (m, 2H, CH_2), 1.22 (t, 9H OCH_2CH_3), 0.65 (t, 2H, SiCH_2). ^{13}C NMR (250 MHz, CDCl_3): δ 171.86, 63.24, 54.92, 42.56, 32.59, 22.68, 7.56.

7.2.2 Preparation of Samples

The preparation of gold film on a thin adhesive layer of either titanium (Ti) or chromium (Cr) was described in section 3.4. A clean glass slide or silicon wafer was coated with 3-5 nm of Ti/Cr, using a vacuum Evaporator (Edwards Auto306) with a deposition rate no more than 0.03 nm s^{-1} , this was followed by deposition of 18-20 nm of Au with a deposition rate 0.04 nm s^{-1} under pressure ca. 1×10^{-6} mbar. Then, the coated samples were immersed in 1 mM of either ODT or MUA solution in degassed ethanol for 24 h. The self-assembled coated surfaces were washed and sonicated in ethanol and dried under a stream of nitrogen prior to use. The samples were kept in ethanol during the entire period of the experiments to avoid the alkanethiol functionalized surfaces from the oxidation reaction.

7.2.3 Photoirradiation of the Samples

The alkanethiol-coated gold surfaces were patterned, using a photomask and by interference lithography, as described in section 3.7.4. The micrometre patterned gold structure was prepared by exposing the surface through a microscopic copper-grid (1000-2000 mesh), the exposed samples were washed and dried under a stream of nitrogen straight after the photooxidation process. Samples were exposed to light from a frequency-doubled argon ion laser (244nm) in Lloyd's mirror interferometer. The angle between the sample and the mirror in the interferometer was 15° . After the exposure process, the samples were etched, using a 0.2 mM solution of mercaptoethylamine hydrochloride in 8% v/v of 35 % of ammonia in ethanol. The etching process was controlled by repeatedly checking of the samples by AFM. After that, the remained ODT or MUA was photo-oxidized to completely remove them on the gold futures, and then they were rinsed with ethanol and blown with nitrogen.

7.2.4 Derivatization of Cr/Ti Region with BIBB-APTES Initiator Molecules

To functionalize the TiO₂ surface with IBB-APTES initiator, the etched samples were cleaned in a cold piranha solution for 3-5 min, then they were washed more than seven times with deionized water. Subsequently, the samples were placed at the 100 °C for 2 h to dry, AFM tapping mode images were taken for each sample to ensure the patterns were not removed by the piranha solution. Afterwards, the samples were immersed in 5 mM of the initiator (BIBB-APTES) solution in HPLC toluene for 24 h, and then they were rinsed and sonicated in toluene and ethanol and dried under a stream of nitrogen.

To form a BIBB-APTES self-assembled monolayer on Cr surface, the samples were cleaned and oxidized in a cooled piranha solution for 3-5 min. Immediately after this, the samples were rinsed in deionized water eight times and rinsed in an alkaline water-ethanol solution (a solution of ethanol (10 mL) and 1 mL of 1 mM of NaOH solution under reflux condition for 30 min). Subsequently, the samples were immersed in 5 mM solution of BIBB-APTES in toluene for 24 h. After the reaction finished, the samples were cleaned and sonicated in toluene and ethanol, and finally, they were dried under a stream of nitrogen prior to use.

7.2.5 Growing PCysMA Brushes Between Gold Features

CysMA monomer was synthesized as described in section 3.5.1, the gold patterned samples were placed in a piranha cleaned carousel tubes, degassed and then filled with nitrogen (this step was repeated 5 times). To 12 mL of deionized water placed in a round bottom flask, (5.0 g, 15.0 mmol) CysMA added and sonicated for 15 min to make a clear monomer solution, which was degassed for 30 min at 20 °C. Cu(I)Br (71.4 mg, 0.5 mmol), bipy (234 mg, 1.5 mmol) and Cu(II)Br₂ (55.6 mg, 0.25 mmol) were added to the solution and degassed for 10 min, then it was quickly sonicated (for 2-3 min). Finally, 2 mL of the reaction mixture was transferred to each carousel tube and the polymerization allowed to continue for 1.5 h. The polymerized samples were washed and sonicated with deionized water and rinsed with ethanol before blowing with N₂.

7.2.6 Preparation of Supported Lipid Bilayers

Supported lipid bilayers were formed on the patterned samples using the procedure described in section 3.8. The polymerized samples took place in a custom-built flow cell, then they were first soaked with buffer solution for 10 min, subsequently, the vesicles were injected and incubated for 24 h at 50 °C. Finally, the samples were rinsed for 20 min with degassed Milli-Q water at a flow rate of 2.6 ml min⁻¹.

7.2.7 Surface Characterization

Contact angle, AFM, and fluorescence recovery after photobleaching (FRAP) were used to characterize the obtained surfaces. Details of each measurement technique were given in chapter 3. The contact angle measurements confirmed the changes of wettability of the surface after functionalization with SAMs. AFM tapping mode topography images in air were used to analyze the patterned samples, typically after etching and polymerization processes. The quality of supported lipid membrane was characterized by using FRAP.

7.3 Result and Discussions

7.3.1 Photopatterning and Etching of Alkanethiolate Functionalized Gold Films on Ti/Cr Layer

The functionalization of gold surfaces with alkanethiol was carried out using the previously recorded protocol⁴⁶⁴. The octadecanethiol (ODT) and 11-mercaptopundecanoic acid deposited on the either glass or silicon wafers were characterized by using contact angle goniometer and XPS. The contact angle measurement for a clean gold surface was 83°±3, increasing to 108°±3 after deposition of ODT. This increase in contact angle is consistent with the formation of an ODT SAM and is in close agreement with the contact angle values reported in the literature⁴⁶⁵. Figure 7.2a shows an XPS C1s high-resolution spectrum obtained for an ODT functionalized Au surface. The spectrum is dominated by a large peak at 285.0 eV, attribute to the carbon atoms in the ODT alkyl chain. A small component also appears at 286.9 eV that is attributed to a carbon atom adjacent to sulfur. This also assigned to ODT self-assembled monolayer on Au surface. While the contact angle decreased to 6-8° for MUA functionalized gold surfaces, this is also attributed to the formation of MUA monolayer and is consistent with previously reported contact angle³³.

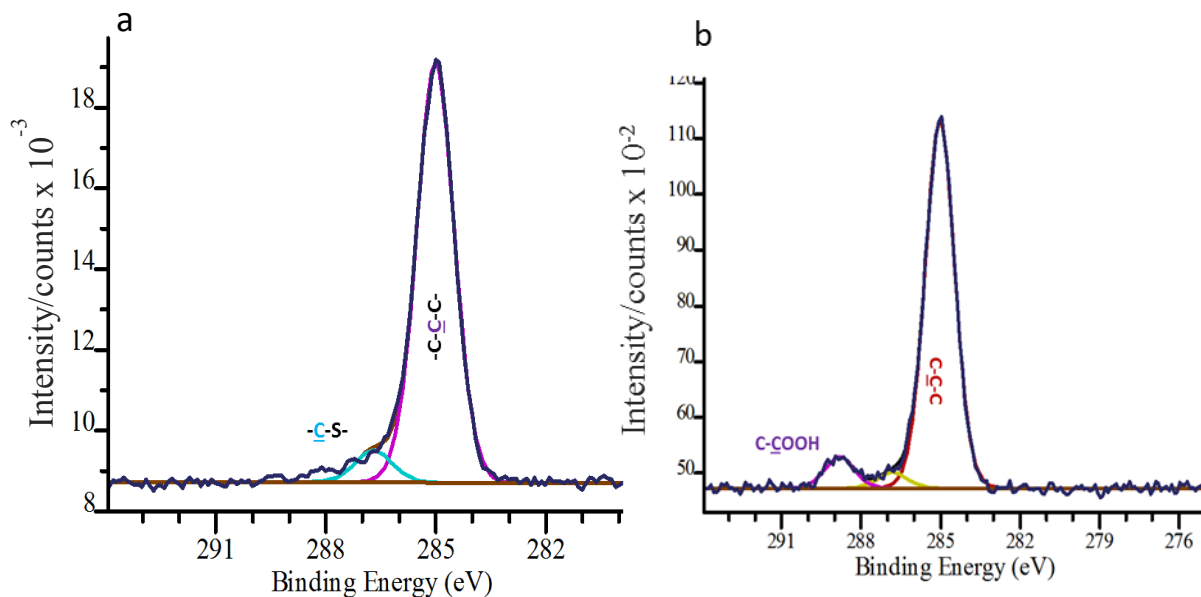
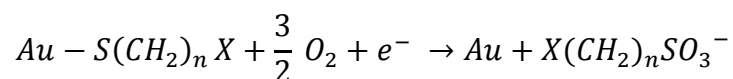


Figure 7.2: Demonstrates high-resolution C1s spectra for a) ODT SAMs and (b) MUA SAMs on the Au surface.

High-resolution C1s spectra were obtained after formation of a SAM of MUA. As expected, peaks were observed adsorbed on the Au surface, the C1s peaks at 285.0, 286.7 and 288.89 eV are attributed to C-C-C, -C-COOH, and -C-COOH respectively, figure 7.2b. This is good evidence for the formation of an MUV self-assembled monolayer on the Au surface.

To characterize the thickness of the gold film on the Ti/Cr adhesive layer coated slides, a sample was functionalized with an ODT SAM and photopatterned by exposure through an electron microscope grid (2000 mesh) with a dose of 40 J cm⁻². The photo-oxidation reaction leads to oxidation of the alkanethiolate to yield a weakly bond alkylsulfonate in the presence of oxygen, due to the formation of hot electrons at the gold surface as shown in the equation below²⁴¹.



Although alkanethiolates strongly adhere onto the gold surface, the alkylsulfonates are only weakly adsorbed that can be removed by washing it with a solvent. The micrometre patterned SAMs was etched in a solution of mercaptoethylamine hydrochloride in ethanol for 15-20 min depending on the thickness of the old film.

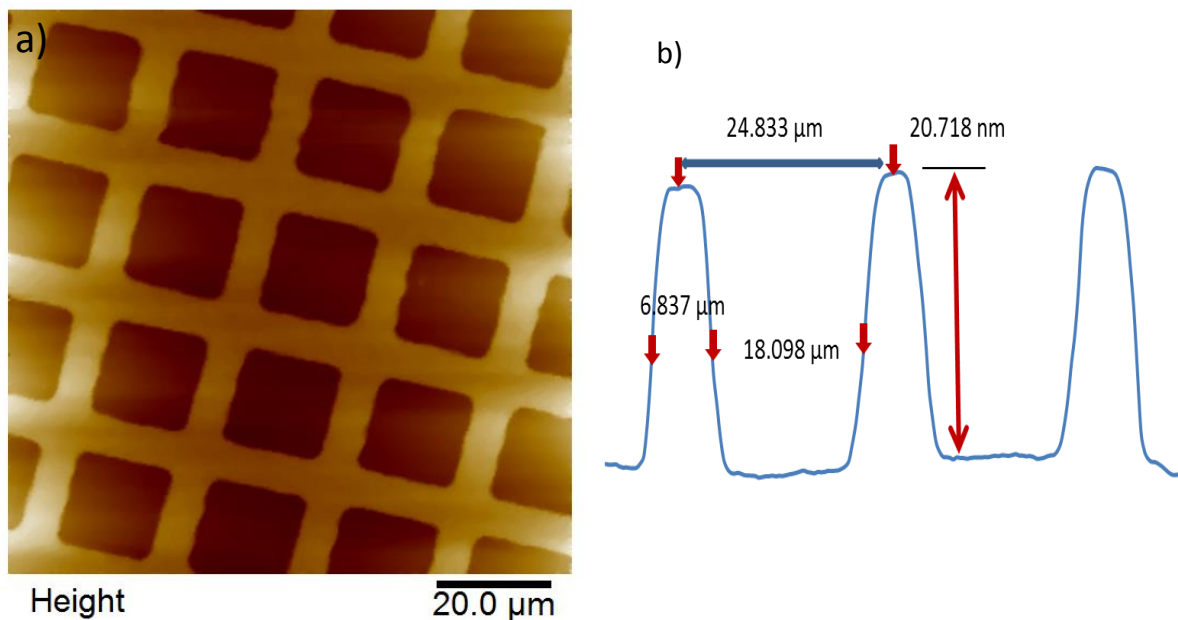


Figure 7.3: (a) Tapping mode AFM height image of a gold microstructure formed by exposure of an ODT SAM on Au to UV light through a mask, followed by subsequent etching with mercaptoethylamine hydrochloride for 15 min. (b) AFM sectional analysis shows that the gold film thickness is 20.718 nm.

The etched sample was characterized using AFM. The thickness of the gold film was acquired by taking an AFM tapping mode image and measuring a line section through a region of the sample (figure 7.3b).

Arrays of gold nanostructures were prepared by using two orthogonal exposures, of an ODT SAM in the Lloyd's mirror interferometer. The exposure was 25 J cm^{-2} and the sample was rotated 90° between exposures. The exposed sample was washed to remove oxidized alkylsulfonate and dried under nitrogen, then it was etched in the solution of mercaptoethylamine hydrochloride for 15 min. AFM tapping mode images confirm that a very good quality patterned sample was formed (figure 7.4a). Section analysis revealed FWHM 186 nm, period 438 nm and height of 20-26 nm.

Samples were also prepared using MUA SAM as the resist, dose of 10.0 J cm^{-2} was used in a first exposure followed by a second orthogonal exposure of 8.3 J cm^{-2} . Subsequently, the oxidized thiol molecules were removed by washing with a proper solvent before drying under nitrogen.

The photopatterned sample was etched in mercaptoethylamine hydrochloride for 16 min that resulted in gold nanodots see figure 7.4b.

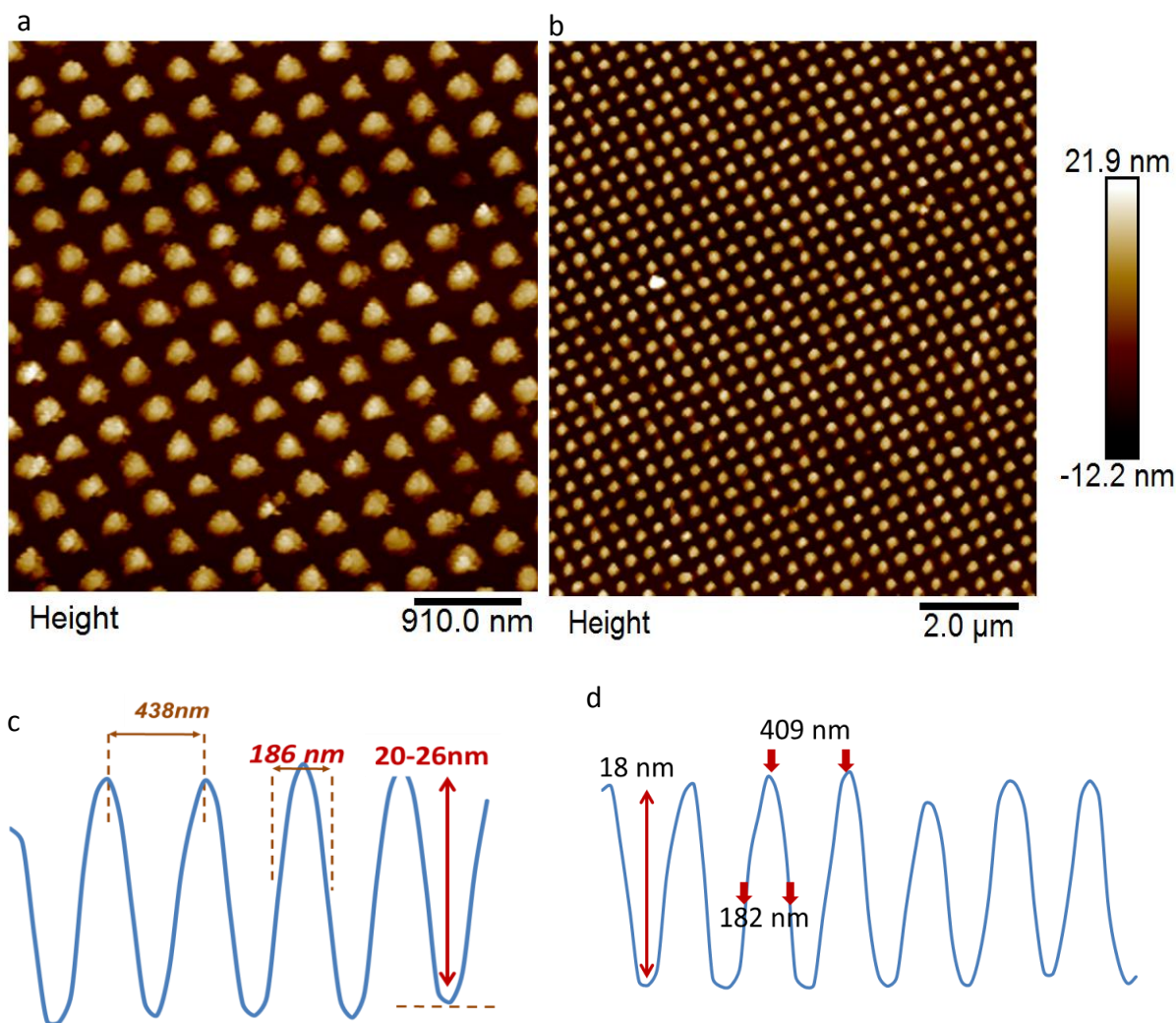


Figure 7.4: The tapping mode height images of an array of gold nanostructures formed using IL to expose (a) an ODT SAM and (b) an MUA SAM. (c) and (d) shows sections through the images in (a) and (b), respectively.

Figure 7.5 shows fabricated gold nanodots on a Cr substrate using the irradiation of ODT and MUA SAMs, the fabricated samples were characterized using AFM. The irradiation and etching processes were performed in a similar way to Ti substrate. The characterized properties of the gold nanodots by using ODT SAMs exhibit FWHM of 170 nm, a period of 512 nm and the thickness of 20 nm. While the dots which resulted from the photodegradation of MUA SAMs and subsequent etching showed 19.9 nm thickness, 507 nm period and 178 nm FWHM.

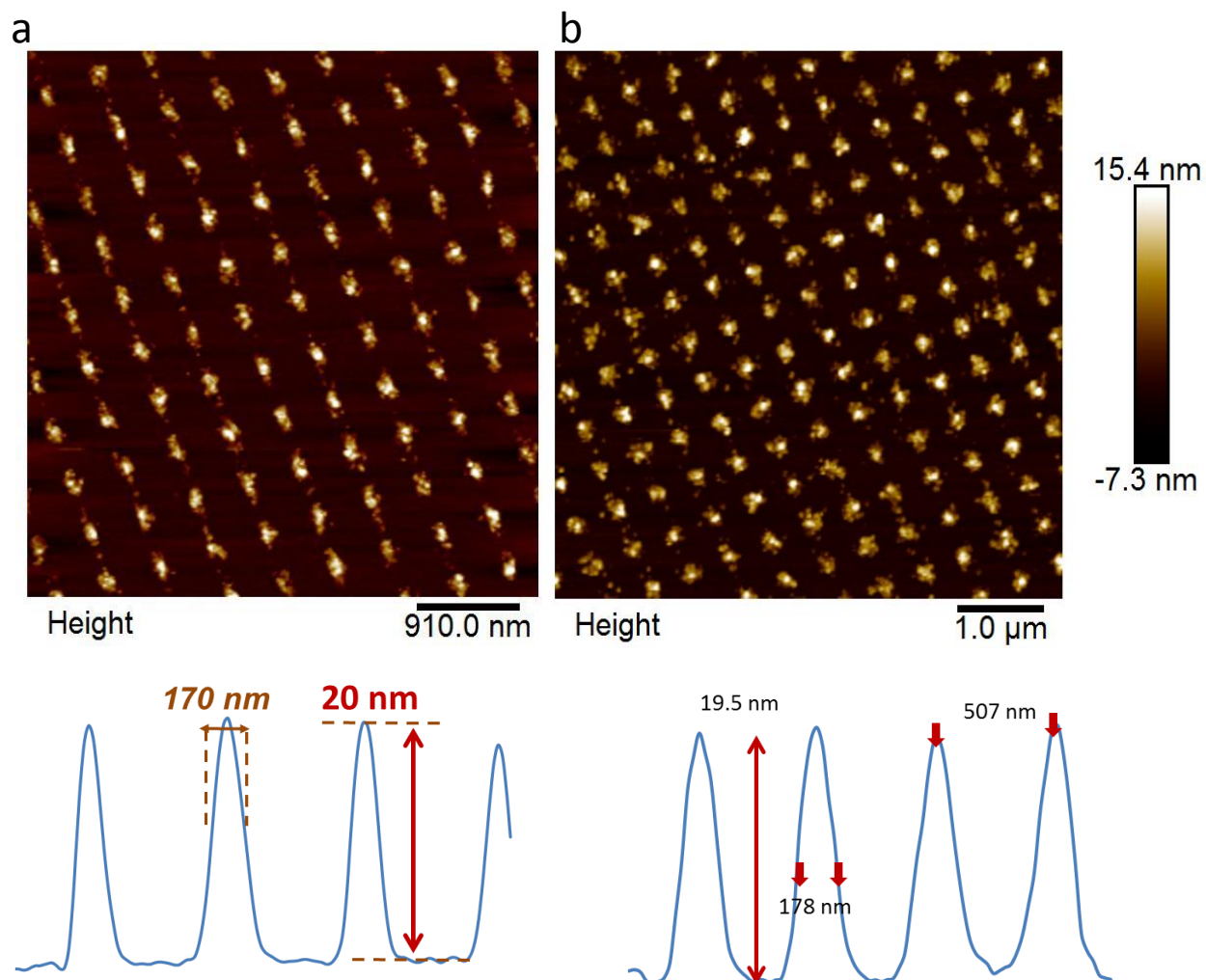


Figure 7.5: The tapping mode height images of an array of gold nanostructures formed using IL to expose (a) an ODT SAM and (b) an MUA SAM. (c) and (d) shows sections through the images in (a) and (b), respectively.

To characterise the composition of the regions between the gold nanostructures after etching, model samples were prepared by UV irradiation of a SAM of MUA without the use of either a mask or the interferometer. Subsequently, the patterned samples were etched and characterized by utilizing contact angle goniometer, AFM and XPS. Figure 7.6a shows an AFM tapping mode topographical image of a fully exposed gold surface. The roughness was 2.01 nm and the contact angle was $83 \pm 3^\circ$. A strong Au4f peak was acquired figure 7.6b.

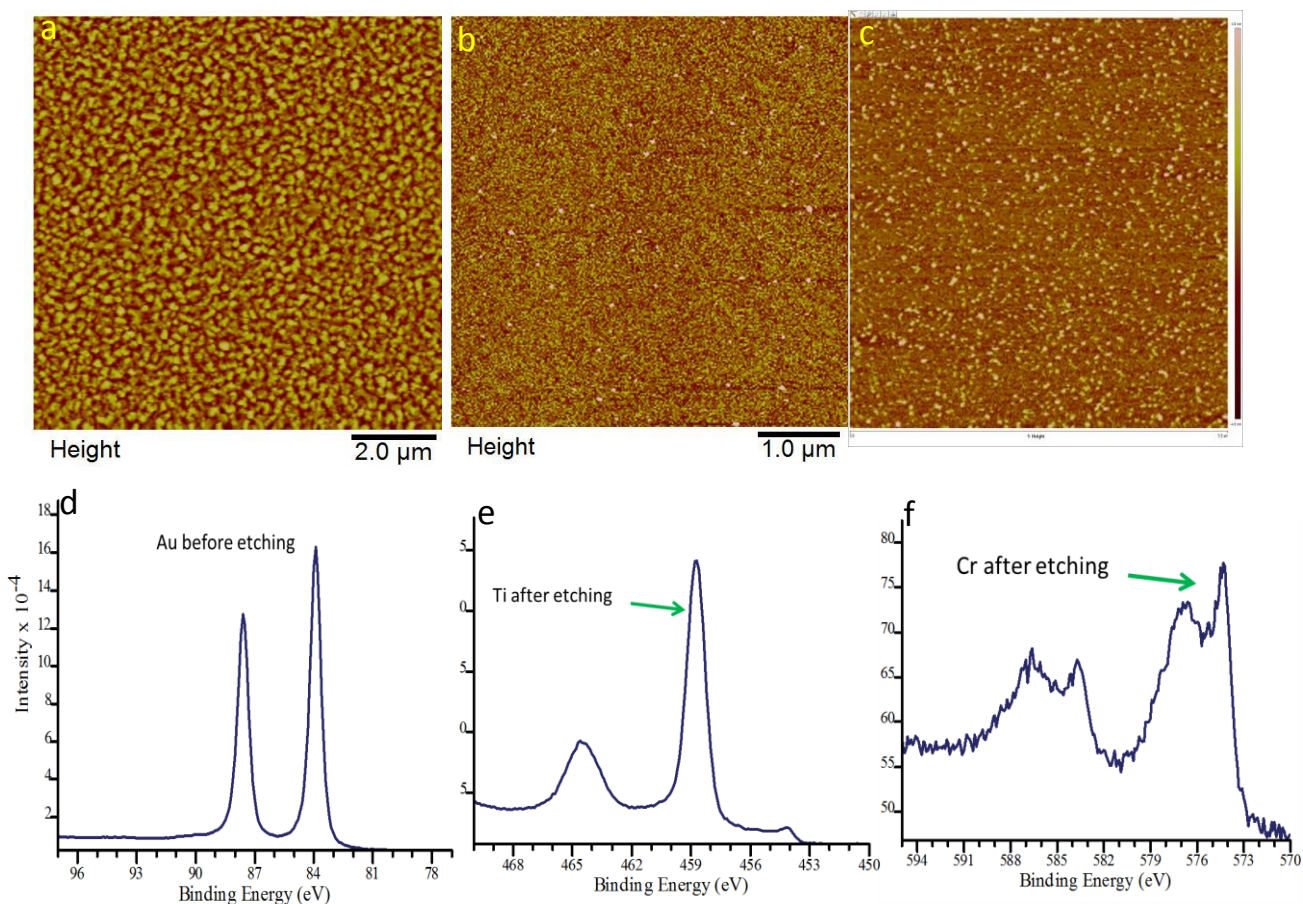


Figure 7.6: shows AFM height images for Au surface before and after etching (a) Au film before etching, $10 \times 10 \mu\text{m}^2$ (b) Ti film, $5 \times 5 \mu\text{m}^2$ and (c) Cr film $3 \times 3 \mu\text{m}^2$ after etching. XPS spectra for (d) Au4f before etching, (e) Ti2p and (f) Cr2p films after etching.

After etching the contact angle reduced to $14 \pm 3^\circ$ and $17 \pm 3^\circ$ for samples formed on Ti- and Cr-primed substrates, etching respectively. Roughness was 0.65 for a primed Ti substrate (figure 7.6c) and 0.83 for Cr-primed surface (figure 7.6e). Figure 7.6d and 7.6f shows XPS spectra for Ti2p and Cr2p respectively, which are a good indication of the presence of Ti and Cr after 20 min etching time. In both cases, the signal for primer layer is strongly indicating that it is not removed by the etch solution. However, the loss of the Au4f peak confirms removal of the gold.

7.3.2 Preparation of Initiator Silane-coated Surfaces

To immobilize the BIBB-APTES initiator on the Ti or Cr adhesive layers of the etched samples, the patterned samples were cleaned in a cooled piranha solution (25°C) for 3-5. The samples were washed with deionized water, and then dried at 100°C prior to use. The Ti samples were immersed in 5 mM solutions of BIBB-APTES in toluene for 24 h.

To make a control Ti sample, a gold functionalized Ti layer etched until all gold film removed and the remaining Ti surface was immersed in 5 mM solution of BIBB-APTES in toluene for 24 h. The contact angle of the TiO₂ surface was 17±3° degree, which is increased to 67±3° after treatment with BIBB-APTES. XPS was performed to determine the chemical composition of the initiator, the C1s core level spectra (figure 7.7a) were fitted using three component binding energy of 285.0, 286.729 and 288.7632 eV, corresponding to C-C-C, C-Br/C-NCO and O=C-N respectively.

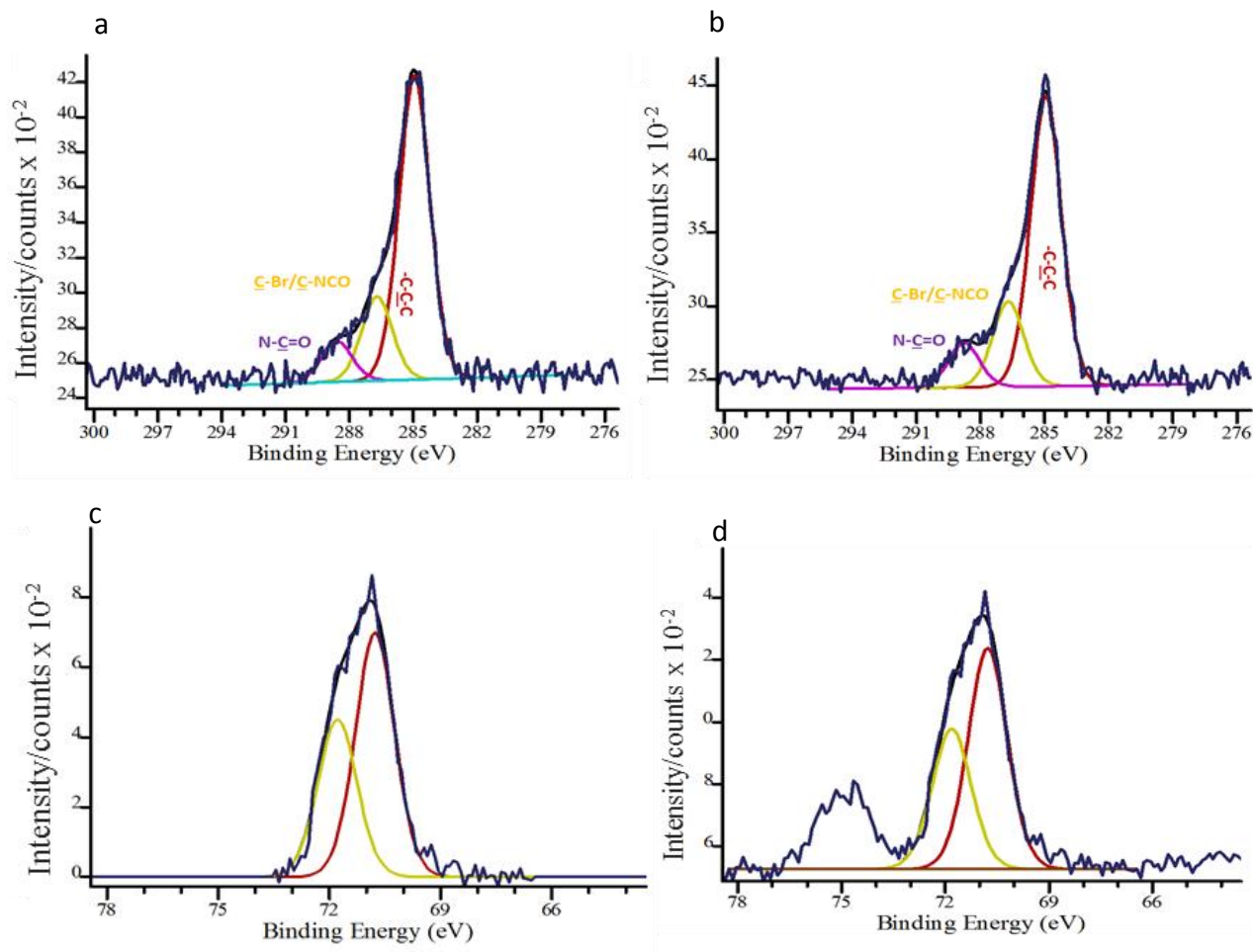


Figure 7.7: Demonstrates XPS high-resolution spectra obtained for 2-bromo-2methyl-N-(triethoxysilyl) propyl) propanamide (BIBB-APTES) adsorbed on Ti and Cr surfaces. (a) C1s high-resolution spectra for the initiator on Ti surface, (b) C1s high-resolution spectra for the initiator on Cr surface, (c) Br3d high-resolution spectra for BIBB-APTES on Ti surface, and (d) Br3d high-resolution spectra for BIBB-APTES on Cr surface.

The ratio between C-C-C, C-Br/C-NCO and O=C-N obtained here is 3.6:1.93:1 which is in close agreement with the theoretical ratio 4:2:1. Figure 7.7c shows high-resolution Br3d spectra, which consistent with the components of the BIBB-APTES initiator.

BIBB-APTES was adsorbed onto the chrome layer using the method of Hild et al. They found that the siloxane group reacted with CrO^- , which is formed after the oxide surface treated with 0.1 M NaOH in a water-ethanol solution under reflux⁴⁶⁶. The contact angle was 16 ± 3 for a clean Cr surface, this was increased to 67° after the surface was treated with the BIBB-APTES initiator. Samples were characterized by XPS. The C1s spectra were fitted using three components with binding energies of 285.0, 286.729 and 288.7632 eV, which were attributed to C-C-C, C-Br/C-NCO and O=C-N respectively figure (7.7b). The calculated ratio of C-C-C:C-Br/C-NCO: O=C-N is 4:2:1. The measured ratio here was 3.97:1.7:1, which means that a nearly complete monolayer has formed. The Br3d spectra were fitted using two components with binding energies 70.78 eV and 71.82 eV, attributed to $\text{Br}3d_{5/2}$ and $\text{Br}3d_{3/2}$. A single peak was observed at 74.88 eV corresponding to Cr3s (figure 7.7c and 7.7d). These results confirming that BIBB-APTES was successfully immobilized on the Ti and Cr surfaces as a prior to starting the polymerization reactions.

7.3.3 Growing PCysMA Brushes Between Gold Nanodots

The poly(cysteine methacrylate) brushes were grown from the Ti or Cr regions between gold nanodots using SI-ATRP. The oxide regions were functionalized with the ATRP initiator (BIBB-APTES) before the polymerization reaction. The polymerization was performed under conditions of [CysMA]: [CuBr]: [CuBr₂]: [Bipy] with a molar ratio of 30: 1.0 : 0.5 : 3, respectively, for 1.5h to yield a polymer with a dry thickness of 7-9 nm. Figure 7.8a shows an AFM tapping mode topographical image of a representative. The cross section analysis suggested that the height difference between gold and Ti regions reduced from 20 nm to ca. 11.23 nm (figure 6.8b) consisting the formation of a brush layer 8.77 nm thick between the gold nanostructures. This is attributed to the fact that the brushes were grown successfully in the fabricated regions. In a similar way, the polymer brushes were grafted on the Cr regions between the patterned gold structures, by immersion the samples into the polymerizationsolution of similar composition for 1.5 h to grow brush with a dry thickness of about 7-9 nm.

Figure 6.8b shows that the brushes were successfully grown from the Cr area, as more evidence can be seen from the sectional analysis, where the height differences between gold nanodots and Cr regions reduced to 11.6 nm.

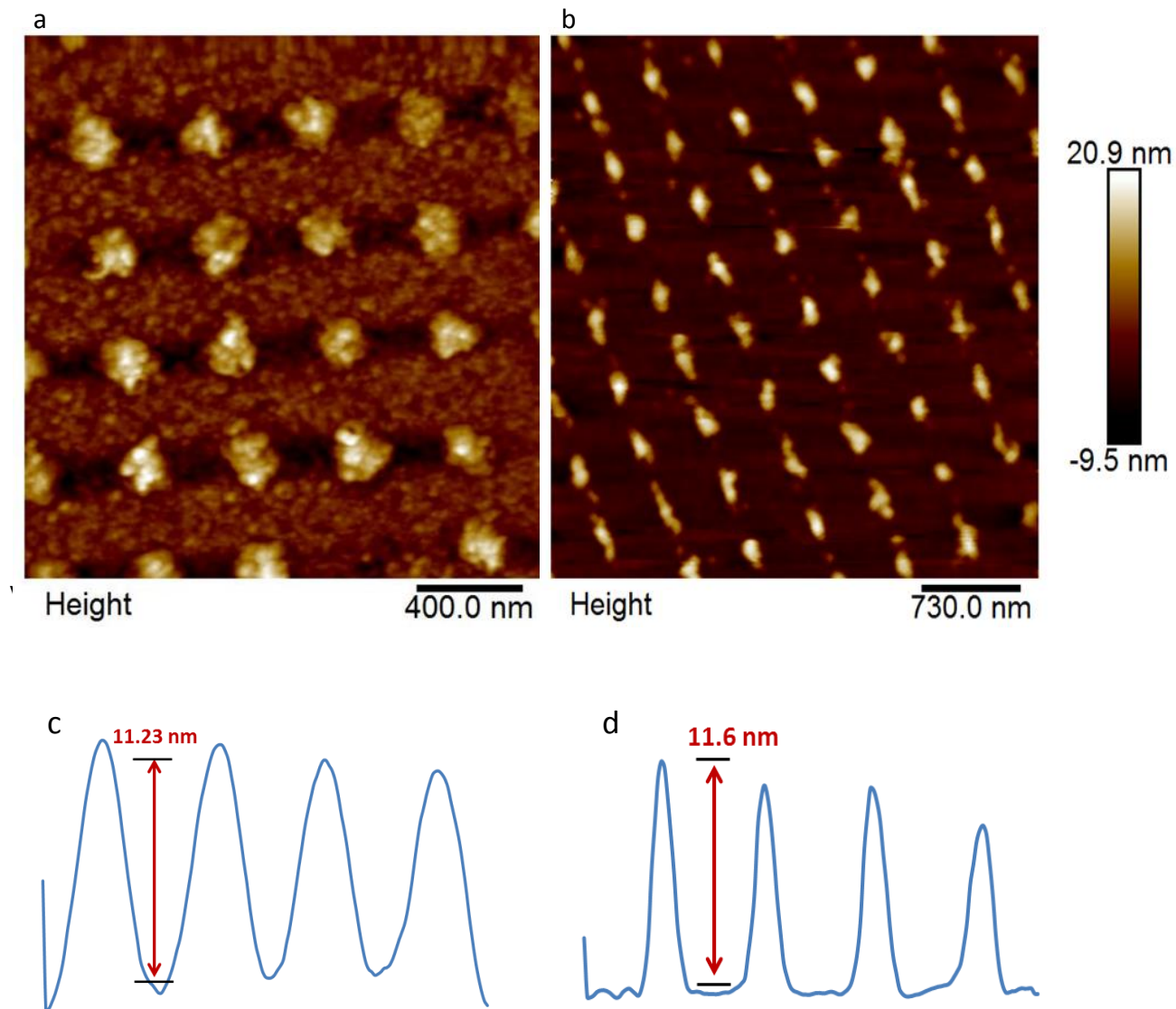


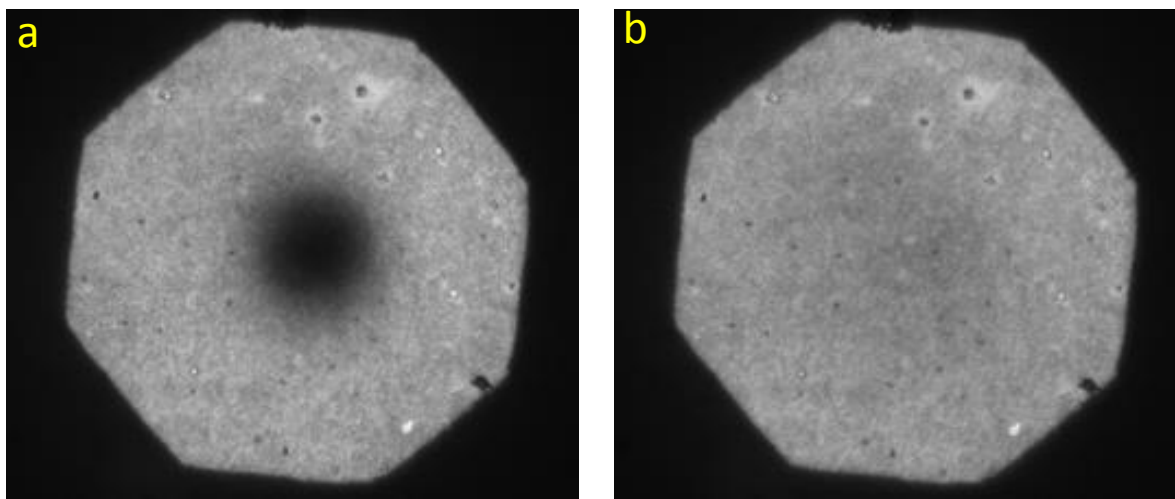
Figure 7.8: shows AFM tapping mode topographical images for binary patterned of gold nanodots/PCysMA brushes. (a) PCysMA brushes grown from Ti regions between gold nanodots, (b) PCysMA brushes grown from Cr regions between gold nanodots. (c) and (d) show the line section through the height images (a) and (b) respectively.

Alswiesh and et al. reported that PCysMA brushes swelled by 7-8 nm in water, so for the structures shown here, which were characterized dry, it is expected that the heights of the swollen brushes would be similar to the heights of the gold nanostructures. It has been shown in our lab, that the height of the PCysMA brushes becomes twice bigger in a good or PBS buffer compared to the dry thickness in the ambient conditions. Thus, the brush and gold nanodots may be at the same height after the brushes swollen in such kind of solvents.

7.3.4 Formation of SLBs on The Binary Patterned Gold Nanodots/PCysMA Brushes

The experiments of lipid bilayer formations were performed in co-operation with Leeds University as a part of the low-dimensional chemistry (LDC) project. As described in chapter 3.8 the fabrication of lipid bilayer was investigated using positively charged lipids of DOTAP POPC in PBS. The fabricated samples were first soaked with buffer solution for 10 min, subsequently, the vesicles were injected and incubated for 24 h at 50 °C, in order to induce vesicles rupture and forming a mobile lipid bilayer on the polymer brush regions. The interaction between vesicles and the gold nanodot surface is expected to be very weak; hence no vesicle adsorption is observed on the gold surfaces. Before performing characterization steps the samples were rinsed for 20 min with degassed Milli-Q water at a flow rate of 2.6 ml min⁻¹. Figure 7.9a shows the FRAP images for the binary gold nanodots/PCysMA brush on Ti surfaces before and after bleaching at 3 min. Bright, uniform fluorescence could be seen on the surface which confirmed the successful rupture of the vesicles, leading to a uniform distribution of lipids, consistent with the formation of SLBs the absorption of the lipids onto the surface. A black spot appeared in the middle image (figure 7.9a) is attributed to the photobleaching region, which results from destruction of the fluorescence properties of the dye molecules under intense illumination. The figure 7.9b shows an image of the same region acquired 3 min after photobleaching. It can be seen from the images that the fluorescence intensity of the bleached spot recovered fully after the 3.0 min. The recoveries of the fluorescence confirm that the lipids are mobile in the SLB: after bleaching, the bleached lipids are replaced by lipids diffusing into the bleached region. The intensity of the bleaching region as a function of time has been plotted as shown in figure 7.9c. Analysis of the recovery curve indicates a diffusion

coefficient of $1.10 \pm 0.15 \mu\text{m}^2/\text{s}$. The mobile fraction of the formed bilayer was calculated to be $129\% \pm 5\%$, which confirms the vast majority of the lipid membrane was mobile.



t = 0 min after

t = 3 min after

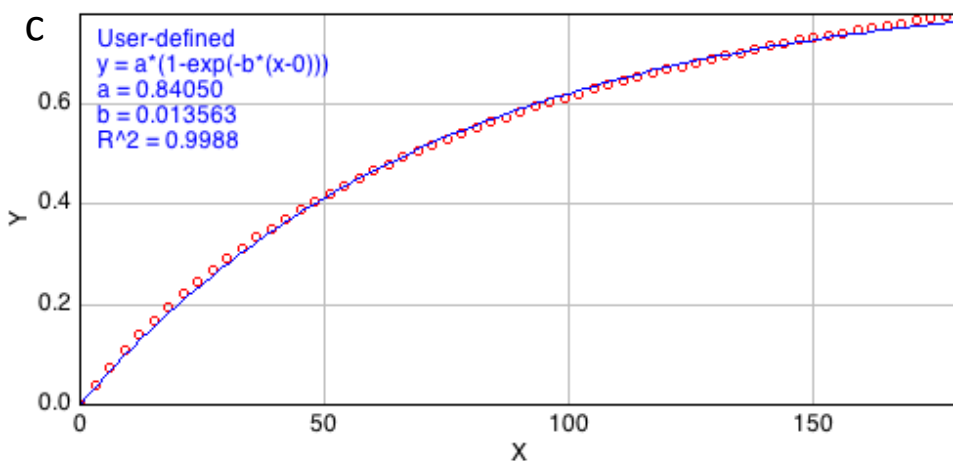


Figure 7.9: Fluorescence image for photo-oxidised lipid bilayer on the binary gold nanodots/brush samples on Ti surface after incubation in POPC vesicles and heating in an oven at 50 °C. The images show the surface immediately (a) and 3.0 min after photobleaching (b). The fluorescence recovery curve for the recovery of the lipids (c). The FRAP data were fitted to a first-order curve by Peng Bao.

Figure 7.10 shows data acquired in a very similar experiment carried out using a sample formed on a substrate primed with Cr rather than Ti. Uniform bright fluorescence was observed prior to bleaching, confirming successful vesicle fusion. After bleaching, a dark spot is observed (7.10a).

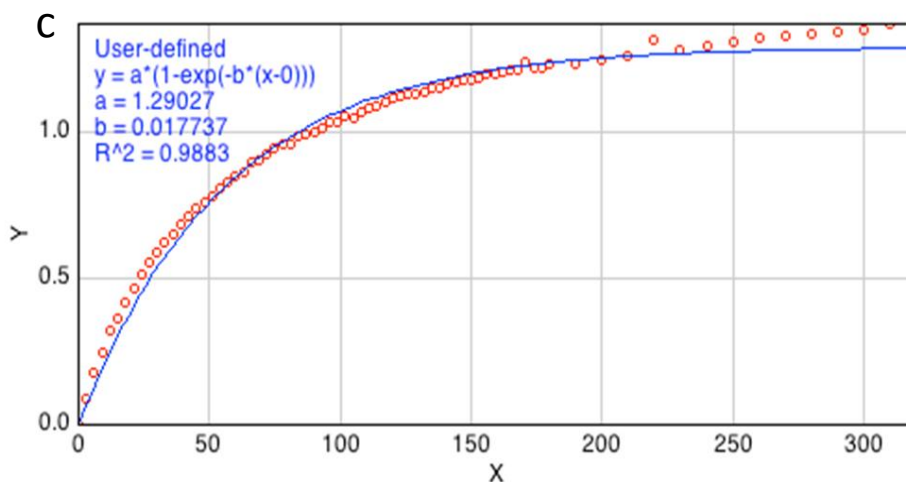
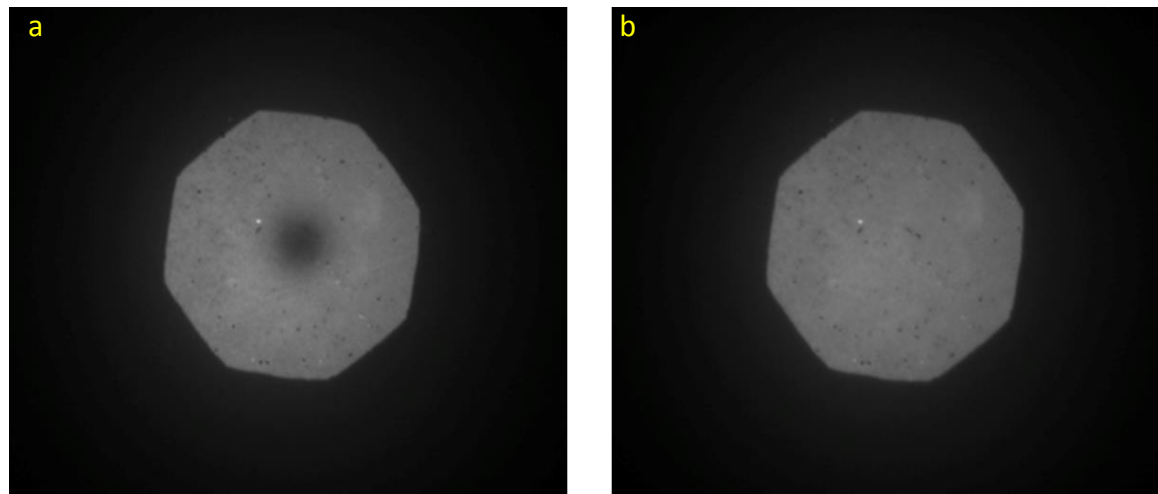


Figure 7.10: Fluorescence image for photo-oxidised lipid bilayer on the binary gold nanodots/polymer brushes on Cr surface after incubation in POPC vesicles and heating in an oven at 50 °C. The images show the surface immediately (a) and 3.0 min after photobleaching (b). The fluorescence recovery curve for the recovery of the lipids (c). The FRAP data were fitted to a first-order curve by Peng Bao.

Fluorescence was fully recovered in the bleached region (figure 7.10b) confirming that the lipids were mobile in the SLB. Figure 7.10c shows the intensity of the photobleaching as a function of recovery time. The diffusion coefficient and the mobile fraction of the bilayer obtained from the analysis of the recovery curve were $D = 0.71 \pm 0.15 \mu\text{m}^2/\text{s}$ and $84 \pm 5\%$, respectively, which confirms the formation of good-quality lipid membrane on the surface.

In the future work, the aim would be to integrate membrane protein structures into lipid bilayers resting on polymer cushions with integral gold nanostructures. This would help to realise the goal of being able to use plasmonic techniques to investigate membrane proteins in situ in biological membranes. The gold dots would be functionalised with nitrilotriacetic acid (NTA), enabling site-specific attachment of light-harvesting complexes from plants or bacteria. Recent work [Tsargorodska et al.]⁴⁶⁷ has shown that there is strong coupling between localised surface plasmons and excitons in light-harvesting complexes; with the result presented here, it seems possible to achieve strong coupling between LSPRs and an intact biological membrane, which would be a very useful advance.

7.4 Conclusion

The thin gold film has been prepared on both Ti and Cr as an adhesive layer, ODT and MUA SAMs has been deposited on the gold films. Contact angle measurements and XPS characterization suggested the high quality of SAMs of both ODT and MUA on the surfaces. To determine the thickness of the gold layer, the ODT self-assembled monolayer was photo-oxidized of a dose of 40 J cm^{-2} through a microscopic grid, using photomask technique. A micrometre gold structure fabricated by etching the photopatterned sample in the etchant solution for 20 min. The AFM tapping mode images suggested a very good agreement between the thickness obtained from patterned sample and the thickness suggested by the evaporator. Nanometer patterned of the SAMs (either ODT or MUA) on the gold film obtained by employing interference lithography (IL). Subsequently, the gold nanodots acquired after the IL patterned samples have been etched for 10-15 min. The AFM characterizations confirmed the high quality of the obtained gold nanodots on both Ti and Cr layers. An ATRP initiator (BIBB-APTES) has been synthesized and immobilized onto the regions (Ti or Cr) between gold nanodots, AFM, contact angle and XPS confirmed that the silane film was successfully formed on the targeted area. A new zwitterionic biocompatible brush (PCysMA) was grown from the initiated area by applying SI-ATRP method, the obtained binary gold nanodots/PCysMA brushes characterized by using AFM. The binary patterned samples were used to study supported lipid bilayers (SLBs) and the FRAP studies suggested a high quality of SLB on the patterned samples with a considerable diffusion coefficient and a mobile fraction.

Chapter 8: Summary of Thesis

The goal of the work presented in this thesis was to develop a polymer-based system that can be used to organise biological interactions at the nanometre-scale. To achieve this, precise control is required of both the conformation and behaviour of the polymer chains at a molecular level and in physiological environments.

8.1 Fabrication of PCysMA Micro – and Nanostructures and Characterisation of their Behaviour as a Function of Feature Size and Grafting Density in Different Environments

Various nanometre and micrometre structures of PCysMA brushes were fabricated from photo-patterned APTES-BIBB film. Micrometre-scale structures were fabricated by exposing the silane film using photomask lithography. Interference lithography at an angle of 10° , 15° , 20° and 30° was used to fabricate nanometre structures with periods of 690, 511, 450, 307 nm respectively. PCysMA brushes were grown from the unmodified regions of the surface using SI-ATRP. Friction force measurements by FFM revealed that the conformation of the brushes depends on the dimensions of the features and the nature of the medium. In a medium in which the polymer chain segments are strongly solvated the friction-load relationship was sublinear. Application of the DMT contact mechanics model provided a good fit to frictional-load plots. The contact mechanics parameters were calculated and found to vary in a way that was consistent with the explanation. Therefore, the polymer chains are expected to be extended and forming brush structures. In contrast, the friction forces were linearly related to the load for those measurements that were carried out in a poor solvent. It is expected that the molecular deformation dominated the energy dissipation pathway in the contact area, due to the collapsed nature of the polymer chains. The friction coefficient values decreased as the scale size of the footprints decreased.

The impact of grafting density on the polymer brush conformation was investigated in different environments. The ATRP initiator was exposed to different doses of 244 nm UV light, using photolithography, the polymer brushes were grown from the unexposed regions of the initiator, using SI-ATRP.

The friction-load relationship was found to be nonlinear in a good solvent for the brushes with high grafting density. However, a linear relationship was observed as the grafting density decreased.

The most reasonable explanation is that at a high grafting density the friction was dominated by dissipation in shearing while this changed to load dependent ploughing as the grafting density decreased. This suggested that the polymer chain provided brush structure at high density, due to the steric hindrance rose between the polymer chain segments. As the distance between two adjacent grafting points decreased the polymer chain started to be collapsed. This was further explored by using DMT mechanism and measuring the contact mechanic parameters. This transformation in the polymer chain conformation was not observed in a poor solvent. A linear friction-load relationship was obtained, regardless of the grafting density of the brushes. This may explained by suggesting that the polymer chains were collapsed and molecular ploughing dominated the interface between tip and sample surfaces. As the grafting density decreased the friction coefficients increased initially, and then decreased as the density further reduced.

8.2 Mesenchymal Stem Cell Cultivation on Nanometer Patterned PCysMA Brushes

2-nitrophenylpropyloxycarbonyl-protected aminosiloxane (NPPOC-APTES) was successfully synthesised, immobilised and characterised using contact angle measurements, XPS. (chloromethyl)phenyltrichlorosilane (CMPTS) and APTES-BIBB were also deposited on a silicon dioxide and characterised using XPS and contact angle. In order to know the chemical conformation of the exposed regions of the SAMs, a photo-patterning of the SAMs was carried out using photolithography. The patterned surfaces were characterised by using AFM, XPS and contact angle measurements. It was found that photo-oxidation of CMPTS, photo-deprotection of NPPOC-protected silane and photo debromination of APTES-BIBB yielded carboxylic acid, free amino and some oxygen-containing functional group regions, respectively. To form nanometer structures, the SAM films were patterned, using IL at an angle of 10° and 30° . PolyCysMA brushes were grown on the patterned SAMs using SI-ATRP. For 10° samples, AFM tapping mode images showed that the period of the features depends on the type of SAMs. However, a close similarity in the period could be observed for the 30° samples.

Cells were seeded onto the nanometre patterned PolyCysMA brushes and cultured for seven days. Fluorescence microscopy imaging was used to study the alignments and organisation of MSCs on the nanostructured and uniform brushes. It was found that both chemistry and morphology play an important role in changes in the distribution of focal adhesions and in the directionality of the actin filaments.

No cells were shown on the uniform brushes, suggesting a good resistance of the brushes to the cells. For 30° BIBB and CMPTS samples the cells were successfully attached, however, the stress fibres were long and thin and followed the direction of the features of the BIBB sample; this was less pronounced than was the case at the CMPTS sample. For 10° BIBB and CMPTS nanostructured, there was evidence of attachment and organisation of the cells, but the focal adhesions were less well defined and randomly distributed on the surfaces. For NPPOC 30° and especially 10° patterned samples the cells attached less successfully, suggesting that the chemical component of the sticky line played an important role in the disruption of the cell alignments.

8.3 Formation of Supported Lipid Bilayers on The Binary Patterned Gold nanodots/PCysMA Brushes

A binary structure consisting of patterned gold nanodots/CysMA brush was fabricated that could be used as a substrate to recreate a cell membrane environment. A gold film on an adhesive layer was prepared and functionalized with a photosensitive SAM (MUA or ODT). Gold nanostructures were formed using IL, with two orthogonal exposures of the SAMs, followed by etching the SAM-free regions. The high quality of the fabricated gold nanodots was confirmed by AFM tapping mode images. An ATRP initiator (BIBB-APTES) was synthesised and immobilised onto the regions (Ti or Cr) between gold nanodots, AFM, contact angle and XPS confirmed that the silane film was successfully formed in the targeted area. A new zwitterionic biocompatible brush (PolyCysMA) was grown from the initiated area by applying SI-ATRP method, the obtained binary gold nanodots/PolyCysMA brushes characterised by using AFM.

The height difference between the dots and dry polymer brushes suggested both of them will be equal in thickness after immersing in the lipid bilayer medium. The binary patterned samples were used to study supported lipid bilayers (SLBs) and the FRAP studies suggested a high quality of SLB on the patterned samples with a considerable diffusion coefficient and a mobile fraction.

8.4 Future Work

It would be interesting to further explore the conformation of various micrometre and nanometer PolyCysMA brushes in a mixture of solvents. The mixture could be made from both good and poor solvents with various concentrations. A transfer in the brush structure could be determined depending on the concentration of the solvents. It would also be useful to explore the effect of thickness on the brushes behaviour in different environments. This could be done by fabricating various micrometre and nanometer structures of the brushes with different thickness, using FFM to obtain friction data, characterising the data by applying contact mechanic models. These studies may enhance the fundamental understanding of the behaviour of the patterned brushes and could be used as a base to the candidate the brush be used in different physiological conditions.

It would also be interesting to further investigate the morphology and chemistry effect of the nanometer patterned PolyCysMA brushes on alignment and organisation of MSCs, using different cultivation time. The cultivation times could start from a very short period of a very long period, including more than a week and month. Not only the stem cells but also different types of cells could be grown on the patterned brushes. Patterned polymer brushes with different thickness could also be fabricated, for instance, 2.0 nm -70.0 nm brushes, and their effects on the cell adhesion can be investigated. Bilayer brushes could also be used, by growing a sticky (fouling) brush between nanometer lines of PolyCysMA. The height difference between both brushes can be controlled by controlling polymerization times, also different morphology can be explored, using AFM, XPS and fluorescence microscopy to characterise the surfaces.

It would be useful to further investigate the mobility and diffusion behaviour of SLBs on a bilayer of gold nanometer lines/ PolyCysMA brushes.

Various gold nanostructures could be fabricated by changing the exposure angle in IL. This also is true for fabricating gold nanodots with different periodicity and widths.

The diffusion coefficient and moving of SLBs around the patterned lines or dots could be investigated using FRAM. The advantage of using nano lines is that the diffusion of the lipids on these structures could be limited and become unidirectional, this may help the formation of the high-quality lipid bilayer. Also, a bilayer of POEGMA/PolyCysMA brushes can be fabricated and used as a substrate to grow cell membrane. Interference lithography can be used to fabricate various nanometer and micrometre structures of the bilayer brushes, then the morphology and chemistry effect on the diffusion and mobility of the SLBs could be investigated.

References

1. Azzaroni, O. Polymer Brushes Here, There, and Everywhere: Recent Advances in Their Practical Applications and Emerging Opportunities in Multiple Research Fields. *J. Polym. Sci. Part A: Polym. Chem.* 2012, **50**, 3225–3258.
2. Santer, S.; Ruhe, J. Motion of nano-objects on polymer brushes. *Polymer* 2004, **45**, 8279–8297.
3. Ulman, A. Formation and Structure of Self-Assembled Monolayers. *Chem. Rev.* 1996, **96**, , 1533–1554.
4. Park, E. J.; Carroll, G. T.; Turro, N. J.; Koberstein, J. T. Shedding light on surfaces—using photons to transform and pattern material surfaces. *J. T. Soft Matt.* 2009, **5**, 36–50.
5. Sun, S.; Chong, K. S.; Leggett, G. J.; Photopatterning of self-assembled monolayers at 244 nm and applications to the fabrication of functional microstructures and nanostructures, *Nanotechnology* 2005, **16**, 1798–1808.
6. Gooding, J. J.; Mearns, F.; Yang, W.; Liu, J. Self-Assembled Monolayers into the 21st Century: Recent Advances and Applications *J. Electroanalysis* 2003, **15**, 81-96.
7. Tour, J. M.; Jones, L.; Pearson, D. L.; Lamba, J. J.; Burgin, T. P.; Whitesides, G. M.; Allara, D. L.; Parikh, A. N.; Atre, S. Self-Assembled Monolayers and Multilayers of Conjugated Thiols, α , ω -Dithiols, and Thioacetyl-Containing Adsorbates. Understanding Attachments between Potential Molecular Wires and Gold Surfaces. *J. Am. Chem. Soc.* 1995, **117**, 9529-9534.
8. Buckholtz, G. A.; Gawalt, E. S. Effect of Alkyl Chain Length on Carboxylic Acid SAMs on Ti-6Al-4V. *Materials* 2012, **5**, 1206-1218.
9. Bigelow, W. C.; Pickett, D. L.; Zisman, W. A. Oleophobic monolayers Films adsorbed from solution in non-polar liquids. *J. Colloid Interface Sci.* 1946, **1**, 513-538.
10. Sagiv, J.; Organized Monolayers by Adsorption, I. Formation and Structure of Oleophobic Mixed Monolayers on Solid Surfaces. *J. Am. Chem. Soc.* 1980, **102**, 92-98.
11. Nuzzo, R. G.; Allara, D. L. Adsorption of Bifunctional Organic Disulfides on Gold Surfaces. *J. Am. Chem. Soc.* 1983, **105**, 4481-4483.

-
12. Folkers, J. P.; Laibinis, P. E.; Whitesides, G. M. Self-assembled Monolayers of Alkanethiols on Gold: Comparisons of Monolayers Containing mixture of short- and long chain constituents with CH₃ and CH₂OH terminal groups. *Langmuir* 1992, **5**, 1331-1341.
 13. Love, J. C.; Estroff, L. A.; Kriebel, J. K.; Nuzzo, R. G.; Whitesides, G. M. Self-Assembled Monolayers of Thiolates on Metals as a Form of Nanotechnology. *Chem. Rev. Columbus* 2005, **105**, 1103-1169.
 14. Rhinow, D.; Hampp, N. A.; Patterned self-assembled monolayers of alkanethiols on copper nanomembranes by submerged laser ablation. *Appl. Phys. A* 2012, **107**, 755-759.
 15. Ulman, A.; Kang, J. F.; Shnidman, Y.; Liao, S.; Jordan, R.; Choi, G. Y.; Zaccaro, J.; Myerson, A. S.; Rafailovich, M. Sokolov, Self-assembled monolayers of rigid thiols. *J. Reviews in Molecular Biotechnol.* 2000, **74**, 175-188.
 16. Senaratne, W.; Andruzzi, L.; Ober, C. K. Self-assembled monolayers and polymer brushes in biotechnology: current applications and future perspectives. *Biomacromolecules* 2005, **6**, 2427-2448.
 17. Niemeyer, C. M.; Semisynthetic DNA-Protein Conjugates for Biosensing and Nanofabrication, *Angew. Chem. Int. Ed.* 2010, **49**, 1200 – 1216.
 18. Janssen, D.; De Palma, R.; Verlaak, S.; Heremans, P.; Dehaen, W. Static solvent contact angle measurements, surface free energy and wettability determination of various self-assembled monolayers on silicon dioxide. *Thin Solid Films* 2006, **515**, 1433–1438.
 19. Jain, S.; Tanwar, V.; Dixit, V.; Verma, S.; Samanta, S. Surface order and structure studies of polymer-solid interface. *Appl. surface science* 2001, **182**, 350-356.
 20. Schwartz, D. K.; mechanisms and kinetics of self-assembled Monolayer formation. *Annu. Rev. Phys. Chem.* 2001. **52**, 107–37.
 21. Kulkarni, S. A.; Mirji, S.; Mandale, A.; Gupta, R.; Vijayamohanan, K. P. Growth kinetics and thermodynamic stability of octadecyltrichlorosilane self-assembled monolayer on Si (100) substrate. *Mat. Lett.* 2005, **59**, 3890 – 3895.
 22. Meucci, S.; Gabrielli, G.; Caminati, G. Comparative investigation of Langmuir-Blodgett films and Self-Assembled Monolayers on metal surfaces. *Mat. Sci. Eng. C* 1999, **8**, 135–143.

-
23. Woodward, J. T.; Meuse, C. W. Mechanism of formation of vesicle fused phospholipid monolayers on alkanethiol self-assembled monolayer supports. *J. Colloid and Interface Sci.* 2009, **334**, 139–145.
 24. Lee, S.; Ishizaki, T.; Saito, N.; Takai, O. Effect of Reaction Temperature on Growth of Organosilane Self-Assembled Monolayers. *Jap. J. Appl. Phys.* 2008, **47**, . 6442–6447.
 25. Bush, B. G.; DelRio, F. W.; Opatkiewicz, J.; Maboudian, R.; Carraro, C. Effect of Formation Temperature and Roughness on Surface Potential of Octadecyltrichlorosilane Self-Assembled Monolayer on Silicon Surfaces, *The J. of Phys. Chem. A* 2007, **111**, 12339-12343.
 26. Kulkarni, S. A.; Mirji, S.A.; Mandale, A.B.; Gupta, R.P.; Vijayamohan, K. P. Growth kinetics and thermodynamic stability of octadecyltrichlorosilane self-assembled monolayer on Si (100) substrate. *Mate. Lett.* 2005, **59**, 3890 – 3895.
 27. Khatri, O. P.; Biswas, S.K.; Thermal stability of octadecyltrichlorosilane self-assembled on a polycrystalline aluminium surface. *Surf. Sci.* 2004, **572**, 228–238.
 28. Jayasundara, D. R.; Cullen, R. J.; Soldi, L.; Colavita, P. E. In Situ Studies of the Adsorption Kinetics of 4-Nitrobenzenediazonium Salt on Gold. *Langmuir* 2011, **27**, 13029–13036.
 29. Doudevski, I.; Schwartz, D. K. Concentration Dependence of Self-Assembled Monolayer Island Nucleation and Growth, *J. Am. Chem. Soc.* 2001, **123**, 6867-6872.
 30. Woodward, J. T.; Doudevski, I.; Sikes, H. D.; Schwartz, D. K. Kinetics of Self-Assembled Monolayer Growth Explored via Submonolayer Coverage of Incomplete Films. *J. Phys. Chem. B* 1997, **101**, 7535-7541.
 31. Jakubowicz, A.; Jia, H.; Wallace, R. M.; Gnade, B. E. Adsorption Kinetics of p-Nitrobenzenethiol Self-Assembled Monolayers on a Gold Surface. *Langmuir* 2005, **21**, 950-955.
 32. Bain, C. D.; Troughton, E. B.; Tao, Y. T.; Evall, J.; Whitesides, G. M.; Nuzzo, R. G. Formation of Monolayer Films by the Spontaneous Assembly of Organic Thiols from Solution onto Gold. *J. Am. Chem. Soc.* 1989, **111**, 321-335.

-
33. Ozlosnik, N.; Gerstenberg, M. C.; Larsen, N. B.; Effect of solvents and concentration on the formation of a self-assembled monolayer of octadecylsiloxane on silico. *Langmuir* 2003, **19**, 1182-1188.
34. Krasnoslobodtsev, A. V.; Smirnov, S. N.; Effect of Water on Silanization of Silica by Trimethoxysilanes. *Langmuir* 2002, **18**, 3181-3184.
35. Ahmad, S. A.; Wong, L.; Hobbs, J.; Leggett, G. J.; Micklefield, J. Micrometer- and nanometer-scale photopatterning using 2-nitrophenylpropyloxycarbonyl-protected aminosiloxane monolayers. *J. Am. Chem. Soc.* 2009, **131**, 1513–1522.
36. Arslan, G.; Özmen, M.; Gündüz, B.; Zhang, X.; Ersöz, M. Surface Modification of Glass Beads with an Aminosilane Monolayer. *Turkish J. Chem.* 2006, **30**, 203 – 210.
37. Fiorilli, S.; Rivolo, P.; Descrovi, E.; Ricciardi, C.; Pasquardini, L.; Lunelli, L.; Vanzetti, L.; Pederzoli, C.; Onida, B.; Garrone, E. Vapour-phase self-assembled monolayers of aminosilane on silicon substrates. *J. Coll. Interface Sci.* 2008, **321**, 235–241.
38. Kim, J.; Seidler, P.; Fill, C.; Wan, L. S. Investigations of the effect of curing conditions on the structure and stability of amino-functionalized organic films on silicon substrates by Fourier transform infrared spectroscopy, ellipsometry, and fluorescence microscopy. *Surf. Sci.* 2008, **602**, 3323–3330.
39. Cui, N. Y., Liu, C.; Yang, W. XPS and AFM characterization of the self-assembled molecular monolayers of a 3-aminopropyltrimethoxysilane on silicon surface, and effects of substrate pretreatment by UV-irradiation, *Surface and Interface Analysis* 2011, **43**, 1082–1088.
40. Kim, J.; Seidler, P.; Wan, L. S.; Fill, C. Formation, structure, and reactivity of amino-terminated organic films on silicon Substrates. *J. Coll. Interface Sci.* 2009, **329**, 114–119.
41. Arkles, B.; Steinmetz, J. R.; Zazyyczny, J. Z.; Mehta, P. Factors controlling to the stability of alkoxy silane in aqueous solution. *J. Adhesion Sci. Technol.* 1992, **91**-104
42. Altmann S.; Pfeiffer, J. The Hydrolysis Condensation Behaviour of Methacryloyloxyalkylfunctional Alkoxy silanes: Structure-Reactivity Relations. *Monatshefte für Chemie*, 2003, **134**, 1081–1092.
43. Johansson, U.; Holmgren, A.; Forsling, W.; Frost, R.; Adsorption of silane coupling agents onto kaolinite surfaces. *Clay Minerals* 1999, **34**, 239-246.

-
44. Zeng, X.; Xu, G.; Gao, Y.; An, Y. Surface Wettability of (3-Aminopropyl)triethoxysilane Self-Assembled Monolayers. *The J. Phys. Chem. B* 2011, **115**, 450–454.
 45. Owen, M.; Williams, D. Surface modification by fluoroalkyl-functional Silanes. *J. Adhesion Sci. Technol.* 1991, **5**, 307-320.
 46. Chirachanchai, S.; Chungchamroenkit, R.; Ishida, H. Adsorption of tetrasulfide-functional silane on high surface area silica treated with aqueous and non-aqueous solutions. *Composite Interfaces* 1998, **6**, 155-167.
 47. Chaki, N.K.; Aslam, M.; Sharma, J.; Vijayamohanan, K. Applications of self-assembled monolayers in materials Chemistry. *Indian Acad. Sci. (Chem. Sci)*, 2001, **113**, 659-670.
 48. Arsalan, G.; Ozmez, M.; Gunduz, B.; Zhangg, X.; Ersoz, M. Surface Modification of Glass Beads with an Aminosilane Monolayer. *Turk J Chem*, 2006, **30**, 203 -210.
 49. Leggett, G. J. Light-directed nanosynthesis: near-field optical approaches to integration of the top-down and bottom-up fabrication paradigms. *Nanoscale*, 2012, **4**, 1840–1855.
 50. Pirrung, M. C.; Dore, T. M.; Zhub, Y.; Rana, V. S.; Sensitized two-photon photochemical deprotection. *Chem. Commun.* 2010, **46**, 5313–5315.
 51. Bhushan, K. R.; DeLisia C.; Laursen, R. A. Synthesis of photolabile 2-(2-nitrophenyl)propyloxycarbonyl protected amino acids. *Tetrahedron Lett.* 2003, **44**, 8585–8588.
 52. Dendane, N.; Hoang, A.; Guillard, L.; Defrancq, E.; Vinet, F.; Dumy, P.; Efficient Surface Patterning of Oligonucleotides Inside a Glass Capillary through Oxime Bond Formation. *Bioconjugate Chem.* 2007, **18**, 671–676.
 53. M. Beier, J. D. Hoheisel, Production by Quantitative Photoleithographic synthesis of individually quality checked DNA Microarray. *Nucleic Acid Research* 2000, **28** (4), 1-6.
 54. Azzaroni, O.; Polymer brushes here, there, and everywhere: Recent advances in their practical applications and emerging opportunities in multiple research fields. *J. Polym. Sci. Part A: Polym. Chem.* 2012, **50**, 3225–3258.
 55. Kim, M.; Schmitt, S. K.; Choi, J. W.; Krutty, J. D.; Gopalan, P. From Self-Assembled Monolayers to Coatings: Advances in the Synthesis and Nanobio Applications of Polymer Brushes. *Polymers* 2015, **7**, 1346-1378.

-
56. Pyun, J.; Kowalewski, T.; Matyjaszewski, K. Synthesis of Polymer Brushes Using Atom Transfer Radical Polymerization. *Macromol. Rapid Commun* 2003, **24**, 1043–1059
57. Tang, C.; Kowalewski, T.; Matyjaszewski, K. Preparation of Polyacrylonitrile-block-poly(*n*-butyl acrylate) Copolymers Using Atom Transfer Radical Polymerization and Nitroxide Mediated Polymerization Processes. *Macromolecules* 2003, **36**, 1465-1473.
58. Nuyken, O.; Pask, S. D. Ring-Opening Polymerization—An Introductory Review. *Polymers* 2013, **5**, 361-403.
59. Zhang, Z.; Wang, W.; Xia, H.; Zhu, J.; Zhang, W.; Zhu, X. Single-Electron Transfer Living Radical Polymerization (SET-LRP) of Methyl Methacrylate (MMA) with a Typical RAFT Agent as an Initiator. *Macromolecules* 2009, **42**, 7360–7366.
60. Mor, H. Living Radical Polymerization: Reversible Addition-Fragmentation Chain Transfer (RAFT) Polymerization. *Encyclopedia of Polym. Nanomater.* 2014, 1-9
61. Jenkins, A. D.; Jones, R. G.; Moad, G. Terminology for reversible-deactivation radical polymerization previously called “controlled” radical or “living” radical polymerization. *Pure Appl. Chem.* 2010, **82**, 483–491.
62. Singh, N.; Wang, J.; Ulbricht, M.; Wickramasinghe, S. R.; Husson, S. M. Surface-initiated atom transfer radical polymerization: A new method for preparation of polymeric membrane adsorbers. *Journal of Membrane Science* 2008, **309**, 64–72.
63. Matyjaszewski, K.; Xia, J. Atom Transfer Radical Polymerization. *Chem. Rev.* 2001, **101**, 2921–2990.
64. Edmondson, S.; Osborne, V. L.; Huck, W. T. S. Polymer brushes via surface-initiated polymerizations. *Chem. Soc. Rev.* 2004, **33**, 14–22.
65. Fristrup, C. J.; Jankova, K.; Hvilsted, S. Surface-initiated atom transfer radical polymerization—a technique to develop biofunctional coatings. *Soft Matt.* 2009, **5**, 4623–4634.
66. Zhong, M.; Wang, Y.; Krys, P.; Konkolewicz, D.; Matyjaszewski, K. Reversible-Deactivation Radical Polymerization in the Presence of Metallic Copper. *Kinetic Simulation. Macromolecules* 2013, **46**, 3816–3827.

-
67. Luzinov, I.; Minko, S.; Tsukruk, V. V. Adaptive and responsive surfaces through controlled reorganization of interfacial polymer layers. *Prog. Polym. Sci.* 2004, **29**, 635–698.
 68. Currie, E.P.K.; Norde, W.; Stuart M.A.C. Tethered polymer chains: surface chemistry and their impact on colloidal and surface properties. *Advances in Coll. Interface Sci.* 2003, **100** – **102**, 205–265.
 69. Wu, J.; Mao, Z.; Tan, H.; Han, L.; Ren, T.; Gao, C. Gradient biomaterials and their influences on cell migration. *Interface Focus* 2012, **2**, 337–355
 70. Brittain, W. J.; Minko, S. A Structural Definition of Polymer Brushes. *Journal of Polymer Science: Part A: Polymer Chemistry* 2007, **45**, 3505–3512.
 71. Dumont, E. L. P.; Belmas, H.; Hess, H. Observing the Mushroom-to-Brush Transition for Kinesin Proteins. *Langmuir* 2013, **29**, 15142–15145.
 72. Elmahdy, M. M.; Drechsler, A. Uhlmann, P.; Stamm, M. Swelling and Surface Interactions of End-Grafted Poly(2-vinylpyridine) Layers in Acidic Solution: Influence of Grafting Density and Salt Concentration. *Langmuir* 2016, **32**, 5451–5459.
 73. Zdyrko, B.; Klep, V.; Luzinov, I. Synthesis and Surface Morphology of High-Density Poly(ethylene glycol) Grafted Layers. *Langmuir* 2003, **19**, 10179-10187.
 74. Penn, L. S.; Huang, H.; Sindkhedkar, M. D.; Rankin, S. E.; Chittenden, K. Formation of Tethered Nanolayers: Three Regimes of Kinetics. *Macromolecules* 2002, **35**, 7054-7066.
 75. Penn, L. S.; Hunter, T. F.; Lee, Y.; Quirk, R. P. Grafting Rates of Amine-Functionalized Polystyrenes onto Epoxidized Silica Surfaces. *Macromolecules* 2000, **33**, 1105-1107.
 76. Quirk, R. P.; Cheong, T. H. Transition from Mushroom to Brush during Formation of a Tethered Layer. *Langmuir* 2004, **20**, 5770-5775.
 77. Bao, Z.; Bruening, M. L.; Baker, G. L. Control of the Density of Polymer Brushes Prepared by Surface-Initiated Atom Transfer Radical Polymerization. *Macromolecules* 2006, **39**, 5251-5258.
 78. Wu, T.; Efimenko, K.; Genzer, J. Combinatorial Study of the Mushroom-to-Brush Crossover in Surface Anchored Polyacrylamide. *J. . Am. Chem. Soc.* 2002, **124**, 9394-9395.

-
79. Wu, T.; Gong, P.; Szleifer, I.; Vlċek, P.; Ṡubr, V.; Genzer, J. Behavior of Surface-Anchored Poly(acrylic acid) Brushes with Grafting Density Gradients on Solid Substrates: 1. Experiment. *Macromolecules* 2007, **40**, 8756-8764.
80. Liu, Y.; Klep, V.; Zdyrko, B.; Luzinov, I. Polymer Grafting via ATRP Initiated from Macroinitiator Synthesized on Surface. *Langmuir* 2004, **20**, 6710-6718.
81. Jones, D. M.; Brown, A. A.; Huck, W. T. S. Surface-Initiated Polymerizations in Aqueous Media: Effect of Initiator Density. *Langmuir* 2002, **18**, 1265-1269.
82. Lilge, I.; Schönherr, H. Control of Cell Attachment and Spreading on Poly(acrylamide) Brushes with Varied Grafting Density. *Langmuir* 2016, **32**, 838-847.
83. Patil, R. R.; Turgman-Cohen, S.; Šrogl, J.; Kiserow, D.; Genzer, J. On-Demand Degrafting and the Study of Molecular Weight and Grafting Density of Poly(methyl methacrylate) Brushes on Flat Silica Substrates. *Langmuir* 2015, **31**, 2372-2381.
84. Yamamoto, S.; Ejaz, M.; Tsujii, Y.; Fukuda, T. Surface Interaction Forces of Well-Defined, High-Density Polymer Brushes Studied by Atomic Force Microscopy. 2. Effect of Graft Density. *Macromolecules* 2000, **33**, 5608-5612.
85. Steenackers, M.; Kuller, A.; Ballav, N.; Zharnikov, M.; Grunze, M.; Jordan, R. Morphology Control of Structured Polymer Brushes. *small* 2007, **3**, 1764 - 1773.
86. Chen, T.; Amin, I.; Jordan, R.; Patterned Polymer Brushes. *Chem. Soc. Rev.* 2012, **41**, 3280-3296.
87. Yu, Q.; Ista, L. K.; Gu, R.; Zauscherc, S.; López, G. P. Nanopatterned polymer brushes: conformation, fabrication and applications. *Nanoscale* 2016, **8**, 680-700
88. Kettling, F.; Vonhören, B.; Krings, J. A.; Saitob, S.; Ravoo, B. J. One-step synthesis of patterned polymer brushes by photocatalytic microcontact printing. *Chem. Commun.* 2015, **51**, 1027-1030.
89. Gao, T.; Wang, X.; Yu, B.; Wei, Q.; Xia, Y.; Zhou, F. Noncovalent Microcontact Printing for Grafting Patterned Polymer Brushes on Graphene Films. *Langmuir* 2013, **29**, 1054-1060.
90. Piner, R. D.; Zhu, J.; Xu, F.; Hong, S.; Mirkin, C. A. Dip-Pen Nanolithography. *Science* 1999, **283 (29)**, 661-663.

-
91. Liu, X.; Guo, S.; Mirkin, C. A. Surface and Site-Specific Ring-Opening Metathesis Polymerization Initiated by Dip-Pen Nanolithography. *Angew. Chem. Int. Ed.* 2003, **42**, 4785–4789.
 92. Kaholek, M.; Lee, W.; LaMattina, B.; Caster, K. C.; Zauscher, S. Fabrication of Stimulus-Responsive Nanopatterned Polymer Brushes by Scanning-Probe Lithography. *Nano Lett.* 2004, **4** (2), 373-376.
 93. Rastogi, A.; Paik, M. Y.; Tanaka, M.; Ober, C. K. Direct Patterning of Intrinsically Electron Beam Sensitive Polymer Brushes. *ACS NANO* 2010, **4** (2), 771–780.
 94. Nie, Z.; Kumacheva, E. Patterning surfaces with functional polymers. *Nat. Mater.* 2008, **7**, 277-290.
 95. Ahmad, S. A.; Leggett, G. J.; Hucknall, A.; Chilkotic, A. Micro- and nanostructured poly[oligo(ethylene glycol)methacrylate] brushes grown from photopatterned halogen initiators by atom transfer radical polymerization. *Biointerphases* 2011, **6**, 8-15.
 96. Cimen, D.; Caykara, T. Micro-patterned polymer brushes by a combination of photolithography and interface-mediated RAFT polymerization for DNA hybridization. *Polym. Chem.* 2015, **6**, 6812–6818.
 97. Watson, H. Biological membranes. *Essays in Biochem.* 2015, **59**, 43-69.
 98. Han, X.; Qi, G.; Xu, X.; Wang, L. Lipid Bilayer Membrane Arrays: Fabrication and Applications. *Future Trends in Biotechn.* 2012, **131**, 121-152.
 99. Katsaras, J.; Kučerka, N.; Nieh, M. Structure from substrate supported lipid bilayers. *Biointerphases* 2008, **3**, FB55-FB63.
 100. Munro, J. C.; Frank, C. W. In Situ Formation and Characterization of Poly(ethylene glycol)-Supported Lipid Bilayers on Gold Surfaces. *Langmuir* 2004, **20**, 10567-10575.
 101. Diamanti, E.; Gregurec, D.; Rodríguez-Presa, M. J.; Gervasi, C. A.; Azzaroni, O.; Moya, S. E. High Resistivity Lipid Bilayers Assembled on Polyelectrolyte Multilayer Cushions: An Impedance Study. *Langmuir* 2016, **32**, 6263–6271.
 102. Terrettaz, S.; Mayer, M.; Vogel, H. Highly Electrically Insulating Tethered Lipid Bilayers for Probing the Function of Ion Channel Proteins. *Langmuir* 2003, **19**, 5567-5569.

-
103. Yoshina-Ishii, C.; Boxer, S. G. Arrays of Mobile Tethered Vesicles on Supported Lipid Bilayers. *J. Am Chem. Soc.* 2003, **125**, 3696-3697.
104. Richter, R. P.; Him, J. L. K.; Brisson A. Supported Lipid Membranes. *Materialstoday* 2003, 32-37.
105. Rozovsky, S.; Forstner, M. B.; Sondermann, H.; Groves, J. T. Single Molecule Kinetics of ENTH Binding to Lipid Membranes. *J. Phys. Chem. B* 2012, **116**, 5122–5131.
106. Cheng, N.; Bao, P.; Evans, S.D.; Leggett, G. J.; Armes, S. P. Facile Formation of Highly Mobile Supported Lipid Bilayers on Surface-Quaternized pH-Responsive Polymer Brushes. *Macromolecules* 2015, **48**, 3095–3103.
107. McCabe, I. P.; Forstner, M. B. Polymer Supported Lipid Bilayers. *J. Biophys.* 2013, **3**, 59-69
108. Jin, Y.; Qiao, Y.; Hou, X. The effects of chain number and state of lipid derivatives of nucleosides on hydrogen bonding and self-assembly through the investigation of Langmuir–Blodgett films. *Appl. Surf. Sci.* 2006, **252**, 7926–7929.
109. Shen, W. W.; Boxer, S. G.; Knoll, W.; Frank, C. W. Polymer-Supported Lipid Bilayers on Benzophenone-Modified Substrates. *Biomacromolecules* 2001, **2**, 70-79.
110. Wang, L.; Roth, J. S.; Han, X.; Evans, S. D. Photosynthetic Proteins in Supported Lipid Bilayers: Towards a Biokleptic Approach for Energy Capture. *small* 2015, **11(27)**, 3306–3318.
111. Johnson, M. J.; Ha, T.; Chu, S.; Boxer, S. G. Early Steps of Supported Bilayer Formation Probed by Single Vesicle Fluorescence Assays. *Biophysical Journal* 2002, **83**, 3371–3379
112. Castellana, E. T.; Cremer, P. S. Solid supported lipid bilayers: From biophysical studies to sensor design *Surface Science Reports* 2006, **61**, 429–444.
113. Rädler, J.; Strey, H.; Sackmanns, E. Phenomenology and Kinetics of Lipid Bilayer on Hydrophilic Surfaces Spreading. *Langmuir* 1995, **11**, 4539-4548.
114. Marquês, J. T.; R.F.Mde Almeida, R. F. M.; Viana, A.S. Lipid bilayers supported on bare and modified gold –Formation, characterization and relevance of lipid rafts. *Electrochimica Acta* 2014, **126**, 139–150.

-
115. Blakeston, A. C.; Alswieleh, A. M.; Heath, G. R.; J. S.; Bao, P.; Cheng, N.; Armes, S. P.; Leggett, G. J.; Bushby, R. J.; Evans, S. D. New Poly(amino acid methacrylate) Brush Supports the Formation of Well-Defined Lipid Membranes. *Langmuir* 2015, **31**, 3668-3677.
116. Albertorio, F.; Diaz, A. J.; Yang, T.; Chapa, V. A.; Kataoka, S.; Castellana, E. T.; Cremer, P. S. Fluid and Air-Stable Lipopolymer Membranes for Biosensor Applications. *Langmuir* 2005, **21**, 7476-7482.
117. DeMond, A. L.; Mossman, K. D.; Starr, T.; Dustin, M. L.; Groves, J. T.; T Cell Receptor Microcluster Transport through Molecular Mazes Reveals Mechanism of Translocation. *Biophys. J.* 2008, **94**, 3286–3292.
118. Jackson, B. L.; Groves, J. T. Scanning Probe Lithography on Fluid Lipid Membranes. *Am. Chem. Soc.* 2004, **126**, 13878–13879.
119. Hughes, L. D.; Boxer, S, G. DNA-based patterning of tethered membrane patches. *Langmuir* 2013, **29**, 1-16
120. Orth, R. N.; Kameoka, J.; Zipfel, W. R.; Ilic, B.; Webb, W. W.; Clark, T. G.; Craighead, H.G. Creating Biological Membranes on the Micron Scale: Forming Patterned Lipid Bilayers Using a Polymer Lift-Off Technique. *Biophys. J.* 2003, **85**, 3066–3073.
121. Morigaki, K.; Baumgart, T.; Offenhäusser, A.; Knoll, W. Patterning Solid-Supported Lipid Bilayer Membranes by Lithographic Polymerization of a Diacetylene Lipid. *Angew. Chem. Int. Ed.* 2001, **40**, 172-174.
122. Lei, M.; Wang, X.; Biodegradable Polymers and Stem Cells for Bioprinting. *Molecules* 2016, **21**, 539-553.
123. Nurlina, W.; Yahya, W.; Kadri, N. A.; Ibrahim, F. Cell Patterning for Liver Tissue Engineering via Dielectrophoretic Mechanisms. *Sensors* 2014, **14**, 11714-11734.
124. Wu, J.; Mao, Z.; Tan, H.; Han, L.; Ren, T.; Gao, C. Gradient biomaterials and their influences on cell migration. *Interface Focus* 2012, **2**, 337–355.
125. Falconnet, D.; Csucs, G.; Grandin, H. M.; Textor, M. Surface engineering approaches to micropattern surfaces for cell-based assays. *Biomaterials* 2006, **27**, 3044–3063.
126. Nelson, C. M.; Tien, J. Microstructured extracellular matrices in tissue engineering and development. *Current Opinion in Biotechnology* 2006, **17**, 518–523.

-
127. Khan, F.; Tanaka, F.; Ahmad, S. R. Fabrication of polymeric biomaterials: a strategy for tissue engineering and medical devices. *J. Mater. Chem. B* 2015, **3**, 8224–8249.
128. Ma, Z.; Mao, Z.; Gao, C. Surface modification and property analysis of biomedical polymers used for tissue engineering. *Colloids and Surfaces B: Biointerfaces* 2007, **60**, 137–157.
129. Moroni, L.; Gunnewiek, M. K.; Benetti, E. M. Polymer brush coatings regulating cell behavior: Passive interfaces turn into active. *Acta Biomaterialia* 2014, **10**, 2367–2378.
130. Alves, M. M.; Pashkuleva, I.; Reis, R. L.; Mano, J. F. Controlling Cell Behavior Through the Design of Polymer Surfaces. *small* 2010, **6 (20)**, 2208–2220.
131. Wu, J.; Mao, Z.; Tan, H.; Han, L.; Ren, T.; Gao, C. Gradient biomaterials and their influences on cell migration. *Interface Focus* 2012, **2**, 337–355.
132. Wilkinson, C.D.W.; Riehle, M.; Wood, M.; Gallagher, Curtis, A.S.G. The use of materials patterned on a nano- and micro-metric scale in cellular engineering. *Mat. Sci. and Eng. C* 2002, **19**, 263–269.
133. Altomare, L.; Riehle, M.; Gadegaard, N.; Tanzi, M.; Farè, S. Microcontact printing of fibronectin on a biodegradable polymeric surface for skeletal muscle cell orientation. *The Int. J. Artif. Organs* 2010, **33**, 535-543.
134. Gautrot, J. E.; Trappmann, B.; Ocegüera-Yanez, F.; Connelly, J.; He, X.; Watt, F. M.; Huck, W. T. S. Exploiting the superior protein resistance of polymer brushes to control single cell adhesion and polarisation at the micron scale. *Biomaterials* 2010, **31**, 5030-5041
135. Tan, K. Y.; Lin, H.; Ramstedt, M.; Watt, F. M.; Huckae, W. T. S.; Gautrot, J. E. Decoupling geometrical and chemical cues directing epidermal stem cell fate on polymer brush-based cell micro-patterns. *Integrative Biology* 2013, **5**, 899-910.
136. Milner, K. R.; Siedlecki, C. A. Fibroblast response is enhanced by poly(L-lactic acid) nanotopography edge density and proximity. *Int. J. Nanomedicine* 2007, **2**, 201–211.
137. Sun, T.; Kovac, J.; Voldman, J. Image-Based Single-Cell Sorting via Dual-Photopolymerized Microwell Arrays. *Analy. Chem.* 2014, **86**, 977–981.

-
138. Peng, R.; Yao, X.; Ding, J. Effect of cell anisotropy on differentiation of stem cells on micropatterned surfaces through the controlled single cell adhesion. *Biomaterials* 2011, **32**, 8048-8057.
139. Revzin, A.; Tompkins, R. J.; Toner, M. Surface Engineering with Poly(ethylene glycol) Photolithography to Create High-Density Cell Arrays on Glass. *Langmuir* 2003, **19**, 9855-9862.
140. Strehmel, C.; Perez-Hernandez, H.; Zhang, Z.; Löbus, S.; Lasagni, A. F.; Lensen, M. C. Geometric Control of Cell Alignment and Spreading within the Confinement of Antiadhesive Poly(Ethylene Glycol) Microstructures on Laser-Patterned Surfaces. *ACS Biomater. Sci. Eng.* 2015, **1**, 747–752.
- 141 Harris, B. P.; Kutty, J. K.; Fritz, E. W.; Webb, C. K.; Burg, K. J. L.; Metters, A. T.; Photopatterned Polymer Brushes Promoting Cell Adhesion Gradients. *Langmuir* 2006, **22**, 4467-4471.
142. Zhou, Z.; Yu, P.; Geller, H. M.; Ober, C. K. Biomimetic Polymer Brushes Containing Tethered Acetylcholine Analogs for Protein and Hippocampal Neuronal Cell Patterning. *Biomacromolecules* 2013, **14**, 529–537.
143. Loesberg, W.A.; te Riet, J.; van Delft, F.C.M.J.M.; Schon, P.; Figdor, C.G.; Speller, S.; van Loone, J.J.W.A.; Walboomers, X.F.; Jansen, J.A. The threshold at which substrate nanogroove dimensions may influence fibroblast alignment and adhesion. *Biomaterials* 2007, **28**, 3944–3951.
144. Gadegaard, N.; Martines, E.; Riehle, M.O.; Seunarine, K.; Wilkinson, C.D.W. Applications of nano-patterning to tissue engineering. *Microelectronic Eng.* 2006, **83**, 1577–1581.
145. Dalby, M. J.; Riehle, M. O.; Sutherland, S.; Agheli, H.; Curtis, A. S. G. morphological and microarray analysis of human fibroblasts cultured on nanocolumns produced by colloidal lithography. *M J Dalby et al. Eur. Cells and Mat.* 2005, **9**, 1-8.
146. Bhushan, B. Nanotribology, nanomechanics and nanomaterials characterization. *Phil. Trans. R. Soc. A* 2008, **366**, 1351–1381.

-
147. Rana, N. ; Kossow, C.; Eisenbraun, E. T.; Geer R. E.; Kaloyeros, A. E. Controlling Interfacial Adhesion of Self-Assembled Polypeptide Fibrils for Novel Nanoelectromechanical System (NEMS) Applications. *Micromachines* 2011, **2**, 1-16.
148. Affatato, S.; Spinelli, M.; Zavalloni, M.; Mazzega-Fabbro, C.; Viceconti, M. Tribology and total hip joint replacement: Current concepts in mechanical simulation. *Medical Eng. Phys.* 2008, **30**, 1305–1317.
149. Palacio, M.; Bhushan, B. Wear detection of candidate MEMS/NEMS lubricant films using atomic force microscopy-based surface potential measurements. *Scripta Materialia* 2007, **57**, 821–824.
150. Beake, B. D.; Goodes S. R.; Shi, B. Nanomechanical and nanotribological testing of ultra-thin carbon-based and MoST films for increased MEMS durability. *J. Phys. D: Appl. Phys.*, 2009, **42**, 065301.
151. Bhushan, B. Nanotribology and nanomechanics. *Wear* 2005, **259**, 7-12, 1507-1531.
152. Mo, Y.; Yang, M.; Lu, Z.; Huang, F. Preparation and tribological performance of chemically-modified reduced graphene oxide/polyacrylonitrile composites. *Composites: Part A* 2013, **54**, 153–158.
153. Zhang Q.; Archer, L. A. Interfacial Friction of Surfaces Grafted with One- and two-component Self-Assembled Monolayers. *Langmuir* 2005, **21**, 5405-5413.
154. Schwartz, D. K.; mechanisms and kinetics of self-assembled monolayer formation. *Annu. Rev. Phys. Chem.* 2001, **52**, 107–37.
155. Vericat, C.; Vela, M. E.; Benitez, G.; Carrob P.; Salvarezza, R. C. Self-assembled monolayers of thiols and dithiols on gold: new challenges for a well-known system. *Chem. Soc. Rev.* 2010, **39**, 1805–1834.
156. Maboudian, R.; Ashurst W. R.; Carraro, C. Tribological challenges in micromechanical systems. *Tribology Letters* 2002, **12**, 2, 95.
157. Vyas, M. K.; Schneider, K.; Nandan, B.; Stamm, M. Switching of friction by binary polymer brushes. *Soft Matt.* 2008, **4**, 1024–1032.
158. Beer, S.; Müser, M. H. Friction in Miscible Polymer Brush Systems and the Role of Transverse Polymer Tilting. *Macromolecules* 2014, **47**, 7666–7673.

-
159. Kreer, T. Polymer-brush lubrication: a review of recent theoretical advances. *Soft Matt.* 2016, **12**, 3479-3501.
160. Urbakh, M.; Klafter, J.; Gourdon, D.; Israelachvili, J. The nonlinear nature of friction. *Nature* 2004, **430**, 525.
161. Gao, J.; Luedtke, W. D.; Gourdon, D.; Ruths, M.; Israelachvili, J. N.; Landman, U. Frictional Forces and Amontons' Law: From the Molecular to the Macroscopic Scale. *J. Phys. Chem. B*, 2004, **108**, 3410-3425.
162. Hansson, P. M.; Claesson, P. M.; Swerin, A.; Briscoe, W. H.; Schoelkop, J.; Ganede P. A. C.; Thormannw, E. Frictional forces between hydrophilic and hydrophobic particle coated nanostructured surfaces. *Phys. Chem. Chem. Phys.*, 2013, **15**, 17893—17902.
163. Bowden F. P.; Tabor, D. *The Friction and Lubrication of Solids*, New York: Oxford Univ. Press, 1950. 337.
- 164- Greenwood, J.A., Williamson, J.B.P. Contact of Nominally Flat Surfaces. *Proc R. Soc London A*, 1966, **295**, 300-319.
165. Landau, L.D., and Lifshitz E. M, *Introduction into Theoretical Physics vol 7* (moscow:Nauka)
166. Yosbizawa H.; Israelachvili, J. Fundamental Mechanisms of Interfacial Friction. 2. Stick-Slip Friction of Spherical and Chain Molecules. *J. Phys. Chem.*, 1993,**97**, 11300-1 1313.
167. Beer, S.; Kenmoe, G. D.; Muser, M. H. On the friction and adhesion hysteresis between polymer brushes attached to curved surfaces: Rate and solvation effects. *Friction* 2015, **3**, 148–160.
168. Brukman, M. J.; Marco, G. O.; Dunbar, T. D.; Boardman, L. D.; Carpick, R. W. Nanotribological Properties of Alkanephosphonic Acid Self-Assembled Monolayers on Aluminum Oxide: Effects of Fluorination and Substrate Crystallinity. *Langmuir* 2006, **22**, 3988-3998.
169. Ikouchi, K.; Kouchiyama, M.; Tomita, N.; Uyama, Y.; Ikada, Y. Friction control with a graft layer of a thermo-sensing polymer. *Wear* 1996, **199**, 197-201.

-
170. Flater, E. E.; Ashurst, W. R.; Carpick, R. W. Nanotribology of Octadecyltrichlorosilane Monolayers and Silicon: Self-Mated versus Unmated Interfaces and Local Packing Density Effects, *Langmuir* 2007, **23**, 9242-9252.
171. Carpick, R. W.; Agraït, N.; Ogletree, D. F.; Salmeron, M. Measurement of interfacial shear (friction) with an ultrahigh vacuum atomic force microscope. *J. Vac. Sci. Technol. B* 1996, **14**, 1289-1295.
172. Noy, A.; Frisbie, C. D.; Rozsnyai, L. F.; Wrighton, M. S.; Liebe, C. M. Chemical Force Microscopy: Exploiting Chemically-Modified Tips To Quantify Adhesion, Friction, and Functional Group Distributions in Molecular Assemblies. *J. Am. Chem. Soc.* 1995, **117**, 7943-7951.
173. Frisbie, C. D.; Rozsnyai, L. F.; Noy, A.; Wrighton, M. S.; Lieber, C. M. Functional Group Imaging by Chemical Force Microscopy. *Science* 1994, **265**, 2071.
174. Da Silva A. C., Deda D. K., da Róz A. L., Prado R. A., Carvalho C. C., Viviani V., Leite F.L. Nanobiosensors Based on Chemically Modified AFM Probes: A Useful Tool for Methyl Detection. *Sensors (Basel)* 2013, **13**, 2, 1477-89.
175. Ito, T.; Grabowska, I.; Ibrahim, S. Chemical-force microscopy for materials characterization. *Trends in Anal. Chem.* 2010, **29**, 225-232.
176. Nakagawa, T.; Ogana, K.; Kurumizawa, T.; Ozaki, S. Discriminating Molecular Length of Chemically Adsorbed Molecules Using an Atomic Force Microscope Having a Tip Covered with Sensor Molecules (An Atomic Force Microscope Having Chemical Sensing Function). *Jpn. J. Appl. Phys.*, 1993, **32**, L294-L296.
177. Beaussart, A.; Chinh, T.; Ngo, Derclaye, S.; Kalinova, R.; Mincheva, R.; Dubois, P.; Leclère, P.; Dufrene, Y. F. Chemical force microscopy of stimuli-responsive adhesive copolymers. *Nanoscale* 2014, **6**, 565-571.
178. Wang, Q. H.; Shih, C.; Paulus, G. L. C.; Strano, M. S. Evolution of Physical and Electronic Structures of Bilayer Graphene upon Chemical Functionalization. *J. Am. Chem. Soc.* 2013, **135**, 18866-18875.

-
179. Fujihira, M.; Tani, Y.; Furugori, M.; Akiba, U.; Okabe, Y. Chemical force microscopy of self-assembled monolayers on sputtered gold films patterned by phase separation. *Ultramicroscopy*, 2001, **86**, 63-73.
180. Dordi, B.; Pickering, J. P.; Schönherr, H.; Vancso, G. J. Probing chemical reactions on the nanometer scale: Inverted chemical force microscopy of reactive self-assembled monolayers. *Surf. Sci.* 2004, **570**, 57–66.
181. Ederth, T.; Tamada, K.; Claesson, P. M.; Valiokas, R.; Colorado, R.; Graupe, J. M.; Shmakova, O. E.; Lee, T. R. Force Measurements between Semifluorinated Thiolate Self-Assembled Monolayers: Long-Range Hydrophobic Interactions and Surface Charge. *J. Coll. and Interface Sci.* 2001, **235**, 391–397.
182. Bastidas, J. C.; Venditti, R.; Pawlak, J.; Gilbert, R.; Zauscher, S.; Kadla, J. F. Chemical force microscopy of cellulosic fibers. *Carbohydrate Polymers*, 2005, **62**, 369–378.
183. Clear S. C.; Nealey, P. F. Chemical Force Microscopy Study of Adhesion and Friction between Surfaces Functionalized with Self-Assembled Monolayers and Immersed in Solvents. *J. Coll. and Interface Sci.* 1999, **213**, 238–250.
184. Beake, B. D., Leggett, G. J. Friction and adhesion of mixed self-assembled monolayers studied by chemical force microscopy. *Phys. Chem., Chem., Phys.*, 1999, **1**, 3345.
185. Brewer, N. J.; Beake, B. D.; Leggett, G. J. Friction Force Microscopy of Self-Assembled Monolayers: Influence of Adsorbate Alkyl Chain Length, Terminal Group Chemistry, and Scan Velocity. *Langmuir* 2001, **17**, 1970-1974.
186. Brewer, N. J.; Leggett, G. J. Chemical Force Microscopy of Mixed Self-Assembled Monolayers of Alkanethiols on Gold: Evidence for Phase Separation. *Langmuir* 2004, **20**, 4109-4115.
187. Gao, J.; Luedtke, W. D.; Gourdon, D.; Ruths, M.; Israelachvili, J. N.; Landman, U. Frictional Forces and Amontons' Law: From the Molecular to the Macroscopic Scale. *J. Phys. Chem. B* 2004, **108**, 3410-3425.
188. Raftari, M.; Zhang, Z.; Carter, S. R.; Leggett, G. J.; Geoghegan, M. Frictional properties of a polycationic brush. *Soft Matt.* 2014, **10**, 2759–2766.

-
189. Zhang, Z.; Morse, A. J.; Armes, S. T.; Lewis, A. L.; Geoghegan, M.; Leggett, G. J. Nanoscale Contact Mechanics of Biocompatible Polyzwitterionic Brushes. *Langmuir* 2013, **29**, 10684-10692.
190. Nikogeorgos, N.; Leggett, G. J. The Relationship Between Contact Mechanics and Adhesion in Nanoscale Contacts Between Non-Polar Molecular Monolayers. *Tribol. Lett.* 2013, **50**, 145-144.
191. Nikogeorgos, N.; Hunter, C. A.; Leggett, G. J. Relationship Between Molecular Contact Thermodynamics and Surface Contact Mechanics. *Langmuir*, 2012, **28**, 17709–17717.
192. Busuttill, K.; Nikogeorgos, N.; Zhang, Z.; Geoghegan, M.; Hunter, C. A.; Leggett, G. J. *Faraday Discuss* 2012, **156**, 325–341.
193. Barthel, A. J.; Al-Aziz, A.; Kim, S. H. Fundamental Understanding of Environmental Effects on Adhesion and Friction: Alcohol and Water Adsorption Cases. *Tribol. Lett.* 2013, **50**, 157-168.
194. Tirrell, M. Measurement of Interfacial Energy at Solid Polymer Surfaces. *Langmuir* 1996, **12**, 4548-4551.
195. Carpick, R. W.; Salmeron, M. Scratching the Surface: Fundamental Investigations of Tribology with Atomic Force Microscopy. *Chem. Rev.* 1997, **97**, 1163-1194.
196. Persson, B.N.J.; Albohr, O.; Tartaglino, U.; Volokitin, A.L.; Tosatti, E. On the nature of surface roughness with application to contact mechanics, sealing, rubber friction and adhesion. *J. Phys:condens Matt.* 2005, **17**, R1-R26.
197. Hertz, H. Uber die Berührung Fester Elastischer Korper. *Journal fur die reine und angewundte Mathematic* 1881, **92**, 156-171.
198. Johnson, K. L.; Kendall, K.; Roberts, A. D. Surface energy and contact of elastic solids *Proc. R. Soc. Lond A* 1971, **324**, 301-313.
199. Szlufarska, I.; Chandross, M.; Carpick, R.W. Recent advances in single-asperity Nanotribology. *J. Phys. D: Appl. Phys.*, 2008, **41**, 123001.
200. Derjaguin, B. V.; Muller, V. M.; Toporov. Y. U. P. Effect of Contact Deformations on the Adhesion of Particles. *J. Coll. and Interface Sci.* 1975, **53**, 314.

-
201. Tabor, D. Surface Forces and Surface Interactions. *J. Coll. and Interface Sci.* 1977, **58**, 2-13.
202. Grerson, D. S.; Flater, E. E.; Carpick, R. W. Accounting for the JKR–DMT transition in adhesion and friction measurements with atomic force microscopy. *J. Adhesion Sci. Technol.* 2005, **19**, 291–311.
203. Greenwood, J.A. Adhesion of elastic spheres. *Math. Phys. Eng. Sci.* 1977, **354**, 1277-1297.
204. Carpick, R.W.; Ogletree, D.F.; Salemron, M. A General Equation for Fitting Contact Area and Friction vs Load Measurement. *J. Coll. and Interface Sci.* 1999, **211**, 395-400.
205. Ruths, M.; Israelachvili, J. N. Surface Forces and Nanorheology of Molecularly Thin Films. *Nanotribol. and Nanomechanics* 2008, 417-515.
206. Vezenov, D. V.; Noy, A.; Rozsnyai, L. F.; Lieber, C. M. Force Titrations and Ionization State Sensitive Imaging of Functional Groups in Aqueous Solutions by Chemical Force Microscopy. *J. AM. Chem. Soc.* 1997, **119**, 2006-2015.
207. Wong, S.; Takano, H.; Porter, M. D. Mapping Orientation Differences of Terminal Functional Groups by Friction Force Microscopy. *Anul. Chem.*, 1998, **70**, 5209-5212.
208. Persson, B.N.J. Contact mechanics for layered materials with randomly rough surfaces. *J. Phys.: Condens. Matter* 2012, **24**, 095008
209. McGuiggan, P.M.; Wallace, J.S.; Smith, D.T.; Sridhar, I.; Zheng, Z. W.; Johnson, K.L. Contact mechanics of layered elastic materials: experiment and theory. *J. Phys. D: Appl. Phys.* 2007, **40**, 5984-5994.
210. Wang, M.; Liechti, K.M.; Srinivasan, V.; White, J.M.; Rossky, P. J.; Stone, T. M. nano mechanical analysis of IFM force profiles on self-assembled monolayers. *J. Phys. Mec.* 2004, 2-12.
211. Kanber, B.; Damerhan, M. Finite element analysis of frictional contact of elastic solids with thin and moderately thick coatings. *Turkish J. Eng. Env. Sci.* 2013, **37**, 162-177.
212. Kot, M. Contact mechanics of coating-substrate systems: Monolayer and multilayer coatings. *Archiv of Civil and Mechan. Eng.* 2012, **12**, 464-470.

-
213. Barthel, E.; Perriot, E.; Dalmas, D.; Sondergard, P.; Nael, P. Surface mechanics of functional thin films on glass surfaces. *Surface and Coating Technol.* 2006, **200**, 6181-6184.
214. Ready, E. D. Thin-coating contact mechanics with adhesion. *J. Matter. Res.* 2006, **21**, 2660-2668.
215. Johnson, K.L.; Sridhar, I. Adhesion between a spherical indenter and an elastic solid with a compliant elastic coating. *J. Phys. D: Appl., Phys.* 2001, **34**, 683-689.
216. Sridhar, I.; Zheng, Z. W.; Johnson, K.L. A detailed analysis of adhesion mechanics between a compliant elastic coating and a spherical probe. *J. Phys. D: Appl., Phys.* 2004, **37**, 2886-2895.
217. Buzio, R.; Boragno, C.; Biscarini, F.; Mongeot, F. B. The contact mechanics of fractal surfaces. *Nature materials*, 2003, **2**, 233-236.
218. Yang, F. K.; Zhang, W.; Han, Y.; Yoffe, S.; Cho, Y.; Zhao, B. "Contact" of Nanoscale Stiff Films. *Lungmuir*, 2012, **28**, 9562-9572.
219. Schirmeisen, A.; Jansen, L.; Fuchs, H. Tip-jump statistics of stick-slip friction. *Phys. Rev. B* 2005, **71**, 245403-1-245403-7.
220. Marti, O.; Colchero, J.; Mlynek, J. Combined scanning force and friction microscopy of mica. *Nanotechnology* 1990, **1**, 141-144.
221. G. Meyer and N. M. Amer, Simultaneous measurement of lateral and normal forces with an optical, beam deflection atomic force microscope. *Appl. Phys. Lett.* 1990, **57**, 2089-2091.
222. Leggett, G.J. Friction force microscopy of self-assembled monolayers: probing molecular organisation at the nanometre scale. *Anal. Chimica Acta* 2003, **479**, 17-38.
223. Attard, P. Friction, adhesion, and deformation: dynamic measurements with the atomic force microscope. *J. Adhesion Sci. Technol.* 2002, **16**, 753-791.
224. Grafstromt, S.; Neitzertt, M.; Hagent, T.; Ackermann, J.; Neumann, R.; Probstt, O.; Woflgets, M. The role of topography and friction for the image contrast in lateral force microscopy. *Nanotechnology* 1993, **4**, 143-151.
225. Ogletree, D. F.; Carpick, R. W.; Salmeron, M. Calibration of frictional forces in atomic force microscopy. *Rev. Sci. Instrum.* 1996, **67**, 9, 3298-3306.

-
226. Schirmeisen, A.; Jansen, L.; Fuchs, H. Tip-jump statistics of stick-slip friction. *Phys. Rev. B* 2005, **71**, 245403-1-245403-7.
227. Bhushan, B. Nanotribology and nanomechanics, *Wear*, 2005, **259**, 1507–1531.
228. Tomlinson, G. A. A molecular theory of friction. *Philosophical Magazine* 1929, 7, 905-939.
229. Chen, B. Y.; Yeh, M.; Tai, N. H. Accuracy of the Spring Constant of Atomic Force Microscopy Cantilevers by Finite Element Method. *Anal. Chem.* 2007, **79**, 1333-1338.
230. Cumpson, P. J.; Clifford, C. A.; Hedley, J. Quantitative analytical atomic force microscopy: a cantilever reference device for easy and accurate AFM spring-constant calibration. *Meas. Sci. Technol.* 2004, **15**, 1337–1346.
231. Hutter, J. L.; Bechhoefer, J. Calibration of atomic-force microscope tips, *Rev. Sci. Instrum.* 1993, **64** (7), 1868-1873.
232. Matei, G. A.; Thoreson, E. J.; Pratt, J. R.; Newell, D. B.; Burnham, N. A. Precision and accuracy of thermal calibration of atomic force microscopy Cantilevers. *Rev. Scientific Ins.* 2006, **77**, 083703-6.
233. Kim, M.S.; Choi, J. H.; Kim, J. H.; Park, Y. K. Accurate determination of spring constant of atomic force microscope cantilevers and comparison with other methods. *Measurement* 2010, **43**, 520–526
234. Butt, H.; Jaschke, M. Calculation of thermal noise in atomic force microscopy. *Nanotechnology* 1995, **6**, 1-7.
235. Kennedy, S. J.; Cole, D. G.; Clark, R. L. A method for atomic force microscopy cantilever stiffness calibration under heavy fluid loading. *Rev. Scientific Ins.* 2009, **80**, 125103-8.
236. Cook, S. M.; Schaffer, T. E.; Chynoweth, K. M.; Wigton, M.; Simmonds, R. W.; Lang, K. M. Practical implementation of dynamic methods for measuring atomic force microscope cantilever spring constants. *Nanotechnology* 2006, **17**, 2135–2145.
237. Matei, G. A.; Thoreson, E. J.; Pratt, J. R.; Newell, D. B.; Burnham, N. A. Precision and accuracy of thermal calibration of atomic force microscopy cantilevers. *Rev. Scientific Ins.* 2006, **77**, 083703-1-083703-6.

-
238. Stark, R. W.; Drobek, T.; Heckl, W. M. Thermomechanical noise of a free v-shaped cantilever for atomic-force microscopy. *Ultramicroscopy* 2001, **86**, 207-215.
239. Walters, D. A., Cleveland J. P., Thomson N.H., Hansma P. K., Wendman M. A., Gurley G., Elings V. Short cantilevers for atomic force microscopy. *Rev. Scientific Ins.* 1996, **67**, 3583-3590.
240. Proksch, R.; Schaffer, T. E.; Cleveland, J. P.; Callahan, R. C.; Viani, M. B. Finite optical spot size and position corrections in thermal spring constant calibration. *Nanotechnology* 2004, **15**, 1344–1350.
241. Leggett, G. J.; Brewer, N. J.; Chong, K. S. L. Friction force microscopy: towards quantitative analysis of molecular organisation with nanometre spatial resolution. *Phys . Chem. Chem.* 2005 , **7**, 1107-1120.
242. Ruan, J. A., and Bhushan, B., Atomic-scale friction measurements using friction force microscopy. I. General principles and new measurement techniques. *ASME J. Tribol*, 1994, **116**, 378 .
243. Liu, E.; Blanpain, B.; Celis, J.P, Calibration procedures for frictional measurements with a lateral force microscope, *Wear*, 1996, **192**, 1, 141-150.
244. Cain, R. G.; Biggs, S.; Page, N. W. Force Calibration in Lateral Force Microscopy, *Journal of Colloid and Interface Science*, 2000, **277**, 55-65.
245. Ogletree, D. F.; Carpick, R. W.; Salmeron, M. Calibration of frictional forces in atomic force microscopy *Rev. Sci. Instrum.* 1996, **67**, 3298-3306.
246. Varenberg, M.; Etsion, I.; Halperin, G. An improved wedge calibration method for lateral force in atomic force microscopy, *Review of Scientific Instruments*, 2003, **74**, 3362-3367.
247. Zhao, X.; Xia, Y.; Whitesides, G.M. Soft lithographic methods for nano-fabrication. *J. Matter. Chem* 1997, **7**, 1069-1074.
248. Ravoo, B. J. Microcontact chemistry: surface reactions in nanoscale confinement. *J. Mater. Chem.* 2009, **19**, 8902–8906.
249. Wendeln, C.; Ravoo, B. J. Surface Patterning by Microcontact Chemistry. *Langmuir* 2012, **28**, 5527–5538.

-
250. Kaufmann, T.; Gokmen, M. T.; Rinnen, S.; Arlinghaus, H. F.; Prez, F. D.; Ravoo, B. J. Bifunctional Janus beads made by “sandwich” microcontact printing using click chemistry. *J. Mater. Chem.*, 2012, **22**, 6190–6199.
251. Eissa, M. M.; Rahman, M. M.; Zine, N.; Jaffrezic, N.; Errachid, A.; Fessi, H.; Elaissari, A. Reactive magnetic poly(divinylbenzene-co-glycidyl methacrylate) colloidal particles for specific antigen detection using microcontact printing technique. *Acta Biomaterialia* 2013, **9**, 5573–5582.
252. Xia, Y.; Whitesides, G. M. Soft Lithography. *Annu. Rev. Mater. Sci.* 1998, **28**, 153–84.
253. Tao Chen, T.; Jordan, R.; Zauscher, S. Extending micro-contact printing for patterning complex polymer brush Microstructures. *Polymer* 2011, **52**, 2461-2467.
254. Wei, Q.; Yu, B.; Wang, X.; Zhou, F. Stratified Polymer Brushes from Microcontact Printing of Polydopamine Initiator on Polymer Brush Surfaces. *Macromol. Rapid Commun.* 2014, **35**, 1046–1054.
255. Ruizab, S. A.; Chen, C. S.; Microcontact printing: A tool to pattern. *Soft Matt.* 2007, **3**, 168–177.
256. Geissler, M.; Xia, Y. Patterning: Principle and Some New developments. *Adv. Mater* 2004, **16**, 1249-1269.
257. Manfrinato, V. R.; Zhang, L.; Su, D.; Duan, H.; Hobbs, R. G.; Stach, E. A.; Berggren, K. K. Resolution Limits of Electron-Beam Lithography toward the Atomic Scale. *Nano Lett.* 2013, **13**, 1555–1558.
258. Liu, K.; Avouris, Ph.; Bucchignano, J.; Martel, R.; Sun, S.; Michl, J. Simple fabrication scheme for sub-10 nm electrode gaps using electron-beam lithography. *Appl. Phys. Lett.* 2002, **80(5)**, 865-867.
259. Nagya, N.; Zolnaia, Z.; Fülöpa, E.; Deáka, A.; Bársony, I. Tunable ion-swelling for nanopatterning of macroscopic surfaces: The role of proximity effects. *Appl. Surf. Sci.* 2012, **259**, 331– 337.
260. Altissimoa, M. E-beam lithography for micro-/nanofabrication. *Biomicrofluidics* 2010, **4**, 026503.

-
261. She, Z.; DiFalco, A.; Hähner, G.; Buck, M. Electron-beam patterned self-assembled monolayers as templates for Cu electrodeposition and lift-off. *Beilstein J. Nanotechnol.* 2012, **3**, 101–113.
262. Zhang, G.; Tanii, T.; Zako, T.; Hosaka, T.; Miyake, T.; Kanari, Y.; Funatsu, T.; Ohdomari, L. Nanoscale Patterning of Protein Using Electron Beam Lithography of Organosilane Self-Assembled Monolayers. *small* 2005, **1**, 833–837.
263. Rastogi, A.; Paik, M. Y.; Tanaka, M.; Ober, C. K. Direct Patterning of Intrinsically Electron Beam Sensitive Polymer Brushes. *ACS Nano* 2010, **4**, 771–780.
264. Herzer, N.; Hoepfner, S.; Schubert, U. S.; Fabrication of patterned silane based self-assembled monolayers by photolithography and surface reactions on silicon-oxide substrates. *Chem. Commun.* 2010, **46**, 5634–5652.
265. Betancourt, T.; Brannon-Peppas, L. Micro- and nanofabrication methods in nanotechnological medical and pharmaceutical devices. *Int. J. Nanomed.* 2006, **1**, 483–495.
266. Pimpin, A.; Srituravanich, W.; Review on Micro- and Nanolithography Techniques and their Applications. *Eng. J.* 2012, **16**, 38–55.
267. Leggett, G. J. Light-directed nanosynthesis: near-field optical approaches to integration of the top-down and bottom-up fabrication paradigms. *Nanoscale* 2012, **4**, 1840–1855.
268. Biswas, A.; Bayer, I. S.; Biris, A. S.; Wang, T.; Dervishi, E.; Faupel, F. Advances in top-down and bottom-up surface nanofabrication: Techniques, applications & future prospects. *Advances in Coll. and Interface Sci.* 2012, **170**, 2–27.
269. Bellah, M.; Christensen, S. M.; Iqbal, S. M. Nanostructures for Medical Diagnostics. *J. Nanomater.* 2011, **2012**, 1–21.
270. Mojarad, N.; Gobrecht, J.; Ekinici, Y. Interference lithography at EUV and soft X-ray wavelengths: Principles, methods, and applications. *Microelectronic Eng.* 2015, **143**, 55–63.
271. Azuma, T.; Ohiwa, T.; Okumura, K.; Farrell, T.; Nunes, R.; Dobuzinsky, D.; Fichtl, G.; Gutmann, A. Impact of reduced resist thickness on deep ultraviolet lithography. *J. Vac. Sci. Technol.* 1996, **14**, 4246–4252.

-
272. Seo, J.; Park, J. H.; Ma, Zh.; Choi, J.; Ju, B. Nanopatterning by Laser Interference Lithography: Applications to Optical Devices. *J. Nanoscience and Nanotechnology* 2014, **14**, 1521-1532.
273. Mojarad, N.; Gobrecht, J.; Ekinici, Y. Interference lithography at EUV and soft X-ray wavelengths: Principles, methods, and applications. *Microelectronic Eng.* 2015, **143**, 55–63.
274. Choi, J.; Chung, M.; Dong, K.; Park, E.; Ham, D.; Park, Y.; Song, I.; Pak, J.; Ju, B. Investigation on Fabrication of Nanoscale Patterns Using Laser Interference Lithography. *J. Nanoscience and Nanotechnology*, 2011, **11**, 778-781.
275. Lu, C.; Lipson, R. H. Interference lithography: a powerful tool for fabricating periodic structures. *Laser Photonics Rev.* 2010, **4**, 568–580
276. Ellman, M.; Rodríguez, A.; Pérez, N.; Echeverría, M.; Verevkin, Y. K.; Peng, C.S.; Berthou, T.; Wange, Z.; Olaizola, S. M.; Ayerdi, I. High-power laser interference lithography process on photoresist: Effect of laser fluence and polarisation. *Appl. Surf. Sci.* 2009, **255**, 5537–5541.
277. Patole, S.; Vasilev, C.; El-Zubir, O.; Wang, L.; Johnson, M. P.; Cadby, A. J.; Leggett, G. J.; Hunter, C. N. Interference lithographic nanopatterning of plant and bacterial light-harvesting complexes on gold substrates. *Interface Focus* 2015, **5**, 0005.
278. O'Reilly, T. B.; Smith, H. I. Linewidth uniformity in Lloyd's mirror interference lithography systems. *Journal of Vacuum Science & Technology B* 2008, **26**, 2131-2134.
279. Murillo, R.; van Wolferen, H. A.; Abelmann, L.; Lodder, J.C. Fabrication of patterned magnetic nanodots by laser interference lithography. *Microelectronic Eng.* 2005, **78–79**, 260–265.
280. Lim, C. S.; Hong, M. H.; Lin, Y.; Xie, Q.; Luk'yanchuk, B. S.; Kumar, A. S.; Rahman, M. Microlens array fabrication by laser interference lithography for super-resolution surface nanopatterning. *Appl. Phys. Lett.* 2006, **89**, 191125.
281. Yu, F.; Mücklich, F.; Li, P.; Shen, H.; Mathur, S.; Lehr, S.; Bakowsky, U. In Vitro Cell Response to a Polymer Surface Micropatterned by Laser Interference Lithography. *Biomacromolecules* 2005, **6**, 1160-1167.

-
282. Inoue, S.; Amano, T.; Itani, T.; Watanabe, H.; Mori, I.; Watanabe, T.; Kinoshita, H.; Miyai, H.; Hatakeyama, M. Development of core technologies on EUV mask and resist for sub-20-nm half pitch generation. *Adv. Opt. Techn.* 2012, **1**, 269–278.
283. Bloomstein, T. M.; Marchant, M. F.; Deneault, S.; Hardy, D. E.; Rothschild, M. 22-nm immersion interference lithography. *Opt. Express* 2006, **14**, 6434–6443.
284. Alswieleh, A. M.; Cheng, N.; Canton, I.; Ustbas, B.; Xue, X.; Admiral, V.; Xia, S.; Ducker, R. E.; El Zubir, O.; Cartron, M.L.; Hunter, N.; Leggett, G. J.; Armes, S. P. Zwitterionic Poly(amino acid methacrylate) Brushes. *J. Am. Chem. Soc.* 2014, **136**, 9404–9413.
285. Bhushan, K. R.; DeLisia, C.; Laursen, R. A. Synthesis of photolabile 2-(2-nitrophenyl)propyloxycarbonyl protected amino acids. *Tetrahedron Letters* 2003, **44**, 8585–8588.
286. Meiron, T. S.; Marmur, A. Saguy, I. S. Contact angle measurement on rough surfaces. *J. Coll. and Interface Sci.* 2004, **274**, 637–644.
287. Tadmor, R. Line Energy and the Relation between Advancing, Receding, and Young Contact Angles. *Langmuir* 2004, **20**, 7659–7664.
288. Henck, S. A.; In situ real-time ellipsometry for film thickness measurement and control. *Journal of Vacuum Science & Technology A* 1992, **10**, 934–938.
289. Gonçalves, D.; Irene, E. A. Fundamental and application of spectroscopic ellipsometry. *Quim.* 2002, **25**, 794–800.
290. Parnell, A. J.; Martin, S. J.; Dang, Ch. C.; Geoghegan, M.; Jones, R. A. L.; Crook, C. J.; Howse, J. R.; Ryan, A. J. Synthesis, characterization and swelling behaviour of poly(methacrylic acid) brushes synthesized using atom transfer radical polymerization. *Polymer* 2009, **50**, 1005–1014.
291. Wu, T.; Efimenko, K.; Genzer, J. Combinatorial Study of the Mushroom-to-Brush Crossover in Surface Anchored Polyacrylamide. *J. Am. Chem.Soc.* 2002, **124**, 9394–9395.
292. Wu, T.; Efimenko, K.; Vlcek, P.; Sýubr, V.; Genzer, J. Formation and Properties of Anchored Polymers with a Gradual Variation of Grafting Densities on Flat Substrates. *Macromolecules* 2003, **36**, 2448–2453.

-
293. Alov, N. V. Fifty Years of X-ray Photoelectron Spectroscopy. *J. Anal. Chem.* 2005, **60**, 297–300.
294. Gomoyunova, M. V.; Pronin, I. I. Photoelectron Spectroscopy of Atomic Core Levels on the Silicon Surface: A Review. *Technical Phys.* 2004, **49**, 1249–1279.
295. Blomfield, C. J. Spatially resolved X-ray photoelectron spectroscopy. *Journal of Electron Spectroscopy and Related Phenomena* 2005, **143**, 241–249.
296. Venezia, A. M. X-ray photoelectron spectroscopy (XPS) for catalysts characterization. *Catalysis Today* 2003, **77**, 359–370.
297. Seah, M.P.; Gilmore, I.S.; Spencer, S.J. Quantitative XPSI. Analysis of X-ray photoelectron intensities from elemental data in a digital photoelectron database. *Journal of Electron Spectroscopy and Related Phenomena* 2001, **120**, 93–111.
298. Jalili, N.; Laxminarayana, K. A review of atomic force microscopy imaging systems: application to molecular metrology and biological sciences. *Mechatronics* 2004, **14**, 907–945.
299. Zhong, J.; Yan, J. Seeing is believing: atomic force microscopy imaging for nanomaterial research. *RSC Adv.* 2016, **6**, 1103–1121.
300. Binnig, G.; Quate, C. F.; Gerber, Ch. Atomic Force Microscope. *Phys. Rev. Lett.* 1986, **56**, 930–933.
301. Zhong, J. From simple to complex: investigating the effects of lipid composition and phase on the membrane interactions of biomolecules using in situ atomic force microscopy. *Integr. Biol.* 2011, **3**, 632–644.
302. Tseng, A. A. Advancements and challenges in development of atomic force microscopy for nanofabrication. *Nano Today* 2011, **6**, 493–509.
303. Gan, Y. Atomic and subnanometer resolution in ambient conditions by atomic force microscopy. *Surface Science Reports* 2009, **64**, 99–121.
304. Dufrêne, Y. F.; Hinterdorfer, P. Recent progress in AFM molecular recognition studies. *Pflugers Arch - Eur J Physiol* 2008, **256**, 237–245.
305. Garcí'a, R.; Paulo, A. S. Attractive and repulsive tip-sample interaction regimes in tapping-mode atomic force microscopy. *Phys. Rev. B* 1999, **60**, 4961–4967.

-
306. Tamayo, J.; Garcí'a, R. Deformation, Contact Time, and Phase Contrast in Tapping Mode Scanning Force Microscopy. *Langmuir* 1996, **12**, 4430-4435.
307. Zhao, B.; Brittain, W. J.; Zhou, W.; Cheng, S. Z. D. AFM Study of Tethered Polystyrene-*b*-poly(methyl methacrylate) and Polystyrene-*b*-poly(methyl acrylate) Brushes on Flat Silicate Substrates. *Macromolecules* 2000, **33**, 8821-8827.
308. Bar, G.; Thomann, Y.; Brandsch, R.; Cantow, H. J. Factors Affecting the Height and Phase Images in Tapping Mode Atomic Force Microscopy. Study of Phase-Separated Polymer Blends of Poly(ethene-*co*-styrene) and Poly(2,6-dimethyl-1,4-phenylene oxide). *Langmuir* 1997, **13**, 3807-3812.
309. Santos, N. C.; , Castanho, M. A. R. B. An overview of the biophysical applications of atomic force Microscopy. *Biophys. Chem.* 2004, **107**, 133-149.
310. Yip, C. M. Atomic force microscopy of macromolecular interactions. *Current Opinion in Structural Biology* 2001, **11**, 567-572.
311. Alonso, J. L.; Goldmann, W. H. Feeling the forces: atomic force microscopy in cell biology. *Life Sci.* 2003, **72**, 2553-2560.
312. Lyubchenko, Y. L.; Shlyakhtenko, L. S. AFM for analysis of structure and dynamics of DNA and protein-DNA complexes. *Methods* 2009, **47**, 206-213.
313. Hao Yan, H.; Park, S.H.; Finkelstein, G.; Reif, J. H.; LaBean, Th. H. DNA-Templated Self-Assembly of Protein Arrays and Highly Conductive Nanowires. *Science* 2003, **301**, 1882-1884.
314. Richter, R. P.; Brisson, A. R. Following the Formation of Supported Lipid Bilayers on Mica: A Study Combining AFM, QCM-D, and Ellipsometry. *Biophysical J.* 2005, **88**, 3422-3433.
315. Hutter, J. L.; Bechhofer, L.; J. Calibration of atomic-force microscope tips. *Rev. Sci. Instrum* 1993, **64**, 1868-1873.
316. Ogletree, D. F.; Carpic, R. W.; Salmeron, M. Calibration of Frictional Force in Atomic Force Microscopy. *Rev. Sci. Instrum* 1996, **67**, 3298-3306.
317. Varenberg M.; Etsion, I.; Halperin, G. An improved Wedge Calibration Methode for Lateral Force in Atomic force Microscopy. *Rev. Sci. Instrum* 2003, **74**, 3362-3367.

-
318. Varenberg M.; Etsion, I.; Halperin, G. An improved Wedge Calibration Methode for Lateral Force in Atomic force Microscopy. *Rev. Sci. Instrum* 2003, **74**, 3362-3367.
319. Rayan, G.; Guet, J.; Taulier, N.; Pincet, F.; Urbach, W. Recent Applications of Fluorescence Recovery after Photobleaching (FRAP) to Membrane Bio-Macromolecules. *Sensors* 2010, **10**, 5927-5948.
320. Meyvis, T.K. L.; De Smedt, S. C.; Van Oostveldt, P.; Demeester, J. Fluorecence Recovery After Photobleaching: A Versatial for Mobility and Interaction Measurements In Pharmaceutical Research. *Pharmaceutical Research* 1999, **16**, 1153-1162.
321. Lippincott-Schwartz, J.; Snapp, E.; Kenworthy, A. Studing protein dynamics in living cells. *Nature review, Molecular cell bilogy* 2001, **2**, 444-456.
322. Brown, C. M. Fluorescence microscopy – avoiding the pitfalls. *J. Cell Sci.* 2007, **120**, 3488-3492.
323. Stephens, D. J.; Allan, V. J. Light Microscopy Techniques for Live Cell Imaging. *Science* 2003, **300**, 82-86.
324. Vermot, J.; Fraser, S. E.; Liebling, M. Fast fluorescence microscopy for imaging the dynamics of embryonic development. *Human Frontier Science Program Journal* 2008, **2**, 143-155.
325. Frigault, M. M.; Lacoste, J.; Swift, J. L.; Brown, C. M. Live cell microscopy –tips and tools. *J. Cell Sci.* 2009, **122**, 753-767.
326. Lichtman J. W.; Conchello, J. A. Fluorescence Microscopy. *Nat. Methods* 2005, **2**, 910-919.
327. Chen, T.; Amin, I.; Jordan, R. Patterned Polymer Brushes. *Chem. Soc. Rev.* 2012, **41**, 3280-3296.
328. Ayres, N. Polymer Brushes: Applications in Biomaterial and Nanotechnology. *Polym. Chem.* 2010, **1**, 769-777.
329. You, J.; Raghunathan V. K.; Son K. J.; Patel D.; Haque A.; Murphy C. J.; Revzin A. Impact of Nanotopography, Heparin Hydrogel Microstructures, and Encapsulated Fibroblasts on Phenotype of Primary Hepatocytes. *ACS Appl. Mater. Interfaces* 2015, **7**, 12299–12308.

-
330. Hou, J.; Shi, Q.; Ye, W.; Fan, Q.; Shi, H.; Wong, Sh.; Xuc, X. and Yin, J. A novel hydrophilic polymer-brush pattern for site-specific capture of blood cells from whole blood. *Chem. Commun.* 2015, **51**, 4200-4203.
331. Jain, P.; Baker, G. L.; Bruening, M. L. Applications of Polymer Brushes in Protein Analysis and Purification. *Annual. Rev. Anal. Chem.* 2009, **2**, 387-408.
332. Sakata, Sh.; Inoue, Y.; Ishihara, K. Quantitative Evaluation of Interaction Force between Functional group in Protein and Polymer brush Surfaces. *Langmuir* 2014, **30**, 27-45-2751.
333. Huck, W. T. S.; Responsive polymers for nanoscale actuation. *Materialstoday*, 2008, 11, 224-32.
334. Champan, P.; Ducker, R. E.; Hurley, R. C.; Hobbs, J. K.; Leggett, G. J. Fabrication of Two-Component, Brush-on-Brush Topographical Microstructures by Combination Of Atom-Transfer Radical Polymerization with Polymer End-Functionalization and Photopatterning. *Langmuir* 2015, **31**, 5935-5944.
335. Azzaroni, O. Polymer Brush Here, There, and Everywhere: Recent Advances in Their Practical applications and Emerging Opportunities in Multiple-research fields. *Journal of Polym. Sci. Part A: Polym. Chemm.* 2012, **50**, 3225-3258.
336. Yu, Q.; Ista, L. K.; Gu, R.; Zauscher, S.; López G. P.; Nanopatterned Polymer Brushes: Conformation, Fabrication and Applications. *Nanoscale* 2016, **8**, 680–700.
337. Ahn, S. J.; Kaholek, M.; Lee, M. K.; LaMattina, B.; LaBeanT.H.; Zauscher, S. *Adv. Mater* 2004, **16**, 2141-2145.
338. Yu, Q.; Shivapooja, P.; Johnson, L. M.; Tizazu, G.; Leggett, G. J.; López, G. P. Nanopatterned polymer brushes as switchable bioactive interfaces. *Nanoscale* 2013, **5**, 3632-7.
339. Jonas, A. M.; Hu,.; Glinel, K.; Huck, W. T. S. Effect of Nanoconfinement on the Collapse Transition of Responsive Polymer Brushes. *Nano Lett.* 2008, **8**. 3819-3824.
340. Morse, A. J.; Edmonson, S.; Dupin, D.; Armes, S. P.; Zhang, Z. Leggett, G. J.; Thompson, R. L., Lewis A. L. Biocompatible Polymer brushes Grwon From Model Quartz Fibers: Synthesis, Characterization and in situ Determination of Friction Coefficient. *Soft Matt.* 2010, **6**, 1571-1579.

-
341. de Beer, S.; Kutnyanszky, E.; Schön, P. M.; Vancso, G. J. Sissi de Beer, Edit Kutnyanszky, Peter M. Schön, G. J.; Martin H. M. Solvent-induced immiscibility of polymer brushes eliminates dissipation channels. *Nat. Comm* 2014,**5**, 1-8.
342. de Beer, S.; Kutnyanszky, E.; Müser, M. H.; Vancso, G. J. Preparation and Friction Force Microscopy Measurements of Immiscible Opposing Polymer Brushes. *J. Vis. Exp.* 2014, **94**, 1-7.
343. Ramakrishna, S. N; Espinosa-Marzal, R. M.; Naik, V.V.; Nalam, P. C.; Spencer, N. D. Adhesion and friction properties of polymer brushes on rough surfaces: a gradient approach. *Langmuir* 2013, **29**, 15251-152560.
344. Zhang, Z.; Morse, A. J.; Armes, S. P.; Lewis, A. L.; Geoghegan, M.; and Leggett, G. J. Effect of Brush Thickness and Solvent Composition on the Friction Force Response of Poly(2-(methacryloyloxy)ethylphosphorylcholine) Brushes. *Langmuir* 2011, **27**, 2514–2521.
345. Kobayashi, M.; Terayama, Y.; Hosaka, N.; Kaido, M.; Suzuki, A.; Yamada, N.; Torikai, N.; Ishiharae, K.; and Takahara, A. Friction behavior of high-density poly(2-methacryloyloxyethyl phosphorylcholine) brush in aqueous media. *Soft Matt.* 2007,**3**, 740-746.
346. Landherr, L. J. T.; Cohen, C.; Agarwal P.; Archer L. A. Interfacial Friction and Adhesion of Polymer Brushes. *Langmuir* 2011, **27**, 9387-9395.
347. Nikogeorgos, N.; Hunter, Ch. A.; and Leggett, G. J. Relationship Between Molecular Contact Thermodynamics and Surface Contact Mechanics. *Langmuir* 2012, **28**, 17709–17717.
348. Ruth, M. Boundary Friction of Aromatic Self-Assembled Monolayers: Comparison of Systems with One or Both Sliding Surfaces Covered with a Thiol Monolayer. *Langmuir* 2003, **19**, 6788–6795.
349. Busuttil, K.; Nikogeorgos, N.; , Zhang, Z.; Geoghegan M., Huntera, C. A.; Leggett, G. J. The mechanics of nanometer-scale molecular contacts. *Faraday Discuss.* 2012, **156**, 325–341.
350. Marti, A.; Hahner, G.; and Spencer, N. D. Sensitivity of Frictional Forces to pH on a Nanometer Scale: A Lateral Force Microscopy Study. *Langmuir* 1995, **11**, 4632-4635.

-
351. Cavalleri, O.; Gonella, G.; Terreni, S.; Vignolo, M.; Floreano, L.; Morgante, A.; Canepa, M.; Rolandi, R. High resolution X-ray photoelectron spectroscopy of L-cysteine self-assembled films. *Phys. Chem. Chem. Phys.* 2004, **6**, 4042-4046.
352. Ahmad, S. A.; Leggett, G. J.; Hucknall, A.; Chilkoti, A. Micro- and Nanostructured Poly[oligo(ethylene glycol)methacrylate] Brushes Grown From Photopatterned Halogen Initiators by Atom Transfer Radical Polymerization. *Biointerphases* 2011, **6**, 8-15.
353. Chen, H.; Zhao, C.; Zhang, M.; Chen, O.; Ma, J.; Zheng, J. Molecular Understanding and Structural-Based Design of Polyacrylamides and Polyacrylates as Antifouling Materials. *Langmuir* 2016, **32**, 3315–3330.
354. Furusawa, H.; Sekine, T.; Ozeki, T. Hydration and Viscoelastic Properties of High- and Low-Density Polymer Brushes Using a Quartz-Crystal Microbalance Based on Admittance Analysis (QCM-A). *Macromolecules* 2016, **49**, 3463–3470.
355. Kobayashi, M.; Terayam, Y.; Kikuchi, M.; Takahara, A. Chain dimensions and surface characterization of superhydrophilic polymer brushes with zwitterion sidegroups. *Soft Matt.* 2013,**9**, 5138–5148.
356. Tairy, O.; Kamp, N.; Driver, M. J.; Armes, S. P.; Klein, J. ense, Highly Hydrated Polymer Brushes via Modified Atom-Transfer-Radical-Polymerization: Structure, Surface Interactions, and Frictional Dissipation. *Macromolecules* 2015, **48**, 140–151.
357. Nomura, A.; Okayasu, K.; Ohno, K.; Fukuda, T.; Tsujii, Y. Lubrication Mechanism of Concentrated Polymer Brushes in Solvents: Effect of Solvent Quality and Thereby Swelling State. *Macromolecules* 2011, **44**, 5013–5019.
358. LeMieux, B. C.; Lin, Y.; Cuong, P. D.; Ahn, H.; Zubarev, E. R.; Tsukruk, V. V. Microtribological and Nanomechanical Properties of Switchable Y-Shaped Amphiphilic Polymer Brushes. *Adv. Funct. Mater.* 2005,**15**, 1529-1540.
359. De Beer, S.; Kutnyanszky, E.; Schön, P. M.; Vancso, G. J.; Muser, M. H. Solvent induced immiscibility of polymer brushes eliminates dissipation channels. *Nat. Comm.* 2014, **5**, 1-6.
360. Liberelle, B.; Giasson, S. Friction and Normal Interaction Forces between Irreversibly Attached Weakly Charged Polymer Brushes. *Langmuir* 2008, **24**, 1550-1559.

-
361. Zhou, T.; Qi, H.; Han, L.; Barbash, D.; Li, C. Y. Towards controlled polymer brushes via a self-assembly-assisted-grafting-to approach. *Nat. Comm.* 2016, **11119**, 1-8.
362. Brittain, W. J.; Minko, S. A Structural Definition of Polymer Brushes. *J. Polym. Sci. A* 2007, **45**, 3505–3512.
363. Liu, Y.; Klep, V.; Zdyrko, B.; Luzinov, I. Polymer Grafting via ATRP Initiated from Macroinitiator Synthesized on Surface. *Langmuir* 2004, **20**, 6710-6718.
364. Ramos, J. I.; Moya, S. E. Effect of the Density of ATRP Thiol Initiators in the Yield and Water Content of Grafted-From PMETAC Brushes. A Study by Means of QCM-D and Spectroscopic Ellipsometry Combined in a Single Device. *Macromol. Chem. Phys.* 2012, **213**, 549–556.
365. Maeda, R.; Hayakawa, T.; Ober, C. K. Dual Mode Patterning of Fluorine-Containing Block Copolymers through Combined Top-down and Bottom-up Lithography. *Chem. Mater.* 2012, **24**, 1454–1461.
366. Chapman, P.; Ducker, R. E.; Hurley, C. R.; Hobbs, J. K.; Leggett, G. J. Fabrication of Two-Component, Brush-on-Brush Topographical Microstructures by Combination of Atom-Transfer Radical Polymerization with Polymer End-Functionalization and Photopatterning. *Langmuir* 2015, **31**, 5935–5944.
367. Nagase, K.; Kobayashi, J.; Kikuchi, A.; Akiyama, Y.; Kanazawa, H.; Okano, T. Effects of Graft Densities and Chain Lengths on Separation of Bioactive Compounds by Nanolayered Thermoresponsive Polymer Brush Surfaces. *Langmuir* 2008, **24**, 511-517.
368. Coad, B. R.; Styan, K. E.; Meagher, L. One Step ATRP Initiator Immobilization on Surfaces Leading to Gradient-Grafted Polymer Brushes. *ACS App. Mater. Interf.* 2014, **6**, 7782–7789.
369. Plunkett, K. N.; Zhu, X.; Moore, J. S.; Leckband, D. E. PNIPAM Chain Collapse Depends on the Molecular Weight and Grafting Density. *Langmuir* 2006, **22**, 4259-4266.
370. Melzak, K. A.; Yu, K.; Bo, D.; Kizhakkedathu, J. N.; Toca-Herrera, J. L. Chain Length and Grafting Density Dependent Enhancement in the Hydrolysis of Ester-Linked Polymer Brushes. *Langmuir* 2015, **31**, 6463–6470.

-
371. Huang, H.; Rankin, S. E.; Penn, L. S. Transition from Mushroom to Brush during Formation of a Tethered Layer. *Langmuir* 2004, **20**, 5770-5775.
372. Gao, J.; Lei, J.; Su, Z.; Zhang, B.; Wang, J. Photografting of Maleic Anhydride on Low Density Polyethylene Powder in the Vapor Phase. *Polym. J.* 2001, **33**, 147-149.
373. Tairy, O.; Kamp, N.; Driver, M. J.; Armes, S. P.; Klein, J. Dense, Highly Hydrated Polymer Brushes via Modified AtomTransfer-Radical-Polymerization: Structure, Surface Interactions, and Frictional Dissipation. *Macromolecules* 2015, **48**, 140–151.
374. Wang, X.; Tu, H.; Braun, P. V.; Bohn, P. W. Length Scale Heterogeneity in Lateral Gradients of Poly(N-isopropylacrylamide) Polymer Brushes Prepared by Surface-Initiated Atom Transfer Radical Polymerization Coupled with In-Plane Electrochemical Potential Gradients. *Langmuir*, 2006, **22**, pp 817–823.
375. Coad, B. R.; Lu, Y.; Glattauer, V.; Meagher, L. Substrate-Independent Method for Growing and Modulating the Density of Polymer Brushes from Surfaces by ATRP. *ACS Appl. Matter. Interfaces* 2012, **4**, 2811–2823.
376. Grubbs, J. B.; Arnold, R. M.; Roy, A.; Brooks, K.; Bilbrey, J. A.; Gao, J.; Locklin, J. Degradable Polycaprolactone and Polylactide Homopolymer and Block Copolymer Brushes Prepared by Surface-Initiated Polymerization with Triazabicyclodecene and Zirconium Catalysts. *Langmuir* 2015, **31**, 10183–10189.
377. Ahmad, S. A.; Hucknall, A.; Chilkoti, A.; Leggett, G. J. Protein Patterning by UV-Induced Photodegradation of Poly(oligo(ethylene glycol) methacrylate) Brushes. *Langmuir* 2010, **26**, 9937-9942.
378. Herzer, N.; Hoepfner, S.; Schubert, U. S. Fabrication of patterned silane based self-assembled monolayers by photolithography and surface reactions on silicon-oxide substrates. *Chem. Commun.* 2010, **46**, 5634–5652.
379. Lane, A. P.; Maher, M. J.; Willson, C. J.; Ellison, C. J. Photopatterning of Block Copolymer Thin Films. *ACS Macro Lett.* 2016, **5**, 460–465.
380. Yamamoto, S.; Ejaz, M.; Tsujii, Y.; Fukuda, T. Surface Interaction Forces of Well-Defined, High-Density Polymer Brushes Studied by Atomic Force Microscopy. 2. Effect of Graft Density. *Macromolecules* 2000, **33**, 5608-5612.

-
381. Zhang, Z.; Morse, A. J.; Armes, S. P.; Lewis, A. L.; Geoghegan, M.; Leggett, G. J. Effect of Brush Thickness and Solvent Composition on the Friction Force Response of Poly(2-(methacryloyloxy)ethylphosphorylcholine) Brushes. *Langmuir* 2011, **27**, 2514–2521.
382. Raftari, M.; Zhang, Z. J.; Carter, S. R.; Leggett, G. J.; Geoghegan, M. Nanoscale Contact Mechanics between Two Grafted Polyelectrolyte Surfaces. *Macromolecules* 2015, **48**, 6272–6279.
383. Ramakrishna, S. N.; Espinosa-Marzal, R. M.; Naik, V. V.; Nalam, P. C.; Spencer, N. D. Adhesion and Friction Properties of Polymer Brushes on Rough Surfaces: A Gradient Approach. *Langmuir* 2013, **29**, 15251–15259.
384. Yang, J.; Chen, H.; Xiao, S.; Shen, M.; Chen, F.; Fan, P.; Zhong, M.; Zheng, J. Salt-Responsive Zwitterionic Polymer Brushes with Tunable Friction and Antifouling Properties. *Langmuir* 2015, **31**, 9125–9133.
385. Erbas, A.; Paturej, J. Friction between ring polymer brushes. *Soft Matter* 2015, **11**, 3139–3148.
386. Bhairamadgi, N. S.; Pujari, S. P.; van Rijn, C. J. M.; Zuilhof, H. Adhesion and Friction Properties of Fluoropolymer Brushes: On the Tribological Inertness of Fluorine. *Langmuir* 2014, **30**, 12532–12540.
387. Landherr, L. J. T.; Cohen, C.; Agarwal, P.; Archer, L. A. Interfacial Friction and Adhesion of Polymer Brushes. *Langmuir* 2011, **27**, 9387–9395.
388. Brady, M. A.; Limpoco, F. T.; Perry, S. S. Solvent-Dependent Friction Force Response of Poly(ethylenimine)-graftpoly(ethylene glycol) Brushes Investigated by Atomic Force Microscopy. *Langmuir* 2009, **25(13)**, 7443–7449.
389. Limpoco, F. T.; Advincula, R. C.; Perry, S. S. Solvent Dependent Friction Force Response of Polystyrene Brushes Prepared by Surface Initiated Polymerization. *Langmuir* 2007, **23**, 12196–12201.
390. Busuttill, K.; Nikogeorgos, N.; Zhang, Z.; Geoghegan, M.; Hunter, C. A.; Leggett, G. J. The mechanics of nanometre-scale molecular contacts. *Faraday Discuss* 2012, **156**, 325–341.
391. Brittain, W. J.; Minko, S. A Structural Definition of Polymer Brushes. *J. Polym. Sci. Part A: Polym. Chem.* 2007, **45**, 3505–3512.

-
392. Dumont, E. L. P.; Belmas, H.; Hess, H. Observing the Mushroom-to-Brush Transition for Kinesin Proteins. *Langmuir* 2013, **29**, 15142–15145
393. Goubko, C. A.; Cao, X.; Patterning multiple cell types in co-cultures: A review. *Mater. Sci. Eng. C* 2009, **29**, 1855–1868.
394. Tay, C. Y.; Irvine, S. A.; Boey, F. Y. C.; Tan, L. P.; Venkatraman, S. Micro-/Nano-engineered Cellular Responses for Soft Tissue Engineering and Biomedical Applications. *small* 2011, **7**, 1361–1378.
395. Alves, N. M.; Pashkuleva, I.; Reis, R. L.; Mano, J. F. Controlling Cell Behavior Through the Design of Polymer Surfaces. *small* 2010, **6**, 1–13.
396. Biggs, J. P.; Richards, R. G.; McFarlane, S.; Wilkinson, C. D. W.; Oreffo, R. O. C.; Dalby, M. J. Adhesion formation of primary human osteoblasts and the functional response of mesenchymal stem cells to 330 nm deep microgrooves. *J. R. Soc. Interface* 2008, **5**, 1231–1242.
397. Flemming, R. J.; Murphy, C. J.; Abrams, J. A.; Goodman, S. L.; Nealey, P. F. Effects of synthetic micro- and nano-structured surfaces on cell behaviour. *Biomaterials* 1999, **20**, 573–588.
398. Milner, K. R.; Siedlecki, C. A. Fibroblast response is enhanced by poly(L-lactic acid) nanotopography edge density and proximity. *Int. J. Nanomed.* 2007, **2**, 201–211.
399. Wilkinson, C. D. W.; Riehle, M.; Wood, M.; Gallagher, J.; Curtis, A. C. G. The use of materials patterned on a nano- and micro-metric scale in cellular engineering. *Mat. Sci. Eng. C* 2002, **19**, 263–269.
400. JCIK-STOTHARD, B.; CURTIS, A.; MONAGHAN, W.; MACDONALD, K.; WILKINSON, C. Guidance and Activation of Murine Macrophages by Nanometric Scale Topography. *Exp. Cell. Res.* 1996, **223**, 426–435.
401. Yoshikawa, T.; Uchimura, E.; Kishi, A.; Funeriu, D. P.; Miyake, M.; Miyake, J.; Transfection microarray of human mesenchymal stem cells and on-chip siRNA gene knockdown. *J. Control. Release* 2004, **96**, 227 – 232.

-
402. Murugan, R.; Molnar, P.; Rao, K. P.; Hickman, J. J. Biomaterial Surface patterning of self assembled monolayers for controlling neuronal cell behaviour. *Int J Biomed Eng Technol* 2009, **2**, 104–134.
403. Chen, Ch. S.; Mrksich, M.; Huang, S.; Whitesides, G. M.; Ingber, D. E. Micropatterned Surfaces for Control of Cell Shape, Position, and Function. *Biotechnol. Prog.* 1998, **14**, 356–363.
404. Yeo, W.; Mrksich, M. Electroactive Self-Assembled Monolayers that Permit Orthogonal Control over the Adhesion of Cells to Patterned Substrates. *Langmuir* 2006, **22**, 10816–10820.
405. Jing, G.; Perry, S. F.; Tatic-Lucic, S. Precise cell patterning using cytophobic self-assembled monolayer deposited on top of semi-transparent gold. *Biomed Microdevices* 2010, **12**, 935–948.
406. Koepse, J. T.; Murphy, W. L.; Patterning Discrete Stem Cell Culture Environments via Localized Self-Assembled Monolayer Replacement. *Langmuir* 2009, **25**(21), 12825–12834.
407. Yamaguchi, M.; Ikeda, K.; Suzuki, M.; Kiyohara, A.; Kudoh, S. N.; Shimizu, K.; Taira, T.; Ito, D.; Uchida, T.; Gohara, K. Cell Patterning Using a Template of Microstructured Organosilane Layer Fabricated by Vacuum Ultraviolet Light Lithography. *Langmuir* 2011, **27**, 12521–12532.
408. Jones, J. A.; Qin, A.; Meyerson, H.; Kwon, K.; Matsuda, T.; Anderson, J. M. Instability of Self-Assembled Monolayers (SAM) as a Model Material System for Macrophage/FBGC Cellular Behavior. *Biomed Mater Res A.* 2008, **86**, 261–268.
409. Tugulu, S.; Klok, H. Stability and Nonfouling Properties of Poly(poly(ethylene glycol) methacrylate) Brushes under Cell Culture Conditions. *Biomacromolecules* 2008, **9**, 906–912.
410. Krishnamoorthy, M.; Hakobyan, S.; Ramstedt, M.; Gautrot, J. E. Surface-Initiated Polymer Brushes in the Biomedical Field: Applications in Membrane Science, Biosensing, Cell Culture, Regenerative Medicine and Antibacterial Coatings. *Chem. Rev.* 2014, **114**, 10976–11026.

-
411. Kobayashi, M.; Takahara, A. Tribological Properties of Hydrophilic Polymer Brushes Under Wet Conditions. *The Chem. Rec.* 2010, **10**, 208–216.
412. Moroni, I.; Gunnewiek, M. K.; Benetti, E. M. Polymer brush coatings regulating cell behavior: Passive interfaces turn into active. *Acta Biomaterialia* 2014, **10**, 2367–2378.
413. Ishihara, K.; Kitagawa, T.; Inoue, Y. Initial Cell Adhesion on Well-Defined Surface by Polymer Brush Layers with Varying Chemical Structures. *ACS Biomater. Sci. Eng.* 2015, **1**, 103–109.
414. Lavanant, L.; Pullin, B.; Hubbell, J. A.; Klok, H. A Facile Strategy for the Modification of Polyethylene Substrates with Non-Fouling, Bioactive Poly(poly(ethylene glycol) methacrylate) Brushes. *Macromol. Biosci.* 2010, **10**, 101–108.
415. Tugulu, S.; Klok, H. Stability and Nonfouling Properties of Poly(poly(ethylene glycol) methacrylate) Brushes under Cell Culture Conditions. *Biomacromolecules* 2008, **9**, 906–912.
416. Chen, S.; Li, L.; Zhao, C.; Zheng, J. Surface hydration: Principles and applications toward low fouling/nonfouling biomaterials. *Polymer* 2010, **51**, 5283–5293.
417. Zhao, H.; Zhu, B.; Luo, S.; Lin, H.; Nakao, A.; Yamashita, Y.; Yu, H. Controlled Protein Absorption and Cell Adhesion on Polymer-BrushGrafted Poly(3,4-ethylenedioxythiophene) Films. *ACS Appl. Mater. Interfaces* 2013, **5**, 4536–4543.
418. Puniredd, S. R.; Jayaraman, S.; Gandhimathi, C.; Ramakrishna, S.; Venugopal, J. R.; Yeo, T. W.; Guo, S.; Quintana, R.; czewski, D. J.; Srinivasan, M. P. Deposition of zwitterionic polymer brushes in a dense gas medium. *J. Coll. Interface Sci.* 2015, **448**, 156–162.
419. Costa, P.; Gautrot, J. E.; Connelly, J. T. Directing cell migration using micropatterned and dynamically adhesive polymer brushes. *Acta Biomaterialia* 2014, **10**, 2415–2422.
420. Loesberga, W. A.; te Rietb, J.; Delftc, F.C.M.J.M.; Schoönd, P.; Figdor, C. J.; Spellerd, S.; van Loone, J.J.W.A.; Walboomersa, X.F.; Jansena, J.A. The threshold at which substrate nanogroove dimensions may influence fibroblast alignment and adhesion. *Biomaterials* 2007, **28**, 3944–3951.
421. Yu, F.; Mucklich, F.; Li, P.; Shen, H.; Mathur, S.; Lehr, M.; Bakowsky, U. In Vitro Cell Response to a Polymer Surface Micropatterned by Laser Interference Lithography. *Articles*

-
- from the Microsymposium on Polymer Biomaterials. *Biomacromolecules* 2005, **6**, 1160-1167.
422. You, J.; Raghunathan, V. K.; Son, K. J.; Patel, D.; Haque, A.; Murphy, C. J.; Revzin, A. Impact of Nanotopography, Heparin Hydrogel Microstructures, and Encapsulated Fibroblasts on Phenotype of Primary Hepatocytes. *ACS Appl. Mater. Interfaces* 2015, **7**, 12299–12308.
423. Gunnewiek, M. K.; Benettl, E. M.; Luca, A. D.; van Blitterswijk, C. A.; Moroni, L.; Vancso, G. J. Thin Polymer Brush Decouples Biomaterial's Micro-/Nano-Topology and Stem Cell Adhesion. *Langmuir* 2013, **29**, 13843–13852.
424. Biggs, M. J. P.; Richards, R. J.; Gadegaard, N.; McMurray, R. J.; Affrossman, S.; Wilkinson, C. D. W.; Oreffo, R. O. C.; Dalby, M. J. Interactions with nanoscale topography: Adhesion quantification and signal transduction in cells of osteogenic and multipotent lineage. *J. Bio. Mat. Res. A* 2009, **91**, 195-208.
425. Nuttelmana, C. R.; Tripodia, M. C.; Anseth, K. S. Synthetic hydrogel niches that promote hMSC viability. *Matrix Biol.* 2005, **24**, 208 – 218.
426. Chana, B. P.; Huia, T. Y.; Yeunga, C. W.; Lib, J.; Mob, I.; Chanb, G. C. F. Self-assembled collagen–human mesenchymal stem cell microspheres for regenerative medicine. *Biomaterials* 2007, **28**, 4652–4666.
427. Short, B.; Brouard, N.; Occhiodoro-Scott, T.; Ramakrishnan, A.; Simmons, P. J. Mesenchymal Stem Cells. *Archives of Med. Res.* 2003, **34**, 565–571.
428. Ahmad, S. A.; Legget, G. J. Micro- and nanostructured poly(oligo, ethylene glycolmethacrylate) brushes grown from photopatterned halogen initiators by atom transfer radical polymerization. *Biointerphases* 2011, **6**, 8-15.
429. Sun, S.; Montague, M.; Critchley, K.; Chen, M. S.; Dressick, W. J.; Evans, S. D.; Leggett, G. J. *Nano Lett.* 2005, **6**, 29-33.
430. Sun, S.; Montague, M.; Critchley, K.; Chen, M.; Dressick, W. J.; Evans, S. D.; Leggett, G. J. Fabrication of Biological Nanostructures by Scanning Near-Field Photolithography of Chloromethylphenylsiloxane Monolayers. *Nano Lett.* 2006, **6**, 29-33.
431. Akiyama, S. K. Integrins in cell adhesion and signaling. *Hum Cell* 1996, **9**, 181-186.

-
432. John, G. S.; Graham J.; Underwood, P. A. Role of serum vitronectin and fibronectin in adhesion of fibroblasts following seeding onto tissue culture polystyrene, *Journal of Biomedical Materials Research* 1992, **26**, 861-884.
433. Garozzo, C.; Filetti, A.; Bongiorno, C.; La Magna, A.; Simone, F.; Puglisi, R. A. Room temperature evolution of gold nanodots deposited on silicon. *Gold Bull* 2014, **47**, 185–193.
434. Green, T. A. Gold etching for microfabrication. *Gold Bull* 2014, **47**, 205–216.
435. Jung, M.; El-Said, W. A.; Cho, J. Fabrication of gold nanodot arrays on a transparent substrate as a nanobioplatfrom for label-free visualization of living cells. *Nanotechnology* 2011, **22**, 1-8.
436. Zheng, J.; Nicovich, P. R.; Dickson, R. M. Highly Fluorescent Noble-Metal Quantum Dots. *Annu. Rev. Phys. Chem.* 2007, **58**, 409–431.
437. Lin, Y.; Zou, Y.; Mo, Y.; Guo, J.; Lindquist, R. J.; E-Beam Patterned Gold Nanodot Arrays on Optical Fiber Tips for Localized Surface Plasmon Resonance Biochemical Sensing. *Sensors* 2010, **10**, 9397-9406.
438. Lu, Ch.; Lipson, R. H. Interference lithography: a powerful tool for fabricating periodic structures. *Laser Photonics Rev.* 2010, **4**, 568-580.
439. Kim, M.; Ha, D.; Kim, T. Crack-photolithography” for high-throughput nanopatterning and nanofluidic applications. *Transducers* 2015, 1366-1369.
440. Tsaia, F. Y.; Jhuo, S. J.; Lee, J. T. Nanopatterning with 248 nm photolithography by photostabilizing bilayer Photoresists. *J. Vac. Sci. Technol. B* 2007, **25**, 426-429.
441. Gorman, B. C.; Biebuyck, H. A.; Whitesides, G. M. Use of a Patterned Self-Assembled Monolayer To Control the Formation of a Liquid Resist Pattern on a Gold Surface. *Chem. Mctter.* 1995, **7**, 252-254.
442. Kleineberg, U.; Brechling, A.; Sundermann, M.; Heinzmann, U. STM Lithography in an Organic Self-Assembled Monolayer. *Adv. Funct. Mater.* 2001, **11**, 208-212.
443. Kim, E.; Kumor, A.; Whitesides, G. M. Combining Potterned Self-Assembled Monolayers of Alkonethiolotes on Gold with Anisotropic Etching of Silicon to Generote Controlled Surfqce Morphologie. *J. Electrochem. Soc.* 1995, **142**, 628-633.

-
444. Mu, X.; Gao, A.; Wang, D.; Yang, P. Self-Assembled Monolayer-Assisted Negative Lithography. *Langmuir* 2015, **31**, 2922–2930.
445. Nicol, M. J. The Anodic Behaviour of Gold part i - oxidation in acidic solutions, *Gold Bull* 1980, **13**, 46–55.
446. Oh, S. Y.; Kim, H. J.; Choi, H. S. Deep UV Photopatterning of Biphenyl Thiol Self-Assembled Monolayer and its Physical Properties. *Molecular Crystals and Liquid Crystals* 2007, **463**, 229-236.
447. Guo, H. C.; Nau, D.; Radke, A.; Zhang, X. P.; Stodolka, J. ; Yang, X. L.; Tikhodeev, S. G.; Gippius, N.A.;Giessen, H. Large-area metallic photonic crystal fabrication with interference lithography and dry etching. *Applied Physics B* 2005, **81**, 271-275.
448. George , M. A.; Glaunsinger, W. S.; Thundat, T.; Lindsay, S. M. Electrical, Spectroscopic, and Morphological Investigation of Chromium Diffusion Through Gold films. *Thin Solid Films* 1990, **189**, 59-72.
449. Martinez, W. E.; Gregori , G.; Mates, T. Titanium diffusion in gold thin films. *Thin Solid Films* 2010, **518**, 2585–2591.
450. Mani, G.; Johnson, D. M.; Marton,D.; Dougherty, V. L.; Feldman, M. D.; Patel, D.; Ayon, A. A.; Agrawal, C. M. Stability of Self-Assembled Monolayers on Titanium and Gold. *Langmuir* 2008, **24**, 6774-6784.
451. Mastrangelo, F.; Fioravanti, G.; Quaresima, R.; Vinci, R.; Gherlone, E. Self-Assembled Monolayers (SAMs): Which Perspectives in Implant Dentistry?. *J. Biomater. Nanobiotechnol.* 2011, **2**, 533-543.
452. Helmy, R.; Fadeev, A. Y. Self-Assembled Monolayers Supported on TiO₂: Comparison of C₁₈H₃₇SiX₃ (X) H, Cl, OCH₃), C₁₈H₃₇Si(CH₃)₂Cl, and C₁₈H₃₇PO(OH)₂. *Langmuir* 2002, **18**, 8924-8928.
453. Xiao, S.J.; Textor, M.; Spencer, N.D.; Wieland, M.; Keller, B.; Sigrist, H. Immobilization of the cell-adhesive peptide Arg–Gly–Asp–Cys (RGDC) on titanium surfaces by covalent chemical attachment *Journal of materials science: Materials in Medicine* 1997, **8**, 867-872.

-
454. Martin, H. J.; Schulz, K. H.; Bumgardner, J. D.; Walters, K. B. XPS Study on the Use of 3-Aminopropyltriethoxysilane to Bond Chitosan to a Titanium Surface. *Langmuir* 2007, **23**, 6645-6651.
455. Panzarasa, G.; Soliveri, G.; Sparnaccia, K.; Ardizzonebc, S. Patterning of polymer brushes made easy using titanium dioxide: direct and remote photocatalytic lithography. *Chem. Commun.* 2015, **51**, 7313-7316.
456. Raynor, J. E.; Petrie, T. A.; Fears, K. P.; Latour, R. A.; Garcí'a, A. J.; Collard, D. M. Saccharide Polymer Brushes To Control Protein and Cell Adhesion to Titanium. *Biomacromolecules* 2009, **10**, 748-755.
457. Sackmann, E.; Tanaka, M. Supported membranes on soft polymer cushions: fabrication, characterization and applications. *Tibtech* 2000, **18**, 58-64.
458. McCabe, I. P.; Forstner, M. B. Polymer Supported Lipid Bilayers. *Open Journal of Biophys.* 2013, **3**, 59-69.
459. Brain, A. A.; Mcconnell, M. A. Allogeneic stimulation of cytotoxic T cells by supported planar membranes. *Proc. Natl. Acad. Sci. USA* 1984, **81**, 6160-6163.
460. Melby, E. C.; Mensch, A. C.; Lohse, S. E.; Hu, D.; Orr, G.; Murphy, C. J.; Hamersb, R. J.; Pedersen, J. A. Formation of supported lipid bilayers containing phase-segregated domains and their interaction with gold nanoparticles. *Environ. Sci.: Nano*, 2016, **3**, 45-55.
461. Cheng, N.; Bao, P.; Evans, S. D.; Leggett, G. J.; Armes, S. P. Facile Formation of Highly Mobile Supported Lipid Bilayers on Surface-Quaternized pH-Responsive Polymer Brushes. *Macromolecules* 2015, **48**, 3095-3103.
462. Mashaghi, S.; van Oijen, A. M. A Versatile Approach to the Generation of Fluid Supported Lipid Bilayers and Its Applications. *Biotechnol. Bioeng.* 2014, **9999**, 1-6.
463. Zhang, Z.; Chao, T.; Chen, S.; Jiang, S. Superlow Fouling Sulfobetaine and Carboxybetaine Polymers on Glass Slides. *Langmuir* 2006, **22**, 10072-10077.
464. Sun, S.; Chong, K. S. L.; Leggett, G. J. Photopatterning of self-assembled monolayers at 244 nm and applications to the fabrication of functional microstructures and nanostructures. *Nanotechnology* 2005, **16**, 1798-1808.

-
465. Arya, S. A.; Solanki, P. R.; Singh, R. P.; Pandey, M. K.; Datta, M.; Malhotra, B. D. Application of octadecanethiol self-assembled monolayer to cholesterol biosensor based on surface plasmon resonance technique. *Talanta* 2006, **69**, 918–926.
466. Hild, R.; David, C.; Müller, H.; Völkel, B.; Kayser, D.; Grunze, M. Formation and Characterization of Self-assembled Monolayers of Octadecyltrimethoxysilane on Chromium: Application in Low-Energy Electron Lithography. *Langmuir* 1998, **14**, 342-346.
467. Tsargorodska, A.; Cartron, M. L.; Vasilev, C.; Kodali, G.; Mass, O. A.; Baumberg, J. J.; Dutton, P. L.; Hunter, C. N.; Törmä, P.; and Leggett, G. J. Strong Coupling of Localized Surface Plasmons to Excitons in Light-Harvesting Complexes, *Nano Lett.* 2016, **16**, 6850–6856.